INELASTIC LIGHT SCATTERING IN LOW DIMENSIONAL QUANTUM SPIN SYSTEMS

BY

ADRIAN MIHAI GOZAR

LIC., University of Bucharest, 1997
MAG., University of Bucharest, 1998

DISSERTATION

Submitted in partial fulfillment of the requirements
for the degree of Doctor of Philosophy in Physics
in the Graduate College of the
University of Illinois at Urbana-Champaign, 2004

Urbana, Illinois

INELASTIC LIGHT SCATTERING IN LOW DIMENSIONAL QUANTUM SPIN SYSTEMS

Adrian Mihai Gozar, Ph.D.
Department of Physics
University of Illinois at Urbana-Champaign, 2004
Miles V. Klein, Advisor

We have studied electronic excitations from lower dimensional spin $S = 1/2$ systems with antiferromagnetic (AF) exchange correlations by means of inelastic light scattering. We focussed on magnetic scattering in the 1 - 500 meV energy range from one and two triplet excitations as well as on their symmetry and corresponding light coupling mechanism.

The data in $Sr_{14-x}Ca_xCu_{24}O_{41}$, which contain quasi-one dimensional (1D) two-leg ladder units, reveal a well defined two-magnon resonance at 370 meV whose spectral width and resonance properties are contrasted to its counterparts in 2D square lattices and the multi-spinon scattering from quasi-1D $S = 1/2$ AF chains. Low energy spectra from lightly doped two-leg ladders reveal characteristic electronic excitations out of a charge density ground state arising from many-body electronic interactions.

One-magnon excitations are observed in the quasi-2D antiferromagnetically ordered $La_{2-x}Sr_xCuO_4$ crystals. We map the anisotropic magnetic field dependence of the 2 mev spin-wave branch arising due to antisymmetric spin exchange and we are able to understand the data using a canonical form of the spin Hamiltonian. We observed magnetic field induced modes whose dynamics allowed us to discover a spin-flop like transition for field orientations perpendicular to the easy-axis.

Based on resonance properties and energy considerations we were able to identify in the 0 - 200 meV range a multi-spinon Raman continuum from the quasi-1D AF spin chains of NaV_2O_5 . At T = 10 K we observed one-magnon scattering whose the selection rules in external magnetic fields were explained in terms of the antisymmetric spin interaction and Fleury-Loudon type coupling.

The symmetry and light coupling mechanisms to elementary triplets and multiparticle bound states were the topics studied in $SrCu_2(BO_3)_2$. The analysis of a four

spin cluster allowed us to propose a resolution of these problems for the real space localized elementary excitations and, again, the antisymmetric spin-exchange was suggested to play an important role in this case. Two distinct light coupling mechanisms were found responsible for the observed resonance behavior of the magnetic modes.

Acknowledgements

Working for a doctorate in physics is not only about physics but is as much an experience of life. What is dicussed in this thesis is not a single person's work so I would like to acknowledge the people who contributed to my education in science and stood by me in the every day life of this exciting time period.

In the first place I would like to express my gratitude to Dr. Girsh Blumberg for his advice, energy, integrity and the many enlivening and insightful discussions from which I learned new physics throughout this time. For teaching me the experimental aspects of optical Raman scattering, cryogenics, etc., and to make me understand that having patience and doing one's best to get good and systematic data often makes the difference between finding a solution to a problem and just fantasizing on a wrong path. I also thank him for teaching me the things that matter in the long run and for showing me that when a "dead end" sign is seemingly unavoidable there has to be a way out.

Next I am grateful to Brian Dennis for his constant support and patience with me in the lab as well as for his good humor and many vivid chats which helped me a lot to overcome the many frustrations involved in research. I owe him much of what I know about the real lab work and goes beyond "being an experimentalist from a theoretical point of view".

I would like to thank Professor Miles Klein for the discussions we had, for his probity and promptitude in his answers whenever I needed to talk to him as well as for offering many times his support for travel or my stay in New Jersey. I truly admire his expertise and subtlety; some of his remarks started to make sense to me

only long time after our discussions.

I enjoyed the exchange of ideas with many Bell Labs people and I want to mention in particular Sriram Shastry with whom I collaborated on many occasions. The work presented here would not have been possible without the help and the samples provided to us by ex Bell Labs and outside collaborators like Yoichi Ando, Hiroshi Eisaki, Paul Canfield, Hiroshi Kageyama and Sang Cheong. I want to thank especially Yoichi Ando with whom I had many useful interactions. I enjoyed working with Peter Abbamonte and I liked his good humor, frankness and the direct way of expressing himself. From the University of Bucharest I am particularly grateful to Professor Dan Brancus and Dr. Andrei Manolescu who guided my first research projects.

I would like to acknowledge all the people in Urbana-Chapaign whom I owe for making my coming to the United States a pleasant and smooth process, especially those from the Physics Department. This is a great place for doing science which emulates and inspires the students. Also, my stay at Bell Labs in good and bad times would not have been possible without the support of people like Federico Capasso, Eric Isaacs, Pierre Wiltzius and Cherry Murray.

Last but not least, my thanks go to all my folks in Romania who always supported and believed in me and also to my friends who made my life more enjoyable and with whom I had a lot of fun. I think here especially of S.C., A.E., T.S., M.M., O.T., S.E., D.C., A.D. and O.M.

Contents

Chapter 1

Introduction

1.1 Introduction to inelastic light scattering

Due to historical reasons Raman scattering is associated most of the time with the inelastic light scattering by molecular vibrations or optical phonons in crystals. Nowadays this term refers to processes in which incoming photons, usually in or around the visible spectrum, are scattered inelastically by any elementary excitations associated with the electronic or vibrational degrees of freedom of solid, liquid or gaseous materials. Exceptions can be long wavelength acoustic excitations like phonons and magnons, and these usually constitute the object of Brillouin scattering. A *Stokes* process is one when the incoming radiation frequency ω_{in} is larger than the energy of the scattered light ω_s. If, instead, $\omega_{in} < \omega_s$, then we have an *anti-Stokes* process and in thermal equilibrium this interaction is strongly temperature dependent because it relies on the probability of finding the system out of its ground state. During the Raman process, one or multiple quanta of elementary excitations can be created defining first, or higher order scattering. Because of the relatively high light frequency employed in current experiments, the dominant contributions to the matrix elements are often due to excitations of electrons across energy band gaps (inter-band transitions) and it is known that one could expect an enhancement of the scattering intensity when either ω_{in} or ω_s are close to these gaps. The study of such dependencies, which

could also provide some information about the high energy electronic degrees of freedom, constitute the object of the *resonant Raman scattering*. In this work we will be concerned with incoming photon energies in the visible spectrum (more specifically λ between 400 and 800 Å) which sets a constraint on the type of excitations we are looking at in crystalline solids because of quasi-momentum conservation, $q = k_{in} - k_s$, where k denotes the wavevector of the light and q the quasi-momentum of an internal excitation. This is a particular case of the general rule according to which any invariance of a given physical system with respect to a certain group of symmetry elements generates a conservation law, for periodic crystals this being the translation with any number of lattice constants. Lattice constants in solids are typically of the order of 5-10 Å which are much smaller than the wavelengths used. As a result $\pi/a \gg 2\pi/\lambda = k$ so one can say with a good approximation that the created excitation is from the Brillouin zone center ($q \approx 0$). Exceptions can occur when disorder destroys the crystal periodicity or under strong absorption conditions when the imaginary parts of the optical parameters are non-negligible.

Macroscopic approach to Raman scattering – The incoming photon field has electric and magnetic components. It turns out that in general the strongest coupling does not come from the direct light coupling to the magnetic moments but through the coupling to the electric moments of the scattering media. In a first approximation one can think about a material as being made of a collection of small electric dipoles (for instance harmonic oscillators made out of charged electrons bound by 'springs' to positive charges, the nuclei) giving rise to a finite macroscopic polarization. No matter what is the fundamental frequency of such harmonic oscillators, in the absence of any internal excitation (which in principle could be generated by some coupling between them) these small dipoles will always oscillate at the frequency of the incident electromagnetic field ω_{in} giving rise solely to elastic light scattering. A characteristic excitation of the medium can modulate its susceptibility, i.e., the polarizability of the system formed by an ensemble of coupled oscillators may depend on whether they are together in the ground state or in, say, an excited collective

vibrational state. If one denotes by Q a certain dynamical variable associated with the excitation, for instance some normal coordinate, the linear relation between the polarization P and the external electric field E can be written as [1]:

$$\mathbf{P} = \chi(\omega_{in})\mathbf{E}_{in} + \frac{\partial \chi}{\partial Q}(\omega_{in}, -\omega)Q(\omega)\mathbf{E}_{in} + ... \tag{1.1}$$

Here ω is the frequency of the internal excitation, $\chi(\omega_{in})$ is the first order susceptibility giving rise to elastic scattering while the next terms generate single or multi-particle scattering with energies $\omega_s = \omega_{in} - \omega, \omega_{in} - 2\omega$ ... etc., and they describe the susceptibility modulation due to the excitations. The second term in Eq. 1.1, which leads to single particle scattering, is a tensor of second rank transforming like a product of two vectors. These tensors can be chosen to constitute basis functions for the irreducible representations of the given symmetry group of the structure studied and for a every representation one can determine their zero elements as well as the relations between the non-vanishing components [1].

For a non-magnetic isotropic medium without free carriers, one can obtain from Maxwell's equations a relation between the fluctuating polarization in Eq. 1.1 and the scattered electric field, as well as a general solution as shown in the following equations:

$$(\nabla^2 + k_s^2)\mathbf{E}_s(\mathbf{r}, \omega_s) = -\frac{4\pi\omega_s^2}{c^2}\mathbf{P}(\mathbf{r}, \omega_s) \;\; \Rightarrow \;\; \mathbf{E}_s(\mathbf{r}, \omega_s) = \frac{\omega_s^2}{c^2}\int_{\bar{V}} d^3\mathbf{r}' \frac{\exp(ik_s|\mathbf{r} - \mathbf{r}'|)}{|\mathbf{r} - \mathbf{r}'|}\mathbf{P}(\mathbf{r}', \omega_s) \tag{1.2}$$

Here k_s is the light wavevector in the medium at the frequency of the scattered light and $\bar{V}$ is the scattering volume [2]. The expression for the incoming, I_{in}, and scattered, I_s, electromagnetic intensities in the directions of $\mathbf{e}_{in}$ and $\mathbf{e}_s$ are given by $I_{in,s} \propto c\ n_{in,s} < |\mathbf{e}_{in,s} \cdot \mathbf{E}_{in,s}^2| >$, where $<>$ means a time average and n denotes the index of refraction at the corresponding frequencies. Taking into account that in defining the cross section $d^2\sigma/d\Omega d\omega_s$, one is interested in the rate at which the energy is removed from the incident beam (an object which is related to the number of photons, see Chapter 2), the energy flux has to be divided by frequency leading to $d^2\sigma/d\Omega d\omega_s = (\omega_{in} I_s)/(\omega_{in} I_{in})$. One obtains, far from the scattering source (where

one can define a vector $\mathbf{k}_s \parallel \mathbf{r}$), the following expression for the differential scattering cross section [2]:

$$\frac{d^2\sigma}{d\Omega d\omega_s} = \frac{\omega_{in}\omega_s^3 n_s \bar{V}}{c^4 n_{in}|E_{in}|^2} \int_{\bar{V}} d^3(\mathbf{r}_1 - \mathbf{r}_2)\ \exp(i\mathbf{k}_s|\mathbf{r}_1 - \mathbf{r}_2|)) < [\mathbf{e}_s \cdot \mathbf{P}^*(\mathbf{r}_1, \omega_s)][\mathbf{e}_s \cdot \mathbf{P}(\mathbf{r}_2, \omega_s)] > \tag{1.3}$$

The most important term in Eq. 1.3 is the one under the integral which is a pair correlation function involving the fluctuating polarization. It is also worth noting the fourth power dependence of the cross section on the photon frequency. The relevant parts of the susceptibility tensor are determined by the polarization to the incoming field and one can see now that by using a polarizer to determine $\mathbf{e}_{in}$ and an analyzer for setting $\mathbf{e}_s$ one can access different components of the Raman tensors within a given group representation.

Quantum theory of Raman scattering – An analogous relation to Eq. 1.3 can be obtained starting from the microscopic Hamiltonian which describes the coupling of the light to a system of electrons. If $\mathbf{A}(\mathbf{r}, t)$ is the vector potential of the radiation field and we have an ensemble of electrons with charge e and mass m, the light coupling is:

$$H_{int} = H_1 + H_2 = \frac{e^2}{2m} \sum_j \mathbf{A}^2(\mathbf{r}_j, t) - \frac{e}{2m} \sum_j [\ \mathbf{p}_j \cdot \mathbf{A}(\mathbf{r}_j, t) + \mathbf{A}(\mathbf{r}_j, t) \cdot \mathbf{p}_j\ ] \tag{1.4}$$

With the help of the number density and number current density operators, which in the coordinate representation, can be written as $\rho(\mathbf{r}) = \sum_j \delta(\mathbf{r} - \mathbf{r}_j)$ and $\mathbf{j}(\mathbf{r}) = (e\hbar/2im) \sum_j [\nabla_j \delta(\mathbf{r} - \mathbf{r}_j) + \delta(\mathbf{r} - \mathbf{r}_j)\nabla_j]$, one can write the terms Eq. 1.4 in the form:

$$H_1 = \frac{e^2}{2m} \int d^3\mathbf{r}\ \rho(\mathbf{r})\ \mathbf{A}^2(\mathbf{r}, t) \quad \text{and} \quad H_2 = e \int d^3\mathbf{r}\ \mathbf{j}(\mathbf{r}) \cdot \mathbf{A}(\mathbf{r}, t) \tag{1.5}$$

Raman scattering is a two-photon process, which means that the matrix elements for the inelastic scattering can be obtained in the lowest orders by writing down the perturbation expressions for $\hat{H}_1$ and $\hat{H}_2$ in first and second order respectively. Using Eq.1.5 and Fermi's golden rule a general expression for the Raman scattering cross section can be obtained in terms of a generalized transition susceptibility χ_R [3]:

$$\frac{d^2\sigma}{d\Omega d\omega_s} = \frac{\omega_{in}\omega_s^3 n_s \bar{V}}{c^2 n_{in}} [\ \sum_f\ | < f|\chi_R|i > |^2\ \delta(\omega_i - \omega_f - \omega)\ ] \tag{1.6}$$

$$\text{with} \quad < f|\chi_R|i >= \frac{e^2\bar{V}}{\omega_{in}\omega_s}\sum_m [\frac{< f|j(\mathbf{k}_s)|m >< m|j(-\mathbf{k}_{in})|i >}{\hbar(\omega_m - \omega_i - \omega_{in} - i\eta)} + \frac{< f|j(-\mathbf{k}_{in})|m >< m|j(\mathbf{k}_s)|i >}{\hbar(\omega_m - \omega_i + \omega_s + i\eta)}] - \frac{e^2}{m\omega_{in}\omega_s}\,\mathbf{e}_{in}\cdot\mathbf{e}_s\,(< f|\rho(-\mathbf{q})|i >) \qquad (1.7)$$

In the equation above $|i>$, $|f>$ and $|m>$ denote initial, final and intermediate states of the system and ω_i, ω_f and ω_m their energies. In particular $|i>$ and $|f>$ represent states of the uncoupled matter-photon system: transverse electromagnetic field and the complete interacting many body system. The infinitesimal number η in the denominator has to do with the correct choice of the boundary conditions for the outgoing wave. The expressions in the equations above involve matrix elements of the Fourier transformed density and current operators, which in the coordinate representation are $\rho(\mathbf{q}) = \int d^3\mathbf{r}\; e^{-i\mathbf{q}\cdot\mathbf{r}}\;\rho(\mathbf{r}) = \sum_j\; e^{-i\mathbf{k}\cdot\mathbf{r}_j}$ and $j(\mathbf{k}_{in,s}) = \int d^3\mathbf{r}\; e^{-i\mathbf{k}_{in,s}\cdot\mathbf{r}}\;[\mathbf{e}_{in,s}\cdot\mathbf{j}(\mathbf{r})] = (1/m)\sum_j e^{-i\mathbf{k}_{in,s}\cdot\mathbf{r}}\;(\mathbf{p}_j + \hbar\mathbf{k}_{in,s}/2)\cdot\mathbf{e}_{in,s}$. If the system is not at zero temperature a statistical average has to be done, for instance in a canonical ensemble there appears an additional sum over the initial states weighted by e^{-E_i/k_BT}. Note that in lowest order discussed here the H_1 term is the non-resonant contribution while H_2 involves transitions to intermediate states and a resonant enhancement can be observed if the photon frequencies are close to the difference in energy between the intermediate and the initial/final states.

Eq. 1.7 can be applied to calculate a phononic Raman scattering cross section. The relevant part in this case is the first term in Eq. 1.7 because the states $|i>$, $|f>$ and $|m>$ as well as the difference $\omega_m - \omega_i$ contain implicit vibrational contributions as a result of electron-phonon coupling. In order to see how this comes about, one can consider for example the case of an insulator within the dipole approximation, which means letting the light and excitation wavevectors, $\mathbf{k}_{in}$, $\mathbf{k}_s$ and $q = \mathbf{k}_{in} - \mathbf{k}_s$, go to zero. In this case, the current operator becomes proportional to the total momentum and, using a relation of the type $(\varepsilon_\beta - \varepsilon_\alpha) < \alpha|\mathbf{r}|\beta >=< \alpha|\mathbf{p}|\beta >$ which can be derived from the commutation relations of the position operators and the Hamiltonian ($|\alpha>$ and $|\beta>$ being energy eigenfunctions), one can relate the matrix

elements of the current operator to those of the total dipole moment $\mathbf{M}$. This change will also absorb the $1/(\omega_{in}\omega_s)$ factor in the first term of Eq. 1.7. Every eigenstate of the system can be written as a product of electronic and phononic contribution. In the adiabatic approximation, the electronic part will depend parametrically on the nuclei coordinates $\{Q\}$. If we deal with an insulator, no electronic excitation will occur and one can consider that the initial and final states can be written as a product of the same electronic ground state with vibrational states corresponding to different phononic quanta. As a result of all these approximations, a more tractable formula can be derived [3]. With $|v_f>$ and $|v_i>$ denoting the vibrational state in the initial and final coupled electron-phonon states, the matrix element $<f|\chi_R|i>$ can be written as $<v_f|\chi_{\{Q\}}|v_i>$ with the susceptibility $\chi_{\{Q\}}$ given by:

$$\chi_{\{Q\}} = \frac{1}{\hbar\bar{V}} \sum_{e\neq g} \left[\frac{<g|\mathbf{M}\cdot\mathbf{e}_{in}|e><e|\mathbf{M}\cdot\mathbf{e}_s|i>}{\omega_e - \omega_g - \omega_{in}} + \frac{<g|\mathbf{M}\cdot\mathbf{e}_s|e><e|\mathbf{M}\cdot\mathbf{e}_{in}|i>}{\omega_e - \omega_g + \omega_s} \right] \tag{1.8}$$

where $|g>$ and $|e>$ are ground and excited states characterized by sets of frozen nuclei coordinates which minimize the adiabatic potential. The dependence on $\{Q\}$ in Eq. 1.8 comes from the parametric dependence of the electronic states on nuclear coordinates. Although still complicated, these approximations simplify considerably the general formulas 1.6 and 1.7.

In terms of electronic scattering, a useful result connecting the electronic Raman scattering cross section due to the off-resonant term H_1 to the linear response function to an external potential (which is related to the density-density correlation function) can be obtained [4, 5]. The relevant term is the second one in Eq. 1.7 and one has:

$$\frac{d^2\sigma}{d\Omega d\omega_s} = \left(\frac{\omega_s}{\omega_{in}}\right)^2 r_0^2 (n_\omega + 1)(\mathbf{e}_{in}\cdot\mathbf{e}_s)^2 \frac{\hbar q^2}{4\pi e^2}\ Im\left[-\frac{1}{\varepsilon(q,\omega)}\right] \tag{1.9}$$

where $n(\omega)$ is the Bose function, $r_0 = e^2/(mc^2)$ is the classical electron radius and $\varepsilon(q,\omega)$ is the dielectric function. Eq. 1.9 says that the off-resonant electronic scattering probes the longitudinal channel, the peaks in the Raman response will be given by the zero's of the dielectric response function $\varepsilon(q,\omega)$. This relation will be used in Chapter 3 to evaluate the longitudinal response of a system of free carriers interacting

electromagnetically with a charge density wave.

A last word about group symmetry analysis. Molecular or crystalline systems have usually a given set of symmetry operations under which they remain invariant. This set of elements which commute with the Hamiltonian of the system forms a group. The eigenfunctions of the Hamiltonian can be projected in order to obtain basis functions for the irreducible representations of the symmetry group. Now, from Eqs. 1.6 and 1.7 one can see that the computation of the cross section involves necessarily evaluations of matrix elements of the form $I = \int d\tau\ \psi_f^*(\tau)\hat{X}(\tau)\psi_i(\tau)$. Assume that $\psi_i(\tau)$, $\psi_f(\tau)$ and the operator $\hat{X}(\tau)$ transform according to the Γ_i, Γ_f and $\Gamma_{\hat{X}}$ representations of the symmetry group and the Hamiltonian. The matrix element I does not vanish only if the representation Γ_f^* is contained in the decomposition of the product $\Gamma_{\hat{X}} \times \Gamma_i$. Equivalently, the fully symmetric representation has to be contained in the product $\Gamma_f^* \times \Gamma_{\hat{X}} \times \Gamma_i$. Because in a given group the character of a product of representations is given by the product of characters, the latter statement can be written as $\sum_{\hat{R}}\ \chi_f^*(\hat{R}) \cdot \chi_{\hat{X}}(\hat{R}) \cdot \chi_i(\hat{R}) \neq 0$, where $\{\hat{R}\}$ is the set of symmetry elements of the Hamiltonian and $\chi_\alpha(\hat{R})$ is the character of the irreducible representation α corresponding to the class of elements to which $\hat{R}$ belongs.

1.2 Magnetic Raman scattering

1.2.1 One-magnon Raman scattering

A phenomenological approach to this coupling may be very useful because one could derive effective magnetic interaction Hamiltonians and general selection rules for one-magnon Raman scattering, a non-trivial result given the sometimes complicated nature of the two-photon Raman process. This can be done by expanding the susceptibility in powers of the spin operators in the manner of Eq. 1.1. A simple and useful example is discussed in Ref. [2] where an effective interaction Hamiltonian originating from the scalar product of the polarization $\mathbf{P}$ from Eq. 1.1 and the scattered electric

field $\mathbf{E}_s$ can be written as $\mathcal{H}_{int} = \sum_{\mathbf{r}} \sum_{\alpha,\beta} \mathbf{E}_{in}^{\alpha} \chi^{\alpha\beta}(\mathbf{r}) \mathbf{E}_s^{\beta}$, where $\mathbf{r}$ runs over the magnetic ions positions and $\mathbf{P}^{\xi}(\mathbf{r}) = \sum_{\eta} \chi^{\xi\eta}(\mathbf{r}) \mathbf{E}_{in}^{\eta}$. One can express the susceptibility as [2, 6]:

$$\chi^{\alpha,\beta}(\mathbf{r}) = \chi_0^{\alpha\beta}(\mathbf{r}) + \sum_{\mu} K_{\alpha\beta\mu}(\mathbf{r}) \mathbf{S}_{\mathbf{r}}^{\mu} + \sum_{\mu\nu} G_{\alpha\beta\mu\nu}(\mathbf{r}) \mathbf{S}_{\mathbf{r}}^{\mu} \mathbf{S}_{\mathbf{r}}^{\nu} + \\ + \sum_{\mu,\nu} \sum_{\delta} H_{\alpha\beta\mu\nu}(\mathbf{r}, \delta) \mathbf{S}_{\mathbf{r}}^{\mu} \mathbf{S}_{\mathbf{r}+\delta}^{\nu} + ... \tag{1.10}$$

In this relation K, G and H are complex tensors, their contraction with spin operators which are axial vectors rendering a second rank tensor. Let us see what the effect of the first order term in spin operators is. For a cubic environment one can show using projection operators that the only non-vanishing components of K are of the type $K_{\alpha\beta\gamma}$ with $\alpha \neq \beta \neq \gamma$ and they satisfy: $K_{xyz} = K_{yzx} = K_{zxy} = -K_{xzy} = -K_{yxz} = -K_{zyx} = K$. Inserting this in Eq. 1.10 one obtains:

$$\mathcal{H}_{int}^{a} = K \sum_{\mathbf{r}} [(E_{in}^{x} E_s^{y} - E_{in}^{y} E_s^{x}) \cdot S_{\mathbf{r}}^{z} + (E_{in}^{y} E_s^{z} - E_{in}^{z} E_s^{x}) \cdot S_{\mathbf{r}}^{x} + \\ + (E_{in}^{z} E_s^{x} - E_{in}^{x} E_s^{z}) \cdot S_{\mathbf{r}}^{y}] = K(\mathbf{E}_{in} \times \mathbf{E}_{in}) \cdot \mathbf{S}_{tot} \tag{1.11}$$

The equation above clearly shows that the strongest one-magnon contribution (which is expected to come from the lowest order magneto-optic coupling) in cubic crystals is to be found in cross polarization. One can also express the terms in Eq. 1.11 in a less compact form but more useful if dealing with (anti)-ferromagnons, excitations out of a long ranged magnetically ordered state [7]. In this case the relevant magnon creation operators (transverse excitations from the ordered state) are $\mathbf{S}_{\mathbf{r}}^{\pm}$, which are defined as $S_{\mathbf{r}}^{x} \pm i S_{\mathbf{r}}^{y}$ [2]. The Stokes contribution can be identified in this case with the $(E_{in}^{z} E_s^{+} - E_{in}^{+} E_s^{z}) \cdot S_{\mathbf{r}}^{-}$ and one obtains scattering contributions only when the prefactor is nonzero.

The terms in Eq. 1.11 can be derived on the basis of microscopic arguments [7]. A cartoon with the Raman process for a simple case is shown in Fig. 1.1. Although apparently the spin part of the wave functions would not allow the end result of two electric dipole transitions to be a state with a flipped spin, this is possible in the presence of the spin-orbit coupling $\lambda \, \mathbf{L} \cdot \mathbf{S}$. This is illustrated in Fig. 1.1 for a

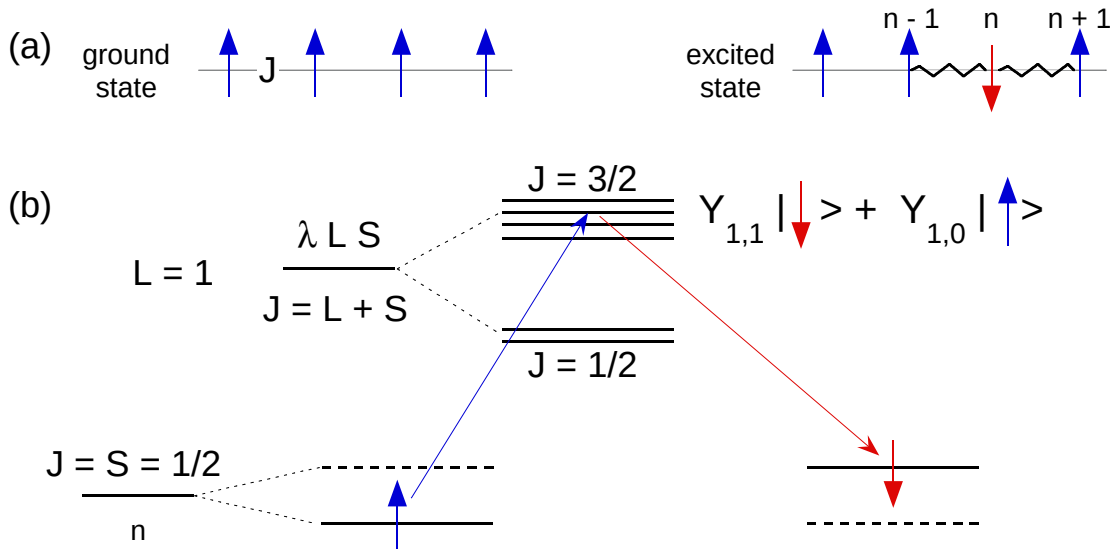

Figure 1.1: (a) The ground state for a $S = 1/2$ ferromagnet (left) and an excited spin state (right). A true eigenstate in the spin wave model is a linear combination of states like the one shown on the right. (b) Cartoon depicting the transition from the ground to an excited magnetic state *via* two electric dipole transitions in the presence of spin-orbit coupling $\lambda\ \mathbf{L}\cdot\mathbf{S}$. We show the case of a $S = 1/2$ ground state whose spin up spin down states are split by the exchange field and a concrete example for two possible electric dipole transitions from the lowest L = 0 doublet to an excited p type multiplet which leave the system in an excited magnetic state. The transitions shown here are between levels of the same ion. $Y_{l,m}$ represent spherical harmonics. Note that J in panel (a) denotes the super-exchange while in panel (b) it denotes the total angular momentum $\mathbf{J} = \mathbf{L} + \mathbf{S}$.

simple case: a ferromagnet with an unpaired spin $S = 1/2$ on the upper S (which means $|\mathbf{L}| = 0$) shell and another higher $|\mathbf{J}| = 3/2$ multiplet split from the ground state by a crystal field. Both of the ground state doublet states, $Y_{0,0} \otimes |\uparrow>$ and $Y_{0,0} \otimes |\downarrow>$, which are split by the exchange field proportional to the super-exchange J can have for instance non-vanishing electric dipole matrix elements with the state $(1/\sqrt{2})(Y_{1,1} \otimes |\downarrow> + Y_{1,0} \otimes |\uparrow>)$ which belongs to the $|\mathbf{J}| = 3/2$ multiplet. Because the spin-orbit coupling mixes spin-up and spin-down states, the spin part of the wavefunctions does not kill the transition.

A calculation from first principles of the effective spin Hamiltonian responsible for one-magnon Raman was done by Fleury and Loudon in Ref. [7]. They considered a slightly more complicated case than in Fig. 1.1, namely their results take into account all possible intermediate states and are applicable for the case for a general spin S

but the transitions taken into account are still between $|\mathbf{L}| = 0$ and $|\mathbf{L}| = 1$ orbital states. The calculation renders a microscopic expression of the tensor components K from Eq. 1.11 for the Stokes scattering:

$$K = \left(\frac{e^2\lambda}{2^{3/2}}\right) < Y_{0,0}|z|Y_{1,0} >< Y_{1,1}|x - iy|Y_{0,0} > \left[\frac{1}{(E - \hbar\omega_{in})^2} + \frac{1}{(E + \hbar\omega_s)^2}\right] \quad (1.12)$$

where E is the energy difference between the S and P orbital states Practical evaluation of K from Eq. 1.12 is still very difficult because the atomic states needed for the calculation of the matrix elements are not accurately known. We note that further contribution to the one-magnon scattering can be obtained from the other terms in Eq. 1.10. There are contributions involving both the tensors G and H but they appear in higher order perturbation theory. The important feature of the term involving tensor H is that it gives rise to two-magnon scattering and this will be discussed in the following.

1.2.2 Two-magnon Raman scattering

When extended to higher order, processes of the type described in Eqs. 1.11 or 1.12 can give a two-magnon contribution. However, two-magnon scattering is usually observed to be stronger than the one-magnon scattering, apparently incompatible with a process occurring in higher order. This difficulty was resolved by the suggestion of an alternative and more efficient mechanism called the exchange scattering mechanism (or photon induced spin exchange) [6, 7]. While one-magnon scattering can take place in both ferro- and antiferromagnets, the spin exchange can occur only in the latter type of materials. The reason is that one can have third order processes with $\Delta S_z = 0$ (second order in the electric dipole interaction and first order in the exchange) which consists of exchanging a pair of coupled spins on *opposite* sublattices, again with the help of high energy electronic states.

Considering the H term in the susceptibility expansion from Eq. 1.10 and particularizing again for the cubic symmetry as it was done in Eq. 1.11, a formula for an effective Raman spin interaction Hamiltonian for two-magnon scattering can be

obtained:

$$\mathcal{H}^b_{int} = \sum_{\mathbf{r},\delta} \left[(H_1 - \frac{1}{3}H_3)\mathbf{E}_{in} \cdot \mathbf{E}_s + H_3(\mathbf{E}_{in} \cdot \hat{\delta})(\mathbf{E}_s \cdot \hat{\delta}) \right] \mathbf{S}_\mathbf{r} \cdot \mathbf{S}_{\mathbf{r}+\delta} \tag{1.13}$$

where $\hat{\delta}$ is a unit vector in the direction of the nearest neighbor and H_1 and H_3 are non-vanishing magneto-optic coefficients. The first terms will give a contribution in the fully symmetric channel while the second one in the Γ_3 representation in the notation of Ref. [8]. For tetragonal crystals like $La_{2-x}Sr_xCuO_4$, Γ_3 becomes the B_{1g} representation. It is worth noting that if we consider only nearest-neighbor Heisenberg interactions between spin, the interaction Hamiltonian given by the first term in Eq. 1.13 commutes with the system Hamiltonian so it will have no contribution to inelastic processes. It is well established by Raman scattering in cubic and tetragonal crystals [2] that it is the second term in Eq. 1.13 which gives the largest contribution.

A microscopic derivation of Eq. 1.13 was done in Ref. [7]. The scalar product of spin in this equation involves terms of form $S_i^- S_j^+$ which destroy/create magnons at the lattice sites i and j which belong to distinct sublattices. A representative matrix element for the double exchange process involving magnons with opposite wavevectors $\mathbf{k}$ and $-\mathbf{k}$ is [7]:

$$M_{i\to j} = \left[\sum_{\mu,\nu} \frac{< \phi_{j\uparrow}|\mathbf{E}_s \cdot \mathbf{r}_i|\phi_{\nu\uparrow} > V_{ij}^{\mu\nu} < \phi_{\mu\uparrow}|\mathbf{E}_{in} \cdot \mathbf{r}_i|\phi_{i\uparrow} >}{(E_\nu + \hbar\omega_k - \hbar\omega_{in})(E_\nu - \hbar\omega_s)} \right] S_i^- S_j^+ \tag{1.14}$$

where ϕ_i and $\mathbf{r}_i$ denote electronic orbital states and the coordinate of the electron responsible for the magnetic properties of ion i respectively. The matrix element due to Coulomb exchange in the intermediate state is given by $V_{ij}^{\mu\nu} =< \phi_{i\downarrow}\phi_{\nu\uparrow}|e^2/r_{ij}|\phi_{j\downarrow}\phi_{\mu\uparrow} >$. A cartoon with the photon induced spin exchange process is shown in Fig. 1.2.

All of the materials presented in the following chapters, $(Sr,La)_{14-x}Ca_xCu_{24}O_{41}$, $La_{2-x}Sr_xCuO_4$, $SrCu_2(BO_3)_2$ or NaV_2O_5 belong to the class of strongly correlated electron systems. This means that the wavefunctions to be used in the calculations like Eq. 1.12 or 1.14 are not single particle but true many-body states. It would be interesting to see if some results derived for more conventional magnetic materials

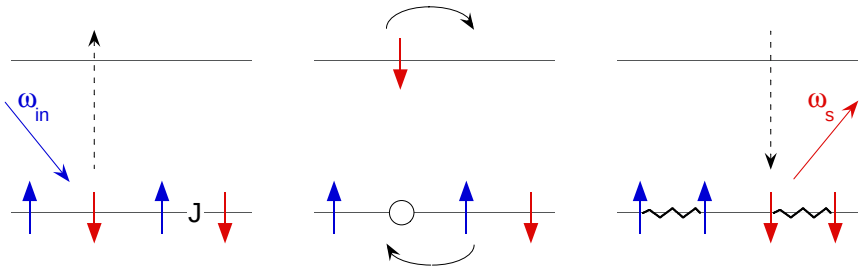

Figure 1.2: Cartoon illustrating the photon induced spin exchange in a two sublattice antiferromagnet (AF). A succession of three processes can lead to two-magnon Raman scattering: (1) by electric dipole interaction an electron is pushed in a higher energy electronic state creating an electron-hole excitation; (2) the Coulomb interaction leads to spin exchanges; (3) the electron-hole state can collapse (with a photon emission) in an excited magnetic state having several broken AF bonds.

are applicable to the case of Mott-Hubbard insulators. Shastry and Shraiman in Ref. [9] present a theory of Raman scattering in the Hubbard model and emphasize the symmetry aspects for the case of two-dimensional square lattices. The Hubbard Hamiltonian reads:

$$-t \sum_{(i,j)\ \sigma} (c^{\dagger}_{j,\sigma} c_{i,\sigma} + c^{\dagger}_{i,\sigma} c_{j,\sigma}) + U \sum_{i} n_{i\uparrow} n_{i\downarrow} \tag{1.15}$$

where the first terms describe the kinetic energy associated with the overlap of atomic orbitals between pairs of sites i and j and the second term represents the on-site Coulomb interaction. In the general formalism for magnetic Raman scattering one can write down relations analogous to Eqs. 1.6 and 1.7 involving matrix elements of the operators $\tau_q^{\alpha,\beta} = \sum_k \left[\partial^2 \varepsilon_k / \partial k^\alpha k^\beta\right] c^{\dagger}_{k+q,\sigma} c_{k,\sigma}$ and $\mathbf{j}_q = \sum_k \nabla_{\mathbf{k}}(\varepsilon_k)\ c^{\dagger}_{k+q,\sigma} c_{k,\sigma}$. The low indexes k and q correspond to the Fourier transformed real space operators in Eq. 1.15 and $\varepsilon_k = 2t[\cos(k_x) + \cos(k_y)]$ for nearest neighbor interactions. The resonant part involves the current operator and has contributions both at half filling (the total number of electrons is equal to the number of lattice sites) and in the doped case. The term involving a density-like operator $\tau_q^{\alpha,\beta}$ is off-resonant and contributes only in the doped case.

For half filling the excitations in the charge channel are gapped, but the spin degrees of freedom will have low lying excitations. Interestingly, in the strong coupling limit ($U \gg t$) it can be shown that in what regards the magnetic excitations, Eq. 1.15

is equivalent, up to t^2/U^2, with a AF Heisenberg Hamiltonian $H_H = J \sum_{(i,j)} \mathbf{S}_i \cdot \mathbf{S}_j$ and a superexchange interaction given by $J = 4t^2/U$. Carrying out the contribution due to the resonant term and remaining in the subspace of states with at most one double occupancy of a given site, one obtains an effective light scattering Hamiltonian [9]:

$$H_{int} = \left(\frac{t^2}{U - \omega_{in}}\right) \sum_{\mathbf{r},\delta} (\mathbf{E}_{in} \cdot \hat{\delta})(\mathbf{E}_s \cdot \hat{\delta}) \left(\frac{1}{4} - \mathbf{S}_\mathbf{r} \cdot \mathbf{S}_{\mathbf{r}+\delta}\right) \tag{1.16}$$

which is the Hamiltonian of Fleury and Loudon [7] from Eqs. 1.13 and 1.14. The term U in the denominator plays the role of the gap energy in band-semiconductors and in the strong coupling limit it gives the splitting between the upper and lower Hubbard bands. Eq. 1.16 represents the leading contribution in t/U and appears in the B_{1g} scattering channel. Carrying out calculations in higher orders can render contributions in all even symmetry representations. The two-magnon feature is a specific Raman excitation but for instance in conjunction with infra-red active phonons and in the presence of the spin-lattice interaction they can be observed as a two-magnon+phonon bands in the optical absorption spectra.

1.3 Scope of this thesis. Magnetism in low dimensions

In this thesis we will present data obtained from a number of different compounds that all belong to the class of strongly correlated electronic systems. Moreover, they all can be included in the category of magnetic materials with lower dimensionality, in the sense that the crystal structures allows the identification of subunits such that the internal electronic interactions associated with these subsystems are stronger than the coupling between them. The experimental technique mostly used in this analysis was inelastic light scattering and the majority of the data is focussed on the study of the magnetic properties of these compounds. Topics related to other electronic excitations as well as lattice dynamics are also discussed. These materials also share

the common property that they are spin $S = 1/2$ systems which, along with their lower dimensionality, make them appropriate playgrounds for studying the importance of quantum mechanical effects.

Generally speaking, one or two-dimensional systems are expected to show novel ground state properties and elementary excitations with a different nature than in higher dimensions. They constitute challenging problems to solve in spite of the fact that they can be apparently described in a simpler and more compact way than in three dimensions. Questions related to the effects of correlations and competing ground states, breaking of Fermi liquid theory, spin-charge separation, instabilities with respect to (spin)-Peierls distortions or to the development of superconducting correlations as well as the way all these properties evolve with increasing the coupling between the low dimensional subunits constitute hot topics in today's condensed matter physics. We will try to address in this work some of these issues. Below is a summary of the contents of this thesis, with an emphasis on the general aspects and questions brought about by the materials we studied. This also serve as a brief tour through parts the complex phase diagram of quantum spin systems.

One simple idealized system to study is a 1D $S = 1/2$ chain with AF nearest neighbor interactions. The corresponding Hamiltonian is $H_1 = J \sum_i \mathbf{S}_i \cdot \mathbf{S}_{i+1}$ where J is a super-exchange interaction and $\mathbf{S}_i$ is the spin at the lattice site i. The ground state of this system, which is exactly known, does not have long range order even at T = 0 K and it is critical in the sense that spin-spin correlations decay algebraically with distance. The characteristic excitations are fractional spin solitons called spinons and their excitation spectrum is gapless. In this respect, integer and half-integer 1D AF chains are very different: integer spin chains have gapped magnetic spectra and exponentially decaying spin-spin correlations. Modulation of the super-exchange in 1D $S = 1/2$ AF chains leads to opening of a spin-gap (defined as the lowest energy triplet excitation above the singlet ground state) and the appearance of magnetic bound states within the gap. Frustration introduced for instance by the presence of next nearest neighbor AF interactions like $\alpha J \sum_i \mathbf{S}_i \cdot \mathbf{S}_{i+2}$ also leads to a quantum

phase transition above a critical value of α.

NaV_2O_5 , discussed in Chapter 5, seems to be in its high temperature phase an example where such excitations can be studied. It has a layered structure made out of corner sharing tetrahedra which render an ensemble of weakly coupled two-chain structures. The fact that the filling factor for this material is 1/4 suggest the possibility of mapping this structure to an array of quasi-1D AF chains. We propose that the strong Raman continuum observed at energies of several J's is due to multi-spinon Raman scattering and suggest that the softening observed with cooling is due to increasing frustration. At T = 34 K, NaV_2O_5 undergoes a phase transition which results in lattice distortions, charge ordering and changes in the magnetic excitation spectrum. We observe one-magnon scattering from the folded triplet branch due to unit cell doubling and suggest an explanation of the selection rules in the presence of magnetic field in terms of antisymmetric spin interaction. Several other resonances in the singlet channel are observed inside the gap region, in particular one which is situated exactly at the spin-gap value. A tempting interpretation of these modes is in terms of newly allowed magnetic bound states below a frustration induced phase transition.

One can imagine now taking a 1D chain and coupling it with another one such that the intra-chain interactions are comparable to the inter-chain super-exchange forming a two-leg ladder structure. If the magnetic coupling between these ladders are small and we remain within the nearest neighbor interactions the relevant ladder Hamiltonian becomes $H_2 = J_{leg} \sum_{i,\alpha=1,2} \mathbf{S}_{i,\alpha} \cdot \mathbf{S}_{i+1,\alpha} + J_{rung} \sum_i \mathbf{S}_{i,1} \cdot \mathbf{S}_{i,2}$, where α is a leg index. The ground state of this system is characterized by exponentially decaying spin-spin correlations and the excitation spectrum is also very different from the 1D $S = 1/2$ AF chain. There is a finite energy required to go from the ground state to the lowest triplet and the spectra, like the dimerized chain, exhibits various magnetic bound states within the gap. As regards the ground state properties in the doped case, two phases were especially considered to be relevant: charge density waves and superconductivity, the latter being theoretically favored due to the rather strong

tendency of carrier pairing in this particular AF environment. Superconductivity under pressure was indeed found in these systems.

In Chapter 3 we have studied two-magnon excitations in $Sr_{14-x}Ca_xCu_{24}O_{41}$, which is an example of two-leg ladder systems and analyzed the data in terms of relaxation, symmetry and resonance properties as well as its evolution with doping. Resemblances as well as differences in comparison with the more studied case of two dimensional AFs were found in the resonant behavior and based on our data it was later suggested that these differences occur because of the different spin-spin correlations in the magnetic ground state. The fact that we found a very sharp two-magnon resonance is intriguing in the context of lower dimensionality where the effects of quantum fluctuations are expected to be enhanced. The situation is opposite to the 2D case where the large scattering width of the two-magnon in this case is still not explained. Are the presence of magnetic bound states and the finite spin gap the factors which stabilize the two-magnon excitation in two-leg ladders? What are the effects of inter-ladder interactions? Is it possible that the sharpness is due to the special dispersion in the reciprocal space of the elementary triplet and an associated backfolding due to an intrinsic instability with respect to a spin-density wave modulation? These are outstanding questions which are discussed in our study. We also found that disorder and doping drastically affect the two-magnon resonance. A resonant soft X-ray study along with low frequency Raman and microwave transport data reveal that a charge density wave is the ground state of low doped two-leg ladders $Sr_{14-x}Ca_xCu_{24}O_{41}$ at and below the ambient pressure and that it persists, at least in a strongly fluctuating regime, up to remarkably high temperatures. The magnitude of the charge modulation is very weak and a highly non-trivial aspect is that this state is driven by many-body effects, no detectable lattice modulation being observed to follow the density wave ordering.

We discussed above that two AF chains put together give something very different than single chains in terms of excitation spectra. Indeed, building a 2D AF square lattice (characteristic of $La_{2-x}Sr_xCuO_4$ systems, see Chapter 4) by coupling

chains one after the other is not a smooth process at all. The alternation mentioned with respect to the integer and half-integer 1D chains is also present in the even and odd legged ladders: even leg ladders have gapped magnetic spectra while the odd-leg ladders are gapless. The gap in the even leg ladder case decreases with the number of legs and this is understandable because it is known that in the 2D limit there is gapless long ranged AF order. We found that a semiclassical approach can describe to a quantitative level the anisotropic dispersion with magnetic field of the long wavelength spin-wave excitations in undoped and 1% Sr doped $La_{2-x}Sr_xCuO_4$. This is a fascinating aspect because it is known that the spin-wave expansion is expected to be an exact result in the limit $S \to \infty$. $S = 1/2$ in $La_{2-x}Sr_xCuO_4$, so $1/S$ is not a small parameter. Application of magnetic fields along certain crystallographic directions in x = 0 and 0.01 $La_{2-x}Sr_xCuO_4$ allowed us to discover a spin-flop like transition to another magnetically ordered state and to study its characteristic excitations as well as its evolution with temperature and doping.

A 2D $S = 1/2$ material without long range order down to temperatures in the mK range is $SrCu_2(BO_3)_2$ (Chapter 6). This compound is thought to be close to a quantum critical point separating a gapped, spin liquid, phase from a state with long range AF order. Worth mentioning is that within a reasonable approximation the ground state of this compound is known exactly to be a simple product of spin singlets of the form $\prod_i (1/\sqrt{2})(|\uparrow_{i1}\downarrow_{i2}> - |\downarrow_{i1}\uparrow_{i2}>)$ where i indexes pairs of antiferromagnetically coupled spins. Like the two-leg ladders and dimerized chains, it is found that many magnetic bound states exist in this system which is a 2D realization of a Shastry-Sutherland model. Our Raman study on this compound is focussed on the symmetry properties of elementary triplet and two-particle states and the light coupling mechanisms to these excitations. Experimental results and group symmetry analysis of a small spin cluster confirm the highly localized nature of the one-particle states and by including additional antisymmetric spin interactions we are able to understand the observed selection rules and intensity variations of these modes for different directions of the applied magnetic field. The experimentally found symme-

tries in the case of two-triplet excitations are only partially consistent with theoretical predictions suggesting that other interactions may have to be taken into account. By doing a resonance study we show that two distinct Raman coupling mechanisms are responsible for the observed triplet $S = 1$ magnetic modes. We suggest that one of them could be the the Fleury-Loudon Hamiltonian in Eq. 1.16, which up to now has been mainly discussed in the literature as the characteristic coupling mechanism to the two-magnon excitation in the singlet channel.

Chapter 2

Experimental

2.1 The Raman setup

When a sample is illuminated by light there are several processes which can take place. The incident photons can be elastically scattered giving rise to Rayleigh scattering, they can lose entirely their energy by creating internal excitations in the sample leading to optical absorption, or there can be processes in which an incident photon loses only a fraction of its energy being inelastically scattered. Raman spectroscopy deals with this latter type of interaction and by analyzing the energy difference between the incoming and outgoing photons one can infer something about the nature of the internal excitations in the sample studied. As a result, a Raman setup involves a source of light (excitation beam), optics to direct the excitation beam towards the crystal and to collect the scattered photons, a spectrometer and a photon detector to analyze the inelastic signal.

The basics of a Raman setup in the (pseudo) back-scattering configuration are shown in Fig. 2.1. The path of the optical beam in our setup is described in the following. We used laser light as the excitation source. The beam is passed through a monochromator (MC) which filters the non-lasing plasma lines from the laser. Then it goes through a beam expander (BE) which consists of a microscope objective and a pinhole sitting in the focus of lens L_1 which collimates the beam. The purpose of

this spatial filter is to improve the beam quality by regenerating its Gaussian profile and to expand the diameter of the beam (the diffraction limit for the size of focussed spot from a circular aperture is $\propto \lambda f/D$, where D is the diameter of the aperture, λ is the photon wavelength and f is the focal distance). After reflection form mirror M_1 the beam is focussed on the sample S by lens L_2 and using mirror M_2. The sample is also in the focus of L_3 which collects the scattered light and collimates the outgoing beam. Here is the difference between a pseudo and a real back scattering geometry (inset of Fig. 2.1). In the latter case mirror M_2 is used to send the light towards the sample and in this case the same lens L_3, which is used for the collection of the scattered light, is also used to focus the light on the sample. An advantage of the pseudo back-scattering setup is that the specular reflection from the sample can be blocked more easily but sometimes one has to use the regular back-scattering configuration. This is the case when a normal incidence of the excitation beam on the sample is required or if there are geometrical constraints imposing a long distance between the sample and lens L_3, as it is the case when the sample sits in the horizontal bore of a superconducting magnet. In Fig. 2.1 P_1 and P_2 are polarizing optics for the incoming and outgoing beams and they are used in order to probe excitations in different symmetry channels.

The lens L_4 focusses the beam on the entrance slit S_1 of the spectrometer and at the end the photons are recorded by a detector. The detector we used was a charge couple device (CCD) which is a 1340×400 two-dimensional array of about 20×20 μm Si pixels. The configuration which was mostly used was not the two-dimensional imaging mode, but a spectroscopy mode in which the relevant vertical pixels were binned into one super-pixel.

What happens after the light is focussed on the entrance slit of the spectrometer is shown schematically in Fig. 2.2. For the analysis of the inelastically scattered light we used a triple grating spectrometer. The last stage shown in the upper part of this figure is a regular grating spectrometer where the light from the slit S_4 is collimated by spherical mirror M_7 on grating G_3. The grating diffracts light in the first order

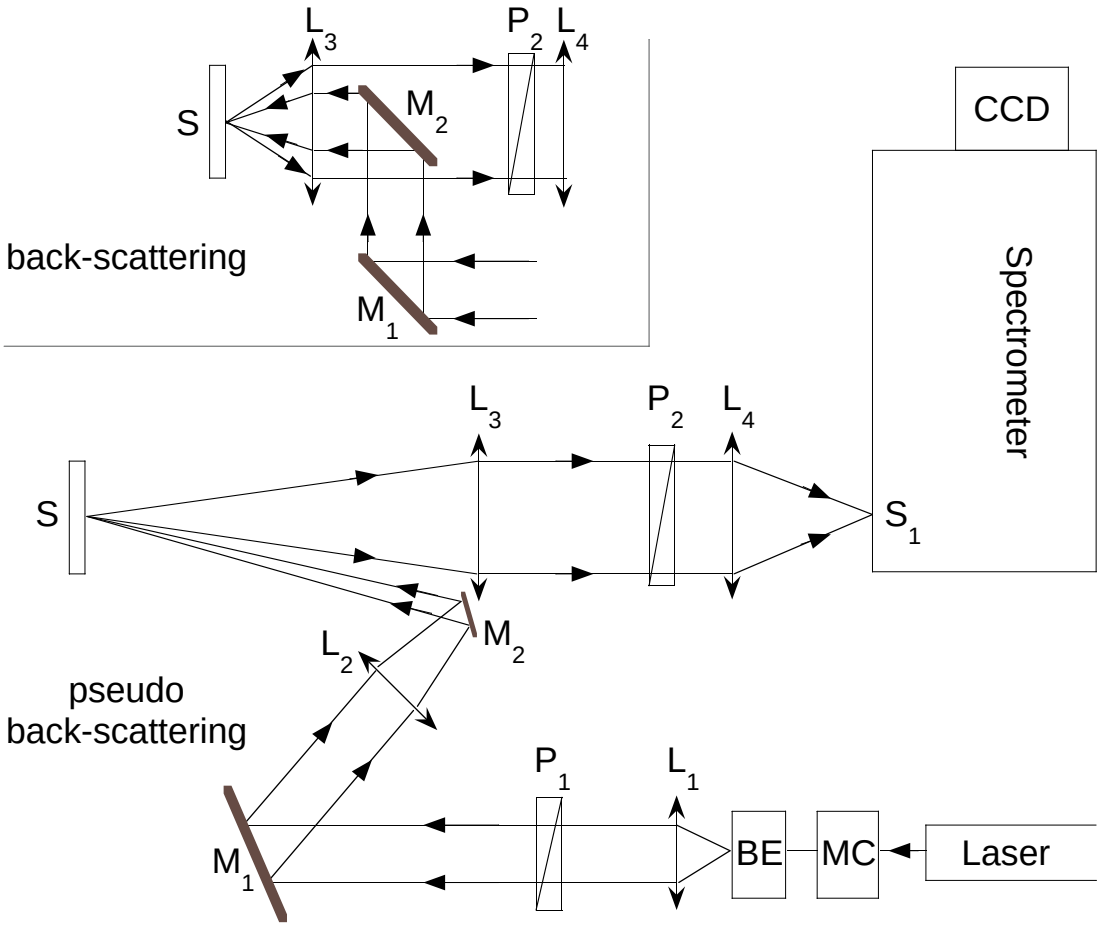

Figure 2.1: The basic Raman setup in pseudo back-scattering configuration. MC - filter monochromator; BE - beam expander; L_1, L_2, L_3 - focussing lenses; M_1, M_2 - mirrors; P_1 - polarizer; P_2 - analyzer; S - sample; S_1 - the entrance slit of the triple grating spectrometer (see Fig. 2.2). The inset in the upper left of the figure shows the differences between a pseudo with respect to a real back-scattering configuration. See the text for details.

and this is subsequently focussed by M_8 on a nitrogen cooled Princeton Instruments CCD. This stage is built using an Acton Research AM-506 scanning monochromator. Because the Rayleigh scattering cross-section is orders of magnitude higher than the one for the Raman signal, a main problem is to find a way to efficiently reject the stray-light, composed of elastically scattered photons. This is done in the box shown in the lower part of Fig. 2.2 called the subtractive stage and roughly speaking it is achieved by using two grating spectrometers (which are similar to the dispersive part in the upper part) in conjunction with a relay stage formed by mirrors M_3 and M_4. This part was built using two monochromators. The first of these spectrometers disperses the light focussed on the entrance slit S_1, the image is flipped in the relay

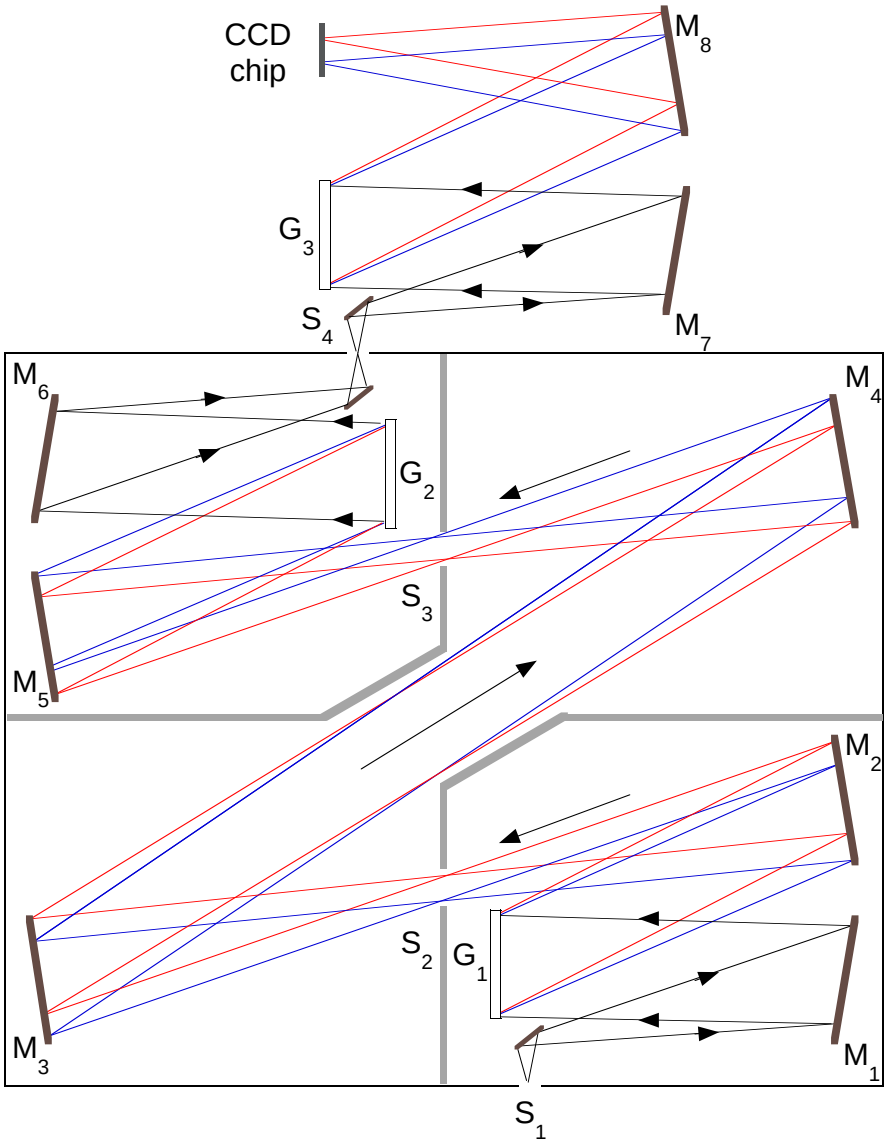

Figure 2.2: Cartoon with beam trajectories in a triple grating spectrometer. Gratings are denoted by G's, slits by S's and mirrors by M's. The two trajectories correspond to longer/shorter wavelength scattered photons. See text for details.

stage and grating G_2 collects the dispersed light into a "white light" beam which is sent into the last stage. A double spectrometer does not contain relay optics but uses a second grating, G_2 to further disperse the light for a greater energy resolution.

The discussion above is illustrated in Fig. 2.2 where we show two optical paths corresponding to light beams of shorter (blue line) and longer (red line) wavelengths. One can see that the intermediate (adjustable) slits S_2 and S_3 are used to define the spectral range one is interested in and also to clean the collection from the elastically scattered photons. It is clear that an efficient stray-light rejection is directly related

to the ability of the mirrors to focus the beam sharply. According to geometrical optics, the surface which is able to insure a perfect focus from point to point is the ellipsoidal surface while the paraboloid can do in principle a perfect focussing of a collimated beam. This is why the focus on the intermediate slits in the subtractive stage is realized by off-axis parabolic mirrors.

The gratings diffract the light in the first order according to $|d\sin(\theta_i) - d\sin(\theta_r)| = \lambda$ where $\theta_{i,r}$ are the angles between the incident/reflected light and the normal to the surface and d is the inter-groove distance. A larger intensity in the first order can be achieved by blazing the gratings, i.e. creating a specially designed groove profile; if the gratings are not blazed the first order diffraction peak contains only about 30% of the incident intensity. Blazing also reduces the intensity in higher orders which is good for stray-light rejection. Depending on the desired energy resolution and spectral range to be covered, gratings with 1800, 600 and 150 grooves/cm were used. For an efficient use of the spectrometer it is important that the numerical aperture of the collection (which is given by the ratio $D/2f$, with D the diameter of the collimated beam between lenses L_3 and L_4 and f the focal length of lens L_4, see Fig. 2.1) matches the numerical aperture of the monochromators.

2.2 Data processing

The measured quantity which can be related to theoretical calculations is the Raman scattering cross section. This can be defined in terms of wavelengths as $N_\lambda/N_0 = d\sigma/d\lambda$ where $N_\lambda\delta\lambda$ is the number of photons scattered in unit time having wavelengths in the interval $(\lambda, \lambda+\delta\lambda)$ and N_0 is the incident photon flux. Similarly, one can define a cross section in terms of energy, $N_\omega/N_0 = d\sigma/d\omega$, and these two quantities are related by $d\sigma/d\omega = \lambda^2 d\sigma/d\lambda$.

The measured signal has to be corrected for the spectral response of the spectrometer and this is done by using a standard calibrated lamp. If $L(\lambda)$ and $N_r(\lambda)$ are the spectral function of the lamp and the measured number of counts at a cer-

tain wavelength, the spectrometer response is $R(\lambda) \propto N_{resp}(\lambda)/\lambda L(\lambda)$. If $N_s(\lambda)$, W_L and λ_L are the measured signal from a sample at a pixel corresponding to a certain wavelength λ, the incident power from the laser and laser wavelength respectively, the Raman intensity is $I(\lambda) \propto N_s(\lambda)/(R(\lambda)W_L\lambda_L)$ and $I(\omega) = \lambda^2 I(\lambda)$. When doing a resonance study (i.e., comparing the Raman scattering efficiency for different laser excitation energies) one has to take into account the corrections introduced by the changes in the optical properties of the sample in different spectral ranges. The cross section is generally given by $d\sigma/d\omega = I(\omega)[\alpha(\omega_L)+\alpha(\omega)][n^2(\omega)+k^2(\omega)]/[T(\omega_L)T(\omega)]$ where α is the absorption coefficient, T denotes the transmission at the sample surface and n and k are the real and the imaginary part of the index of refraction. The Stokes Raman cross section $d\sigma_S/d\omega$ is related to the Raman response function $\chi''(\omega)$ by $d\sigma/d\omega = [n(\omega)+1]\chi''(\omega)$ where $n = 1/(\exp(\hbar\omega/k_BT) - 1)$ is the Bose function. With only few exceptions (for instance if time reversal symmetry is broken) on can write for the anti-Stokes signal a related equation: $d\sigma_{AS}/d\omega = n(\omega)\chi''(\omega)$. It follows that the ratio of the cross sections in anti-Stokes and Stokes scattering is given by $\exp(-\hbar\omega/k_BT)$. This relation is very useful for accurate temperature determinations and when one cannot estimate reliably the heating of the sample due to the focussing of the laser in a very small spot. An example where such a relation was used is in Chapter 2. The temperature of every spectrum above room temperature was determined from this ratio followed by an exponential fit.

Measurements as a function of temperature were done by inserting the sample in a continuous He flow cryostat with horizontal sample loading. This cryostat could be introduced in the room temperature horizontal bore of a superconducting magnet (Oxford Instruments) which enabled low temperature data taking in magnetic fields up to 11 T. We developed software for data analysis (C language) and spectrometer control (LabView).

Chapter 3

Electronic and Phononic Raman Scattering in $S = 1/2$ two-leg ladders $(Sr,La)_{14-x}Ca_xCu_{24}O_{41}$

3.1 $(Sr,La)_{14-x}Ca_xCu_{24}O_{41}$: the structure and general properties

In 1988, material research focussed around the study of high temperature superconducting cuprates (high T_c's) brought about new phases of Cu-O based systems. These are the two-leg spin-ladders (2LL's), with the general formula $(A_{1-x}A'_x)_{14}Cu_{24}O_{41}$, with A an alkaline earth metal and A' a trivalent (transition or lanthanide) metal [10, 11]. There were well-founded hopes that these materials could provide useful insight for the unresolved problems posed by the two-dimensional (2D) cuprates [12, 13] and from this perspective two main reasons triggered the interest of the scientific community. One of them was based on a number of physical properties that are common for both ladders and high T_c's. These include the presence of similar Cu-O-Cu antiferromagnetic (AF) correlations which give rise to a finite spin gap and were predicted to generate d-wave like pairing of doped carriers [14], the evidence for 'pseudogap'

phenomena in optical absorption spectra [15] and, most importantly, the discovery of superconductivity under pressure evolving with hole doping in the AF environment [16, 17]. The second reason resides in the crystal similarities and more precisely the fact that one can imagine building the 2D square Cu-O lattice by gradually increasing the coupling between individual the two-leg ladders [18], the simplicity of the latter making them more tractable for theoretical analysis.

The unit cell of $Sr_{14}Cu_{24}O_{41}$ contains four formula units, 316 atoms in all, this large number of atoms being due to the presence of two nearly commensurate substructures: the CuO_2 chains and the Cu_2O_3 two-leg ladders. A better understanding of the two interacting blocks can be achieved by decomposing the chemical formula into $(Sr_2Cu_2O_3)_7(CuO_2)_{10}$: planes of CuO_2 chains are stacked alternately with planes of Cu_2O_3 ladders and these are separated by Sr buffer layers. See Fig. 3.1. The lattice constants of the individual sub-systems satisfy the approximate relation $7\ c_{ladder} \approx 10\ c_{chain}$. The b-axis is perpendicular to the Cu-O layers which define the (ac) plane, the c-axis being along the ladder/chain direction. A valence counting shows that $Sr_{14}^{2+}Cu_{24}O_{41}^{2-}$ is intrinsically doped, the average valence per Cu atoms being +2.25. Optical conductivity [19], X-ray absorption [20], *dc* resistivity and magnetic susceptibility [21] measurements, as well as evaluations of the Madelung potential [22] and valence-bond-sums [21] support the idea that in this compound the holes reside mainly in the chain structures and the isovalent Ca substitution for Sr in $Sr_{14-x}Ca_xCu_{24}O_{41}$ induces a transfer of holes into the more conductive ladders. A relatively large ladder carrier density change from 0.07 holes per Cu for $x = 0$ to about 0.2 for $x = 11$ due to Sr substitution was inferred from low energy optical spectral weight transfer [19], but X-ray absorption [20], while still supporting the hole migration scenario, is in favor of a less pronounced hole transfer. On the other hand, La^{3+} and Y^{3+} substitutions for Sr decrease the total hole concentration, the $La_6Ca_8Cu_{24}O_{41}$ compound containing no holes per formula unit. As a result, the ladder systems provide the opportunity to study not only magnetism in low dimensional quantum systems like undoped ladders but also competing ground states and car-

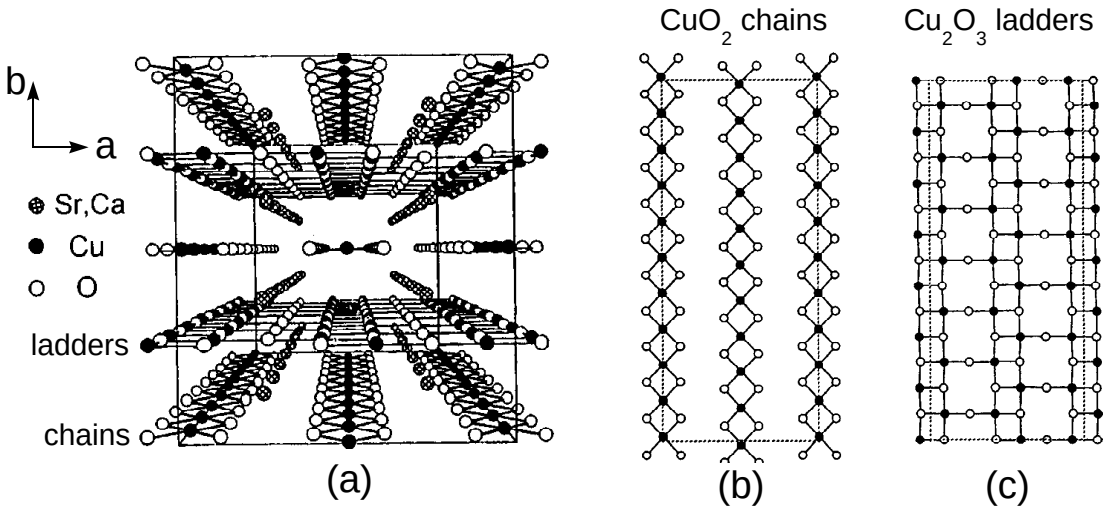

Figure 3.1: (a) The 3D structure of $Sr_{14}Cu_{24}O_{41}$ viewed in the (ab) plane; (b) the CuO_2 chains. (c) the Cu_2O_3 two-leg ladders. In (b) and (c) the black dots are Cu atoms and the empty circles represent O atoms.

rier dynamics in an antiferromagnetic environment. Data interpretation, encumbered by the presence of two interacting subsystems in $(Sr,La)_{14-x}Ca_xCu_{24}O_{41}$ crystals, is being helped by experimental realizations of other related compounds like $SrCu_2O_3$, which contains only 2LL planes (Fig. 3.1c), or Sr_2CuO_3 and $SrCuO_2$, which incorporates only quasi-1D Cu-O chain units with a similar coordination as in Fig. 3.1b. Unfortunately, doping in these latter systems has not been achieved so far.

Ca substitution in $Sr_{14-x}Ca_xCu_{24}O_{41}$ has an important impact on the transport properties because of the chain-ladder hole transfer. Indeed, while $Sr_{14}Cu_{24}O_{41}$ is an insulator showing an activation gap $\Delta \approx 2100$ K (180 meV), a crossover from insulating to metallic conduction at high temperatures takes place around $x = 11$ and for $x = 12$ the c-axis dc resistivity has a minimum around 70 K separating quasi-linear metallic (above T = 70 K) and highly insulating behavior at low temperatures [15]. At higher Ca concentrations superconductivity under pressure has been observed, for example a T_c of 12 K under a pressure P = 3 GPa was found in x = 13.6 $Sr_{14-x}Ca_xCu_{24}O_{41}$ [16].

These properties, many of them common also to the 2D superconducting cuprates, underscore the potential value of the ladder systems for the understanding of superconductivity and also for the problem of identifying possibly competing order pa-

rameters in doped Mott-Hubbard systems. The plan for this chapter is to present the magnetic properties of $S = 1/2$ 2LL's along with our Raman scattering data on the two-magnon (2M) excitation in $Sr_{14}Cu_{24}O_{41}$, showing its polarization, resonance and relaxation properties. This is followed by the the analysis of Ca substitution effects on the low and high energy charge/spin degrees of freedom, our data supporting a scenario involving density-wave fluctuations as one of the competing orders for superconductivity.

3.2 Magnetic properties of $Sr_{14}Cu_{24}O_{41}$

3.2.1 Energy scales

Responsible for the magnetic properties are the Cu atoms which carry a spin $S = 1/2$ due to a missing electron on their $3d$ shells. The AF super-exchange between them is mediated by the O ligand $2p$ orbitals. The optical absorption due to transitions across the charge-transfer gap (determined by the energy difference between the Cu$3d$ and O$2p$ orbitals) is seen to occur at around 2 eV [19]. The sign of the super-exchange as a function of the Cu-O-Cu bond angle can be qualitatively estimated semi-empirically as the balance of two terms: the first term is a relatively small, weakly bond angle dependent, ferromagnetic interaction while the second is antiferromagnetic, large for a 180° Cu-O-Cu bond but strongly varying with the bond angle, tending to zero around 90° [23].

Cu-O chains – As a result of nuclear magnetic and nuclear quadrupole resonance (NMR/NQR) [24], X-ray [25] and inelastic neutron scattering (INS) [26, 27] measurements, the following picture emerged and provided more clarification over some controversial aspects regarding charge/spin ordering in these structures. NMR/NQR data identified two Cu_{chain} sites. One carried spin 1/2, and one was non-magnetic because of Zhang-Rice (ZR) singlet formation. This is a spin $S = 0$ state made out of a O$2p$ hole and a Cu$3d$ hole due to orbital hybridization. The data suggested the

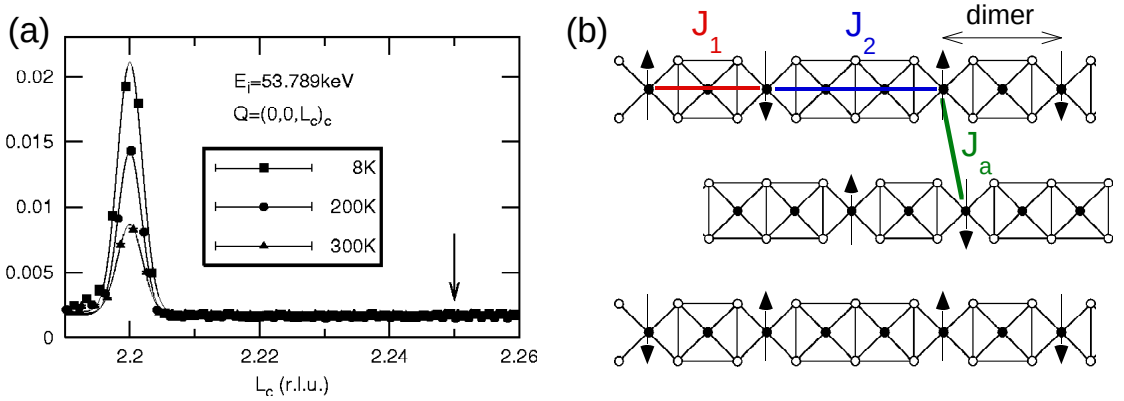

Figure 3.2: (a) X-ray intensity of the super structure peak seen at (0,0,2.2) in a $\theta - 2\theta$ scan for several temperatures indicating a 5-fold charge modulation, from Ref. [25]. Q is the momentum transfer measured in chain reciprocal units. (b) Charge pattern in the chains and the associated AF interactions as determined from Ref. [27]. The squares denote Zhang-Rice singlets and the arrows the spins on Cu sites. The size of dimers is shown in the upper right corner.

existence of a superstructure from the multipeak structure of the NMR spectra below about 150 K [24]. X-ray studies [25] established a five-fold charge modulation along the c direction in the chains' ground state at all temperatures below 300 K and a correlation length longer than 200 Å, confirming an ordered pattern involving AF spin dimers separated by two ZR singlets. See Fig. 3.2. Neutron scattering further supports such a superstructure by analyzing magnetic excitations out of the chain structures and evaluates the dominant intra-dimer exchange to be $J_1 \approx = 10$ meV [26, 27] which is also sets the value of spin gap in the dimerized chain. Surprisingly, the inter-dimer and inter-chain exchanges were found to be of the same order of magnitude but of different signs: $J_2 \approx$ -1.1 meV and $J_a \approx = 1.7$ meV [27] and, consistent with NMR/NQR data [24], 2D spin correlations due to J_a were shown to develop below a characteristic temperature of about 150 K. Notable is the fact that if the ZR complexes are effectively made of truly Cu^{3+} ions, the modulation shown in Fig. 1.2 would correspond to a Cu_{chain} valence of 2.6+ meaning that all the holes are located in the chains. Residual carriers are however present in the ladders and microwave [28] and NMR/NQR [24] data suggested the possibility of charge ordering in these systems too.

Cu-O ladders – At low temperatures $Sr_{14}Cu_{24}O_{41}$ can be regarded in a good

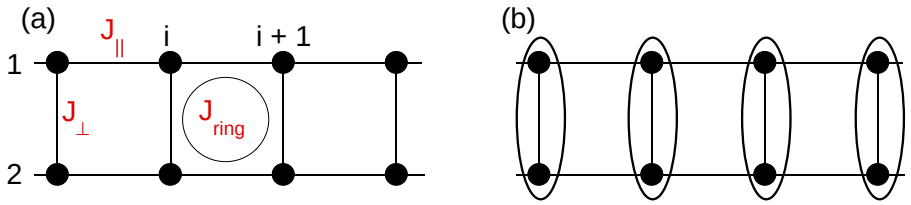

Figure 3.3: (a) Schematic of a two-leg ladder. $J_{\|}$ and $J_{\perp}$ represent the nearest neighbor AF exchanges along the ladder legs and rungs respectively. The circle is an example of a higher order spin interaction, in this case the ring exchange J_{ring}, which is thought to play an important role in the magnetic dynamics of the ladders. See text. (b) The ground state of the two-leg ladder in (a) in the limit $y = J_{\|}/J_{\perp} \rightarrow 0$. The ovals represent spin singlet states: $1/\sqrt{2}(|\uparrow\downarrow> - |\downarrow\uparrow>)$

approximation as an example of a 2LL structure at half-filling (with one $S = 1/2$ per Cu site). Moreover, an individual two-leg ladder, shown in Fig. 3.3 is expected to incorporate the essence of the spin dynamics in this subsystem. This is because the Cu-O-Cu bonds which are close to 180° generate a strong super-exchange $J_{\|}$ and $J_{\perp}$ (see Fig. 3.3) of the order of 130 meV ($\approx 1000\text{cm}^{-1}$). This value is about two orders of magnitude stronger than the (frustrated) ferromagnetic inter-ladder interaction (see Fig. 3.1). From the 2D cuprates experience, an expected Raman signature at energies of several J's is a two-magnon (2M) like excitation consisting of a pair of spin-flips. Low temperature behavior seen in magnetic susceptibility and NMR data show that, unlike in the cuprates, the low frequency spin behavior is not determined by gapless spin-wave modes (expected when one ignores small anisotropies which can create long wavelength gaps). Here there is a substantial spin-gap from the singlet ground state to the lowest triplet ($S = 1$) excitation. The gap value for $Sr_{14}Cu_{24}O_{41}$ extracted from the temperature dependent Knight shift in Cu-NMR data was $\Delta_S \approx 32$ meV (260 cm^{-1}) [24, 29], in good agreement with the gap extracted from neutron scattering data [26] in the same material as well as with the quasi-activated magnetization data ($\chi(T) \propto (1/\sqrt{T})e^{-\Delta/k_BT}$ see Ref. [12]) in the two-leg ladder $SrCu_2O_3$ [30]. Spin-gap determination from magnetization measurements in $Sr_{14}Cu_{24}O_{41}$ is more ambiguous due to the prominent contribution from the chains. The magnetic properties of the $Sr_{14}Cu_{24}O_{41}$ ladders, is the concern of the following sections.

3.2.2 Undoped two-leg ladders: Theoretical aspects

The starting point for the determination of the ladder excitation spectrum has been the AF nearest-neighbor isotropic Heisenberg Hamiltonian, allowing for the leg and rung couplings $J_{\parallel}$ and $J_{\perp}$ (see Fig. 3.3a). This Hamiltonian reads:

$$H = H_{\parallel} + H_{\perp} = J_{\parallel} \sum_{i,\alpha=1,2} \mathbf{S}_{i,\alpha} \cdot \mathbf{S}_{i+1,\alpha} + J_{\perp} \sum_{i} \mathbf{S}_{i,1} \cdot \mathbf{S}_{i,2} \tag{3.1}$$

From the crystal structure one can anticipate that the relevant parameter range for the leg to rung super-exchange ratio is $y = J_{\parallel}/J_{\perp} \approx 1$. The excitation spectrum could be easily understood starting from the strong coupling limit, $J_{\parallel}/J_{\perp} \to 0$. The ground state is a simple product of singlets sitting on each rung (Fig 3.3b). Excited N-particle states (where N is the number of triplets) are highly degenerate and are obtained by exciting elementary triplets on N different rungs [12, 13, 14, 31]. The nature of the ground and first excited states evolves smoothly when a small $J_{\parallel}$ is present. This allows the rung triplets to propagate along the ladder giving rise to dispersion in the reciprocal space. The bandwidth is proportional to $J_{\parallel}$ and the band minimum of the one-triplet branch is at the Brillouin zone boundary, $k = \pi$ in units of $1/c_{ladder}$ [31]. In the limit of uncoupled AF $S = 1/2$ chains, $J_{\parallel}/J_{\perp} \to \infty$, the result is also known and the ground state is characterized by an algebraic decay of magnetic correlations, the excitation spectrum is gapless with soliton-like $S = 1/2$ excitations (spinons) [32].

The picture described above is supported by theoretical calculations, and it turns out that in the general case the 'physics' of undoped 2LL's is dominated by the strong coupling limit. 1) *The ground state* is disordered and has exponential falloff of the spin-spin correlations. A good description of the magnetic correlations is achieved within the resonance valence bond (RVB) model [33]. For a pictorial representation see Fig. 3.6b and discussion. Although a high $J_{\parallel}/J_{\perp}$ increases singlet correlations beyond nearest-neighbors, a ground state built up as a superposition of short-ranged resonating valence bonds remains a good approximation. For odd-leg ladders long-ranged singlets must be included in the ground state description [33]. 2) *The one*

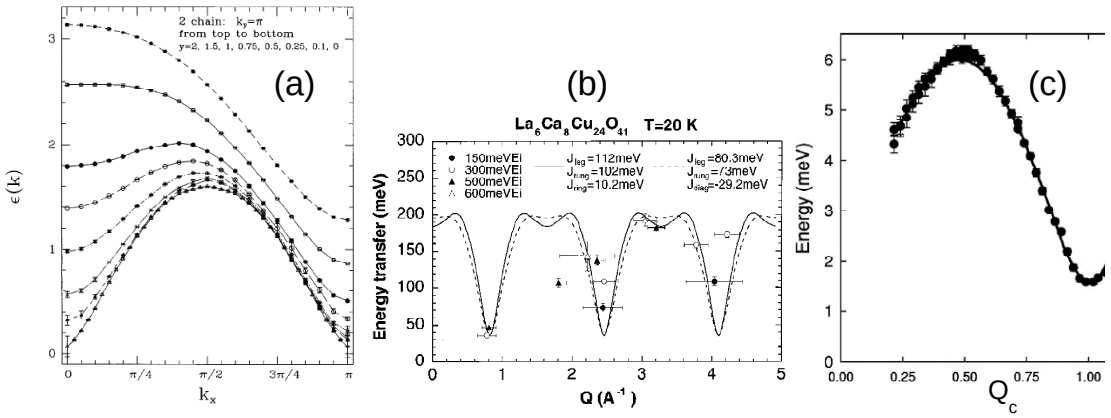

Figure 3.4: (a) Results of series expansions (Ref. [34]) around the Ising limit for the Hamiltonian in Eq.(1.1). From top to bottom the elementary triplet excitation was computed for an increasing ratio $J_\perp/J_\parallel$ from 2 to 0 (ϵ and k are in units of $J_\parallel$ and $1/c$ rspectively). The limit $J_\perp/J_\parallel \to 0$ corresponds to spinons. (b) Neutron scattering results for the elementary triplet dispersion in $La_6Ca_8Cu_{24}O_{41}$ (from Ref. [35]) (c) Dispersion inferred from neutron scattering data (Ref. [36]) along the chain direction in the Haldane system $CsNiCl_3$. Q_c is in units of π/c, where c is the distance between nearest neighbor spins, i.e. it corresponds to $k = \pi$ in panel (a).

particle excitations of the ladder have a gap Δ_S because any finite $J_\perp$ confines the $S = 1/2$ spinons binding them to an integer $S = 1$ 'magnon'. Results of series expansions around the Ising limit for 2LL's at various couplings $y = J_\parallel/J_\perp$ from Ref. [34] are shown in Fig. 1.4a. These results are further confirmed by exact diagonalizations [14], numerical [31] and perturbative [37] analysis. It has been also found that the spin gap remains finite for even leg ladders (although the gap decreases with increasing the number of legs) while odd-legged ladders are gapless and have a power law fall-off of spin-spin correlations [33]. This resembles the gapless and gapped alternance of the spectrum for isotropic AF half-integer and integer spin chains. The similarity is not accidental since a spin S chain can be described as $2S$ coupled spin $S = 1/2$ chains with appropriately chosen interchain coupling. This analogy is confirmed by the dispersion found above the Néel temperature in an experimental realization of a Haldane system, $CsNiCl_3$, [36] which is a quasi-1D nearly isotropic $S = 1$ AF chain (the dispersion below $Q_c \approx 0.2$ of the well defined triplet branch could not be measured because of intensity loss and the presence of the magnetic continuum). In Fig. 3.4 we show for comparison the experimental elementary magnon dispersion in

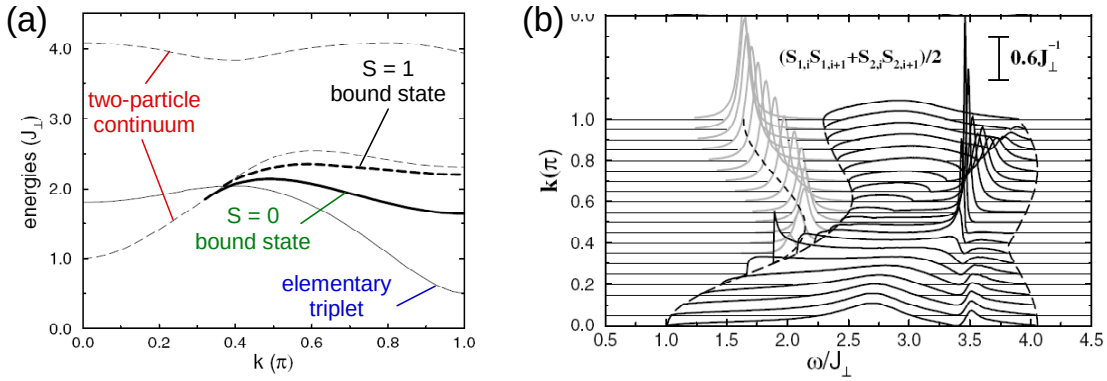

Figure 3.5: (a) Excitation spectrum in the one and two-particle channels at isotropic coupling $J_{\parallel}/J_{\perp} = 1$ from Ref. [37]. The elementary triplet, the two-particle continuum as well as the two-magnon singlet and triplet bound states are indicated in the figure. (b) The k-resolved spectral density $I(k,\omega)$ of the $\mathbf{S}_{i,1}\cdot\mathbf{S}_{i+1,1}+\mathbf{S}_{i,2}\cdot\mathbf{S}_{i+1,2}$ operator. This is proportional to the magnetic Raman response in parallel polarization with the electric field along the leg direction. The divergences observed around $k \approx 0.6$ are due to the hump-dip structure of the $S = 0$ bound state in (a). Data from Ref. [37].

$CsNiCl_3$ along with experimental and theoretical prediction for two-leg ladder. 3) *The two-particle states*: The elementary magnon branch will generate a two-magnon continuum starting from $2\Delta_S$ at $k = 0$. In addition, this spectrum contains additional magnetic bound/antibound states. These are states with discrete energies which are found below/above the two particle continuum [38]. Bound states have been found in the singlet ($S = 0$), triplet ($S = 1$) and quintuplet ($S = 2$) sectors. A typical excitation spectrum calculated perturbatively for isotropic coupling, $J_{\parallel}/J_{\perp} = 1$, and containing several types of two-particle excitations discussed above is shown in Fig. 3.5. A particularity of 2LL's is the fact that the bound states 'peel off' the continuum at finite values of k. The importance of higher order spin terms will be stressed in the following sections in connection with data analysis. This analysis will show that one has to go beyond the nearest neighbor Heisenberg Hamiltonian of Eq. 3.1 in order to explain the experimental data. Regarding the question whether the best description at all energies is in terms of fractional or integer spin excitations, it is worth noticing that, at least in the limit $J_{\parallel}/J_{\perp} \leq 1$, there is no necessity to resort to fractional spin states. A description in terms of truly bosonic excitations works well in the sense that spectral densities of spin-ladders can be described well by using

integer spin excitations [37].

3.2.3 Low temperature two-magnon light scattering in $Sr_{14}Cu_{24}O_{41}$

In this section we will discuss symmetry, spectral and resonance properties of the 2M excitation in $Sr_{14}Cu_{24}O_{41}$ at T = 10 K. Figure 3.6 shows Raman spectra in (cc), (aa) and (ac) polarization taken with an excitation energy $\omega_{in} = 1.84$ eV (the (xy) Raman notation means that the incoming (outgoing) photons are polarized along the x (y) directions). The spectra consist of a lower energy part where phonons are observed (see caption of Fig. 3.6) and a sharp asymmetric peak at 3000 cm^{-1} present in parallel polarizations. In both (aa) and (cc) polarizations the 3000 cm^{-1} peak is situated at exactly the same energy. In (ac) polarization this feature is not present. The energy of the 3000 cm^{-1} mode, much larger than the relevant magnetic interactions in the chain structures, allows an unambiguous assignment of this excitations to the ladder systems. A comparison with the 2D tetragonal cuprates [39, 40] in terms of energy scales argues for the interpretation of the 3000 cm^{-1} peak in terms of ladder 2M excitations. Moreover, in 2D cuprates, the 2M feature has B_{1g} symmetry, which becoms the identical representation in the orthorhombic group to which the ladder structure belongs. Indeed, as can be seen from Fig. 3.6, in $Sr_{14}Cu_{24}O_{41}$ this excitation is fully symmetric.

Although for the 2D cuprates a semi-classical counting of broken magnetic bonds within a local Néel environment (see Fig. 3.6b) gives a good estimate ($3J$) for the 2M energy (which is found by more elaborate calculations to be situated around 2.7 J), in 2LL's this approach is not suitable. On one hand any small anisotropy in the exchange parameters $J_{\parallel}$ and $J_{\perp}$ should lead to different peak energies in (aa) and (cc) polarizations, see Fig. 3.6b, which is not observed, and on the other hand, even in the improbable case of less than 0.03% anisotropy given by our energy resolution, this 'Ising counting' estimates $J \approx 200$ meV which is almost 50% higher than the

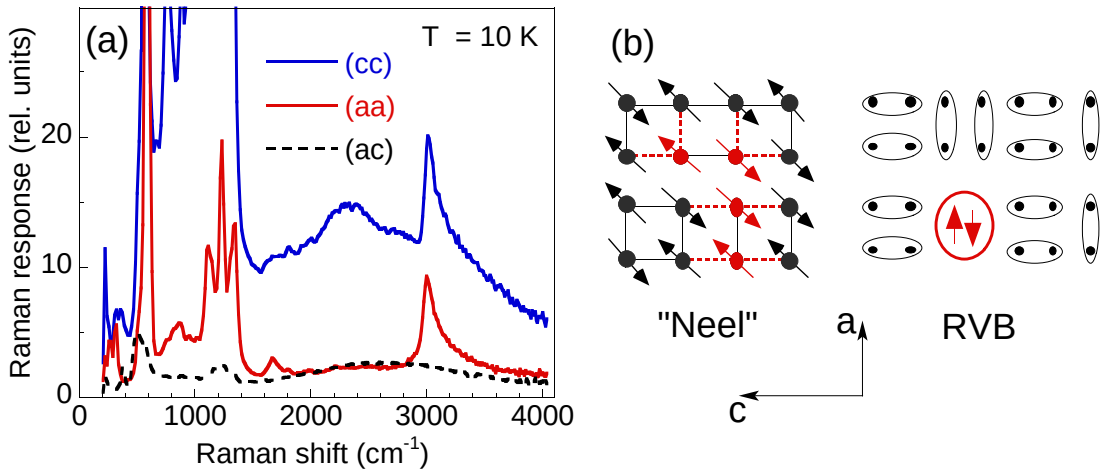

Figure 3.6: (a) Low temperature Raman spectra in several polarizations. The sharp, asymmetric peak at 3000 cm^{-1} is the two-magnon feature. The strong features below about 1200 cm^{-1} as well as the bump around 2350 cm^{-1} (which has about four times the energy of the 580 cm^{-1} Oxygen mode) in (cc) polarization represent single and multi phonon excitations. (b) Cartoon showing the two-magnon excitation. Left: assuming a local AF Néel order the spin exchange can take place along the rungs/legs of the ladder. Broken bonds and exchanged spins are shown in red. Right: a snapshot of the short-range RVB ground state which is a superposition of states like the top figure. The bottom picture represents a locally excited singlet state of two triplets.

super-exchange in related 2D cuprates. The failure of this approach may be related to the fact that the ground state of the 2LL's cannot be described classically. A RVB description of the ladder ground state has been proposed [33]. This can be understood as a coherent superposition of 'valence bonds', which are spin singlets, shown in Fig. 3.6c. For even leg ladders the RVB states are short ranged (the singlets extend only over nearest neighbor Cu spins) and in this context, starting from an 'instantaneous configuration' of the ground state, the 2M excitation can be visualized as a state in which two neighboring singlets get excited into a higher energy singlet state made out of two triplet excitations.

Symmetry – The polarization selection rules for the 2M scattering can be explained using the effective spin Hamiltonian corresponding to the photon induced spin exchange process [7, 9] which reads

$$H_{FL} \propto \sum_{<i,j>} (\mathbf{e}_{in} \cdot \mathbf{r}_{ij})(\mathbf{e}_{out} \cdot \mathbf{r}_{ij})\mathbf{S}_i \cdot \mathbf{S}_j \tag{3.2}$$

where $\mathbf{S}_i$, $\mathbf{S}_j$ are Cu spins on the lattice sites i and j, $\mathbf{r}_{ij}$ in the vector connecting

these sites and $\mathbf{e}_{in}/\mathbf{e}_{out}$ are the unit vectors corresponding to the incoming/outgoing polarizations. The polarization prefactor shows that the 2M scattering should occur only in parallel polarizations, consistent with the experimental observations.

Determination of J's – The problem of quantitatively estimating the magnitude of the super-exchange integrals is non-trivial in spite of the fact that there are several experimental techniques which probed magnetic excitations like neutron scattering [26, 35], Raman [41, 42] and IR spectroscopy [43, 44]. For the latter technique, the authors claim that the strong mid-IR absorption features between 2500 and 4500 cm^{-1} are due to phonon assisted 2M excitations. The main problem was to reconcile by using only the Hamiltonian from Eq. 3.1 the smallness of the zone boundary spin gap $\Delta_S = 32$ meV [26] with respect to the magnitude of the one triplet energies close to the Brillouin zone center (see Ref. [35] and Fig. 3.4), which is thought to determine the position of the 2M Raman peak [45] as well as the structure and the large energy range in which the mid-IR magnon absorption is seen [43, 44].

The proposed solution to this problem was to consider, besides $J_{\parallel}$ and $J_{\perp}$ the presence of a ring exchange J_{ring} [46], which is a higher order spin correction whose effect can be understood as a cyclic exchange of the spins on a square plaquette determined by two adjacent ladder rungs, see Fig. 3.4. The net effect of including such an interaction, which has the form $H_{ring} = 2J_{ring}[(\mathbf{S}_{1,i} \cdot \mathbf{S}_{1,i+1})(\mathbf{S}_{2,i} \cdot \mathbf{S}_{2,i+1}) + (\mathbf{S}_{1,i} \cdot \mathbf{S}_{2,i})(\mathbf{S}_{1,i+1} \cdot \mathbf{S}_{2,i+1}) - (\mathbf{S}_{1,i} \cdot \mathbf{S}_{2,i+1})(\mathbf{S}_{1,i+1} \cdot \mathbf{S}_{2,i})]$, is to renormalize down the spin gap so that the ratio of the magnon energy at the zone boundary with respect to the one at the zone center is decreased. The introduction of $J_{ring} \approx 0.1 J_{\perp}$ helped fitting the INS data (see Ref. [35] and Fig. 3.4) and an even higher ratio is able to better reproduce the experimental Raman and IR data (see Fig. 3.7). The parameter sets used for the quantitative analysis of the spectroscopic data have $J_{\parallel}/J_{\perp}$ between 1.25 and 1.3 and a sizeable cyclic exchange, $J_{ring}/J_{\perp}$ of about 0.25 - 0.3. The absolute value chosen for $J_{\perp}$ is 1000 - 1100 cm^{-1}. Both the value of J and J_{ring} are quantitatively consistent with those inferred for the 2D AF cuprates [47]. In the latter case, the cyclic exchange was used in order to reproduce the neutron scattering findings regarding

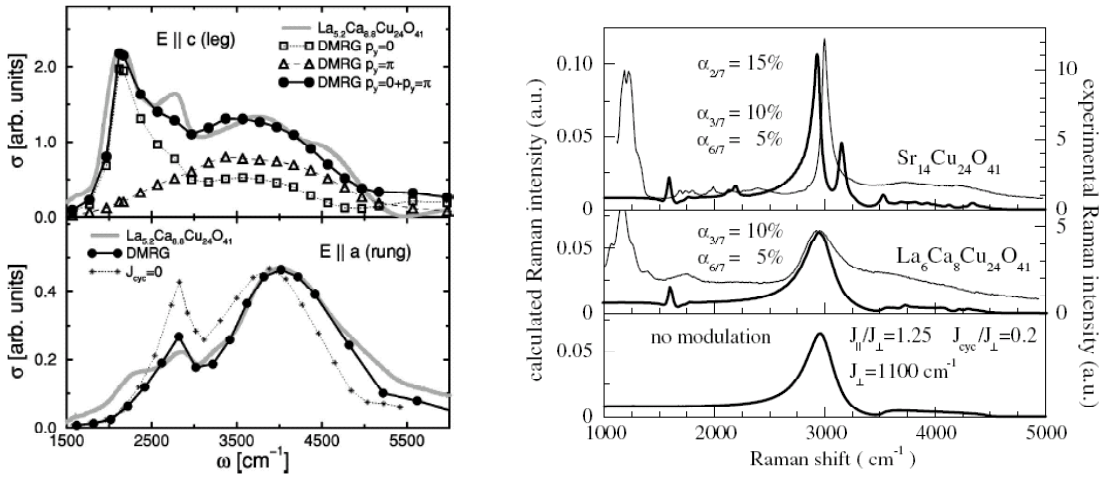

Figure 3.7: Left: IR absorption data (thick grey line) for two polarizations of the electric field along with theoretical calculations for the phonon assisted two-magnon absorption (from Ref. [44]). The parameters used are: $y = J_{\|}/J_{\perp} = 1.3$, $J_{\perp} = 1000$ cm^{-1} and a ring/cyclic exchange (see text and Fig. 3.4) $J_{ring}/J_{\perp} = 0.2$ Right: Calculated (thick lines) Raman response for the two-magnon scattering using a perturbative approach from Ref. [45]. The parameters used are: $y = J_{\|}/J_{\perp} = 1.25$, $J_{\perp} = 1100$ cm^{-1} and $J_{ring}/J_{\perp} = 0.2$. The experimental data (thin lines) in $La_6Ca_8Cu_{24}O_{41}$ and $Sr_{14}Cu_{24}O_{41}$ was taken from Ref. [41]. The upper two panels are calculated using an additional super-modulation on the magnon dispersion due to the interaction induced by the charge ordering in the chain structures (see the text for discussion). The parameter α specifies the kind of the superimposed supermodulation.

the k dependence of the energy of the one-magnon excitations in the proximity of the Brillouin zone boundary [47]. However, as opposed to the cuprates, the 2M seen in Fig. 3.6 at 3000 cm^{-1} cannot provide a direct determination of the super-exchange, even if no terms other than $J_{\|}$ and $J_{\perp}$ had to be included in the spin Hamiltonian. This problem is related to the fact that, in spite of the theoretical results shown in Fig. 3.7b which suggest good agreement with the experiment, the spectral shape of the sharp 2M feature and its origin is still an open question; this issue will be discussed in the following.

Two-magnon relaxation – While in the case of 2D cuprates theory has problems with explaining the large scattering width of the 2M excitation, in 2LL's the situation is reversed; this is one of the most interesting points made in Ref. [42]. To emphasize the 2M sharpness, we compare it in Fig. 3.8 to the corresponding excitation in $Sr_2CuO_2Cl_2$ which has one of the sharpest 2M feature among 2D AF copper

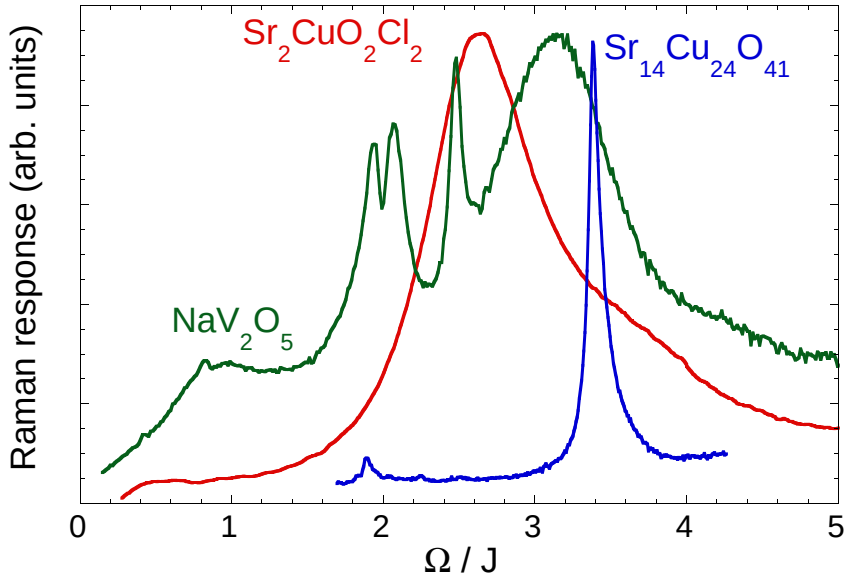

Figure 3.8: Magnetic Raman continua in several AF spin $S = 1/2$ systems. Red: $Sr_2CuO_2Cl_2$ (a 2D square lattice with long range order). Green: NaV_2O_5 (a two-leg ladder at quarter filling factor which can be mapped on a quasi 1D AF chain). Blue: $Sr_{14}Cu_{24}O_{41}$, the excitation seen in Fig. 3.7 but in this case taken with $\omega_{in} = 2.65$ eV incoming laser energy.

oxides [39] as well as to the multi-spinon scattering from 2LL at quarter filling (which can be mapped on a quasi 1D $S = 1/2$ AF chain), as seen in the high temperature phase of NaV_2O_5. For $Sr_2CuO_2Cl_2$ the FWHM is about 800 cm^{-1} [39] and this is comparable, in relative units, with the large scattering width observed for the spinon continuum. In $Sr_{14}Cu_{24}O_{41}$ the width is only about 90 cm^{-1}. The 2M approximation for the magnetic light scattering in 2D cuprates, while giving a good estimate for the 2M peak energy, cannot reproduce its spectral profile. This approximation makes the following three basic assumptions: (*i*) the ground state is a fully ordered Néel state; (*ii*) the spin pair excitations consist of states which have exactly two spins flipped with respect to the Néel configuration; (*iii*) since the light wavelength is much larger than the unit cell, only combinations of $(k, -k)$ magnons are allowed. This approach neglects quantum fluctuations which means that the true ground state will also contain configurations of flipped spins and also that the spin-pair states will be admixtures of 2, 4, 6 ... spin flips in the ground state. The narrow calculated width of the 2M was found, however, to be stable with respect to the inclusion of higher

order spin interactions. Neither exact diagonalization nor Monte Carlo simulations were able to fully reproduce the 2M scattering width [48] although these calculations improved the results obtained within the 2M approximation. It has been proposed by Singh *et al.* in Ref. [49] that it is the quantum fluctuations effects inherent to the Heisenberg model with $S = 1/2$ which lead to the observed broadening. The importance of intrinsic inhomogeneities and the role of phonons have also been invoked in the literature.

We were surprised that even in lower dimensionality (the structure determined by the 2LL's is quasi-1D), where the quantum fluctuations are expected to be stronger, the 2M Raman spectra display a narrow profile, a phenomenon which questions the importance attributed to these effects in low spin systems [49]. This prominent question triggered theoretical work, part of which is shown in Fig. 3.7. The authors of Ref. [45] challenged our point and claimed a resolution in terms of both the existing quasi-commensuration between the unit cell constants of the chain and ladder structures ($7\ c_{ladder} \approx 10\ c_{chain}$) and the supermodulation induced by the charge order in the chain structures, which is shown in Fig. 3.2 . The calculation of the 2M Raman response without the modulation (lower panel in Fig. 3.7b) reveals indeed a broader 2M peak [50], while inclusion of chain-ladder interaction renders a sharp 2M excitation because of the backfolding of the dispersion of the elementary triplet (Figs. 1 and 2 in Ref. [45]). This opens gaps at the points of intersection with the supermodulation wavevectors and will have a drastic effect in the spectral shape because of the induced divergences in the density of states.

The agreement with the experimental data in Fig. 3.7 is good; however, these claims have recently been put to rest by a Raman experiment, Ref. [51], in the undoped 2LL compound $SrCu_2O_3$ (which contains no chains but only undoped 2LL's), experiment which revealed a 2M peak as sharp as in $Sr_{14}Cu_{24}O_{41}$. This clearly shows that the sharpness is related neither to the interaction between the two substructures in $Sr_{14}Cu_{24}O_{41}$ nor to the residual carriers in the 2LL structure of $Sr_{14}Cu_{24}O_{41}$ but instead it is due to intrinsic 2LL's effects. Two major differences between the 2LL's

and 2D cuprates or 1D AF spin chains are the facts that in the former the low energy relaxation channels are suppressed due to the presence of a spin gap and also that the excitation spectrum of 2LL's supports the existence of magnetic bound states outside the continuum of excitations. Although this may be a plausible explanation, the 2M singlet bound state peels off the continuum only at finite values of k, see Fig. 3.5, and besides that, the energy at $k = 0$ is too small ($2\Delta_S = 64$ meV $= 512$ cm^{-1}) to account for the observed peak energy at 3000 cm^{-1}. If the sharpness is from the hump-dip feature in the dispersion of the elementary triplet close to the Brillouin zone center, Fig. 3.5b and the corresponding Van Hove singularities, it seems that such divergences are found only at finite values of k while at $k = 0$ the spectral density is quite broad [37]. This is why we suggest here an explanation in relation to a possible spin density wave (SDW) modulation which is intrinsic to 2LL's and will lead to a backfolding of the magnon dispersion. This effect is similar in spirit with the one proposed in Ref. [45] but this time due to intrinsic effects. Regarding the asymmetry of the 2M feature it would also be worth considering multi-magnon interaction effects which may lead to the asymmetric Fano-like shape of the sharp 3000 cm^{-1} feature due to the interaction with the underlying magnetic continuum.

Noteworthy is the resemblance of the elementary triplet dispersion in 2LL's and the k dependence of the one-magnon excitation in La_2CuO_4 away from the Brillouin zone center. There are several articles, some of them very recent [52], which stress the failure of the spin wave models in 2D cuprates arguing that the 'physics' of magnetic excitations is fundamentally different at low and high energies: while semi-classical magnon theory holds at low energies, it has been argued that at short wavelengths the effect of fluctuations is more pronounced and the spin dynamics suggest an underlying structure similar to the one provided by 2LL's, which is due to a SDW-like modulation in the 2D planes. Interestingly, the data in $Sr_2CuO_2Cl_2$ and NaV_2O_5 from Fig. 3.8 suggest instead a more pronounced similarity to the magnetic scattering in 1D $S = 1/2$ AF chains. It seems at this point that not only the 2M profile in 2LL's but also the one in 2D cuprates constitute open questions which have recently received

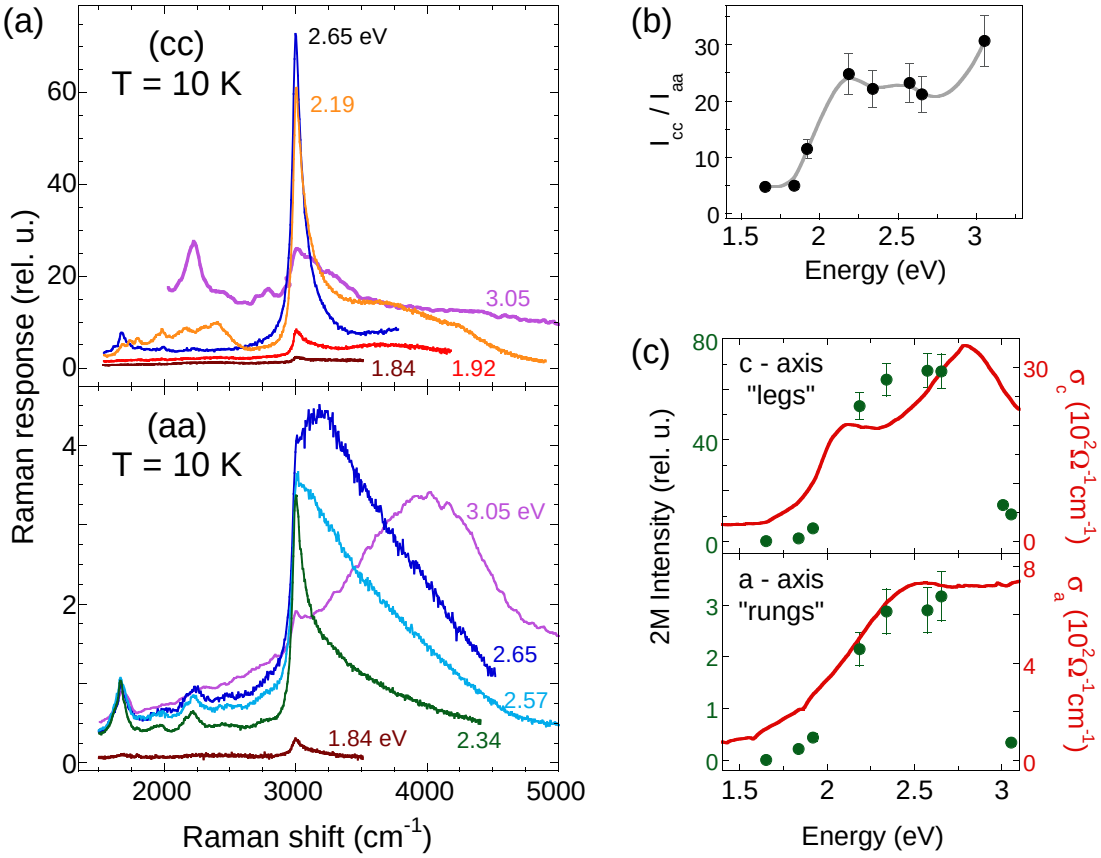

Figure 3.9: Two-magnon resonance profile in $Sr_{14}Cu_{24}O_{41}$ at T = 10K. (a) Data in (cc) (upper panel) and (aa) (lower panel) polarizations for different excitation energies ω_{in}. (b) The relative intensity of the 2M excitation in (cc) compared to (aa) polarization as a function of the incoming photon energy. (c) The resonance profile of the 2M peak (filled circles, left scale) and the optical conductivity (solid line, right scale). As in (a), the upper/lower panels refer to the data in which the electric field is parallel to the ladder legs/rungs.

renewed attention. It would be very interesting if the physics in these two systems is found to be related to each other.

Two-magnon excitation profile – A summary of our experimental study of the 2M dependence on the incoming photon energy is shown in Fig. 3.9. Like the 2D cuprates, the Cu-O based ladders are known to be charge-transfer (CT)-type Mott insulators, the CT gap being determined by the energy difference between the Cu $3d$ and O $2p$ orbitals. A Raman resonant study is interesting since, along with optical absorption, it gives information about the nature of the ground as well as of high energy electronic states across the CT gap. This is because the photon induced spin exchange takes place in two steps: a photoexcited state consisting of an electron-

hole pair is created by the interaction of the system in its ground state with an incoming photon and then this intermediate state collapses into an excited magnetic state characterized by broken AF bonds. One expects therefore that such a process in which the interaction with light occurs in the 2^{nd} order perturbation theory to show a strong dependence on the incoming photon energy [39].

This is what we observe in $Sr_{14}Cu_{24}O_{41}$: the Raman data at T = 10 K are shown in Fig.3.9a. In Fig. 3.9b we show the ratio of the 2M intensity (determined from peak height) in (cc) polarization with respect to (aa) configuration as a function of ω_{in} and in Fig. 3.9c the resonant Raman excitation profile (RREP) is plotted along with the optical conductivity data provided by the authors of Ref. [19]. For both (cc) and (aa) polarization the resonant enhancement has a maximum around 2.7 eV, about 0.7 eV higher than the CT edge. The intensity is small for $\omega_{in} < 2$ eV and increases monotonically as the photon energy approaches the CT gap, this increase being followed by a drop for excitations about 3 eV. The intensity displays an order of magnitude variation as the incident photon energy changes in the visible spectrum. Besides the correction for the optical response of the spectrometer and detector, by using the complex refractive index derived from ellipsometry and reflectivity measurements, the 'raw' Raman data were also corrected for the optical properties of the material at different wavelengths (see Chapter 2).

We observe changes in the spectral shape of the 2M as the incident frequency is changed, in the 2LL's case the 2M acquiring sidebands on the high energy side. These changes are more pronounced in (aa) polarization where for instance the 2.65 eV spectrum (which is close to the edge seen in the a-axis conductivity) shows a 2M as a gap-like onset of a continuum. While the fact that the 2M profile changes substantially with ω_{in} is also true for 2D cuprates, one can notice several differences too. One of them is that the RREP in 2LL's follows more closely the edges of the optical conductivity data. Moreover, if in the case of cuprates *two* peaks were predicted (and confirmed experimentally) to occur for the 2M peak at $2.8J$ in the RREP [53] (when the incoming energy is in resonance with the bottom and top of the electron-hole

continuum) from the data we show in Fig. 3.9c up to $\omega_{in} = 3.05$ eV we observe only one, rather broad, peak. It has been argued from numerical diagonalizations of finite clusters [54] that this dissimilarity between the 2D cuprates and 2LL's is due to the difference in the spin correlations characterizing the initial and final excited magnetic states, i.e. the weight of the long ranged Néel type spin-spin correlations in calculating the matrix elements of the current operator plays an important role. It also turns out that, due to the special topology of 2LL's, a study of the 2M RREP in conjunction with an angular dependence of the 2M intensity in parallel polarization in 2LL's can be helpful for determining a relation between the ratio of the super-exchange integrals $J_{\parallel}$ and $J_{\perp}$ and microscopic parameters like hopping integrals and on site Coulomb interactions [55]. Using the effective expression for the photon induced spin exchange coupling mechanism, Eq. 3.2, taking into account the anisotropy of the coupling constants denoted by A and B along the rung and leg directions and using the relationship between H_{FL} and the 2D Heisenberg ladder Hamiltonian from Eq. 3.1, one can derive the following angular dependence of the 2M intensity for $\mathbf{e}_{in} \parallel \mathbf{e}_{out}$: $I_{\parallel}(\omega,\theta) = I(\omega,\theta)[\cos^2(\theta) - \frac{A}{B}\frac{J_{\perp}}{J_{\parallel}}\sin^2(\theta)]$ [55]. From this formula, $J_{\perp}/J_{\parallel}$ can be calculated if the A to B ratio is known. At angles $\theta \neq 0°, 90°$ from an experimental point of view one has to be careful that the different optical properties of the ladder materials along the a and c axes will induce a non-negligible rotation of the polarization of the incident electric field inside the crystal [56]. As we see from Fig. 3.9b the value of A/B is excitation energy dependent and our data suggest that this ratio approaches a constant value in the preresonant regime. From Fig. 3.9 and using an anisotropy ratio $y = J_{\parallel}/J_{\perp} = 1.25$ (see Fig. 3.7) we obtain $A/B \approx 2.5$ in the preresonant regime, which would be compatible with an anisotropic local Cud-Op excitation and slightly different hopping parameters along and across the ladder [55].

3.3 Effects of temperature and Ca(La) substitution on the phononic and magnetic excitations in $Sr_{14}Cu_{24}O_{41}$

3.3.1 Temperature dependent electronic and magnetic scattering in $Sr_{14}Cu_{24}O_{41}$

The effects of temperature and Ca(La) substitution for Sr discussed in this part set the stage for the following section in which low energy Raman, transport and soft X-ray data argue for the existence of charge/spin density wave correlations in $(Sr,La)_{14-x}Ca_xCu_{24}O_{41}$ compounds. In Fig. 3.10a we show the temperature dependence of the c-axis conductivity $\sigma_c(\omega)$ and in panel (b) the Raman response in $Sr_{14}Cu_{24}O_{41}$ for T =300 and 10 K. In both IR and Raman data large changes are observed as the $Sr_{14}Cu_{24}O_{41}$ crystal is cooled from room temperature. In Fig. 3.10a there is a strong suppression of spectral weight below an energy scale of about 1 eV. The same figure shows two relevant energy scales of this system: one is the CT gap around 2 eV which was discussed in connection to the resonance properties of the 2M, and the other one is the activation energy inferred from the Arhenius behavior of the *dc* resistivity above about 150 K [58]. As for the optical sum rule, all the weight is recovered above the CT gap, within an energy scale of $\omega_c \approx 3$ eV. The rapid decrease of the conductivity in the region below 1 eV is correlated to the high activation energy of about 180 meV (= 1450 cm^{-1} = 2090 K). Concomitant to this suppression, which is surprisingly 'uniform' in the 0 to 1 eV range, one observes the development of a broad mid-IR feature and also a sharpening and a spectral weight gain in the phononic features below 1000 cm^{-1}. Interestingly, the position of the mid-IR band seems to be close to the semiconducting-like activation energy revealed by the *dc* resistivity. Fig.3.10b shows that a similarly large reduction in the overall intensity of Raman response takes place in an energy range of at least 0.5 eV (4000 cm^{-1}). The

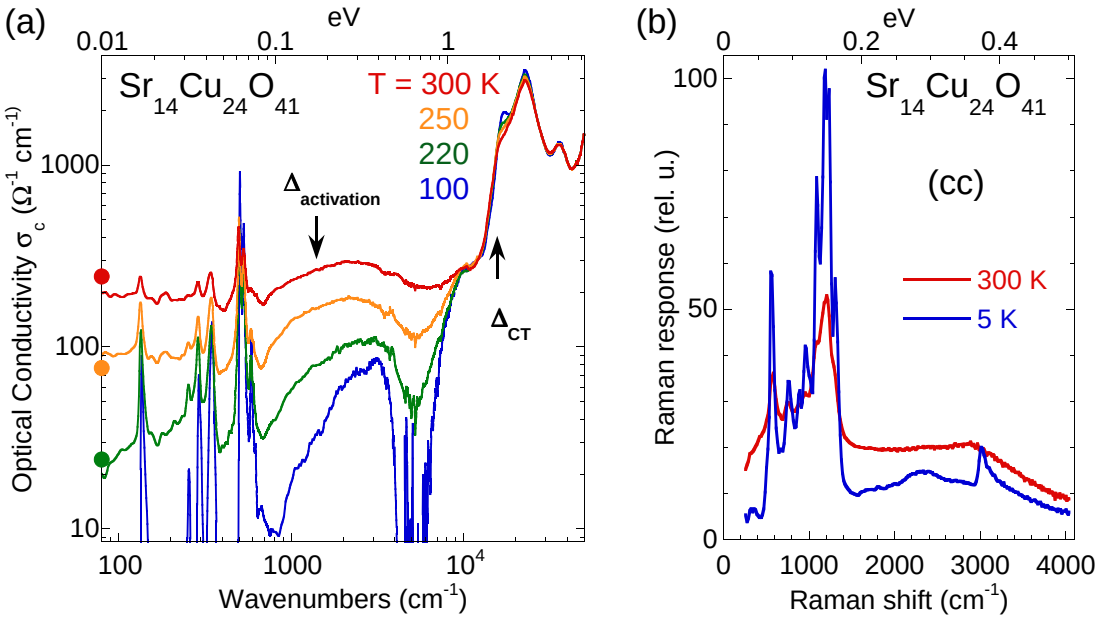

Figure 3.10: (a) Temperature dependence of the c-axis optical conductivity (data provided by the authors of Ref. [57]) in log-log scale. The arrows point towards the activation energy determined by dc resistivity above about 150 K and the characteristic energy corresponding to the charge transfer gap. The circles on the vertical axis represent the dc conductivity values. (b) Raman response in $Sr_{14}Cu_{24}O_{41}$ taken with $\omega_{in} = 1.84$ eV in (cc) polarization at 300 and 5 K.

features which become sharp with cooling are the single and multi-phonon excitations seen around 500, 1200 and 2400 cm^{-1} as well as the 2M feature at 3000 cm^{-1}.

In Fig. 3.11 we show temperature dependent Raman data in two frequency regions: one below 1000 cm^{-1} (panel a) and one around 3000 cm^{-1} where the 2M feature lies (panel b). A different spectral shape than in Figs. 3.6 and 3.10 is seen due to resonantly enhanced side band structures (see Fig. 3.9). The 2M peak is weak and heavily damped at room temperature. Upon cooling we notice two main features: firstly, the spectral weight increases by almost an order of magnitude, and secondly, the 2M peak sharpens from a width of about 400 cm^{-1} at 300 K to 90 cm^{-1} FWHM at T = 10 K. Because J/k_BT remains a large parameter even at room temperature, the magnitude of the observed effects are surprising. For example, in 2D cuprates the 2M peak remains well defined even above 600 K [59]. The side bands around 3660 and 4250 cm^{-1} observed for the $\omega_{in} = 2.2$ eV also gain spectral weight, proportionally with the sharp 2M feature. Fig. 3.11b shows that these sidebands are situated about 650

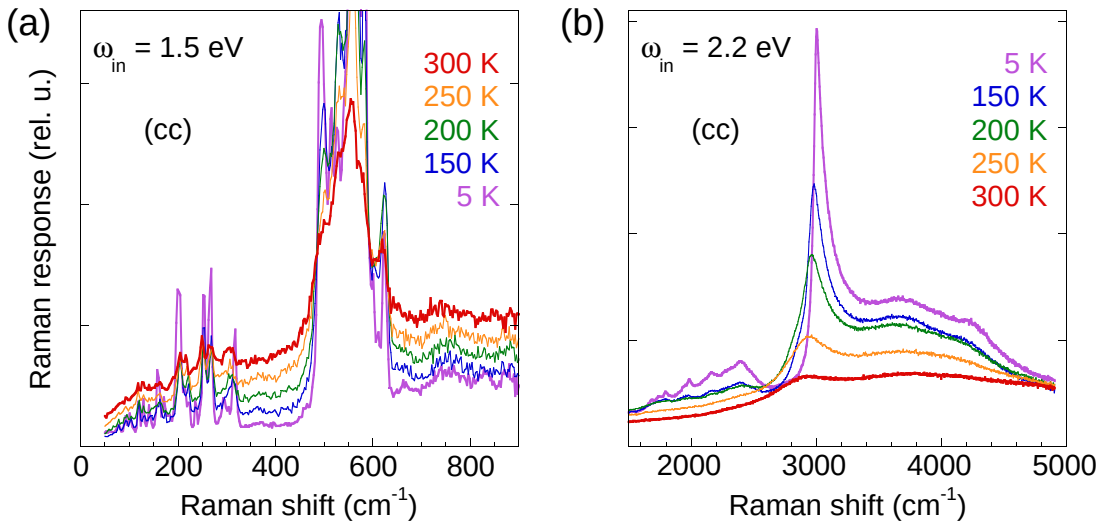

Figure 3.11: Temperature dependent Raman spectra in (cc) polarization for $Sr_{14}Cu_{24}O_{41}$. (a) Phononic spectra taken with $\omega_{in} = 1.5$ eV (some phonons are truncated). (b) The 2M peak at 3000 cm^{-1} for different temperatures. The spectra in this panel are taken using $\omega_{in} = 2.2$ eV

and 2 $\times$ 650 cm^{-1} from the 3000 cm^{-1} resonance. Taking into account that strong phonon scattering characteristic of O modes is found at this frequency, one may argue that these side bands are due to coupled magnon-phonon scattering and bring evidence for spin-lattice interaction in $Sr_{14}Cu_{24}O_{41}$. These energy considerations favor this scenario compared to one involving multi-magnon scattering because the magnetic continuum starts lower, at $2\Delta_S = 510$ cm^{-1}. The latter interpretation remains however a reasonable possibility because in these higher order processes the spectral weight can integrate from a larger part of the Brillouin zone and the boundary of the 2M continuum is dispersive.

The continuum shown in Fig. 3.11a also gets suppressed with cooling. Our data confirms the presence of low lying states at high temperatures, observed also in NMR and c axis conductivity, Refs. [15, 57] and Fig. 3.10. We observe that there is a sharp onset of scattering around 480 cm^{-1}, close to twice the spin-gap energy. The 495 cm^{-1} mode has been interpreted as evidence for Raman two-magnon scattering [41]. However, the temperature dependence of this mode which follows that of the other phonons, the similar suppression with cooling seen not only below this energy but also at higher energies in the 650 to 900 cm^{-1} region and the absence of magnetic

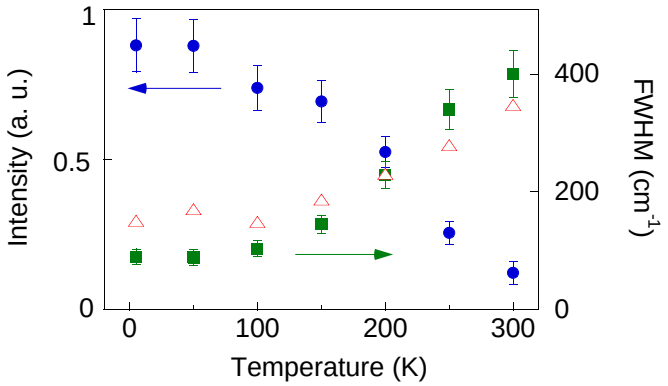

Figure 3.12: The integrated intensity (blue circles, left scale), and the FWHM (green squares, right scale) of the two-magnon peak in $Sr_{14}Cu_{24}O_{41}$ from Fig. 3.11b as a function of temperature. The triangles represent the continuum intensity (in arbitrary units) around 700 cm^{-1} from the data in Fig. 3.11a.

field effects contradict this proposal.

The connection between the low and high degrees of freedom in Fig. 3.11a-b is presented in Fig. 3.12. The increase of the electronic Raman background intensity with heating is correlated with the damping of the 2M peak at 3000 cm^{-1}. The introduced low energy states reduce the lifetime of the magnetic excitation due to additional relaxational channels provided by the small amount of ladder self-doped carriers. We note that the drastic changes with temperature take place roughly above 150 K while below this temperature the variation with temperature is much weaker. This is the temperature at which the *dc* resistivity changes its activation energy from 2090 K to about half its value, 1345 K [62]. $T^* = 150$ K is also the temperature at which the charge ordering in the chain structures is fully established [25, 27] suggesting an interaction between chains and ladders, possibly due to a charge transfer between these systems. It is possible that this charge transfer takes place also as function of temperature and that it gets suppressed below T^*.

3.3.2 The chain-ladder interaction in $Sr_{14}Cu_{24}O_{41}$. Superstructure effects in the phononic spectra

Raman data in $Sr_{14}Cu_{24}O_{41}$ reveals the presence of a very low energy excitation in parallel polarizations. At low temperatures this mode is found around 12 cm^{-1} and we

observe a softening of about 20% with warming up to 300 K. The temperature dependence of the Raman spectra is shown in Fig. 3.13 for both (cc) and (aa) polarizations. An excitation at similar energy is seen also in IR absorption data [60] consistent with the lack of inversion symmetry in the $Sr_{14}Cu_{24}O_{41}$ crystal. Applied magnetic fields up to 8 T do not influence the energy of this excitation which suggests that its origin is not magnetic. This peak is absent in x = 8 and 12 $Sr_{14-x}Ca_xCu_{24}O_{41}$ crystals but it is present around 15 cm^{-1} in the $La_6Ca_8Cu_{24}O_{41}$ compound [61]. These properties along with the unusually low energy make us interpret this excitation as a phononic mode associated with the superstructure determined by the chain and the ladder systems. The chain-ladder commensurability given by the approximate relation 7 c_{ladder} = 10 c_{chain} will result in a back-folding of the phononic dispersions, which in the case of the acoustic branches will lead to a low energy mode. The high effective mass oscillator is understood in this context as a collective motion involving the large number of atoms in the big unit cell of the $Sr_{14}Cu_{24}O_{41}$ crystal.

In Fig. 3.13b-c we plot the temperature dependent energy and width of this low energy phonon. The crossover below a characteristic temperature of about 120 - 150 K mentioned in the previous subsection is emphasized again by the these data. The energy of the peak increases rather uniformly with decreasing temperature from 300 to about 15 K but its FWHM shows a variation with temperature which is diminished below 150 K. The behavior of the integrated intensity of this mode is different in (cc) and (aa) polarizations. Fig. 3.13b shows that in (cc) configuration a kink appears about 150 K in the temperature dependent spectral weight while a maximum is seen in the (aa) polarized spectra around this temperature.

In the scenario presented above the presence of the low energy mode Fig. 3.13 is evidence of ladder-chain interaction. Such an excitation should be sensitive to disorder and even slight modifications in the crystal structure as happens if Sr is substituted by Ca/La. Symmetry arguments discussed in the next subsection confirm the requirement to consider the full crystal structure for the phononic analysis in $Sr_{14}Cu_{24}O_{41}$ and the fact that the disorder introduced by Ca substitution smears out

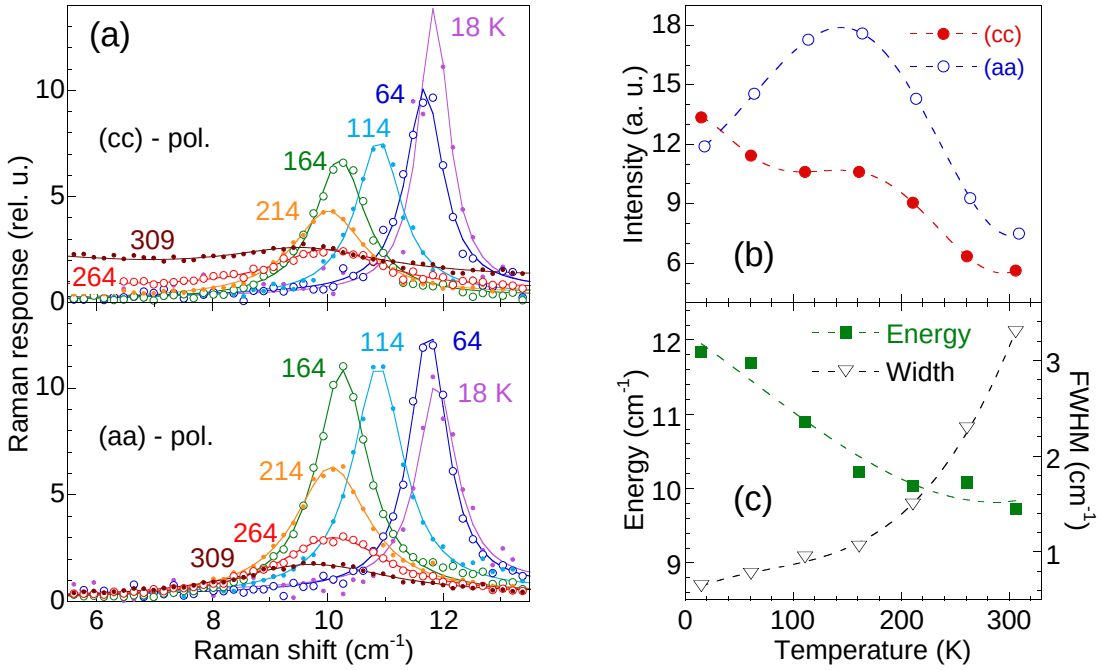

Figure 3.13: (a) Temperature dependence of a low energy $Sr_{14}Cu_{24}O_{41}$ phonon taken with $\omega_{in} = 1.65$ eV in (cc) (upper panel) and (aa) (lower panel). Points represent Raman data and the solid lines are Lorentzian fits. (b) The dependence on temperature of the phonon intensity in (cc) (filled red circles) and (aa) (empty blue circles) polarizations. (c) The phonon energy (left scale) and the width (right scale) of the phononic excitation from (a). Dashed lines in panels (b) and (c) are guides for the eye.

the rich phononic spectra due to the superstructure. The absence of this mode in Ca substituted crystals thus supports our interpretation.

3.3.3 Disorder induced by Ca(La) substitution

This part deals with the effects of inter Cu-O layers cation substitution. If Sr is replaced by Ca then the nominal hole concentration in $Sr_{14-x}Ca_xCu_{24}O_{41}$ does not change, but what may happen is that the amount of holes in the chain and ladder structures gets redistributed [19, 20]. Sr^{2+} substitution by La^{3+} reduces the amount of holes and in $La_6Ca_8Cu_{24}O_{41}$ the chains and the ladders are at half filling. So in analyzing the spin/charge response of the two-leg ladders one has to consider both the doping and the disorder effects induced by inter-layer cation replacement.

An investigation of these effects is certainly worth pursuing in the context of the constraints imposed by the low dimensionality on the charge dynamics and the occur-

rence of superconductivity. Most of the studies in the literature have been focussed on the spin and charge dynamics in pure crystals, although cation substitution is also a source of a random potential. It is known that in 1D an arbitrary random field localizes all electronic states [63] and, in view of the existence of collective excitations of the charge density wave type (see section 1.3.4), pinning effects due to disorder change qualitatively the *dc* and the finite frequency transport properties. X-ray structural analysis show that the ladder interatomic bonds are modulated upon Sr replacement by Ca [64] and it was pointed out in a Raman study [65] that the phononic width increases with Ca concentration in $Sr_{14-x}Ca_xCu_{24}O_{41}$. Theoretical work shows that the gapped phases of 1D spin systems like 2LL's or dimerized chains are stable against weak disorder and magnetic bond randomness [66]. However, in the doped case, superconductivity in the *d*-channel was found to be destroyed by an arbitrarily small amount of disorder.

Ca substitution and phononic scattering – If inhomogeneous broadening plays an important role it has to be seen in all the sharp spectroscopic features. What we try to argue in the following is that the width of both cation and the Cu-O plane modes are renormalized with Ca content. Fig. 3.14a shows low temperature phononic Raman spectra in the 0 - 700 cm^{-1} energy region. The data is taken in (*cc*) polarization with the excitation energy $\omega_{in} = 2.57$ eV; the higher the incoming photon energy the more pronounced is the phononic resonant enhancement.

For $Sr_{14}Cu_{24}O_{41}$ we observe a total of 22 clearly resolved phononic modes extending from 25 to 650 cm^{-1}. For $La_6Ca_8Cu_{24}O_{41}$ and $Sr_{14-x}Ca_xCu_{24}O_{41}$ crystals the features characteristic of O vibrations in the $400 < \omega < 700$ cm^{-1} region broaden into an unresolved band and the rich fine structure below $\omega < 400$ cm^{-1} is smeared out. Clear evidence for the interaction between the chain and the ladder structures in $Sr_{14}Cu_{24}O_{41}$ can be inferred from symmetry considerations alone. If these two units were considered separately a total number of six fully symmetric phonons should be observed in (*cc*) polarization [67], three from the chain structure, *Amma* (D_{2h}^{17}) space group, and three from the ladder structure, *Fmmm* (D_{2h}^{23}) space group [10]. If one

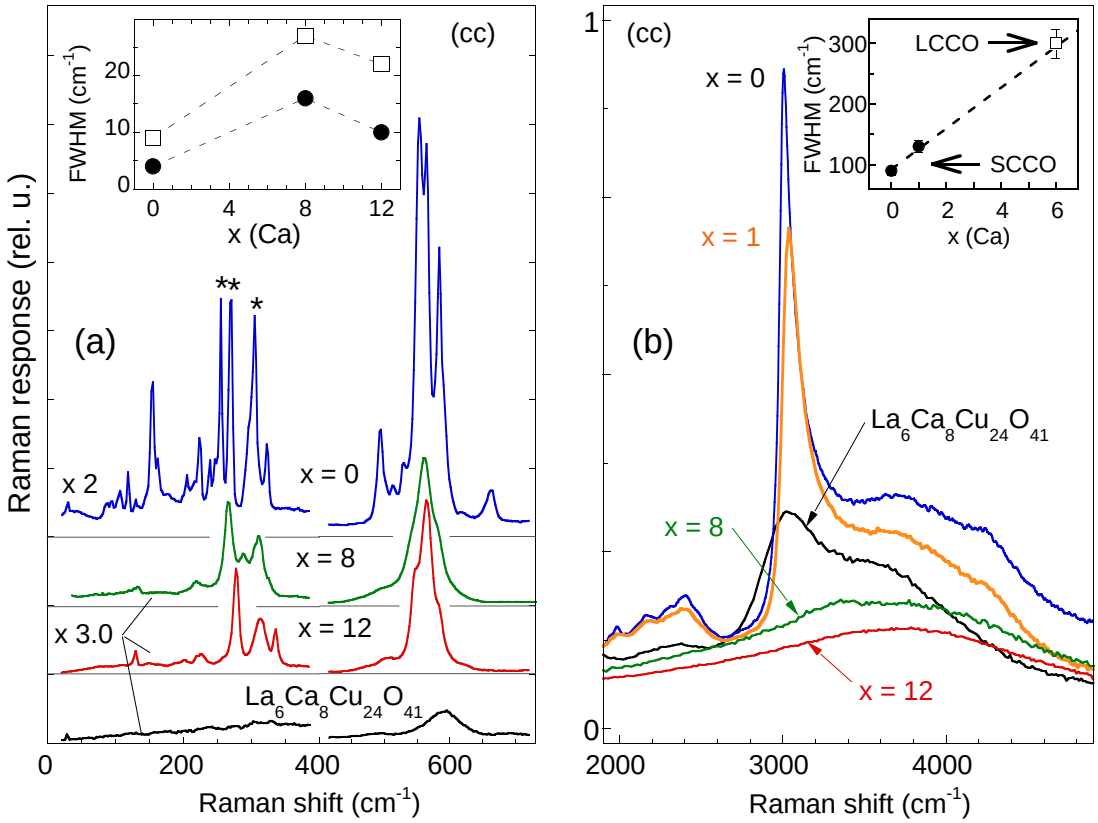

Figure 3.14: (a) T = 10 K Raman data for ω_{in} = 2.57 eV in $La_6Ca_8Cu_{24}O_{41}$ and $Sr_{14-x}Ca_xCu_{24}O_{41}$ with x = 0, 8, 12 in (*cc*) polarization. The inset shows the full width at half maximum of the 255 and 565 cm^{-1} phonons which corresponds to Sr(Ca) (filled circles) and O (empty squares). Dashed lines are guides for the eye. (b) Two-magnon spectra taken with ω_{in} = 2.2 eV in (*cc*) polarization at T = 10 K in $La_6Ca_8Cu_{24}O_{41}$ and $Sr_{14-x}Ca_xCu_{24}O_{41}$ with x = 0, 1, 8, 12. The inset shows the FWHM of the 3000 cm-1 peak as a function of the numbers of Ca atoms in the formula unit.

considers the full crystal structure, two 'options' are available. The first one is to take into account a small displacement of the adjacent Cu-O chains with respect to each other (see Fig. 3 in Ref. [10]) and analyze the phonons within the $Pcc2$ (C^3_{2v}) space group which will give a total of 237 A_1 modes. The second one is to neglect this small displacement, as it is the case of $Sr_8Ca_6Cu_{24}O_{41}$ which belongs to the $Cccm$ (D^{20}_{2h}) centered space group [10] and this approach renders a number of 52 A_{1g} modes. The 22 observed modes in $Sr_{14}Cu_{24}O_{41}$ show that one has to include the chain-ladder interaction and the consideration of the higher $Cccm$ symmetry is sufficient.

Marked with asterisks in Fig. 3.14 are three modes in the region between 250 and 320 cm^{-1} which show a blue shift consistent with the lower mass of Ca atoms

and the reduction in the lattice constants upon Ca substitution [21]. Based on the energy shift and on previous phonon analysis done for the $(SrCa)_2CuO_3$ [68] compound we assign the modes to Sr/Ca vibrations. The FWHM of the 255 cm^{-1} phonon in $Sr_{14}Cu_{24}O_{41}$ is 4 cm^{-1} as compared to 16 and 10 cm^{-1} in the x = 8 and 12 $Sr_{14-x}Ca_xCu_{24}O_{41}$ samples respectively. We observe a similar behavior in the phononic modes originating from Cu-O planes. Three prominent features are seen in the 550-600 cm^{-1} region for the $Sr_{14}Cu_{24}O_{41}$ crystal. We assign the mode with intermediate energy around 565 cm^{-1} to O_{ladder} vibration. The lower and upper modes around 545 and 585 cm^{-1} have frequencies close to vibrations of the O atoms in the chains as observed in $(SrCa)_2CuO_3$ and CuO [67, 68] compounds. Fits for the 550 cm^{-1} band in SCCO crystals reveal that the FWHM of the 565 cm^{-1} mode increases from 9 cm^{-1} for $Sr_{14}Cu_{24}O_{41}$ to 27 and 22 cm^{-1} for x = 8 and 12 $Sr_{14-x}Ca_xCu_{24}O_{41}$ crystals, see the inset of Fig. 3.14a. This is similar to what happens to the 255 Ca/Sr mode suggesting that the $Sr_{14-x}Ca_xCu_{24}O_{41}$ crystals become again more homogeneous at higher Ca substitution level. The data for the LCCO crystal shows that in this material phonons are affected the strongest by disorder which is most likely due to the high La mass and atomic size compared to Ca or Sr atoms.

Ca substitution and magnetic scattering – Regarding the sharp 2M Raman resonance, Fig. 3.14b, one can see dramatic changes taking place with Ca substitution at T = 10 K and that these changes also affect the 2M sidebands. In $Sr_{14}Cu_{24}O_{41}$ the FWHM is 90 cm^{-1}. Ca substitution leads to hardening and to substantial broadening of the magnetic peak accompanied by a drastic decrease in its scattering intensity. One Ca atom in the formula unit of $Sr_{14-x}Ca_xCu_{24}O_{41}$ increases the spectral width by 30%, see inset of Fig. 3.14b. This effect can be ascribed to the intrinsic inhomogeneity rather than a marginal effect on the lattice constants and hole transfer from the chains to the ladders [19]. The FWHM in x = 8 $Sr_{14-x}Ca_xCu_{24}O_{41}$ and $La_6Ca_8Cu_{24}O_{41}$ are about the same within the error bars which is remarkable because the latter is an undoped material so the width of the peak seems not to be related to the presence of

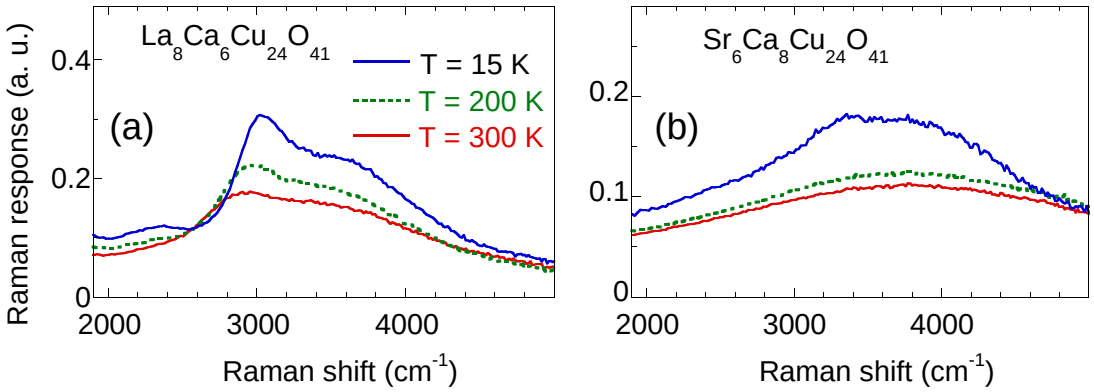

Figure 3.15: Two-magnon scattering in $La_6Ca_8Cu_{24}O_{41}$ and x = 8 $Sr_{14-x}Ca_xCu_{24}O_{41}$ in (cc) polarization for three temperatures.

carriers in the ladders. Comparison of our data in $La_6Ca_8Cu_{24}O_{41}$ and $SrCu_2O_3$ [51], both containing 2LL's at half filling, shows clearly that out-of-plane inhomogeneities have major impact on the magnetic properties of the ladders.

By comparing Fig. 3.11b and 3.14b One can also note a resemblance between the effect of temperature in $Sr_{14}Cu_{24}O_{41}$ and Ca substitution in $Sr_{14-x}Ca_xCu_{24}O_{41}$. Fig. 3.15 shows that temperature effects in $La_6Ca_8Cu_{24}O_{41}$ and $Sr_6Ca_8Cu_{24}O_{41}$ are suppressed compared to $Sr_{14}Cu_{24}O_{41}$. In this sense one could introduce an 'effective' temperature associated with the cation substitution level. A comparison to 2D cuprates is again interesting: in the latter case the 2M is broad to start with even in pure materials, but a different number of cation types between the Cu-O layers (higher in insulating $Bi_2Sr_2Ca_{0.5}Y_{0.5}Cu_2O_8$ than for instance La_2CuO_4) does not lead to qualitative changes in the 2M width [40].

The data in Fig. 3.14b suggest that an appropriate phenomenological model to describe the ladder Hamiltonian in Ca doped crystals is $H = \sum_{leg} J_{||}^{ij} \mathbf{S}_i \cdot \mathbf{S}_j + \sum_{rung} J_{\perp}^{ij} \mathbf{S}_i \cdot \mathbf{S}_j$ where the super-exchange integrals J^{ij} in the lowest order have a contribution proportional to the relative local atomic displacements $\mathbf{u}_{ij}$ according to $J^{ij}(\mathbf{u}) = J_0 + (\nabla J)\mathbf{u}_{ij}$. The effects of thermal fluctuations on the super-exchange integrals J_{ij} can be included in a similar phenomenological approach [69] which could explain the strong resemblance between the Ca substitution and temperature seen in Figs. 3.14b and 3.15. We expect the ratio $< J_{\perp} > / < J_{||} >$ to change with Ca content

as structural studies show that the Cu-O bonds along the rungs are less affected by Ca substitution than the Cu-O bonds parallel to the ladder legs [64]. Also the hardening of the magnetic peak from 3000 cm^{-1} in $Sr_{14}Cu_{24}O_{41}$ to about 3375 cm^{-1} in x = 8 $Sr_{14-x}Ca_xCu_{24}O_{41}$ is consistent with the reduction in the lattice constants at higher Ca substitutional level which will lead to a higher super-exchange J, a parameter very sensitive to the interatomic distances [70].

3.4 Density-wave correlations in doped two-leg ladders.

3.4.1 Density waves: competing ground state to superconductivity.

So far we have been investigating mainly the magnetic properties of two-leg ladders around half filling factor and analyzed the effects of temperature and Sr substitution especially in terms of their influence on the high energy 2M scattering around 3000 cm^{-1}. We observed that both the temperature and the isovalent cation substitution produce drastic changes in the optical and Raman spectra from far IR up to energies of several eV. These properties, along with the established metal-insulator transition found around 60% Ca doping, the occurrence of superconductivity and the similarities with 2D cuprates, nurture the hope that a study of low energy physics in $Sr_{14-x}Ca_xCu_{24}O_{41}$ may reveal universal aspects related to the nature of the ground states in low dimensional correlated spin $S = 1/2$ systems. It is the purpose of this section to bring evidence for the existence of density wave correlations in doped 2LL's at all Ca substitution levels [61]. Ground states with broken translational symmetry have been discussed in the context of low dimensional systems [18]. Examples are states which display a long ranged oscillation of the charge and/or spin densities as well as ones which acquire a topological bond order due to the modulations of the

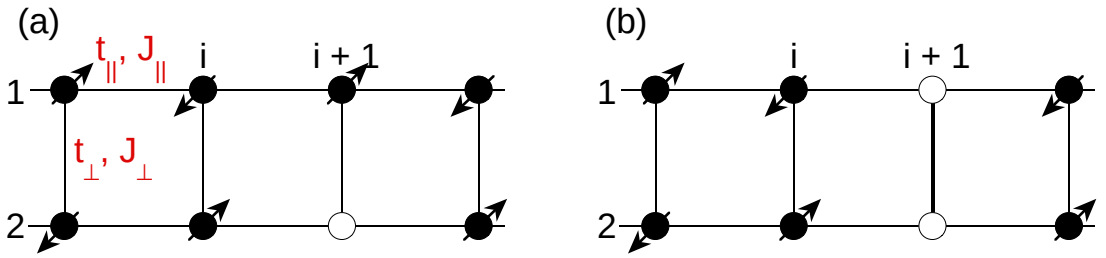

Figure 3.16: Intuitive understanding of the origin of hole pairing in two-leg ladders in the strong coupling limit ($J_\perp \gg J_\parallel$). If an initial hole sits on rung 'i+1' (panel a) the second added hole (panel b) sits on the same rung in order to minimize the number of broken AF bonds.

inter-atomic coupling constants, for example of the super-exchange integrals. It has been indeed found that the charge density waves (CDW) and superconductivity are the predominant competing ground states and the balance between them is ultimately determined by the microscopic parameters of the theoretical models [12, 13].

So, what are the low energy excitations one expects from a doped 2LL? Most of the theoretical studies of 2LL's consist of numerical evaluations, especially exact diagonalization (ED) and density matrix renormalization group techniques (DMRG), performed within the $t_\parallel - J_\parallel, t_\perp - J_\perp$ model, see Fig. 3.16, but not taking in to account the long range Coulomb interactions. It is interesting to discuss first the cases corresponding to only one or two holes in the ladder structure. If one hole is present on a ladder rung (Fig. 3.16a) it can sit on a bonding or antibonding orbital. Hopping will lead to bands separated roughly by $2t_\perp$ and a bandwidth proportional to $t_\parallel$ [71]. How tight is the charge bound to the remaining free spin? This question is connected to the problem of possible spin-charge separation. Evaluations of hole-spin correlations on a 2×10 cluster suggest that the unpaired spin remains tightly bound to the injected hole [71], so that this composite state carries both charge and spin, in this sense being similar to a quasi-particle. This is in contrast with the spin-charge separation in the 1D AF chain.

If two holes are present (Fig. 3.16b) there appears a property which seems to be very robust for 2LL's: pairing. The following discussion can be intuitively understood starting from the strong coupling limit but studies of finite clusters within the $t_\parallel -$

$J_\parallel, t_\perp - J_\perp$ model show that this qualitative discussion holds to the relevant isotropic limit $J = J_\parallel = J_\perp$ and $t = t_\parallel = t_\perp$. If one additional hole is injected in the ladder, it will tend to align on the same ladder rung, see Fig. 3.16b, in order to minimize the magnetic energy [12, 13]. The lowest band will be generated by the coherent propagation of hole pairs and it is found in the spin singlet channel. At finite energies there will be continua of electronic states generated by breaking the pairs, the singlet and the triplet states being almost degenerate when the holes are far apart [71]. One can note that in the case of 2LL's it is the purely spin-spin correlations which effectively lead to hole pairing and not an explicit hole-hole attractive interaction and also that the main energy gain due to pairing is given by the magnitude of the spin gap. The 'easy' pairing and the kinetic energy gain of the paired holes when pairs are far apart from each other is a non-trivial difference with respect to the 2D cuprates in the sense that in the latter case evaluations prompted by the above arguments lead to macroscopic phase separation.

Since the spin gap Δ_S is to some degree a measure of the hole binding energy it is interesting to discuss what is its evolution with doping. In the undoped case the lowest triplet excitation is the branch with a minimum at π shown in Fig. 3.5 and its magnitude is governed by $J_\perp$. The spin gap remains substantial at isotropic coupling, relevant for experiments, and in this case it is known exactly to be $J/2$ in the model of Eq. 3.1. This excitation evolves continuously with doping. For instance, calculations on a 2×24 cluster at 1/8 doping and isotropic coupling shows that the spin gap is about $0.275J$, about half of the value in the undoped case [72]. Interestingly, pairing generates a different type of singlet-triplet transition [71, 72]. This excitation, present only in the doped case, will consist of breaking of a singlet hole pair into two separate quasi-particles in the triplet channel. The different kinetic energy gain of the separate holes versus the magnon in the undoped case will lead to different energies of these two types of magnons. It was argued [71] that the spin gap evolves discontinuously in 2LL's because it is the 2^{nd} type of magnon which costs less energy. Later ED and DMRG work [73] confirmed this point and showed that in a relevant parameter range

the energy of this new type of spin-gap is smaller than the pair breaking continua because a triplet can hybridize with a state formed by two holes (one in bonding and one in antibonding orbitals) forming bound $S = 1$ magnon-hole states.

Once the stability of the hole pair is confirmed to exist in the relevant ranges of the microscopic parameters, it is up to the estimation of residual interactions between the hole pairs and spins to determine what kind of ground state is chosen. Superconductivity fluctuations were probed within the $t - J$ model by evaluating numerically the pair-pair correlation function, a measure of the stability of the motion of the hole pair in the spin-gapped phase. This function, which is to be evaluated in the limit of $l \rightarrow \infty$, is defined as $P(l) = \frac{1}{N} \sum_i < \Delta_i^\dagger \Delta_{i+l} >$ where Δ_i is the pair destruction operator at site 'i' given by $\Delta_i = \frac{1}{\sqrt{2}}(c_{i1,\uparrow} c_{i2,\downarrow} - c_{i1,\downarrow} c_{i2,\uparrow})$ (here the 'c' operators are defined within the subspace of no double occupancy). Early work showed an increase in the pairing tendency as the ratio $J_\perp / J_\parallel$ was increased [14] It has been found for a 2×30 cluster at $n = 1/8$ doping that SC correlations are dominant and they decay algebraically with l [74]. The exponent was found to be smaller than one while density-density correlations were observed to decrease as l^{-2} implying that SC is the dominant phase. In the same system, by using Green's function techniques, the frequency and wavevector dependence of the superconducting gap [72] showed a structure with nodes, much like the d-wave pairing symmetry in 2D cuprates.

Pairing does not necessarily mean superconductivity. Another possibility is that the bound (or single) holes form a spatially ordered pattern, i.e. a CDW ground state. It has been argued from DMRG calculations that a phase diagram of the isotropic $t - J$ 2LL's, in a relevant range given for instance by $J/t < 0.4$, will have as generic phase one with gapped spin modes and gapless charge mode [75]. This phase [76] is characterized by d-wave like pairing and $4k_F$ CDW correlations, with superconductivity being the dominant phase [75]. Note that this $4k_F$ CDW renders a wavelength which is half of the one in conventional Peierls transition. Phase separation will occur roughly at values $J/t > 2.5$ [71, 75]. These numerics also argue that besides these two phases, there are small fully gapped regions (for both

spin and charge sectors), to be found generally at commensurate dopings, where a CDW occurs [75]. The characteristic wavevector of this state is given by $2(k_{Fb}+k_{Fa})$ where k_{Fb}/k_{Fa} stand for the Fermi wavevectors of the bonding/antibonding electronic orbitals, discussed in the paragraph related to the charge dynamics in a ladder with one hole. Interestingly, a finite spin gap is not found to be crucial for the existence of such a CDW so, if the spin gap determines the pairing, the hole crystal can be made either out of single hole or out of hole pairs [75].

The study of low energy physics in $(Sr,La)_{14-x}Ca_xCu_{24}O_{41}$ is encumbered on the experimental side by the following 'non-intrinsic' facts: (1) The structure is quite complicated due to the presence of the chains and ladders. We found that these subsystems interact, so one expects that supermodulation will affect carrier dynamics. (2) $Sr_{14}Cu_{24}O_{41}$ has a finite hole concentration in the ladder structure to start with. Ca substitution (and maybe temperature) redistributes the charges between chains and ladders but up to now there is no accurate quantitative determination of this effect. On the contrary, there are conflicting views in the literature [19, 20]. (3) The effect of O stoichiometry at the crystal surface may be important in accurately determine the carrier concentration; besides, fresh surfaces are not easy to obtain because these materials do not cleave in the (ac) plane.

The problem of what happens with the spin gap in the doped ladder is an open issue from an experimental point of view. On one hand neutron scattering finds $\Delta_S = 32$ meV in both $Sr_{14}Cu_{24}O_{41}$ [26] and x = 11.5 $Sr_{14-x}Ca_xCu_{24}O_{41}$ [77] which says that the spin gap does not change its value. On the other hand, from the Knight shift (proportional to the uniform susceptibility) and the spin-lattice relaxation data, NMR measurements find a decrease by about 50% of the ladder spin gap [29]. Mayaffre *et al.*, by using the same technique, tried to relate directly the disappearance of the spin gap to the occurrence of superconductivity under pressure [78]. Although a finite spin gap is a central issue which underlies the up to date theories predicting that doped ladders are superconducting, it is still not quite clear what the origin of the discrepancy between the INS and NMR data is.

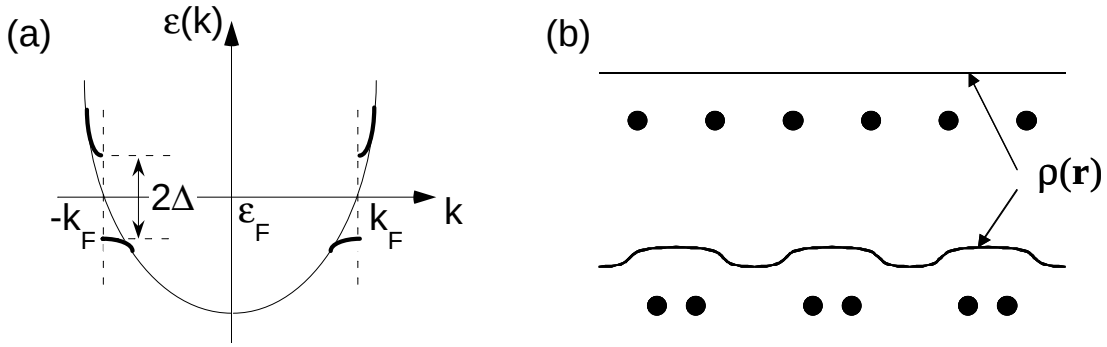

Figure 3.17: (a) The single particle conduction band in the metallic state (finite DOS at the Fermi energy ϵ_F) and in the insulating CDW state (a gap 2Δ opens at ϵ_F). (b) The electron density in the metallic and CDW state. Although generic, the doubling of the unit cell shown here is appropriate for a half filled band.

3.4.2 Electromagnetic response of charge density wave systems.

The purpose of this section is to discuss at a very general level the main properties of CDW systems. A brief introduction to the mean field description of the Peierls transition in 1D will be followed by a qualitative discussion of the electronic excitations and the low energy transport properties.

The Peierls transition in 1D – One good example of the way the phase space constraints act in low dimensions is to evaluate the susceptibility $\chi(q) \propto \int d\vec{k}(f_k - f_{k+q})/(\epsilon_k - \epsilon_{k+q})$ for 1, 2 and 3 dimensions. This expression of the (Lindhard) susceptibility connects the linear response of the density of a non-interacting electron gas to an external potential in the mean field approximation. Here $\epsilon_k = \hbar^2 k^2/2m$ is the free electron energy and $f_k = 1/(\exp((\epsilon - \mu)/k_B T) + 1)$ is the Fermi function. While in 3D and 2D this function is continuous and singularities and/or discontinuities appear in the derivatives, in 1D $\chi(q, T = 0)$ diverges at $q = 2k_F$. The instability with respect to charge modulation characterized by $\lambda = \pi/k_F$ has to do with the Fermi surface topology and it is generated by the existence of a large number of states having the same energy and being $2k_F$ apart, see Fig. 3.17 and Ref. [79].

Many results of the mean-field theory for the CDW transition are similar to the the ones for BCS superconductivity in the weak coupling limit. The starting Hamiltonian

used by Fröhlich [80] is:

$$H = \sum_{k,\sigma} \epsilon_k c^\dagger_{k,\sigma} c_{k,\sigma} + \sum_q \hbar\omega_q b^\dagger_q b_q + \sum_{k,q,\sigma} g(q) c^\dagger_{k+q,\sigma} c_{k,\sigma} (b_q + b^\dagger_{-q}) \tag{3.3}$$

where c and b are electron and longitudinal acoustic phonon operators and $g(q)$ is the electron-phonon coupling constant given by $g(q) = i(\hbar/2M\omega_q)|q|V_q$ (M is the ionic mass and V_q is the Fourier transform of the potential of a single ion). Writing down the equations of motions for the normal coordinates in terms of the commutators between them and the Hamiltonian 3.3 and taking into account that the electronic response can be 'fed back' using the Lindhard susceptibility in the extra term appearing due to electron-phonon coupling, one obtains an expression of renormalized acoustic phonon frequency of the form: $\omega_q^{ren} = \sqrt{\omega_q^2 + 2g_q^2\omega_q\chi(q,T)/\hbar}$. The divergence of the electronic susceptibility will single out the phonon at $2k_F$ and will render a temperature T_c at which the phononic frequency goes to zero (the Kohn anomaly - macroscopic occupation of the $2k_F$ state). This enables one to define an order parameter $\Delta e^{i\phi} = g < b_{2k_F} + b^\dagger_{-2k_F} >$ (here $g = g(2k_F)$) and one can obtain the following relations: (1) $\Delta(T=0) = 2D\exp(-1/\lambda)$ and $2\Delta = 3.56k_BT_c$ where λ is a dimensionless electron-phonon coupling and $D = 2\epsilon_F$ is the bandwidth. These are similar to the BCS expression but in the latter case the bandwidth is replaced by the Debye frequency ω_D. (2) $\rho(x) = \rho_0 + (\rho_0\Delta/\lambda v_F k_F)\cos(2k_F + \phi)$, where v_F is the Fermi energy of the electron gas. The average ionic displacement u, will also be proportional to the gap since it is proportional to $< b_{2k_F} + b^\dagger_{-2k_F} >$. This comes from the decomposition of the lattice displacements in terms of creation and annihilation operators. (3) Using the definition of the order parameter and Eq. 3.3 one obtains a single particle excitation spectrum defined by $E_k = \epsilon_F + sgn(k-k_F)\sqrt{\hbar^2 v_F^2(k-k_F)^2 + \Delta^2}$. (4) the condensation energy calculated as the gain in the kinetic energy minus the loss in the elastic energy is given again by a relation similar to the one in BCS theory: $E_{cond} = D(\epsilon_F)\Delta^2/2$.

So, as a result of the transition, a gap will open at the Fermi energy and this will be observed in *dc* transport as a metal insulator transition taking place at T_c. Due

to the change in the lattice constant there will also be new phononic modes allowed in the CDW state. In real systems, which are not strictly 1D, it is possible that not all the Fermi surface gets gapped, so the metallic behavior can continue below T_c, as is the case of $NbSe_3$. Since the CDW transition involves ionic motions, it can be directly probed by X-rays or neutron scattering [79].

Excitations out of the CDW state – One feature which can be seen in the optical absorption spectra is due to the excitations of electrons across the CDW gap 2Δ. This belongs to the single particle channel. Since the Debye energy is much smaller than the Fermi energy the superconducting gaps from BCS theory are typically smaller than the gap excitations in the CDW state. For instance, in blue bronze ($K_{0.3}MoO_3$) which is one of the most studied quasi-1D CDW materials, this energy is found at about $2\Delta = 125$ meV [81]. There are also collective excitations out of the condensate and they are related to the space and time variations of the complex order parameter. Excitations can occur which are due to both phase (phasons) and amplitude (amplitudons) fluctuations. Pictorial images of such excitations are shown in Fig. 3.18. The interest is to understand the long wavelength limit of these excitations shown in Fig. 3.18d-e. As for the amplitude mode, its energy ω_A in the limit $q \to 0$ is finite. An oscillation of the gap amplitude $\delta(\Delta)$ will also lead to an oscillation of the ionic positions $\delta(u)$. The decrease in the condensation energy, $\delta(E_{cond}) = D(\epsilon_F)\delta(\Delta^2)/2$ will be equal to the extra kinetic energy associated with ionic displacements, $MN\omega_A^2(q=0)\delta(u^2)/2$ where M, N are the ionic mass and number respectively. As a result one obtains a finite value for $\omega_A(q \to 0)$.

The situation is different for the long wavelength phase mode. Such motion is a superposition of electronic charge along with ionic oscillations which leads to a high 'effective mass', m^*. In Fig. 3.18e one can see that this excitation in the $q \to 0$ limit involves a translational motion of the undistorted condensate so it will cost no energy. Its dispersion in the $q \to 0$ limit is given by $\omega_\Phi^2(q) = (m/m^*)v_F^2q^2$ [82]. Since phase fluctuations involve dipole fluctuations due to the displacements of the electronic density with respect to the ions the phason is a feature which will be seen

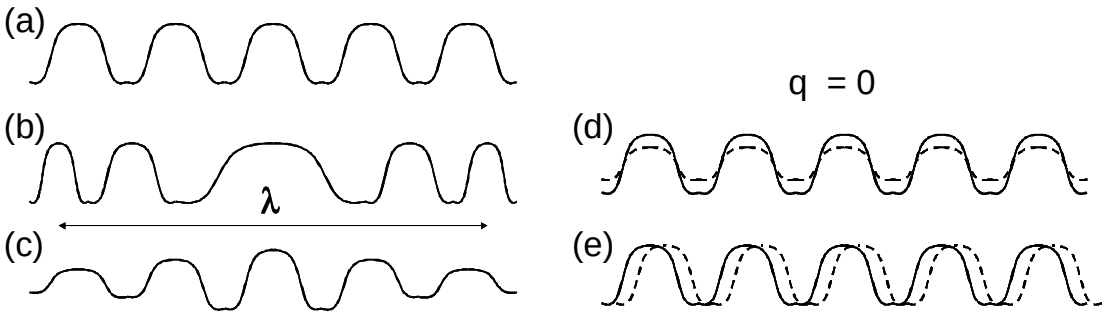

Figure 3.18: Phase and amplitude modes of the CDW order parameter. (a) The undistorted ground state. Phase (b) and amplitude (c) excitations at wavevector $q = 2\pi/\lambda$. Amplitude (d) and phase (e) excitations (dashed lines) at $q = 0$ with respect to the ground state (solid line).

in the real part of the optical conductivity data. The amplitude mode at $q = 0$ does not involve such displacements so it is expected to be a Raman active mode.

Most interesting is that in the ideal case considered here the phase mode is current carrying and it can slide without friction [80]. As a result this excitation will be seen as a δ function at zero frequency. The spectral weight of this peak is given by m/m^* and this is stolen from the single particle conductivity which becomes an edge, instead of a singularity reflecting the divergence in the density of states [82], see also Figs. 8 and 9 in Ref. [81]. The interaction with impurities or lattice commensurabilities destroys the infinite conductivity and the mode in Fig. 3.18e will be pinned. As a result, this excitation will be shifted to finite frequencies which characterize the particular impurity potential. In Fig. 3.19 is shown the example of the blue bronze, the pinning mode as well as the gap feature being seen around 2 and 1000 cm^{-1} respectively.

Zero frequency and microwave transport in the CDW state – The existence of a gap and low energy collective excitations lead to several other properties which were seen in *dc* and finite frequency (typically in the microwave region) conductivity. In a $I - V$ characteristic one can talk roughly speaking about three regimes. At low electric fields there is an Ohmic behavior and the conductivity at finite temperatures will be due to thermally excited electrons (normal carriers) out of the condensate. Above a threshold field, $E_T^{(1)}$, related to the magnitude of the pinning

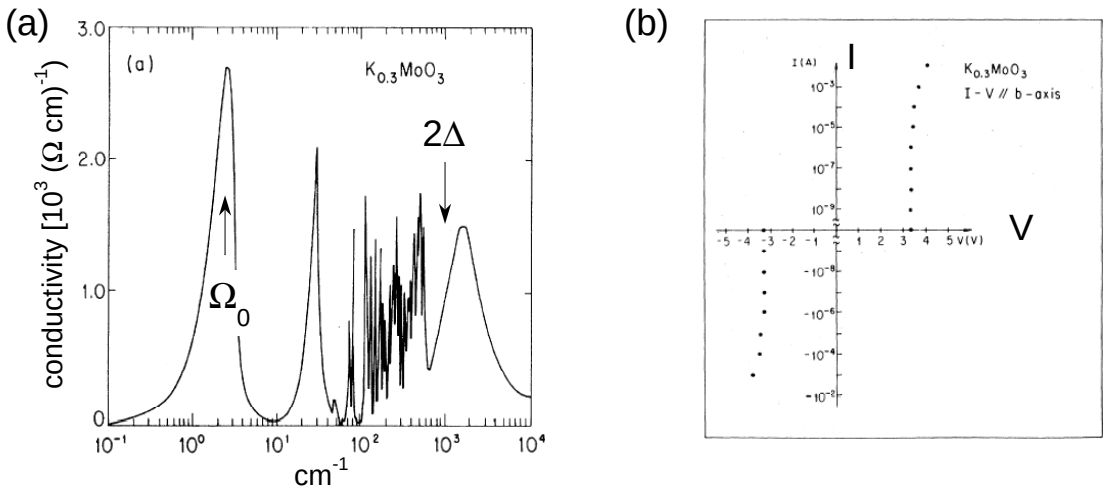

Figure 3.19: Collective excitations and transport in $K_{0.3}MoO_3$. (a) Optical conductivity in the CDW phase from Ref. [81] showing the pinned mode at Ω_0 and the single particle edge starting at 2Δ. Many new electron-phonon coupled modes appear in the mid-IR region below the transition. (b) The observation of the second threshold, Fröhlich superconductivity, in $K_{0.3}MoO_3$ (from Ref. [83]).

potentials, the contribution of the condensate sets in. The CDW starts moving as a whole and this motion is accomplished through distortions of the phase and/or amplitude of the condensate. At high fields, above some other threshold field $E_T^{(2)}$, the external forces cause a fast sliding motion of the CDW which 'ignores' the underlying pinning potentials and the current increases very steeply (almost infinite differential conductance) for small variations of the applied voltage, see Fig. 3.19b. This regime is reminiscent of the ideal case where 'Fröhlich superconductivity' should occur. The $I-V$ curve in 2^{nd} and 3^{rd} regimes is non-linear and temperature dependent. Notable is that for an applied *dc* voltage, the motion of the CDW as shown in Fig. 3.18 will also lead in a clean sample to a finite frequency component of the current. The fundamental frequency of this oscillatory component is directly related to the wavelength of the density wave.

Low frequency CDW relaxation – Another low energy feature observed in many well established CDW compounds is a relaxational peak which has a strong temperature dependent energy and damping related to the *dc* conductivity of the material. This loss peak is seen typically in the microwave region at energies much lower than the pinning frequency. For example in $K_{0.3}MoO_3$ the frequency range

is 10^4 - 10^6 Hz for temperatures between 50 to 100 K while the pinned mode is roughly at $\Omega_0 \approx 60$ GHz see Figs. 3.20d and Figs. 3.19a respectively. In Ref. [85] the author proposes a scenario to reconcile the observations at low and high frequencies, a summary of the results being shown in Fig. 3.20a-c. The interpretation of the damped excitation is that it is a longitudinal density wave relaxational mode due to the interaction with normal carriers. It is argued that this mode, which should not be seen in the transverse channel, is seen however in the dielectric response because of the non-uniform pinning which introduces disorder. By making the wavevector k, according to which the modes can be classified as transverse or longitudinal, a 'not so good quantum number', disorder mixes the pure longitudinal and transverse character of the excitations. In other words, breaking of the selection rules make the longitudinal modes appear as poles, rather than zeros, of the dielectric response function.

The main results of the theory in Ref. [85] are shown in Fig. 3.20 where the CDW dielectric function is plotted as a function of frequency. The distribution of pinning centers is modeled by the function $g_n(x) = (n^{n+1}/n!)x^n \exp(-nx)$ (a measure of disorder) which is peaked at $x = 1$ and satisfies $g_{n\to\infty}(x) = \delta(x-1)$. In Fig. 3.20a one can see that the disorder leads to the appearance of a mode at lower frequencies which steals spectral weight from the pinning mode situated at the average frequency Ω_0. The stronger the disorder, the higher is the spectral weight redistribution between the two modes. Panels (b) and (c) in Fig. 3.20 show the real and the imaginary part of the CDW dielectric function for a given n. They are related by Kramers-Krönig relations, so the drop in $Re(\varepsilon)$ leads to a peak in $Im(\varepsilon)$. These data are plotted for several values of the relaxational time τ_1 which mimics (through the dependence on conductivity, see the caption of Fig. 3.20) a linear variation in temperature. Decreasing temperature leads to a decrease in conductivity and a higher τ_1 and to the softening of the relaxational peak which moves away from Ω_0.

CDW coupling to the uncondensed carriers – Here we derive in a simplified version the longitudinal screening mode shown in Fig. 3.20. In this approach the

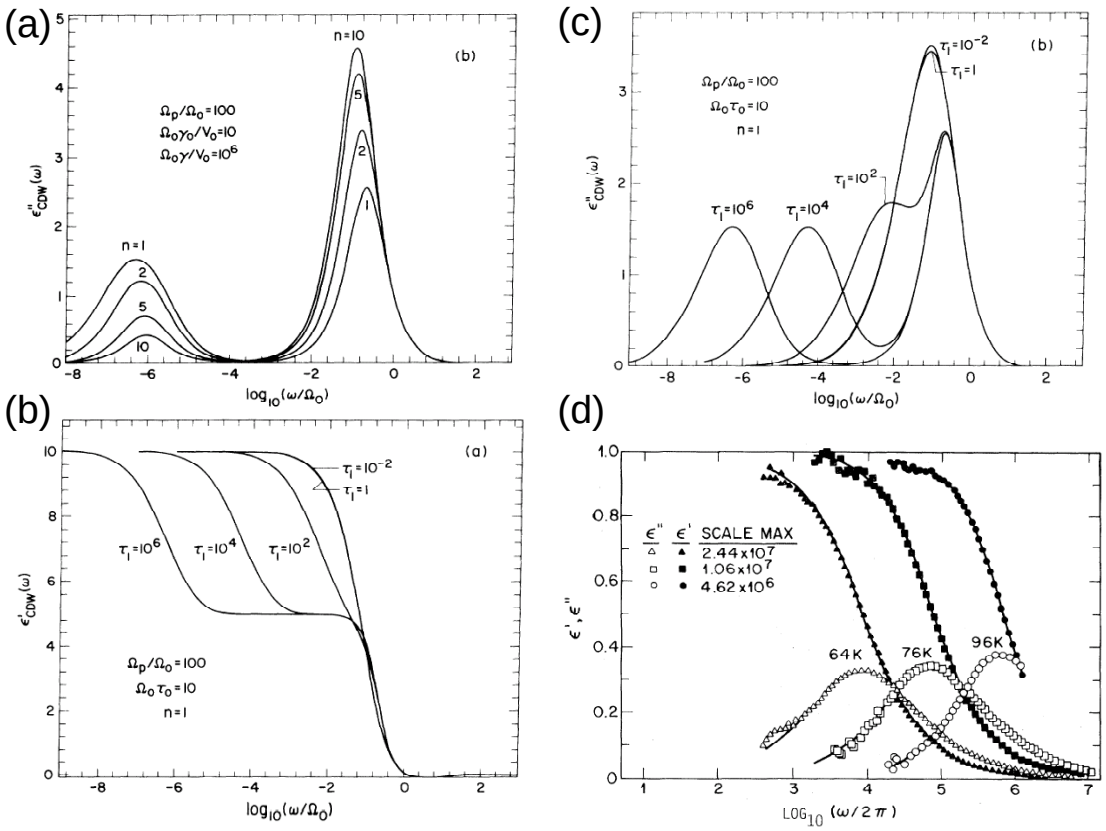

Figure 3.20: The dependence of the real and imaginary part of the CDW dielectric function on frequency on the log scale. Panels (a), (b) and (c) show theoretical results from Ref. [85]. Ω_0 and Ω_p are the pinning and the CDW plasma frequencies, γ_0 is an intrinsic damping parameter and V_0 in panel (a) is the pinning potential. τ_0 and τ_1, defined by $\tau_0 = \gamma_0/V_0$ and $\tau_1 = \gamma/V_0 = \rho_c^2/\sigma V_0$ (with σ and ρ being the *dc* conductivity and the CDW density), are characteristic relaxational times. The parameter n represents a measure of the distribution in pinning frequencies: $n \to \infty$ means that there is only one mode in the distribution, the smaller n is, the broader the distribution. Panel (d) shows experimental determination of the real and imaginary parts of the dielectric function for three representative temperatures (data from Ref. [84]).

CDW is modeled by an oscillator with a characteristic pinning frequency Ω_0 and we neglect internal distortions. The only other ingredients of the model are the presence of a finite electron density corresponding to thermally activated quasi-particles and the assumption that the interaction between these two fluids is only *via* an electromagnetic field. The calculation of the longitudinal CDW modes as well as the coupling to the normal, uncondensed, electrons follows almost identically the treatment of longitudinal phonons and their coupling to plasma oscillations in metals. In the following, $\vec{u}$ is a uniform displacement of the CDW (in a real crystal this will be

within a volume determined by the longitudinal and transverse correlation lengths), ρ_c and m^* are the CDW charge and mass densities and γ_0 is an intrinsic damping coefficient. The time derivatives for oscillations at a given frequency ω are replaced by $\partial/\partial t \rightarrow -i\omega$. The derivation can be made using the general relations of the Born and Huang model [86]:

$$-\omega^2\vec{u} = -\Omega_0^2\vec{u} + i\omega\gamma_0\vec{u} + \frac{\rho_c}{m^*}\vec{E} \tag{3.4}$$

$$\vec{P} = \rho_c\vec{u} + \frac{\varepsilon_\infty - 1}{4\pi}\vec{E} \tag{3.5}$$

Here ε_∞ takes care of the background carrier contributions arising from interband transitions. In the absence of carriers, neglecting the damping and using the electrostatic approximation ($\nabla \times \vec{E} = 0$ which means that the field is purely longitudinal and as a result $\vec{E} = \vec{E}_L$), these equations allow us to determine the characteristic transverse and longitudinal frequencies. The equation $-\omega^2\vec{u}_T = -\Omega_0^2\vec{u}_T$ (because $\vec{E}_T = 0$) allows the identification $\Omega_0 = \Omega_T$, i.e. the frequency of the transverse mode. The longitudinal modes will generate a finite electrostatic field. Eq. 3.5 and Gauss' law $\nabla(\vec{E} + 4\pi\vec{P}) = 0$ lead to $\nabla(4\pi\rho_c\vec{u}_L + \varepsilon_\infty\vec{E}) = 0$ so $\vec{E} = -4\pi\rho_c\vec{u}_L/\varepsilon_\infty$. Plugging this relation in 3.4 one obtains $-\omega^2\vec{u}_L = -\Omega_0^2\vec{u}_L - 4\pi\rho_c^2/\varepsilon_\infty m^*\vec{u}_L$ which gives the frequency of the longitudinal mode $\Omega_{in} = \sqrt{\Omega_0^2 + \Omega_p^2/\varepsilon_\infty}$ where the plasma frequency is given by $\Omega_p^2 = 4\pi\rho_c^2/m^*$.

What is the dynamics of the CDW in an external field E_0 of frequency ω? In the transverse channel the force in the right hand side of Eq. 3.4 will be $\rho_c E_0/m^*$ leading to $\vec{u}_T = [(\rho_c/m^*)/(-\omega^2+\Omega_0^2-i\omega\gamma_0)]\vec{E}_0$. Using Eq. 3.5, the relation $\varepsilon = 1+4\pi\chi$, where $\chi = P/E$, as well as the fact that the conductivity is given by $\varepsilon(\omega) = 1 + 4\pi i\sigma/\omega$, one obtains for the collective contribution to the dielectric function and the real part of the conductivity:

$$\varepsilon_{CDW}(\omega) = \frac{\Omega_p^2}{\Omega_0^2 - i\omega\gamma_0 - \omega^2} \qquad \sigma_{CDW}(\omega) = \frac{1}{4\pi}\frac{-i\omega\Omega_p^2}{\Omega_0^2 - i\omega\gamma_0 - \omega^2} \tag{3.6}$$

These equations will render a peak at the pinning frequency Ω_0 in both $\varepsilon(\omega)$ and $\sigma(\omega)$.

We deal now with the dynamics of the longitudinal modes in the presence of carriers. One has to worry in this case about the associated internal fields and screening

effects. One can derive a relation between the CDW displacement $\vec{u}_L$ and the local field which should become $\vec{E} = -4\pi\rho_c\vec{u}_L/\varepsilon_\infty$ in the limit of zero *dc* conductivity. The only difference now is that the first Maxwell equation changes to $\nabla(\vec{E}+4\pi\vec{P}) = 4\pi\rho_{qp}$, where ρ_{qp} is the quasi-particle density. The continuity equation $-i\omega\rho_{qp} + \nabla\vec{j} = 0$ and Ohm's law $\vec{j} = \sigma_{qp}\vec{E}$ lead to the relation $i\omega\rho_{qp} = \sigma_{qp}\nabla\vec{E}$ so, using Gauss' law, one obtains $\nabla(4\pi\sigma_{qp}\vec{E} - i\omega\vec{E} - 4\pi i\omega\vec{P}) = 0$. Inserting the expression for polarization from Eq. 3.5 and taking into account that we deal with longitudinal fields one obtains:

$$\vec{E} = \frac{4\pi i\omega\rho_c}{4\pi\sigma_{qp} - i\omega\varepsilon_\infty}\vec{u}_L \tag{3.7}$$

Obviously, for $\sigma_{qp} = 0$, Eq. 3.7 gives the result of obtained in the previous paragraph in the absence of carriers. For calculating the longitudinal response, one has thus to replace $\vec{E}$ in 3.4 with the sum of the external field $\vec{E}_0$ and the polarization field given by 3.7 obtaining a linear relation between $\vec{u}_L$ and $\vec{E}_0$. Using 3.5 one obtains the CDW contribution to the longitudinal dielectric function ε_L, which is relevant for Raman scattering, as:

$$\varepsilon_L(\omega) = \frac{\Omega_p^2}{\Omega_0^2 - \omega^2 - i\gamma_0\omega - \frac{i\omega\Omega_p^2}{4\pi\sigma_{qp} - i\omega\varepsilon_\infty}} \tag{3.8}$$

In the limit of high frequencies this function has a pole at $\sqrt{\Omega_0^2 + \Omega_p^2/\varepsilon_\infty}$ corresponding to the CDW plasmon and which is the energy of the longitudinal collective mode. In the limit of low frequencies and neglecting the intrinsic damping γ_0, Eq. 3.8 reduces to the following relaxational mode:

$$\varepsilon_L(\omega) = \frac{A}{1 - i\omega\tau} \quad \text{with} \quad A = \frac{\Omega_p^2}{\Omega_0^2} \quad \text{and} \quad \Gamma = \frac{1}{\tau} = 4\pi\sigma_{qp}\frac{\Omega_0^2}{\Omega_p^2} = 4\pi\sigma_{qp}\frac{1}{\varepsilon_0 - \varepsilon_\infty} \tag{3.9}$$

Equations 3.6 and 3.9 describe the features seen in Fig. 3.20. The proportionality in 3.9 between Γ and the *dc* conductivity is the result of normal carrier backflow which screens the collective polarization and dissipates energy, suffering lattice momentum relaxation.

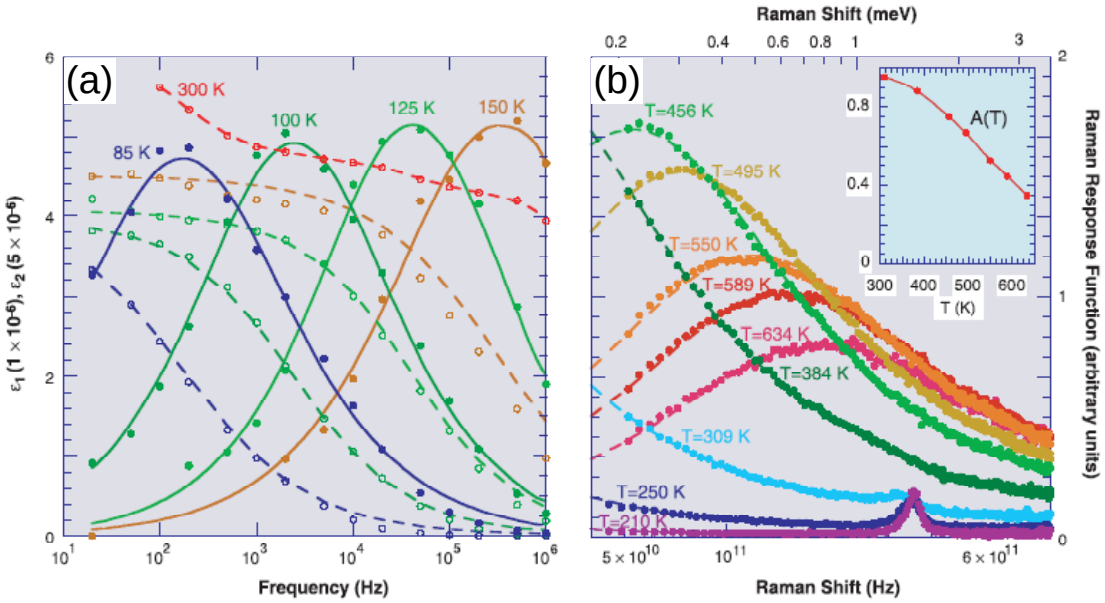

Figure 3.21: (a) The temperature dependence of the real (open circles) and imaginary (solid circles) of the complex dielectric function between 85 and 300 K. The solid and dashed lines are guides for the eye. (b) Raman response function in (cc) polarization at several temperatures. The dots are the data and solid lines are fits to a relaxational behavior as described by Eq. 3.10. The excitation energy used is $\omega_{in} = 1.55$ eV. The excitation around 350 GHz seen for $T < 300$ K is the phonon shown in Fig. 3.13. The inset shows the temperature dependence of the quasielastic intensity $A(T)$.

3.4.3 Density waves in $Sr_{14}Cu_{24}O_{41}$

Low energy transport and Raman – In Fig. 3.21a we show the components of the dielectric response $\varepsilon = \varepsilon_1 + i\varepsilon_2$ as a function of frequency (in log scale) for several temperatures [62]. The imaginary part shows strongly damped, inhomogeneously broadened peaks whose energies are temperature dependent. These relaxational modes lead to variations in the real part of the dielectric function ε_1 up to 300 K and even above. These data resemble the dielectric response measured in the CDW compound $K_{0.3}MoO_3$ which is shown in Fig. 3.20. Fig. 3.21b shows Raman data in a higher temperature range. Similarly to Fig. 3.21a we observe an overdamped feature which moves to lower frequencies with cooling. This excitation disappears below our lower energy cut-off of about 1.5 cm^{-1} (equivalent to 50 GHz or 0.185 meV) below about T = 200 K. The Raman response function can be well fitted with the expression:

$$\chi''(\omega, T) = A(T)\frac{\omega\Gamma}{\omega^2 + \Gamma^2} \tag{3.10}$$

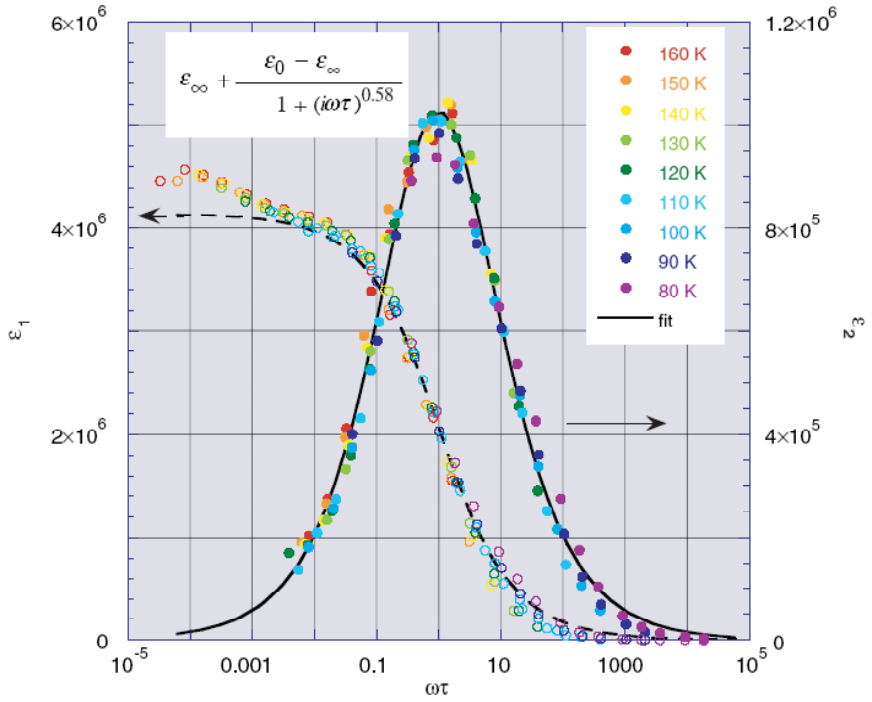

Figure 3.22: Scaling of the complex dielectric function $\varepsilon = \varepsilon_1 + i\varepsilon_2$. Empty (solid) circles correspond to the real (imaginary) part of ε.

The temperature dependence of the peak intensity is shown in the inset of Fig. 3.21. $A(T)$ decreases by about 60% from 300 to 640 K. The temperatures shown in this figure include laser heating effects and they were determined from the ratio of Stokes anti-Stokes spectra for each temperature.

The data in Fig. 3.21a also allow the extraction of a characteristic transport relaxational time $\tau(T)$ at every temperature by a fit to a relaxational type behavior. Using this result, in the entire temperature range the dielectric response between 20 Hz and 10^6 Hz from Fig. 3.21a can be scaled on a universal generalized Debye relaxational curve given by:

$$\varepsilon(\omega) = \varepsilon_\infty + \frac{\varepsilon_0 - \varepsilon_\infty}{1 + [i\omega\tau(T)]^{1-\alpha}} \tag{3.11}$$

The parameter α characterizes the width of the distribution of relaxation times. The equation for the conventional Debye relaxation has $\alpha = 0$. The fit to Eq. 3.11 is shown in Fig. 3.22 where the real and imaginary part of ε is plotted as a function of the dimensionless parameter $\omega\tau$. The parameter α determined from the fit is $\alpha = 0.42$.

The temperature dependencies of the relaxational frequencies extracted from the

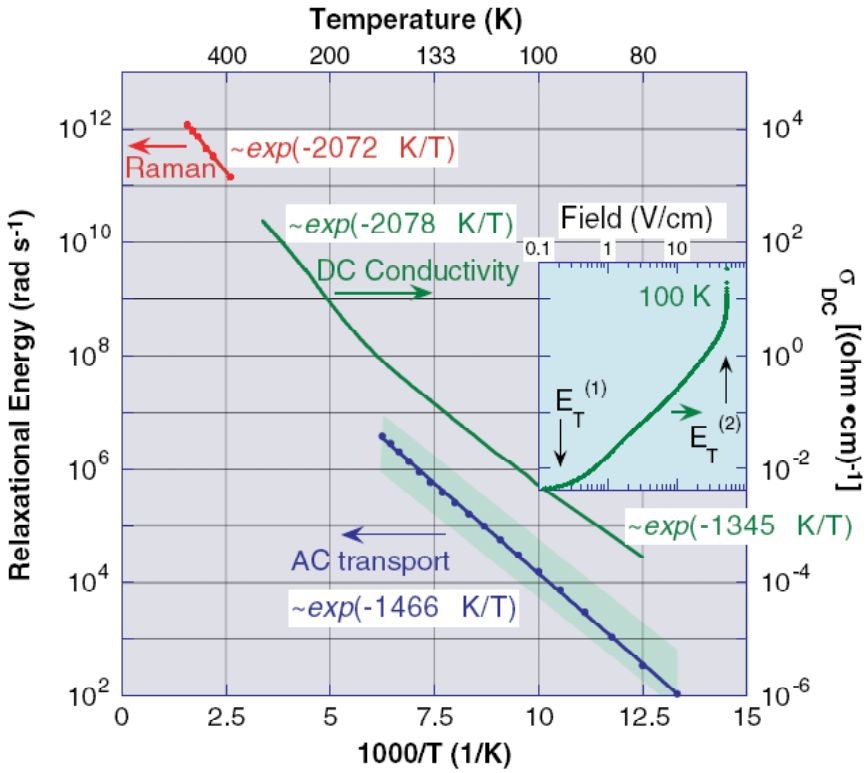

Figure 3.23: Measured *dc* conductivity (right scale) and the scattering rates (left scales) obtained from fits to the Raman data (using Eq. 3.10) and the imaginary parts of the complex dielectric function (using Eq. 3.11) shown in Fig. 3.21. Green line: *dc* conductivity. Red: the dots are the scattering rates $\Gamma(T)$ from the Raman data in Fig. 3.21b and the line is an Arhenius fit showing an activated behavior with $\Delta_{Raman} = 2072$ K. Blue: the dots are the scattering rates $\tau^{-1}(T)$ from the dielectric response in Fig. 3.21b and the line is a similar exponential fit rendering $\Delta_{\varepsilon} = 1466$ K. In both regimes the scattering rates show the activated behavior of the *dc* conductivity. The shaded area show the range of scattering rates calculated as described in the text. The inset shows the nonlinearity in the *dc* conductivity as a function of applied electric field measured at $T = 100$ K. Note that the vertical scale for the inset coincides with the vertical scale of the main panel. The horizontal log scale is for the electric field in V/cm.

Raman data, $\Gamma(T)$, and from the microwave conductivity data, $\tau^{-1}(T)$, are plotted as a function of inverse temperature in Fig. 3.23. On the same plot we show the Arhenius behavior of the *dc* conductivity. The *dc* conductivity in this figure shows activated behavior and the break around $T^* = 150$ K points to the existence of two regimes. At high temperatures the activation energy we obtained is $\Delta_{dc}^{T>T^*} = 2078$ K, consistent with previous results [58]. A value $\Delta_{dc}^{T<T^*} = 1345$ K is obtained at low temperatures. In this figure we observe that the relaxational frequencies have an activated behavior and that the corresponding activation energies match those of the conductivity both

above T^* (the Raman data) and below T^* (the microwave transport data). This characteristic temperature at which the *dc* activation changes was discussed also in the end of section 1.3.1 where we noted that it was related to the increase of the electronic Raman continuum, to the variation of the 2M scattering width and also to the temperature dependent intensity of the chain superstructure peaks seen by X-ray scattering.

The inset in Fig. 3.23 shows the *dc* conductivity as a function of the applied field. The arrows mark two threshold fields. Below $E_T^{(1)} \approx 0.2$ V/cm the conductivity obeys Ohm's law and it has the Arhenius temperature dependence shown in the main panel. For electric fields above $E_T^{(1)}$ the $I-V$ characteristics change from linear to approximately quadratic. At much higher fields, above 50 V/cm, there is a second threshold which marks a very sharp rise of the current. The differential conductivity in this regime is very high, more than $10^5\ \Omega^{-1}cm^{-1}$, an estimate limited by contact effects. Here the current is most likely carried by inhomogeneous filamentary conduction.

We turn now to the interpretation of the data shown in Figs. 3.21, 3.22 and 3.23. We remark that the energy range of the relaxational peaks seen in Fig. 3.21 is much lower than the thermal energy or the magnetic and *dc* activation gaps. Therefore, this is incompatible with single-particle type excitation and suggest that the low energy charge dynamics is driven by correlated collective behavior. We identify this strongly temperature dependent feature to be a CDW relaxational mode in the longitudinal channel, screened due to the interaction with thermally excited quasiparticles, as described in the previous section. We note that electronic Raman scattering can probe directly the longitudinal channel [87] because the Raman response function, $\chi''(\omega)$, is proportional to $\mathrm{Im}[1/\varepsilon(\omega)]$, a quantity proportional to ε_L from Eq. 3.8. We can support in what follows this assignment by quantitative comparison with this simple two-fluid model and by the results of the non-linear conductivity measurements as a function of electric field. Microwave and millimeter wave spectroscopy [28] supports our assignment. In the end of this chapter, we discuss recent (and direct) evidence for the existence of CDW correlations in $Sr_{14}Cu_{24}O_{41}$ provided by X-ray measure-

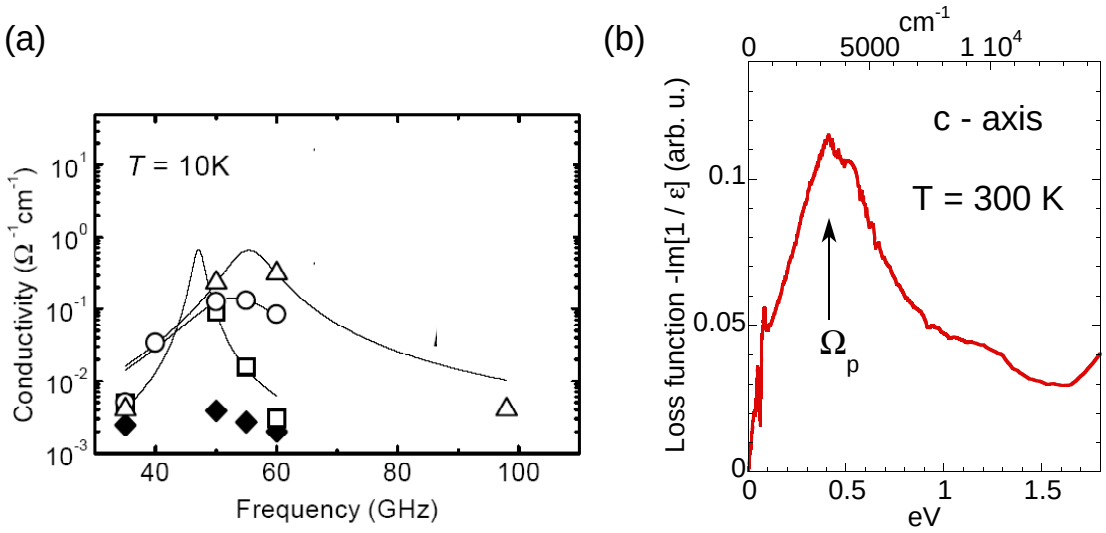

Figure 3.24: (a) Low temperature microwave c (a) axis conductivity at T = 10 K for $Sr_{14}Cu_{24}O_{41}$ crystals from three different batches is shown by open (solid) symbols (data from Ref. [28]). The solid lines are Lorentzian fits. (b) The c-axis loss function in $Sr_{14}Cu_{24}O_{41}$ at 300 K. Ω_p indicates a plasma edge around 3300 cm^{-1}.

ments [88].

The immediate question prompted by our claim, which essentially ascribes to a common origin our observations in Fig. 3.21 and the properties of $K_{0.3}MoO_3$ (an established CDW material) shown in Figs. 3.19 and 3.20, is: If we observe a property related to the pinning of an existent CDW, where is the pinned phase mode? A microwave experiment performed by Kitano *et al.* reported a relatively small and narrow peak between 30 and 70 GHz in the c-axis conductivity which was observed up to moderately high temperatures [28]. The authors attributed this resonance to a collective excitation and speculated about a possible CDW origin. It turns out that our data along with the results of Kitano *et al.* as well as results of reflectivity measurements form a basis on which these results can be analyzed quantitatively. In Fig. 3.24 are shown the main result in [28] and the plot of -Im$[1/\varepsilon(\omega)]$ obtained by our Kramers-Krönig analysis of 'raw' reflectivity data, see Ref. [19].

We believe that the microwave resonance in the 30 to 70 GHz range in Fig. 3.24a corresponds to the average pinning frequency of the CDW in $Sr_{14}Cu_{24}O_{41}$. Along with a plasma edge $\Omega_p \approx 3300$ cm^{-1} extracted from the loss function shown in Fig. 3.24b and using Eq. 3.6 which gives $\varepsilon_0 - \varepsilon_\infty = \Omega_p^2/\Omega_0^2$, one obtains for the low frequency

dielectric function values of the order of 10^6, consistent with the experimental observations in Fig. 3.21. The two-fluid model described in the previous section, see Eq. 3.9, predicts that the relaxational energy is proportional to the activated *dc* conductivity. Indeed, the Arhenius behavior of the relaxational energies, extracted both from Raman and transport measurements in Fig. 3.21, shows from fits with $e^{-\Delta/k_BT}$ activation energies similar to those of *dc* conductivity. Moreover, we remark that the similarity is not only up to a proportionality factor, but the calculated theoretical values for $\tau^{-1}(T)$ according to Eq. 3.9 using the measured values of ε_0 and σ_{qp} are in agreement with the experiment. This can be seen in Fig. 3.23 where the calculated values (the shaded area whose thickness takes into account the error bars in the determination of the *dc* value of the dielectric function ε_1) match the measured τ^{-1} (blue dots).

The non-linear transport data shown in the inset of Fig. 3.24 for T = 100 K further confirm the existence of density wave correlations in $Sr_{14}Cu_{24}O_{41}$. The three regimes observed are typical for systems in which the CDW is pinned by impurities [79, 83]. Below $E_T^{(1)}$ the pinned CDW does not contribute to transport and σ_{dc} is governed by the quasiparticle response. Around this value of the field there is an onset of the CDW conductivity due to the relatively slow sliding of the condensate. In this 2^{nd} regime the predominant damping mechanism is the screening of internal electric fields produced by local CDW deformations by backflow quasi-particle currents. The 3^{rd} regime defined by fields $E > E_T^{(2)}$, indicates a regime of free sliding CDW, the Fröhlich 'superconductivity', also observed in $K_{0.3}MoO_3$, see Fig. 3.9. In this case the velocity of the condensate is so high that it does not feel the background quasi-particle damping.

The overall consistency among the measured temperature dependencies of the dielectric function, *dc* conductivity and relaxational energies demonstrates the applicability of the hydrodynamic model description for the low energy carrier dynamics in a CDW ground state. However, there are several issues which have to be mentioned. One difference with respect to what happens in well established CDW systems is

that the observed relaxational peak in Raman response is at higher energies than the pinned mode at Ω_0. This may be because there is a broad distribution of pinning frequencies and the origin of the Raman relaxational peak is in the high energy side of this distribution. Thus far there are no measurements of the pinned phase mode at or above 300 K. Another issue is that although the absolute values of $\tau^{-1}(T)$ calculated according to Eq.3.9 are in agreement with the experiment, the same is not true for the Raman relaxation frequencies $\Gamma(T)$. The calculated values are about 50 times smaller than the measured ones. A reduction in the density wave amplitude, as suggested by the decrease in the peak intensity, inset of Fig. 3.21b, would produce a concomitant increase in Γ. Further enhancement in the scattering rate may come from additional relaxational channels due to low lying states which are seen at temperatures higher than about 150 K by magnetic resonance [24], c-axis conductivity (Fig. 3.10) or Raman scattering (Fig. 3.11).

The existence of density wave correlations in $Sr_{14}Cu_{24}O_{41}$ at temperatures of the order of 650 K gives this compound a distinctive property compared to classical CDW systems. These high temperatures suggest that in this case it is not the phonons which support the CDW but rather the strong magnetic exchange $J \approx 1300$ K may play an important role in the charge and spin dynamics. One aspect mentioned in the previous section was that hole pairing in 2LL's is a robust feature due to the AF exchange correlations. In this respect, an interesting question is what is the fundamental current carrying object? Is it due to single or paired electrons? Helpful in this regard would be to try to measure current oscillations and interference effects (For a description see Chapter 11 in Ref. [79]). In fact this is probably the only prominent 'classical' transport signature of a CDW state which has not been checked yet in $Sr_{14}Cu_{24}O_{41}$ and it would be an interesting project.

Soft X-rays scattering in $Sr_{14}Cu_{24}O_{41}$ – The most direct way to measure CDW ordering is by neutron or X-ray scattering because they can measure directly super-lattice peaks associated with the distortions of the lattice or electronic clouds. In conventional CDW materials this is the case and the electron-phonon interaction

causes atomic displacements and local electronic density modulations of the order of the atomic numbers. However, up to date, conventional hard X-ray experiments (using photons with typical energies of the order of tens of keV) failed to detect carrier ordering in the ladder structure of $Sr_{14-x}Ca_xCu_{24}O_{41}$ compounds.

Is there any way to observe weak charge modulations which do not involve detectable distortions in the structural lattice? One way to enhance the scattering amplitude from the doped holes is by exploiting those changes in the optical properties of the materials which occur as a result of doping. This often involves, as is the case for cuprates, using incident photons with energies about two orders of magnitude smaller than in conventional X-ray experiments. A real space charge modulation will lead to a proportional change in the Fourier transformed density which in turn is proportional to the dielectric susceptibility of the material, $\chi(k, \omega)$. The X-ray scattering amplitude is determined by the electronic density and as a result will scale proportionally to $\chi(k, \omega)$.

It turns out that in 2D cuprates [89] and $Sr_{14-x}Ca_xCu_{24}O_{41}$ ladders [20] there are features seen in the X-ray absorption spectra (XAS) which arise directly as a result of hole doping. The situation is simpler in 2D cuprates and it can be illustrated for $La_2CuO_{4+\delta}$: For the insulating compounds the Oxygen K edge around 540 eV (which marks the beginning of a continuum of excitations consisting of electron removals from O1s orbitals), has also a prepeak at 538 eV which, due to hybridization, corresponds to intersite O1$s \rightarrow$ Cu3d transitions. If holes enter O2p orbitals, there will be another prepeak appearing at 535 eV due to the fact that additional O valence states are available to be filled by the excited O1s electron. The spectral weight of this carrier induced feature is stolen from the 538 eV prepeak. It is clear that the opening of a new absorption channel at 535 eV will change the optical properties at this energy, in particular of the susceptibility $\chi(k, \omega)$. This also means that X-ray scattering amplitude for 535 eV incident photons will be enhanced with respect to the non-resonant case by factor proportional to the 'susceptibility contrast' which can be defined as the percentage change of the susceptibility in the doped versus undoped

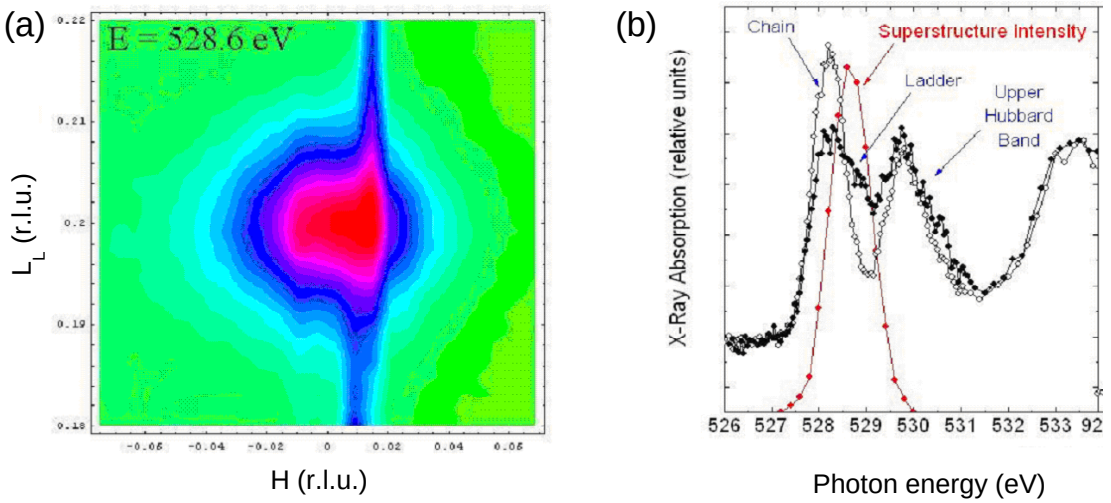

Figure 3.25: (a) The superlattice peak seen at 528.6 eV OK ladder carrier prepeak in the reciprocal space in $Sr_{14}Cu_{24}O_{41}$. L_L on the vertical axis refers is in ladder units. The rod at $H = 0.01$ is due to the specular reflection from the sample surface. (b) Black symbols represent X-ray absorption spectra taken with photon polarizations $E \parallel c$ (filled circles) and $E \parallel a$ (empty circles). The carrier prepeaks corresponding to the chains/ladders are indicated by arrows. Red symbols are for the integrated intensity of the superlattice reflection seen in panel (a) as a function incident photon frequency. Data from Ref. [88].

case [89]. Note that this enhancement applies only to the signal from the doped carriers.

In $(Sr,La)_{14-x}Ca_xCu_{24}O_{41}$ the XAS spectra have the same general characteristics but the situation is more complicated because the mobile carrier absorption feature is split into chain and ladder features [20]. However these excitations can be resolved and they are shown in Fig. 3.25b. This figure shows the characteristic energies of the OK edge. The carrier prepeaks are resolved by using different polarizations of the incoming photon fields and one can see that the ladder absorption at 528.6 eV occurs at about 0.5 eV higher energy than the corresponding feature in the chains, consistent with the XAS study in Ref. [20]. A 2D scan in reciprocal space for incident photon energies of 528.6 eV is shown in Fig. 3.25a. In this figure the momentum transfer $Q = (2\pi/a\ H, 2\pi/b\ K, 2\pi/c_L\ L_L)$ is in ladder reciprocal units along the c-axis. The vertical line is due to specular reflection from the surface and the displacement from $H = 0$ is due to crystal miscut, the normal to the surface making a finite angle with respect to the c-axis. A superlattice reflection at $(0, 0, 0.2)$ indicates a a charge

modulation of 5 ladder units. In terms of the large crystal structure this momentum transfer corresponds to $L = (c/c_L)\ L_L = 1.4$, where c and c_L are the lattice constants corresponding to the big unit cell and ladder unit cell satisfying $c = 7c_L = 27.3$ Å [10]. This Bragg reflection is a true superlattice peak since it does not have the periodicity of the 27.3 Å unit cell and it should not be confused with the five-fold modulation in the chain structures [25].

The $(0, 0, 0.2)$ reflection has an unusual excitation profile. The resonance is shown in Fig. 3.25b where the energy dependence is plotted along with the absorption spectra. One can notice that this reflection is seen only in resonance with the ladder absorption at 528.6 eV, being absent for all other energies, including the OK edge. This proves two main aspects: The Bragg peak arises solely from the doped *ladder* holes, and it cannot be due to any structural modulation which would track *all* the features in the OK absorption. The superlattice peak width in k space gives the correlation lengths $\xi_c = 255$ Å and $\xi_a = 274$ Å indicating that the order is at least two dimensional. This observation is very interesting given the fact that magnetic properties due to the different exchange parameters (Cu-O-Cu bonds making 90° or 180° degrees along the a and c axes respectively, see Fig. 3.1) as well as the dc transport remain anisotropic, highlighting the importance of inter-ladder Coulomb interactions.

This X-ray scattering study confirms the transport data shown in the previous section in establishing the existence of charge density modulations in doped 2LL's. The findings are consistent with the predictions of a crystalline order of ladder holes as a competing state to superconductivity [14, 75]. The absence of structural distortions argues that it is not the conventional electron-phonon interactions, but many-body electronic effects which drive the transition. One question to address is whether the CDW correlations exist in Ca substituted $Sr_{14}Cu_{24}O_{41}$ crystals. This is the topic of the next section where, based on the similarities with the Raman data in $Sr_{14}Cu_{24}O_{41}$ we argue that fluctuations of the density wave order persist at high Ca concentrations and high temperatures.

3.4.4 Signatures of collective density wave excitations in $Sr_{14-x}Ca_xCu_{24}O_{41}$. Low energy Raman data.

In Fig. 3.26a we show low frequency Raman response in x = 12 $Sr_{14-x}Ca_xCu_{24}O_{41}$ at several temperatures. The (*cc*) polarized spectra above 300 K are dominated by a quasi-elastic peak, very similar to the one in $Sr_{14}Cu_{24}O_{41}$, see Fig. 3.21. The solid lines are fits using the same Eq. 3.10, as in Fig. 3.21. A small contribution of the background, as shown in the inset, was subtracted. The polarization and doping dependence of this relaxational feature are shown in Fig. 3.26b-e. We note that the quasi-elastic feature is present only in (*cc*) polarization and we find it in $Sr_{14-x}Ca_xCu_{24}O_{41}$ for all Ca concentrations studied (x = 0, 8 and 12). This low energy excitation is absent however in $La_6Ca_8Cu_{24}O_{41}$ which contains no holes per formula unit confirming the fact that it is due to the presence of doped carriers. We confirmed also that there is no influence of magnetic fields either on this feature or on the modes seen in panels (a) and (c) at 12 and 15 cm^{-1} respectively. This supports the assignment of these modes, shown also in Fig. 3.13 for $Sr_{14}Cu_{24}O_{41}$ to a phonon.

Interestingly, it turns out that the temperature dependent relaxational energy $\Gamma(T)$ for x = 12 $Sr_{14-x}Ca_xCu_{24}O_{41}$ reveals, similarly to $Sr_{14}Cu_{24}O_{41}$ in Fig. 3.23, an activated behavior of the form $\Gamma(T) \propto \exp(-\Delta/k_BT)$. Moreover, the activation energies are found to be about the same: $\Delta \approx 2100$ and 2070 K in $Sr_{14}Cu_{24}O_{41}$ and x = 12 $Sr_{14-x}Ca_xCu_{24}O_{41}$, respectively, see Fig. 3.27c. While this energy is close to the activation energy of the *dc* conductivity in x = 12 $Sr_{14-x}Ca_xCu_{24}O_{41}$, for x = 12 the temperature dependence of the conductivity is far from exponential, and this can be seen comparing panels (a) and (b) of Fig. 3.27. In fact, the behavior shown in panel (b) is very similar to the one in underdoped 2D cuprates: there is a low temperature insulating and a high temperature metallic behavior, in this latter regime the resistivity growing linearly with temperature [15, 90].

In the previous paragraphs we argued that the quasi-elastic Raman scattering in $Sr_{14}Cu_{24}O_{41}$ is a signature of collective CDW dynamics. The main argument in this

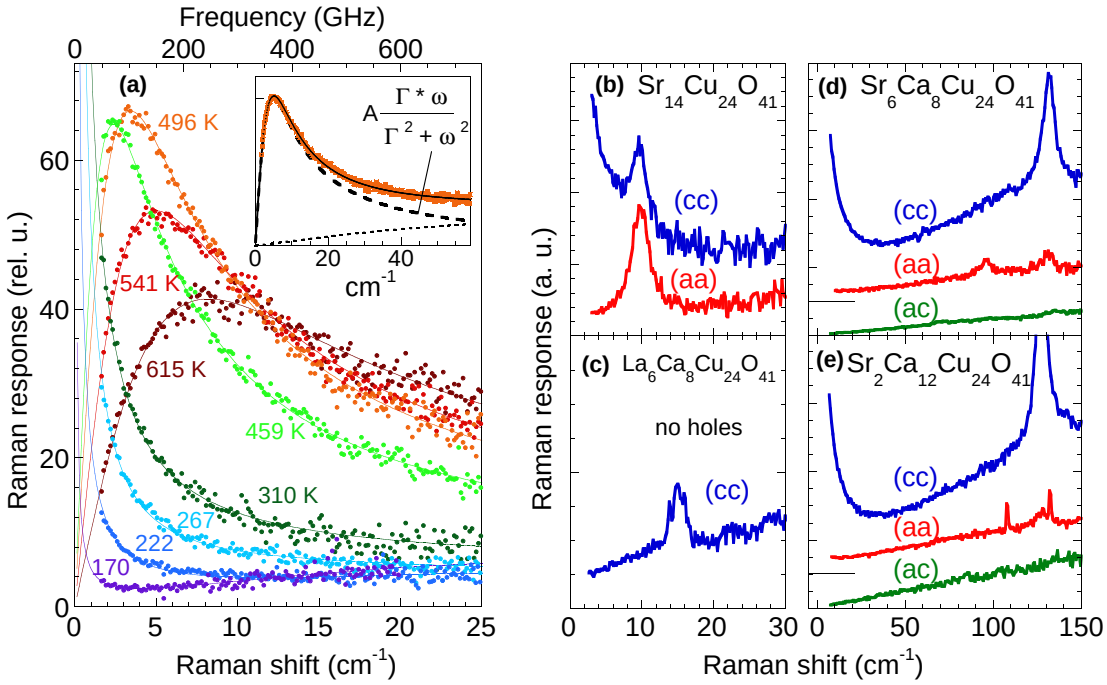

Figure 3.26: A summary of the quasi-elastic Raman scattering in $Sr_{14-x}Ca_xCu_{24}O_{41}$ and $La_6Ca_8Cu_{24}O_{41}$ compounds. (a) Temperature dependence of the Raman response in x = 12 $Sr_{14-x}Ca_xCu_{24}O_{41}$ in (*cc*) polarization taken with ω_{in} = 1.55 eV. This plot is the analogue of Fig. 3.21b. The inset shows a typical fit of the Raman data with a relaxational form, Eq. 3.10, and a small contribution from an underlying background. Panels (b), (c), (d) and (e) show polarized low energy Raman response for $Sr_{14}Cu_{24}O_{41}$, $La_6Ca_8Cu_{24}O_{41}$ and x = 8 and 12 $Sr_{14-x}Ca_xCu_{24}O_{41}$ respectively. Note that the quasi-elastic Raman peak is absent in the undoped $La_6Ca_8Cu_{24}O_{41}$ crystal and it is present, only for the polarization parallel to the ladder legs, in all studied $Sr_{14-x}Ca_xCu_{24}O_{41}$ samples.

respect was the Arrhenius behavior of the scattering rate with the activation given by the *dc* transport. The low energy scale and the strong similarity between the Raman results in x = 0 compared to x =8 and 12 $Sr_{14-x}Ca_xCu_{24}O_{41}$ allow us to claim that collective density wave excitations are also present at all Ca substitutional levels. Confirmation of this scenario comes also from more recent transport and optical conductivity data of Vuletić *et al.* [91] who observe the persistence of the microwave relaxational mode in x = 3 and 9 $Sr_{14-x}Ca_xCu_{24}O_{41}$. The authors of this work argue however that Ca substitution suppresses the CDW phase and long range order does not exist above x = 10. In this respect we argue that the feature observed in the Raman data in Fig. 3.26 at quite high temperatures in x = 12 $Sr_{14-x}Ca_xCu_{24}O_{41}$ is due to local fluctuations of the CDW order.

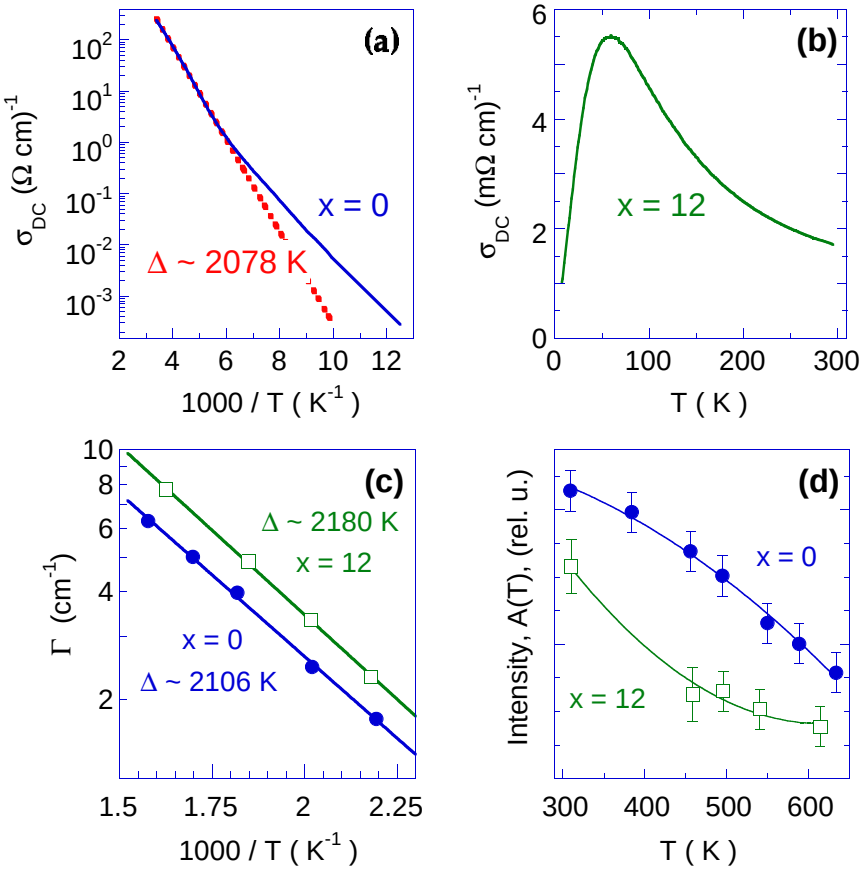

Figure 3.27: Panels (a) and (b) show the temperature dependent *dc* conductivity for x = 0 and 12 $Sr_{14-x}Ca_xCu_{24}O_{41}$. Panel (c) shows Arhenius temperature dependence of the relaxational rate $\Gamma(T)$ for x = 0 (filled circles) and x = 12 (empty squares). The variation of the quasi-elastic peak intensity, $A(T)$, with temperature (solid lines are guides for the eye) is shown in panel (d).

How can one reconcile the observation of the same activation energy for $\Gamma(T)$ with the fact that in the insulating regime σ_{dc} in x = 12 $Sr_{14-x}Ca_xCu_{24}O_{41}$ is not activated and, moreover, it turns metallic at high temperatures, a behavior clearly not consistent with the prediction of Eq. 3.9? One possible explanation suggested by the *c*-axis optical conductivity data is the following: In $Sr_{14}Cu_{24}O_{41}$ one can observe a relatively broad mid-IR peak with an onset around 140 meV, see Fig. 3.10 and Refs. [19, 57]. In $Sr_{14-x}Ca_xCu_{24}O_{41}$ this peak continues to be present [19] and remains a distinct feature although there is a large spectral weight transfer to low energies. We propose that the common mid-IR feature is responsible for the similarly activated behavior of the relaxation parameter $\Gamma(T)$ and observe that the energy scale of this peak (which is also seen in high T_c cuprates) is set by the ladder AF exchange energy of

about 135 meV. In this perspective, a speculative explanation for non-Fermi-liquid like metallic *dc* conductivity at high Ca substitution levels could be based on a collective density wave contribution. Ca substitution introduces disorder that could lead to a much broader distribution of pinning frequencies which may extend to very low energies, towards the *dc* limit, rendering a Fröhlich type component contributing to σ_{dc}. Intuitively one can imagine that the current carrying objects are not quasi-particles but (because of a small CDW correlation length) 'patches' of holes organized in a density wave order.

Another more conventional scenario for x = 12 $Sr_{14-x}Ca_xCu_{24}O_{41}$ regarding its metallic behavior could be based on an anisotropic and partially gapped Fermi surface in the context of higher dimensionality of the electronic system. The soft X-ray study described before, see Fig. 3.25, shows that the CDW correlations are two dimensional in $Sr_{14}Cu_{24}O_{41}$ and recent low frequency dielectric response measurements [92] were able to track down the relaxational peak in a configuration with the electric field parallel not only to the ladder legs but also to the rung direction (One should keep in mind however that the transport along the rung and leg directions is different, as proven by the ratio of the *a* to *c*-axis conductivities, $\rho_a/\rho_c \approx 10$, for a large range of Ca dopings. This can also be related to the fact that we do not observe in Fig. 3.27a the screened longitudinal CDW relaxational mode in (*aa*) polarization although the hole ordering is two dimensional). Additional support for this conjecture comes from an angle resolved photoemission study [93] which shows that while for $Sr_{14}Cu_{24}O_{41}$ the gap is finite, for $Sr_5Ca_9Cu_{24}O_{41}$ the density of states rises almost to the chemical potential and also from the fact that it is known that the low energy optical spectral weight transfer is enhanced with further increase in Ca substitution [19]. In this picture, the insulating behavior in x = 12 $Sr_{14-x}Ca_xCu_{24}O_{41}$ below 70 K can be understood in terms of carrier condensation in the density wave state which leads to a completely gapped Fermi surface. In order to explain the similar relaxation rates $\Gamma(T)$ for $Sr_{14}Cu_{24}O_{41}$ and x = 12 $Sr_{14-x}Ca_xCu_{24}O_{41}$ one has to invoke however a strongly momentum dependent scattering rate and coupling of the condensate to

normal carriers.

The low energy properties of $Sr_{14-x}Ca_xCu_{24}O_{41}$ crystals bring challenging and unresolved aspects, irrespective of the exact microscopic model. Moreover, the proof for existence of CDW correlations along with strong similarities between local structural units and transport properties in Cu-O based ladders and underdoped high-T_c materials suggest that carrier dynamics in 2D Cu-O sheets at low hole concentration could be also governed by a collective density wave response.

3.5 Summary

In this chapter we focussed on magnetic and electronic properties of two-leg ladder materials. We observed at high frequencies (3000 cm^{-1}) in the $Sr_{14}Cu_{24}O_{41}$ compound a two-magnon (2M) resonance characteristic of an undoped ladder which we analyze in terms of symmetry, relaxation and resonance properties. Our findings regarding the spectral properties of this excitation were contrasted to 2M Raman measurements in other magnetic crystals and existing theoretical calculations, emphasizing the sharpness of the 2M peak in the context of increased quantum fluctuations in one-dimension. This comparison made us suggest that the spin-spin correlations in an undoped two leg ladder may have a modulated component besides the exponential decay characteristic of a spin liquid ground state. We found that the 2M peak resonates with the Mott gap determined by O2p $\rightarrow$ Cu3d transitions, following the behavior of the optical conductivity in the 2-3 eV region. Interplane Sr substitution for Ca in $Sr_{14}Cu_{24}O_{41}$ introduces strong disorder leading to inhomogeneous broadening of the 2M resonance in the undoped system. The doped holes in the spin liquid ground state further dilute the magnetic correlations, suppressing considerably the spectral weight of this excitation.

$Sr_{14-x}Ca_xCu_{24}O_{41}$ crystals at high Ca concentrations are superconducting under pressure and hole pairing was proposed to be a robust feature of doped ladders. The measured dielectric response in the microwave region, the low energy Raman

data, the non-linear transport properties along with soft X-ray scattering allowed us to conclude that the ground state in $Sr_{14-x}Ca_xCu_{24}O_{41}$ for a wide range of Ca concentrations ($x \leq 12$) is characterized by charge density wave correlations. This state seems to be driven not by phonons but by Coulomb forces and many-body effects. We highlighted the similarity in the finite frequency Raman response as opposed to the very different behavior of the *dc* resistivity between undoped and doped ladders. We found that at high Ca concentrations, although the resistivity shows a crossover between insulating and linear in temperature metallic regime, the carrier relaxation is characterized by the same large activation energy ($\approx$ 2000 K) which determines the Arrhenius behavior of the CDW compound $Sr_{14}Cu_{24}O_{41}$. This observation prompted us to suggest an unconventional metallic transport driven by collective electronic response.

Chapter 4

Magnetic and phononic Raman scattering in $La_{2-x-y}Nd_ySr_xCuO_4$

4.1 The phase diagram and structural properties of the high temperature superconductor $La_{2-x}Sr_xCuO_4$

$La_{2-x}Sr_xCuO_4$ is one of the most studied Cu-O based layered perovskites [94]. It exibits some of the most important aspects related to the physics of strongly correlated electrons and, more important, is one of the compounds which belong to the family of high temperature superconducting cuprates. In fact the high T_c superconductivity (SC) rush which began in 1986 started with a variant of $La_{2-x}Sr_xCuO_4$, a Ba-La-Cu-O based compound [95], where the authors observed a highest onset SC temperature T_c in the 30 K range.

The phase diagram of $La_{2-x}Sr_xCuO_4$ is shown in Fig. 4.1, see also Ref. [96]. Several electronic ground states as well as structural phases evolve with Sr concentration. For $x(\mathrm{Sr}) \leq 0.02$ the crystals have long range antiferomagnetic (AF) order and one can observe a very rapid suppression of the Néel ordering temperature T_N with the amount of Sr. While for $x = 0$ the AF transition is slighly above room temperature,

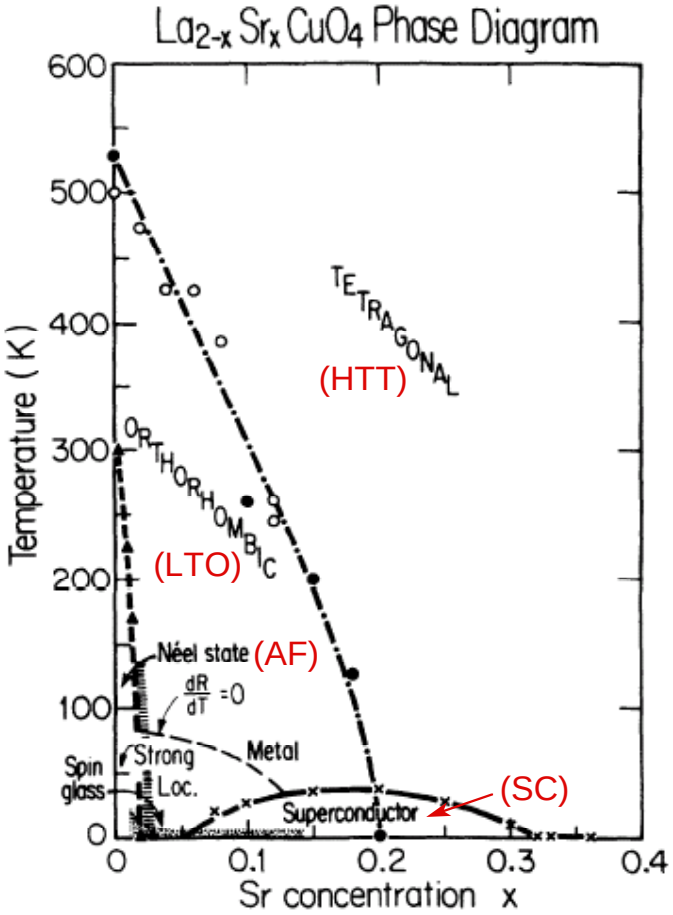

Figure 4.1: Phase diagram of $La_{2-x}Sr_xCuO_4$ from Ref. [96]. HTT and LTO stand for the high temperature tetragonal and low temperature orthorhombic phases respectively. AF denotes the long ranged antiferromagnetic region (Néel state) at low dopings and SC denotes the superconductivity dome with a maximum around $x = 0.2$ Sr concentration.

T_N decreases in the 150 - 200 K range for $x = 0.01$ and it is completely suppressed above $x = 0.02$. The phase diagram shows also a SC dome starting at $x = 0.05$ and ending around $x = 0.32$. The maximum T_c of about 40 K is reached at the optimal doping $x = 0.2$. The highest SC temperature ($T_c = 51.5$ K) in the $La_{2-x}Sr_xCuO_4$ family was achieved in thin films under epitaxial strain [97]. There are also two structural phases of the this compound. One is tetragonal and the other one is orthorhombic, see Fig. 4.2. Sr substitution for La decreases the orthorhombicity and the crystal remains tetragonal at all temperatures at values of x(Sr) which correspond roughly to the region of maximum T_c. Other intervening phases shown in Fig. 4.1, spin glass at low temperatures and low Sr concentration, Fermi or non-Fermi liquid

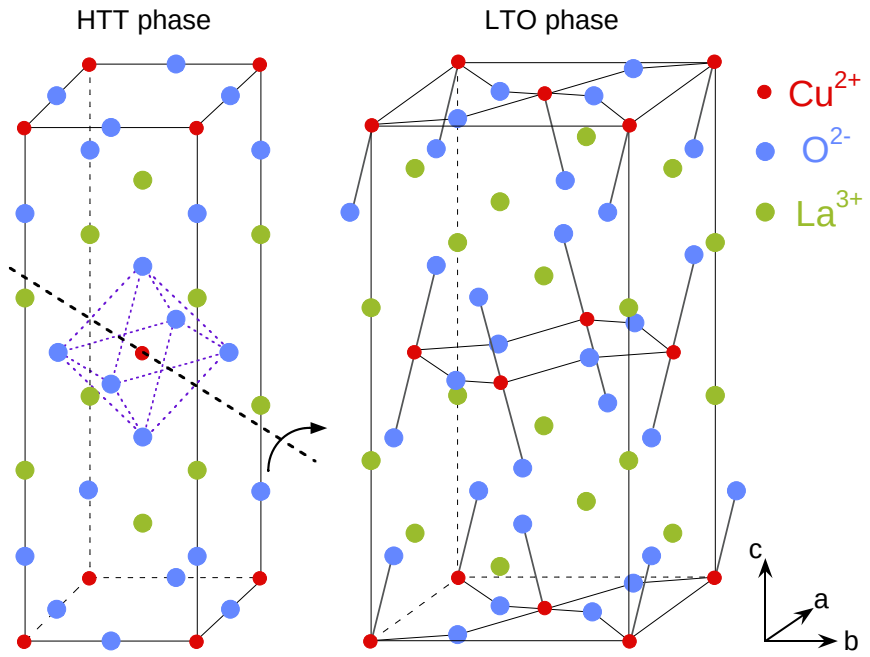

Figure 4.2: The layeres perovskite structure of $La_{2-x}Sr_xCuO_4$. Left: the high temperature tetragonal (HTT) phase where the CuO_2 planes are flat. Right: the low temperature orthorhombic (LTO) phase, ($Bmab$) space group which is obtained from the HTT structure by rigid CuO_6 octahedra rotations as shown. In the $Bmab$ setting the b-axis is parallel to the corrugation in the CuO_2 planes.

behavior depending on if one is in the far right side of the phase diagram or not, are discussed in literature [94].

The crystal structure of $La_{2-x}Sr_xCuO_4$ is shown in Fig. 4.2. The occurence of several structural phases is typical for perovskites and they generally happen as a result of the lattice strain between the rare-earth and the Cu-O layers. The strain is often released by various bucklings of the transition metal - oxygen planes and this is also the case here. The HTT phase has flat CuO_2 planes and the transition to the LTO phase can be understood within a good approximation as a rigid rotation of the CuO_6 octahedra around an axis making 45° with respect to the orthorhombic axes. As a result, half of the O atoms will be situated above and the other half below the plane determined by the Cu atoms, see Fig. 4.2. The lattice constants of the LTO phase at low temperatures are $a = 5.354$ Å, $b = 5.401$ Å and $c = 13.153$ Å. So the orthorombicity, defined by $2(a-b)/(a+b)$, is small, only of about 0.8%.

In the parent compound, La_2CuO_4, one has La^{3+} and O^{2-} non-magnetic ions so copper will be in a Cu^{2+} oxidation state to insure neutrality. As a result, the last

Cu $3d^9$ shell will contain a hole carrying a spin $S = 1/2$ which is responsible for the magnetic properties. Sr^{2+} substitution for La leads to hole doping of the CuO_2 planes. It is believed that hole pairing and the acquirement of 3D coherence lead to the occurence of superconductivity.

In this chapter we will also discuss properties of Nd doped $La_{2-x}Sr_xCuO_4$ and we mention here some well established effects associated with Nd substitution for La. One is that Nd in $La_{2-x-y}Nd_ySr_xCuO_4$ suppresses superconducting correlations. For instance magnetic susceptibility data in $La_{2-x-y}Nd_ySr_xCuO_4$ with $x = 0.2$ show that SC vanishes for values of y greater than about 0.6 [98]. Another effect is that this suppression of SC is accompanied by the enhancement of other types of correlations, the appearance of the so called 'stripes' [99], which are proposed to be quasi-1D in plane charge and/or spin super-modulations. While the discussion above suggests that these two states act against each other, it is not clear at this moment if the stripes are helping or competing with SC. Another effect is related to changes in the crystal structure as a result of inter-layer chemical modifications. Nd doping brings in another phase, the low temperature tetragonal (LTT) structure, which can be imagined as a rigid CuO_6 octahedra tilt around the axis whose vector is defined by $1/\sqrt{2}(\hat{a} + \hat{b})$ where a and b are the orthorhombic axes of the LTO phase.

In the following we will discuss low energy magnetic properties of $La_{2-x}Sr_xCuO_4$ at light x(Sr) doping level. Although much is known about the physics of 2D $S = 1/2$ antiferromagnets, there are recent experiments which show surprising properties in macroscopically orthorhombic crystals in the presence of external magnetic fields. It is worth mentioning in this respect that recent neutron scattering in such crystals studies show that even the crystal structure has not rigorously been determined yet [100] although the deviations from the *Bmab* symmetry may be very small. We will show later in this chapter, especially in connection to the phononic and electronic properties, that the effects of orthorhomobicity are surprisingly large. In the following we discuss long wavelength spin-wave excitations as a function of temperature, doping and magnetic field. We show that the low energy spin dynamics allows us to observe

a spin ordered state induced by magnetic fields, a state whichs persist up to quite high temperatures in crystals with long range AF order [101]. It will be shown that although the orthorhombicity is small, there are dramatic anisotropy effects in the in plane electronic and phononic excitations. Our data indicate that at commensurate hole doping $x = 1/8$ $La_{2-x-y}Nd_ySr_xCuO_4$ and independent of Nd concentration there are local deviations in the crystal structure due to a spread in the CuO_6 tilt angle. We will dicuss this behavior in connection with possible spin and charge modulations in the CuO_2 planes [102].

4.2 Magnetic and electronic properties of macroscopically orthorhombic $La_{2-x}Sr_xCuO_4$ at light doping ($0 \leq x \leq 0.03$)

4.2.1 Why is a study of low energy magnetism interesting?

SC as well as the normal properties of 2D Mott-Hubard systems have already triggered a lot of effort to understanding the evolution of the ground state and of the AF correlations as a function of doping. However, in spite of the small orthorhombicity, the impact of the low energy magnetism on the carrier and lattice dynamics in *detwinned* $La_{2-x}Sr_xCuO_4$ crystals has recently been shown to be significant and suprprising new effects were found.

What does detwinned mean in the first place? On cooling from the HTT to the LTO phase the crystal develops orthorhombic domains, called twins, on the nanometer to micron scale. The sign of the orthorhombic distortions changes across the twin boundaries, as shown in Fig. 4.3a. Accordingly, for a macroscopic probe (and a Raman setup which uses a focussed laser spot larger than about several μ diameter is an example) the sample looks effectivey tetragonal. If uniaxial pressure of about 15-30 MPa is applied while slowly cooling the crystal through the HTT-LTO phase transi-

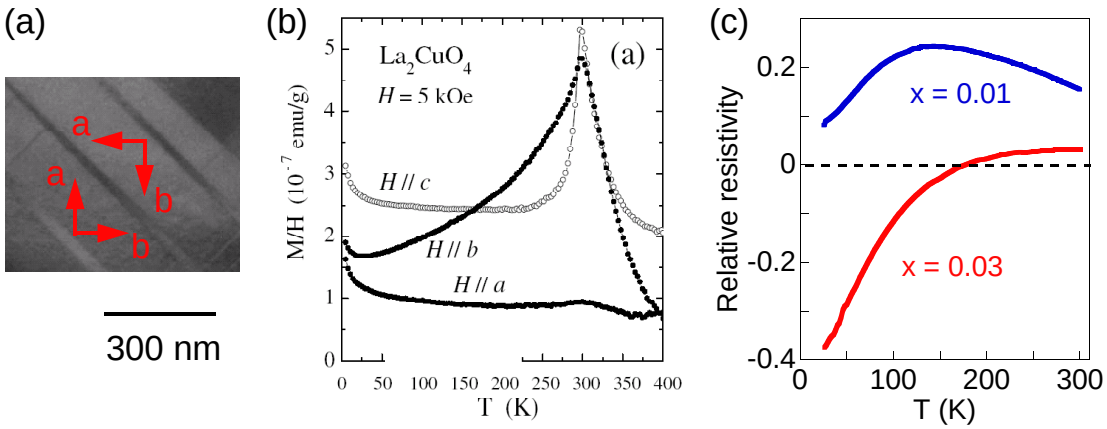

Figure 4.3: (a) Typical orthorhombic domains in a twinned $La_{2-x}Sr_xCuO_4$ sample (from Ref. [103]). (b) Magnetic susceptibility in a detwinned single crystal of La_2CuO_4 (data from Ref. [104]). (c) Relative resisitivity defined by $2(\rho_a-\rho_b)/(\rho_a+\rho_b)$ in x = 0.01 and 0.03 detwinned $La_{2-x}Sr_xCuO_4$ crystals (see also Ref. [105]).

tion, a detwinned, i.e. macroscopically orthorhombic, crystal can be grown [104].

This leads to non-trivial effects if one looks in Fig. 4.3b-c. The magnetization data shows two peaks at the Néel transition of around 300 K in La_2CuO_4 and the magnetic anisotropy is preserved in a wide range of temperatures above T_N. The susceptibility along the a-axis, $\chi_a(T)$, is featureless showing that this axis is magnetically inert, at least at small fields. The structure with two peaks is due to the various spin anisotropy terms present in $La_{2-x}Sr_xCuO_4$ crystals, they will be discussed in more detail later in the section [104]. La_2CuO_4 is an insulator, but small carrier concentrations in the CuO_2 planes give rise to metallic behavior of the resistivity at high temperatures. Moreover, the *dc* resistivity shows also sizeable anisotropy if measured along the a and b orthorhombic axes. The relative anisotropy is almost 30% for x = 0.01 around the metal-insulator transition and goes beyond this value in x = 0.03 at low temperatures. One can also notice at high temperaturs a decrease of the resistivity anisotropy with doping from x = 0.01 to x = 0.03 and that there is a sign change in this anisotropy around170 K for x = 0.03 [105]. The magnetoresistance can be very large (up to 80%) at low temperatures [106].

One can conclude form Fig. 4.3 that detwinned samples show non-negligible effects in transport and magnetization data. The Zeeman energy in finite external magnetic fields becomes comparable with the spin-anisotropy induced gaps and this

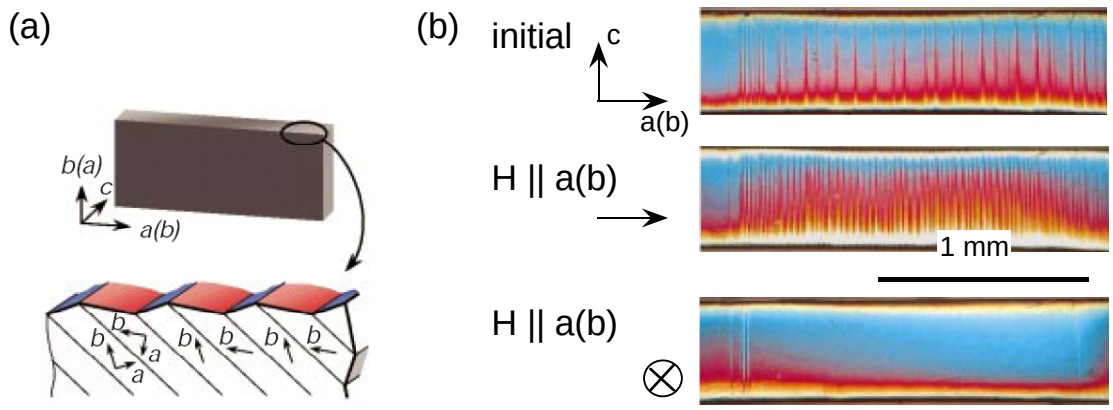

Figure 4.4: (a) A 3D picture with a twinned x = 0.01 $La_{2-x}Sr_xCuO_4$ crystal whose top surface is parallel to the c-axis. The blue and red areas correspond to different twins, (ac) or (bc) domains. (b) The upper figure is an image of the top crystal surface in zero external magnetic field taken with an optical microscope. Vertical stripes represent the (ac) and (bc) LTO domains as in panel (a). The middle and botoom images show the structural chages occuring with an application of an external field of about H = 14 T. One can see that the b orthorhombic axis follows the direction of $\vec{H}$.

will influence the low temperature thermodynamics. As for the intrinsic ground state properties at small dopings, inelastic neutron scattering (INS) argues that there are changes in the low frequency magnetic scattering (45° rotation in the k space of low energy incommensurate magnetic peaks) when superconductivity occurs around $x = 0.05$ in $La_{2-x}Sr_xCuO_4$ [107] and also that macroscopic phase separation takes place below $x = 0.02$ [108].

All the above consitute general arguments for a detailed high energy resolution study of long wavelength spin excitations as a function of doping and temperature. Even more interesting is a recent magnetic field experiment done at room temperature in $x = 0.01$ $La_{2-x}Sr_xCuO_4$. The main result of the experiment is shown in Fig. 4.4 and it says that the b orthorhombic axis follows the direction of the applied field [104]. So magnetic fields of about 10-14 T are able to produce structural changes and detwin the $La_{2-x}Sr_xCuO_4$ crystal. The switch of the crystallographic axes is reversible and can be monitored by using a regular optical microscope. It is worth noting that 300 K is roughly about 100 K above the 3D long range AF ordering temperature in 1% doped crystals. Two interesting points can be mentioned in this regard. One is that there is strong spin-latice interaction in this material. The

other one is rlated to the coupling of the spins to the external field. While magnetic field induced structural changes are easier to be understood in ferromagnetic crystals because the net magnetic moment can provide a substantial coupling to the external field, the fact that these effects take place in a AF system makes $La_{2-x}Sr_xCuO_4$ a unique compound. The rotation of the orthorhombic axes can be also observed in *dc* resistivity or magnetic susceptibility measurements by monitoring the changes in the anisotropic properties shown in Fig. 4.3 as a function of the direction of the applied external magnetic field $\vec{H}$.

These results highlight the importance of a magnetic field study of the low energy magnetism in low doped $La_{2-x}Sr_xCuO_4$. We believe that the field induced spin ordering we observe at temperatures up to 300 K in samples displaying long range AF order is related to the effects shown in Fig. 4.4.

4.2.2 Low energy magnetism in detwinned $La_{2-x}Sr_xCuO_4$ with $(0 \leq x \leq 0.03)$

The 2D Heisenberg antiferromagnets and effects of inter-layer coupling – CuO_2 planes form 2D square lattices and the $S = 1/2$ Cu spins interact antiferromagnetically *via* the intermediate O atoms. The nearest neighbor super-exchange J takes place along the 180° Cu-O-Cu bonds it has a value of approximately 140 meV [110]. The inter-layer correlations are weak for two reasons: on one hand the spacing between the layers is large and on the other hand the magnetic interaction along this direction is frustrated. So in the first approximation the spin dynamics (especially in the paramagnetic phase) will be dominated by the properties of a 2D isotropic Heisenberg antiferromagnet. The starting Hamiltonian to characterize these systems is then:

$$\hat{H}_{2D} = \sum_{<i,j>} J_{ij} \vec{S}_i \cdot \vec{S}_j \tag{4.1}$$

where $\vec{S}_i$, $\vec{S}_j$ are spins on the sites i and j and $J_{ij} = J \approx 140$ meV when $< i, j >$ corresponds to a pair of nearest neighbor (NN) spins.

The spin-spin correlation function $\xi(T)$ is one of the fundamental parameters characterizing the paramagnetic state. This quantity is extracted from an equation relating the average staggered magnetization to the inter-site distance, of the type: $< \vec{S}_i \cdot \vec{S}_j > \propto \exp(-r_{ij}/\xi)$. Here r_{ij} is the distance between the sites i and j. Continuum field theory predicts in the paramagnetic phase a spin-spin correlation length given by: $\xi(T) \propto \frac{c}{2\pi\rho_s} \exp[\frac{2\pi\rho_s}{k_B T}]$ [111]. The parameters c and ρ_s are for the spin-wave velocity and spin stiffness respectively. This correlation length diverges as $T \rightarrow 0$ leading to true long range magnetic order only at zero temperature. This microscopic result is consitent with a theorem showing rigorously that at any finite temperature a 1D or 2D isotropic Heisenberg model with finite-range interactions can be neither ferromagnetic nor antiferromagnetic [112]. However, in agreement with theoretical predictions, neutron scattering measurements show that the number of correlated spins within the 2D Cu-O planes is substantial even at high temperatures. For example, at 500 K which is about 200 K above the 3D ordering temperature in La_2CuO_4 , ξ is of the order of 50 Å [96], approaching values of 200 - 300 lattice constants around T_N.

A small interlayer coupling $J_\perp$ pushes the Néel ordering temperature to finite values but does not affect significantly the 2D magnetic correlations. It is believed that the magnitude of the inter-layer exchange is very small, $J_\perp \approx 10^{-5} J < 0.02$ K [94, 111, 113]. In spite of such a small perpendicular exchange, the AF ordering temperatures are quite high and this is due to the large in-plane correlation lengths. Agreement in terms of the order of magnitude for T_N using the above value for $J_\perp$ can be obtained simply by comparing the thermal and magnetic energies in:

$$k_B T_N \approx J_\perp (m_s S)^2 \left[\frac{\xi(T_N)}{a}\right]^2 \tag{4.2}$$

where m_s is the sublattice magnetization in units of $g\mu_B$ and $[\xi(T)/a]^2$ is proportional to the number of 'ordered' spins in each Cu-O plane. It should be noted that in the HTT phase of $La_{2-x}Sr_xCuO_4$ every Cu atom has eight nearest neighbors in the adjacent planes (four above and four below its own Cu-O plane). Due to symmetry,

the super-exchange is almost exactly cancelled and the effective $J_\perp$ is even smaller than $10^{-5}J$. It is the distortion associated with the LTO phase, see Fig. 4.2 which partially lifts this degeneracy giving rise to a reasonably sized, although very small, inter-layer exchange.

Eq. 4.2 leaves an open question: how to reconcile similar 3D ordering temperatures (T_N's typically in the range between 200 and 300 K) for various layered Cu-O based materials (examples are $La_{2-x}Sr_xCuO_4$, $Sr_2CuO_2Cl_2$, $YBa_2Cu_3O_{6+\delta}$, Nd_2CuO_4 or Pr_2CuO_4, see Refs. [94, 114]) with rather different exchange paths and accordingly values of $J_\perp$ that can be quite far apart. For instance in $Sr_2CuO_2Cl_2$ the Cu-O planes are exactly flat so it is expected that the cancellation of terms because of the inter-layer frustration would decrease $J_\perp$ by another few orders of magnitude, requiring anomalously high $\xi(T_N)$ in order to satisfy Eq. 4.2. It has been suggested that the 3D ordering temperature T_N follows immediately after a 2D Kosterlitz-Thouless (KT) phase transition at T_{KT} due to the in-plane spin anisotropy of the XY type which characterizes all the above mentioned AF materials. It was found that T_{KT} is appreciable, $\approx 0.25J/k_B$, and quite insensitive to the magnitude of the in-plane anisotropy [114]. This would explain the magnitude as well as the similarity between the measured T_N's in various Cu-O based 2D AF's.

What does the excitation spectrum of a 2D AF ordered square lattice look like? Within the spin-wawe approximation the excitations are coherent transverse oscillations of the ordered moments. Taking into account only the nearest neighbor exchange J the wavevector dependent spin-wave energies are given by

$$\omega(k) = zSJ\sqrt{1-\gamma_k^2} \quad \text{with} \quad \gamma_k = \frac{\cos(k_x)+\cos(k_y)}{2} \tag{4.3}$$

where $S = 1/2$ is the total spin and $z = 4$ is the number of nearest neighbors for the simple square lattice [115]. Note that in the 2D isotropic Heisenberg AF lattice there will be two degenerate accoustic spin-wave branches. In Fig. 4.5 we show relatively recent INS results for the spin-wave dispersion up to high energies.

While the dispersion predited by the nearest neighbor isotropic Hamiltonian repro-

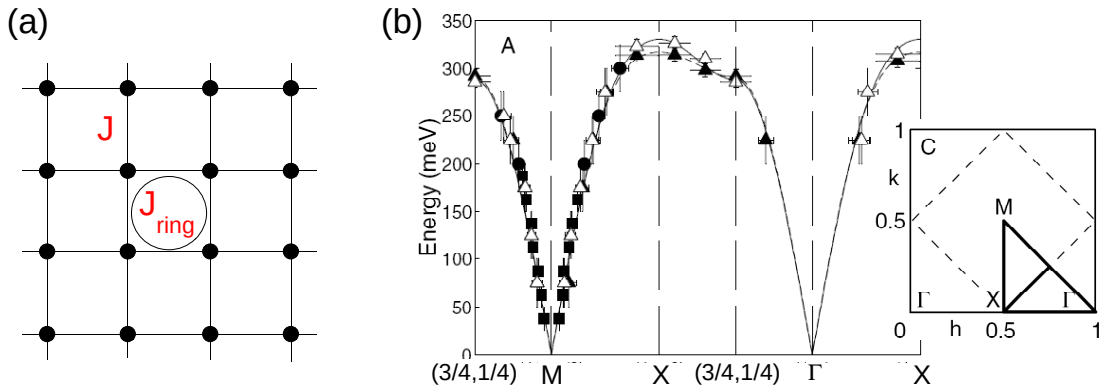

Figure 4.5: (a) The 2D square lattice. The nearest neighbor superexchange is denoted by J and the circle represents a higher order term considered important for the cuprates, the ring exchange J_{ring}. (b) The main panel shows the dispersion of the magnetic excitations in La_2CuO_4 at T = 10 K along different directions in the 2D Brillouin zone (shown in the lower left panel). The inelastic neutron scattering data is from Ref. [110]. Squares, circles and triangles correspond to incoming neutron energies of 250, 600 and 650 meV respectively. The solid line is a fit to the data as described in the text.

duces qualitatively the experimetal results, there are discrepancies at high energies. One can note that along the AF zone boundary we have $k_x + k_y = \pi$ and this implies that the spin-wave energy along this line is a constant given by $2J$. The experimental data in Fig. 4.5 shows that there is substantial dispersion for instance along the X-(3/4,1/4) line. The authors resolve this discrepancy by including higher order spin interactions. In particular, the most prominent term is due to J_{ring} which corresponds to a spin exchange around a square plaquette as shown in Fig. 4.5a. Quantitatively, from the fit to the experimetal data which includes quantum corrections [116] (the solid line in Fig. 4.5b), this term turns out to be as high as 41% of the nearest neighbor J at low temperatures, $J_{ring} \approx 61$ meV, and it is about twenty times larger than the second and third nearest neighbor exchanges [110]! In support for such a claim we note that a large value of J_{ring} was needed to explain the dispersion of the elementary triplet excitations in two-leg ladder materials, see section 1.2.3 in Chapter 3 of this thesis. The same J_{ring} seems also to improve the results concerning the large absorption frequency range in which the phonon induced two-magnon excitation is thought to be observed in 2D insulating cuprates [117].

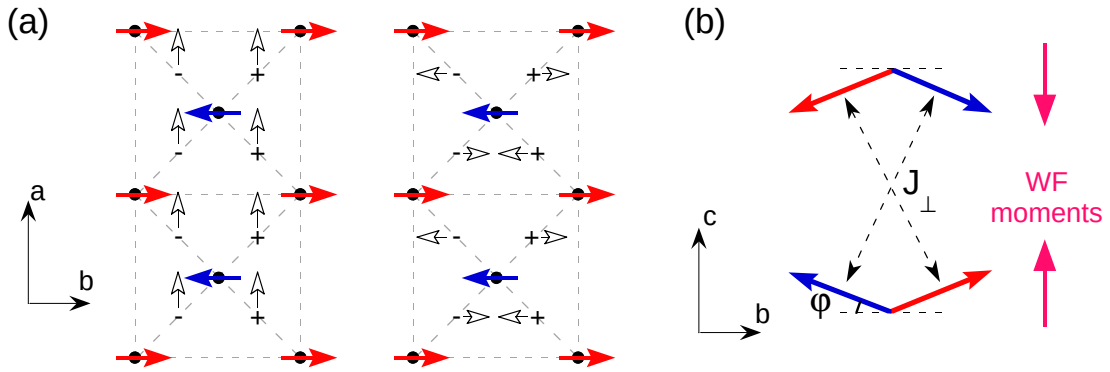

Figure 4.6: (a) Top views of the Cu-O planes corresponding to the two possible configurations of the DM interactions (black arrows). Cu atoms are represented by black dots; their spins (lying mainly in the (ab) plane because of the XY spin aniostropy and forming a two-sublattice AF structure) are shown by red and blue arrows. By '+' and '-' signs we denote the intermediate O atoms which are below and above the plane of the paper, see Fig. 4.2. (b) Cartoon with the 3D four-sublattice configuration of spins seen in the (bc) plane and the weak ferromagnetic moments (proportional to the canting angle ϕ) of each Cu-O plane due to the Dzyaloshinskii-Moriya interaction $\vec{d} \parallel \hat{a}$ shown in the left of panel (a).

In-plane magnetic anisotropies – There are two dominant in-plane magnetic anisotropies characterizing each Cu-O plane. In general these terms, arising as a result of spin-orbit coupling, connect the spin space to the real space and can be sometimes described in terms of effective magnetic interactions. One of these interactions is the XY exchange anisotropy term mentioned above in connection to the 3D Néel ordering and its origin is in the layered structure of the cuprates, i.e., it has nothing to do with the buckling of the Cu-O plane in the LTO phase. Due to to the XY term the NN spin-exchange interaction in Eq. 4.1 changes to $(J+\alpha)(S_i^x S_j^x + S_i^y S_j^y) + J S_i^z S_j^z$. Because $\alpha > 0$ the classical configuration giving the minimum energy is one with all the spins lying in the (ab) plane. The other important aniotropy term is due to the antisymmetric Dzyaloshinskii-Moriya (DM) interaction and it has the form: $\vec{d}_{ij} \cdot (\vec{S}_i \times \vec{S}_j)$ where $\vec{d}_{ij}$ is the DM vector [118, 119]. The two-spin classical ground state configuration for this interaction considered alone is one with $\vec{S}_i \perp \vec{S}_j \perp \vec{d}_{ij}$.

The balance of these terms determines the equilibrium position of the spins. These anisotropoy terms are expected to be much smaller than J and can be quantitatively determined from the energy of the spin-waves in the long wavelength limit as will be

discussed in the next section. A few words are in order about the DM term. Due to the existence in the LTO phase of a C_2 (rotation by 180°) symmetry axis which passes through in-plane O atoms and is perpendicular to the (ab) surface, the DM vector between two adjacent Cu atoms has to satisfy $\vec{d} \perp \hat{c}$ [120]. The symmetry elements of the $Bmab$ space group associated to the LTO phase allow the DM vectors $\vec{d}_{ij}$ to form the configurations shown in Fig. 4.6a. Once a convention is made that the order of spins in the vector product of the $\vec{d}_{ij} \cdot (\vec{S}_i \times \vec{S}_j)$ term is always from a given sublattice to the other, it can be noted that there are two possible arrangements for the DM vectors: one involving $\vec{d} \parallel \hat{a}$ and the other one in which the DM vectors are parallel to the b-axis but have alternating signs.

The effective two-dimensional spin Hamiltonian and the associated free energy density at T = 0 K which takes the XY, DM terms as well as an external field into account can be written as:

$$\hat{H} = \sum_{<i,j>} [(J+\alpha)(S_i^x S_j^x + S_i^y S_j^y) + J S_i^z S_j^z + \vec{d}_{ij} \cdot (\mathbf{S}_i \times \mathbf{S}_j)] - \vec{H} \cdot \sum_i \vec{S}_i \quad (4.4)$$

$$f = z(J+\alpha)(M_1^x M_2^x + M_1^y M_2^y) + zJ M_1^z M_2^z + z\vec{d} \cdot (\vec{M}_1 \times \vec{M}_2) - \vec{H} \cdot (\vec{M}_1 + \vec{M}_2) \quad (4.5)$$

In Eq. 4.4 the sum runs over the nearest neighbors. In Eq. 4.5 z is the number of nearest neighbors and $M_{1,2}$ are the sublattice magnetizations. The 'thermodynamic' Dzyaloshinskii vector $\vec{d}$ in Eq. 4.5 is given in terms of the 'microscopic' Moriya terms $\vec{d}_{ij}$ in Eq. 4.4 by $\vec{d} = (1/z) \sum_{NN} \vec{d}_{ij}$ and from Fig. 4.6 one can infer that $\vec{d} \parallel \hat{a}$ [121]. The relative strength of the DM terms corresponding to the two configurations in Fig. 4.6a is determined by microscopic parameters. It is interesting to note here a point made by the authors of Ref. [121], i.e. that the indentification of $\vec{d}$ to the microscopic $\vec{d}_{ij}$ is a non-trivial problem in the sense that a difference between them is a necessary condition for the existence of an observable weak ferromagnetism (WF) with a specific value of the net WF moment. In other words, although $\vec{d}$ is parallel to the a-axis, it is required that the DM vectors in both configurations shown in Fig. 4.6a are finite. If on one hand only vectors $\vec{d}_{ij} \parallel \hat{b}$ are considered (frustrating interaction), then $\vec{d} \equiv 0$ and the spins order antiferromagnetically without any WF moment. On

the other hand if one takes into account only vectors $\vec{d}_{ij} \parallel \hat{a}$ (non-frustrating interaction) the classical ground state cannot be characterized as ferromagnetic because it consists of a manifold of degenerate configurations having a net WF moment ranging continuously from zero to some finite value [121].

The equilibrium position of the spins in zero external field is shown in Fig. 4.6b. For a 2D plane this can be obtained from the minimization of the free energy in Eq. 4.5 with respect to the angles between the magnetizations and crystallographic axes with the constraint $m = |\vec{M}_1| = |\vec{M}_2|$. The canting angle is given by $\tan(2\varphi) = 2d/(2J+\alpha)$ and since $d \ll J$ (in reality $\varphi < 0.5^\circ$) the net WF moment of each plane is approximately $M_F \approx 2m\varphi = 2dm/(2J+\alpha)$. Here m is the sublattice magnetization. The interaction $J_\perp$ does not significantly change this angle.

Long wavelength spin-wave excitations – On general grounds, from Eq. 4.5 one can say the following about the behavior the spin-wave modes in the long wavelength limit: (1) if $\alpha = d = 0$ there will be two acoustic modes; (2) if $\alpha \neq 0$ and $d = 0$ or $\alpha = 0$ and $d \neq 0$ there will be one acoustic and one gapped spin-wave branch; (3) if $\alpha \neq 0$ and $d \neq 0$ both spin-wave branches will be gapped. This is because unless we are in case (3), there is a global continuous symmetry which is broken at the AF transition due to the ordering of the magnetic moments (the gapless branches are typical Goldstone modes). $La_{2-x}Sr_xCuO_4$ is an example where case (3) is realized while $Sr_2CuO_2Cl_2$ is an example of a 2D system with only XY anisotropy only, case (2).

The situation described above is shown schematically in Fig. 4.7. One can intuitively understand how the spin gaps look like at a classical level by solving the equations of motion:

$$\beta \frac{\partial \vec{M}_j}{\partial t} \;=\; \vec{M}_j \times \nabla_{\vec{M}_j} f \qquad j = 1, 2 \tag{4.6}$$

where β is a constant related to the Bohr magneton and f is the free energy from Eq. 4.5. The equilibrium condition $\nabla_{\vec{M}_j} f = 0$ gives the ground state shown in Fig. 4.6b. Linearizing the equations of motion from 4.6 around equilibrium and choosing oscillatory solutions for the obtained set of homogeneous equations one can

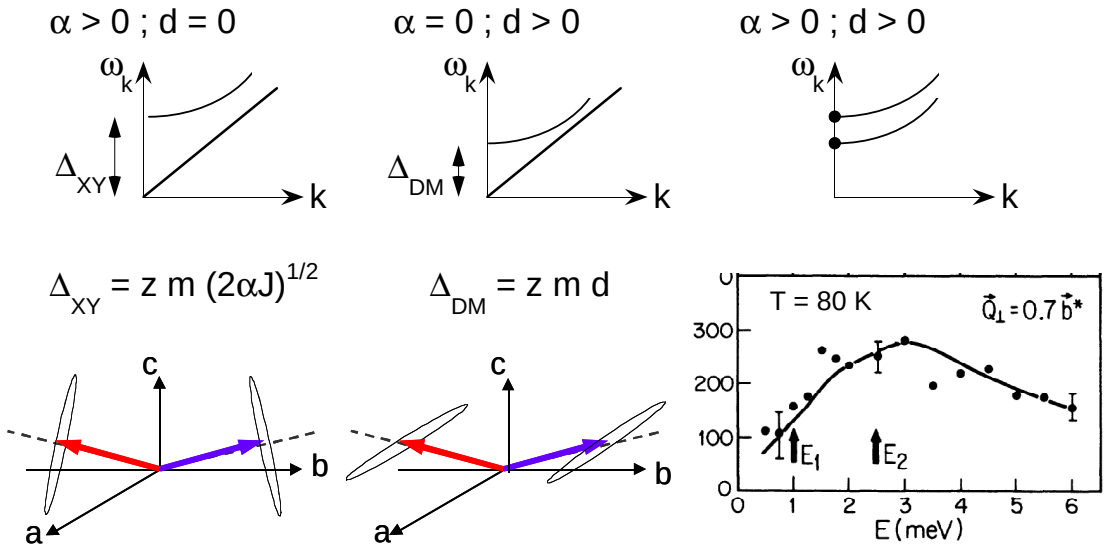

Figure 4.7: The upper row shows schematically the dispersions of the spin-wave branches in the limit $k \to 0$ if: only the XY (left), only the DM (middle) and both of these anisotropy terms are present (right). The lower row shows the pattern of oscillating magnetizations corresponding to the XY (left) and DM (middle) spin gaps at $k = 0$ as well as the INS experimental data from Ref. [122] showing these two gaps in La_2CuO_4 (E_1 and E_2 correspond to the DM and XY gaps respectively).

get (to first order in anisotropy terms) the following energies corresponding to the XY and DM gap respectively:

$$\omega_{XY} = z\ m\ \sqrt{2\alpha J} \quad \text{and} \quad \omega_{DM} = z\ m\ d \tag{4.7}$$

With $z = 4$, $m = 1/2$ and taking $J = 145$ meV [110] one can calculate from Eq. 4.7 the anisotropy parameters α and d if ω_{XY} and ω_{DM} are known. If the quantum corrections for the spin-wave velocity are taken into account [116] the expressions for the gap enegies become $\omega_{XY} = 2.34\sqrt{2\alpha J}$ and $\omega_{DM} = 2.34dJ$ [94]. The ellipses shown in Fig. 4.7 are very elongated, the ratio of their small and big axes being essentially given by ratios of the anisotropy parameters with respect to the large super-exchange J. This is why in the literature the XY mode (which corresponds to the precession of the net WF moment around the c-axis) is also called the out-of-plane gap while the DM mode (which corresponds to the c-axis oscillations of the WF moment) is called the in-plane gap.

In Fig. 4.7 we also show the low energy INS measurements in La_2CuO_4 of Peters *et al.* [122]. The dots are the experimental data and the solid line is a fit using the

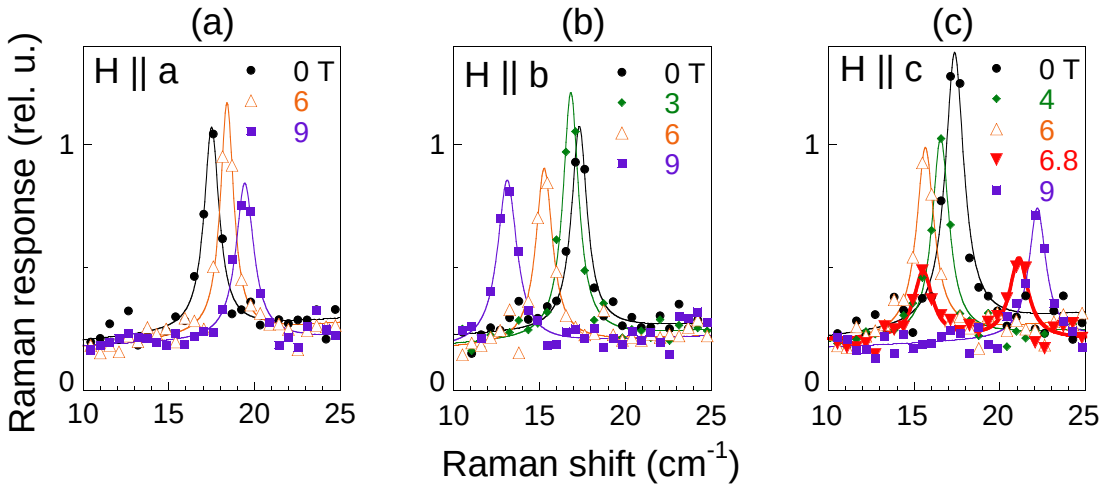

Figure 4.8: T = 10 K magnetic field dependence of the Dzyaloshinskii-Moriya gap in La_2CuO_4. The Raman spectra are taken in (RL) polarization. The dots are experimental data and the solid lineas are Lorentzian fits.

spin-wave approximation convoluted with the experimental resolution. The energies of these two gaps are shown by arrows. The most direct way to check the magnetic nature of these modes is to apply an external magnetic field which has not been done so far. It is also desirable that such a study be performed with a higher energy resolution probe.

4.2.3 Magnetic field, temperature and doping dependence of the Dzyaloshinskii-Moriya gap in $La_{2-x}Sr_xCuO_4$ $(0 \leq x \leq 0.03)$

Field dependent Dzyaloshinskii-Moriya gap in La_2CuO_4 – Fig. 4.8 shows 10 K Raman spectra taken from 93% detwinned La_2CuO_4 crystal using circular (RL) polarization. A sharp resonance is seen in zero field at 17 cm^{-1}. This excitation disperses continuously upwards (downwards) for $\vec{H} \parallel \hat{a}$ ($\vec{H} \parallel \hat{b}$) axes. For $\vec{H} \parallel \hat{c}$, Fig. 4.8c, the mode disperses downwards until the magnetic field reaches the value $H_{WF} \approx 6$ T. At this point a tansition to the WF state takes place. Initially observed in magnetic field dependent magnetization data [113] this first order transition could be also studied by neutron scattering measurements [123] because due to the change

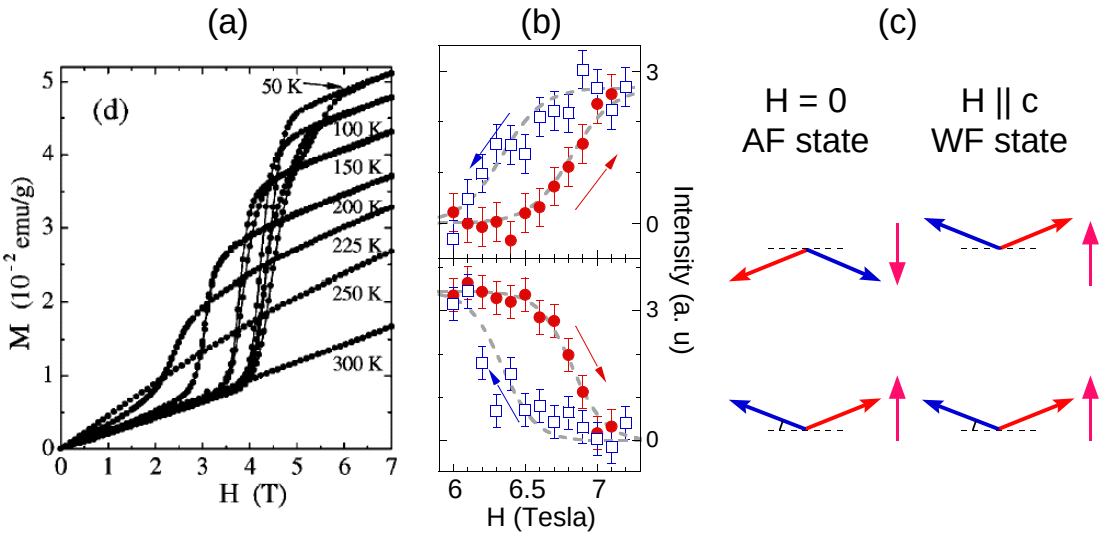

Figure 4.9: (a) Magnetization as function of magnetic field parallel to the c-axis for several temperatures. Data are from Ref. [106] and taken from a x = 0.01 $La_{2-x}Sr_xCuO_4$ crystal. (b) Hysteretic loops of the 21 cm^{-1} (upper panel) and 15 cm^{-1} (lower panel) modes from Fig. 4.8c at the WF transition. (c) The spin arrangements in the 3D AF and WF states.

in magnetic symmetry the scattering form factors allowed new Bragg peaks. In the 6 - 7 T range the resonance remains around 15 cm^{-1} but decreases in intensity and we observe a concomitant appearance of another feature around 21 cm^{-1}. The 6.8 T spectrum in Fig. 4.8c shows clearly the coexistence of AF and WF states. Recent magnetization data [106] and a cartoon comparing the spin configuration in zero field and in the WF state are shown in Fig. 4.9. The hysteretic loops in the magnetic field dependent magnetization correspond to the hysteretic loops of the 15 and 21 cm^{-1} modes shown in Fig. 4.8b. This is in turn very similar to the behavior of the (100) and (201) magnetic Bragg peaks [123], reflecting the dynamics of magnetic domains in the presence of small crystalline imperfections.

The energies of the 17 cm^{-1} resonance as a function of magnetic field are plotted in Fig. 4.10a. The expressions for the fitting functions and the values for the fitting parameters used for the data in this figure are summarized in the following. If $\vec{H} \parallel \hat{a}$ and $\vec{H} \parallel \hat{b} \Rightarrow \Delta_H = \sqrt{\Delta_{DM}^2 + \gamma H^2}$ with $\Delta_{DM} = 17.35 \pm 0.25$ cm^{-1} and $\gamma_{H\|a} = 0.96$ and $\gamma_{H\|b} = -1.65$ (cm T)$^{-2}$. If $\vec{H} \parallel \hat{c}$ and $H \geq H_{WF} \Rightarrow \Delta_H = \sqrt{\Delta_{DM}^2 + \beta H}$ with $\beta = 22.6$ cm^{-2}T^{-1}. The quadratic dependence in the first two cases can be

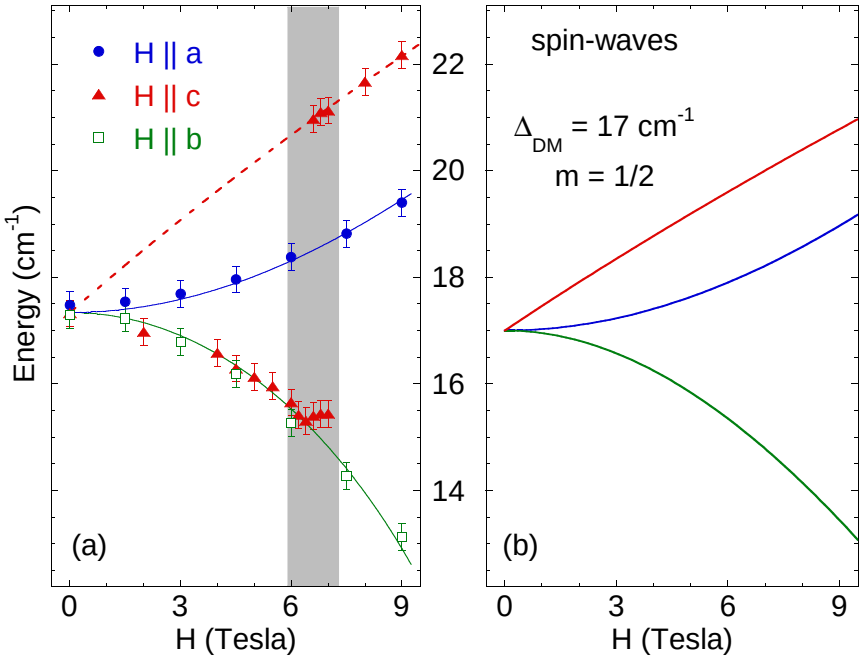

Figure 4.10: (a) Magnetic field dependence of the DM gap in La_2CuO_4 for $\vec{H} \parallel \hat{a}$ (filled blue circles), $\vec{H} \parallel \hat{b}$ (empty green squares) and $\vec{H} \parallel \hat{c}$ (filled red triangles). The $\vec{H} \parallel \hat{c}$ data show the transition to the WF state depicted in Fig. 4.9c. The shaded area corresponds to the region of coexistence of the AF and WF states. The continuos lines are fits as described in the text. (b) Results of a 2D spin-wave calculation for the DM gap dispersion using Eqs. 4.5 and 4.6 and assuming a fully ordered moment on Cu sites.

understood because the spin re-arrangement in finite magnetic fields is independent of the directions parallel to the a or b axes along which the field is applied. This is not the case if $\vec{H} \parallel \hat{c}$ and the system is in the WF state, see Fig. 4.9c. Note that if $\vec{H} \parallel \hat{c}$ but $H \leq H_{WF}$ one observes again a quadratic dispersion with field. Moreover, the similar field dispersion for $\vec{H} \parallel \hat{b}$ versus $\vec{H} \parallel \hat{c}$ ($H < H_{WF}$) seen in Fig. 4.10a is intriguing because this degeneracy does not follow from the model of Eq. 4.5 but it rather suggests rotational symmetry with respect to the a-axis.

Confirmation that the 17 cm^{-1} (in zero field) resonance observed in Fig. 4.8 is the DM spin-wave gap comes from a 2D semiclassical spin-wave calculation. Assuming a fully ordered moment on Cu sites ($m = 1/2$), a zero field DM gap $\Delta_{DM} = 17$ cm^{-1} and minimizing Eq. 4.5, one can obtain the dispersions of the $k = 0$ DM gap for the three directions of the applied field. The results are shown in Fig. 4.10b and the reasonable agreeement with the experimental data allows one to assign this exitation

to the DM interaction induced spin gap. Two comments on Fig. 4.10b. The first is that the 2D calculation can account only for the situation where the two sublattices in adjacent Cu-O planes 'respond similarly' to the external field. This is the case for $\vec{H} \parallel \hat{a}$, $\vec{H} \parallel \hat{b}$ and $\vec{H} \parallel \hat{c}$ with $H \geq H_{WF}$ and one can see that in all these cases the theoretical predictions agree with the experiment. If $\vec{H} \parallel \hat{c}$ and $H \leq H_{WF}$ the 2D approximtion clearly breaks down and Eq. 4.5 cannot be used in this region. The second comment is just a remark that it is surprising that a semi-classical spin-wave calculation as shown in Fig. 4.10 is able to reprodce with relatively good accuracy the experimetal data in a low spin system. This is in view of the expectation that such an approximation is valid to order $1/S$ [124] which is not a 'small' number for $S = 1/2$. One may conclude from here that in order to explain the low energy spin dynamics in undoped 2D cuprates one does not need to go beyond a semiclassical approximation.

We believe that the magnetic field dependent data shown in Figs. 4.8 and 4.10 may also be relevant for a quantitative estimation of higher order spin interactions which are thought to be important in cuprates. One example is the ring exchange, see Fig.4.5, and it would be interesting to check the influence of J_{ring} on the DM gap energy and possible renormalization effects on its magnetic field dependence. An example of a system where substantial effects of J_{ring} on the spin-gap were pointed out is that of two-leg spin ladders, see section 1.2.3 in Chapter 3 of this thesis. Using the expression $\Delta_{DM} = 2.34d$ we can extract for La_2CuO_4 the value $d = 0.92 \pm 0.013$ meV.

Doping and temperature effects on the Dzyaloshinskii-Moriya gap – The results of doping and temperature on the DM gap are summarized in Fig. 4.11. The Néel temperatures for the x = 0 and 0.01 crystals studied here are 310 and 215 K respectively. The 1 and 3% Sr doped crystals were detwinned in proportion of 98 and 97%. In Fig. 4.11a we show the gap as a function of doping at 10 K. The 17 cm^{-1} resonance in the undoped crystal seen in the B_{1g} orthorhombic channel becomes weaker in intensity, remains as sharp as in La_2CuO_4 and softens to 12.5 cm^{-1} for x = 0.01, an energy 30% smaller compared to what we see for x = 0. We note

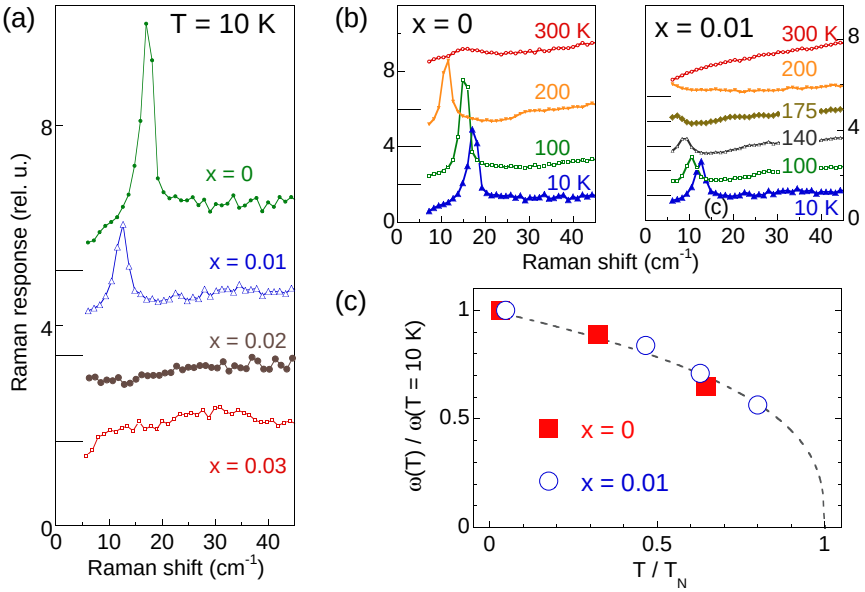

Figure 4.11: Doping and temperature dependence of the DM gap in $La_{2-x}Sr_xCuO_4$ in (ab) polarization for zero applied field. (a) T = 10 K data for x = 0, 0.01, 0.02 and 0.03. (b) Temperature dependent spectra for x = 0 and 0.01. (c) The energy of the DM gap with respect to the value at 10 K, $\omega(T)/\omega(10K)$, as a fnction of T/T_N. The dashed line is a guide for the eye.

also the absence of the DM mode in x = 0.02 and 0.03 $La_{2-x}Sr_xCuO_4$ crystals.

The doping dependence shows that the the DM mode is present at low temperatures only in the long range AF ordered region of the phase diagram (Fig. 4.1). This behavior is somehow surprising because one would expect to see for 2 or 3% doping at least a broadened feature in view of the large 2D magnetic correlations just outside the AF ordered phase. Such fluctuations are not observed in our data and this suggests that the presence of the long wavelength DM excitation is related to the existence of a true 3D order. A point discussed in the preceeding section was related to the fact that it is the orthorhombicity which generates the DM interaction. The decrease of almost 30% in its energy from x = 0 to 0.01 is much more pronounced compared with the decrease in orthorhombicity and this relates this renormalization effects to a strong sensitivity on hole doping and points to a considerable renormalization of the ordered Cu moment at only 1% hole doping. Our data suggest that the antisymmetric interaction is strongly competing with other sources of disorder in the magnetic system and we suggest that this is most likely due to the frustration effects

and the associated spin distortions induced by hole doping [125]. A last point we make regarding Fig. 4.11a is in regard to the macroscopic phase separation scenario proposed by the authors of Ref. [108] to take place for $x \leq 0.02$. If this were true than one would observe in the $x = 0.01$ crystal two features: one corresponding to the undoped region which woulod be found at 17 cm^{-1} and another one corresponding to the region with carrier concentration $c_h \approx 0.02$. The 30% decrease in energy observed in the $x = 0.01$ crystal with respect to the undoped case seems to rule out the scenario proposed in Ref. [108].

As a function of temperature what we see in Fig. 4.11b-c is that the DM gap softens with raising the temperature and disappears below 5 cm^{-1} as we approach the Néel temperature from below in both $x = 0$ and 0.01 $La_{2-x}Sr_xCuO_4$ samples. The temperature dependencies of the peak energies in the two crystals are shown in Fig. 4.11c to be similar and point toward a conventional soft mode behavior of this excitation, i.e. both its energy and its intensity approach zero in the limit $T \rightarrow T_N$, $T < T_N$. These spectra support the statement made in the previous paragraph that the DM induced gap exists in the narrow (T,x) region of the phase diagram from Fig. 4.1 where the AF order is long ranged. It is possible that the reason it disappears at higher dopings is because the low energy magnetic fluctuations move away from the Brillouin zone center [52]. Interestingly, a broad peak at 300 K is seen around 15 cm^{-1} for $x = 0$. This peak becomes a kink at 200 K and, as opposed to the conventional behavior of the DM gap, it disappears with further cooling. It is the purpose of the following section to investigate this excitation.

4.2.4 Magnetic field induced spin ordering in $x = 0$ and $x = 0.01$ $\mathbf{La_{2-x}Sr_xCuO_4}$

Magnetic field dependent (RR) polarized Raman spectra in La_2CuO_4 at several temperatures in $\vec{H} \parallel \hat{b}$ configuration are shown in Fig. 4.12a. At 10 K and in zero external field the Raman spectrum is featureless. For $H = 6$ T we see a sharp field

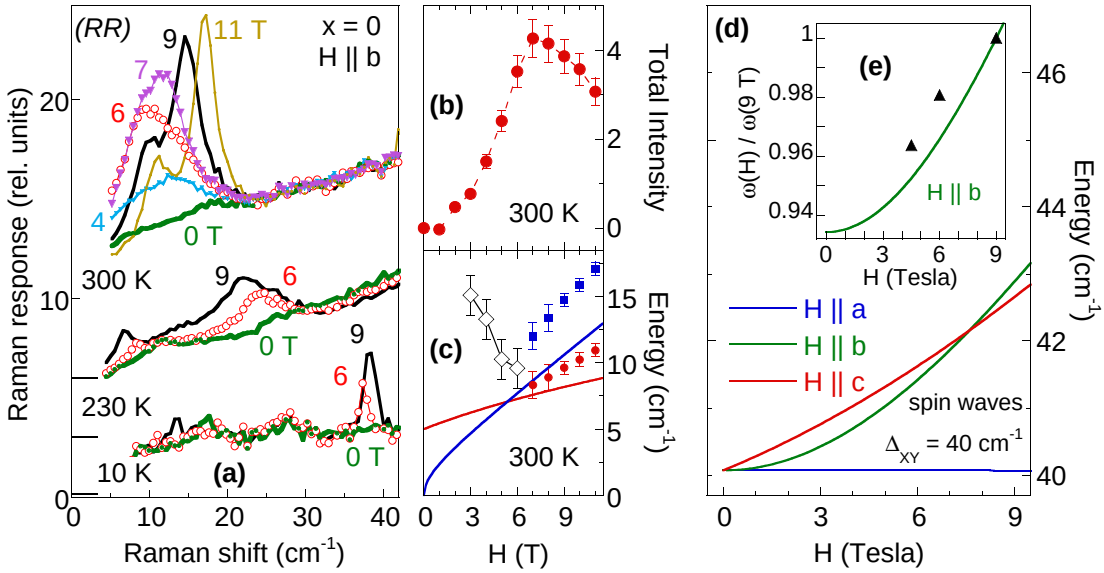

Figure 4.12: (a) Magnetic field dependence of (RR) polarized spectra in La_2CuO_4 at T = 10, 230 and 300 K. Data are vertically offset. (b) Integrated intensities obtained by subtracting the room temperature 0 T spectrum from the finite field data at the same temperature. (c) The energies of the observed magnetic modes at T = 300 K. Empty diamonds show the energy of the broad peak seen for magnetic fields $H \leq 6$ T. The solid lines in this panel are calculated using eqs. 4.5 and 4.6 assuming $\alpha = 0$, see the tetx for a discussion. (d) This panel shows the results of a T = 0 K spin-wave calculation similar as the one shown in Fig. 4.10 but in this case for an XY gap assumed to be at $\Delta_{XY} = 40$ cm^{-1}. (e) Using the calculation from (d), the solid line in the inset shows the magnetic field dependence of the ratio $\omega(H)/\omega(9T)$ for fields $\vec{H} \parallel \hat{b}$ axis. The dots represent the same quantity extracted from the T = 10 K experimental data in panel (a).

induced mode (FIM) situated at 37.5 cm^{-1} which moves to slightly higher frequency (38.3 cm^{-1}) for $H = 9$ T. The triangles in Fig. 4.12e show the relative energy of this excitation with respect to the value at 9 T. The extra data point corresponding to the 4.5 T Raman spectrum (not shown for clarity in panel (a)) marks the magnetic field at which the FIM starts to be seen. We remark only a small hardening (of about 4%) with magnetic field from 4.5 to 9 T. At 230 K the FIMs in 6 and 9 T fields are broader than at 10 K. However, with increasing field the FIM softens gaining spectral weight from the lower energy side. At 300 K, as long as the field is less than about 6 T, we observe qualitatively similar behavior as at 230 K. For magnetic fields beyond that value we see the emergence of two independent peaks and both of them harden with further increasing the field. Fig. 4.12b we plot the total integrated intensity of

the magnetic modes (for T = 300 K) at a given field, the data showing a maximum around $H = 7$ T, and in panel (c) the symbols denote the position of the FIMs as the magnetic field is sweeped from 0 to 11 T.

If $\vec{H} \parallel \hat{a}$ or $\vec{H} \parallel \hat{c}$ we do not observe any changes in the (RR) polarized Raman spectra. Note that the spectra showing the DM gap in Fig. 4.8 were taken in (RL) polarization. Circular polarizations probe 'good' symmetries if the crystal has a symmetry higher than tetragonal. Because the orthorhombicity in our samples is small it allows to separate the excitations appearing in these two geometries, but because it is finite we observe small 'leakage' effects. Their magnitude can be estimated for instance by looking at the small feature corresponding to the DM gap which is found around 6-7 cm^{-1} in the H = 9 T and T = 230 K spectrum from Fig. 4.12a.

In La_2CuO_4 the FIMs dynamics marks two events. The first seems to be a phase transition at 300 K and fields around 6 T. This is indeed the case because we know that the Néel temperature in La_2CuO_4 is around 310 K and that the magnetic susceptibility χ_b shows T_N decreasing at a rate of about 1 K/T if the magnetic field is applied parallel to the b-axis, as is the case in Fig. 4.12. Moreover, the narrow widths of the magnetic excitations above 6 T (2 $cm^{-1} \approx 0.25$ meV) at temperatures more than two orders of magnitude higher (300 K ≈ 25 meV) argue strongly for the collective nature of these excitations which correspond to another magnetically ordered state with a well-defined gap in the excitation spectrum. Such a transition is expected from the low temperature data shown in Figs. 4.8 and 4.10, more precisely from the behavior of the DM gap for $\vec{H} \parallel \hat{b}$. In this configuration we can fit the behavior of the DM gap by $\sqrt{\Delta_{DM}^2 + \gamma_b H^2}$ with $\gamma_b < 0$. Extrapolating to higher fields would lead to a collapse of this gap marking a field induced transition. The second event, a crossover taking place between 230 and 10 K, is reflected in the opposite dispersion with field and different peak widths at these two temperatures.

As for the doping dependence, except for a much weaker intensity (see Fig. 4.13), we observed the same qualitative behavior in x = 0.01 $La_{2-x}Sr_xCuO_4$. The FIM is not seen (in fields up to 9 T) at any temperature for $x \geq 0.02$. Accordingly, it

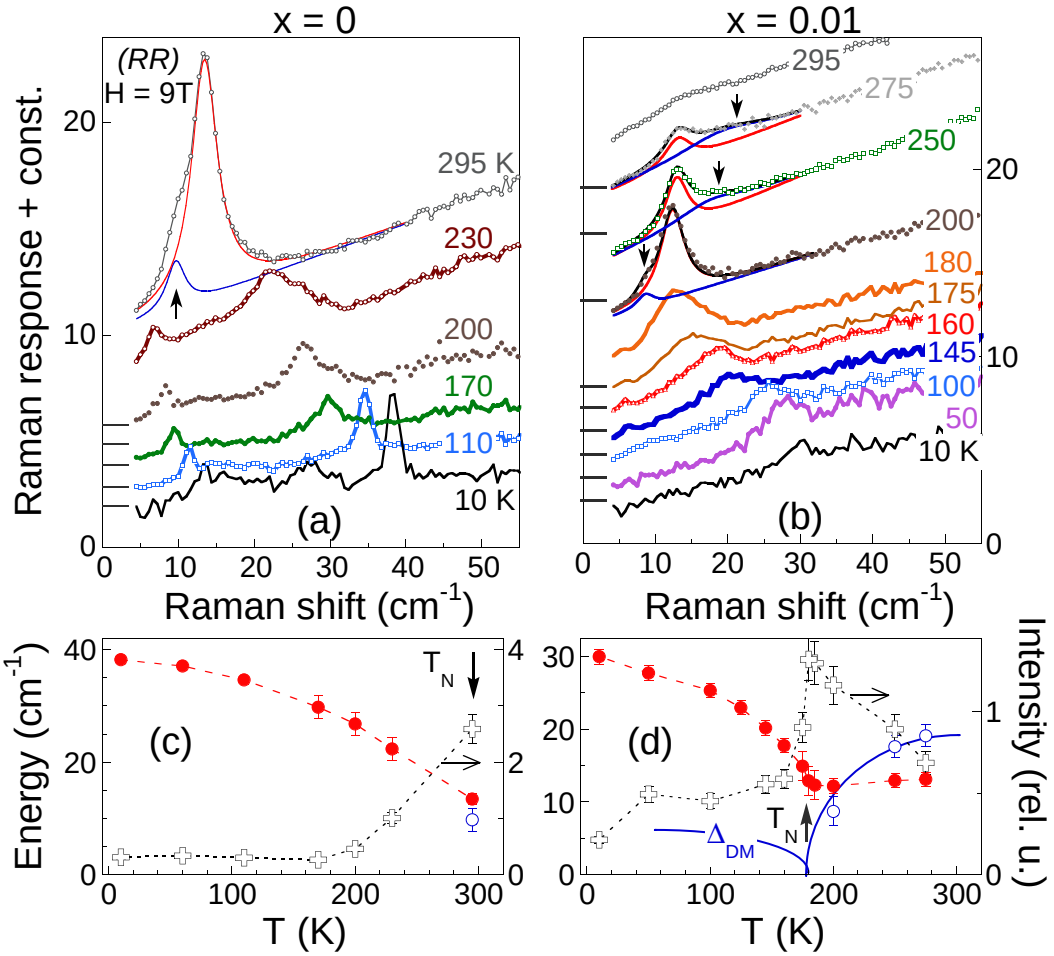

Figure 4.13: Temperature dependence of the field induced mode (FIM) in $La_{2-x}Sr_xCuO_4$ for $x = 0$ (left) and 0.01 (right). (a-b) Data (vertically offset) in (RR) polarization for $\vec{H} \parallel \hat{b}$ at 9 T. The continuous lines for T = 295 K in (a), T = 200, 250 and 275 K in (b) are two-Lorentzian fits to the data. (c-d) Variation with temperature of the FIM energies (filled red circles, left scales) and intensities (crosses, right scales). The empty blue circles correspond to the arrows in (a-b). The blue lines in (d) are guides for the eye. We also show by arrows the Néel temperatures for $\vec{H} \parallel \hat{b}$ at 9 T in the two samples.

seems that, like the DM gap, this feature is a charactersitic of the phase diagram where long range AF order exists. As for the DM gap, the reason for its absence at higher dopings could be because the low energy magnetic excitations move away from $k = 0$ concomitant to the development of incommensurate magnetic excitations. In the following we try to identify the nature of the FIM and field induced transition by looking at the effects of the temperature on the Raman data in magnetic fields.

Fig. 4.13 shows temperature dependent (RR) polarized spectra in a 9 T field $\vec{H} \parallel \hat{b}$ for $x = 0$ and 0.01. The data in panel (a) show that the crossover mentioned

above (regarding the change in the FIM width and energy dispersion with field) takes place around 150 K. This is the temperature below which the FIM width narrows. Fig. 4.13c shows that the intensity of this excitation increases as we approach T_N from below and that around 300 K we observe the splitting due to the occurrence of the field induced ordering. At this temperature the data for $x = 0$ can be clearly fit with two peaks, see panel (a), and these two peaks correspond to those observed in Fig. 4.12a for T = 300 K and $H \geq 7$ T.

The temperature dependence of the FIM across the Néel boundary can be studied in the x = 0.01 crystal which has a lower T_N, see the panels (b) and (d) from Fig. 4.13. We mention here that for the $x = 0.01$ $La_{2-x}Sr_xCuO_4$ crystal T_N was measured (for fields lower than 7 T) to decrease on the average by almost 4 K/T for fields $\vec{H} \parallel \hat{b}$ axis. Given a $T_N(0T) \approx 215$ K, in a 9 T field one expects that $T_N(9\ T) \approx 180$ K. Indeed, at 9 T and below 180 K the behavior for x = 0.01 is very similar to that in the undoped crystal showing a softening of the FIM as we warm to T_N but the situation changes with further warming. The 200 K data show that the FIM has, similarly to the 295 K data for x = 0, a low energy shoulder which is marked by an arrow. The data at 250 and 275 K can also be fitted by two Lorentzians. Along with the 200 K spectrum, these data seem to suggest the following picture: above 180 K we observe two features, one whose energy does not show significant magnetic field dependence and another one which softens from 20 to about 8 cm^{-1} with decreasing the temperature from 275 to 200 K. This latter excitation is marked by arrows in Fig. 4.13c and its energy is plotted in panel (d) by empty circles. The filled red circles in the same panel show the energy of the other mode (whose frequency is almost magnetic field independent above 180 K). The solid lines offer an explanation for the softening of the peak marked with arrows in panel (b): this is a magnetic soft mode corresponding to the field induce spin order taking place at $T \approx 180$ K in x = 0.01 $La_{2-x}Sr_xCuO_4$ for $\vec{H} \parallel \hat{b}$ and $H = 9$ T. Its energy approaches zero on cooling towards T_N and we propose that it becomes the DM gap in the Néel phase. Fig. 4.13d also shows that the plot of the integrated intensities of the FIMs as a

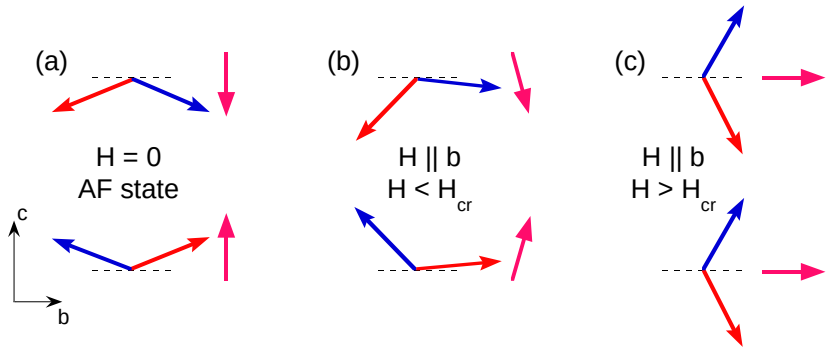

Figure 4.14: Cartoon showing the proposed changes in the spin structure in x = 0 and 0.01 with the application of magnetic fields $\vec{H} \parallel \hat{b}$ axis, starting from the AF state, panel (a). For small fields there is a slight rotation of the WF moments, panel (b), which will lie in the (ab) planes at high fields, panel (c).

function of temperature is peaked at T_N. This points toward an unusual behavior in the sense that in a conventional picture the intensities of long wavelength gap modes scale with the AF order parameter, i.e. both of them vanish as T_N is approached from below [126].

What is the nature of the FIM within the AF phase? A possible explanation is its identification to the XY gap. Support for this assignment is the presence of this mode only in x = 0 and 0.01 $La_{2-x}Sr_xCuO_4$ as well as the comparison to INS data [96, 126] which estimates $\Delta_{XY} \approx 40$ cm^{-1} at 10 K in La_2CuO_4. The very small experimentally found hardening of the FIM with increasing field from 4.5 to 9 T at T = 10 K shown in Fig. 4.12e is consistent within 20% with the predictions of the spin-wave theory, which was found to decribe fairly well the DM gap. This difference may be also accounted for if one invokes possible gap renormalization effects induced by higher order spin interactions [110].

Regarding the nature of the magnetic field induced order we propose a state like the one depicted in Fig. 4.14c. This is suggested by the magnetic susceptibility data which shows that the moments on Cu sites remain confined in the (bc) plane above T_N [104] and also by recent magnetoresistance measurements [106] which are consistent with a gradual rotation of the WF moments. In fact a departure from a two step transition [127], involving a spin-flop process occuring between the states shown in Fig. 4.14b-c and which is characterized by a large component of the staggered

magnetization along the a orthorhombic axis, is expected. In a regular spin-flop transition a magnetic field applied parallel to the easy axis (which in our case is the b orthorhombic axis, see Fig. 4.6b) will end up rotating the staggered magnetization along a direction perpendicular to this axis. The reason is that above some critical value of the field the magnetic anisotropy energy becomes smaller than the gain in magnetic energy due to the larger transverse susceptibility in the AF state [128]. In the $La_{2-x}Sr_xCuO_4$ case, the situation seems not to be the same: because the transverse susceptibility, χ_a, is the smallest below 300 K for x = 0 and 0.01 (see Fig. 4.3), the spins cannot partake of the field energy $-(\chi_a - \chi_b)H^2/2$. Accordingly, a flop along the a-axis is not favorable from this point of view.

The identification of the FIM with the XY gap can also explain other observed features. The crossover around 150 K shown in Figs. 4.12 and 4.13 may be understood as a departure of the direction of the WF moments from perpendicular to the (ab) plane to a direction almost parallel to the b-axis (see Fig. 4.14) where the XY anisotropy, weaker due to temperature fluctuations, ceases to play a decisive role. Physically, this corresponds to the fact that the conventional out-of-plane XY mode changes its nature as the WF moment rotates away from the c-axis. Prompted by this idea we calculated (solid lines in Fig. 4.12c) the spin-wave dispersions using Eq. 4.5 and 4.6 in the extreme case of $\alpha = 0$ and a small DM gap which still confines the moments in the (bc) plane. Although finite temperature effects have to be taken into account, we note that this simple estimation reproduces, at least qualitatively, the experimental dispersions. We also comment on the possible relevance of our findings to the switch of orthorhombic axes in magnetic fields [109]. If a state like Fig. 4.14c is realized (which is shown in Fig. 4.13b to persist to temperatures close to 300 K even for x = 0.01) then the magnetic force in an external field is significantly enhanced due to the net in-plane ferromagnetic moment. Still, the origin of the coupling between the spins and the tilt of the CuO_6 octahedra remains as a very interesting question.

The qualitative scenario we propose regarding the nature of the FIMs and the nature of the magnetic field induced order leaves several open questions. One of

them is the following: if the FIM in the AF state is the XY gap, why is its spectral weigth peaked at T_N, as shown in Fig. 4.14b for x = 0.01 $La_{2-x}Sr_xCuO_4$? A second question is related to the finite intensity of the FIMs only for magnetic fields $\vec{H} \parallel \hat{b}$-axis. On the other hand if we assume that the FIM mode is an excitation other than the XY gap, arising for instance as a result of the 4-sublattice structure, then the common interpretation of the excitation around 40 cm^{-1} found in several 2D layered AF's has to be reconsidered.

One may wonder if up to now there are any other transport signatures of this magentic field induced transition which could back up our spectroscopic conclusions. As for the undoped La_2CuO_4 crystal, where the transition should be most prominent and which has strongly insulating behavior, to our knowledge there are no magnetoresistance measurements so far and in terms of magnetization it would be highly desirable to see measurements especially as a function of magnetic field at several temperatures down to 10 K. Higher fields than 7 T are needed though as the temperature is decreased below 300 K. However, relative magnetoresistance data in twinned samples of x = 0.01 $La_{2-x}Sr_xCuO_4$ (Fig. 2 in Ref. [106]) show a 'peel off' from a temperature independent curve. For a given magnetic field value, this phenomenon is seen to occur at temperatures where magnetization data indicate the transition outside the AF order. This shows that the *dc* transport responds to field induced changes in the AF environment in the anticipated (H,T) parameter space. Supplementary magnetization, magnetoresistance and especially neutron scattering measurements in magnetic field would be necessary to verify our claims.

4.2.5 Phononic and electronic anisotropy in detwinned $La_{2-x}Sr_xCuO_4$

We observed in the previous section that detwinned $La_{2-x}Sr_xCuO_4$ crystals revealed strong anisotropy effects in terms of the dynamics of long wavelength spin excitations. Here we show that the small lattice orthorhombicity has drastic effects also

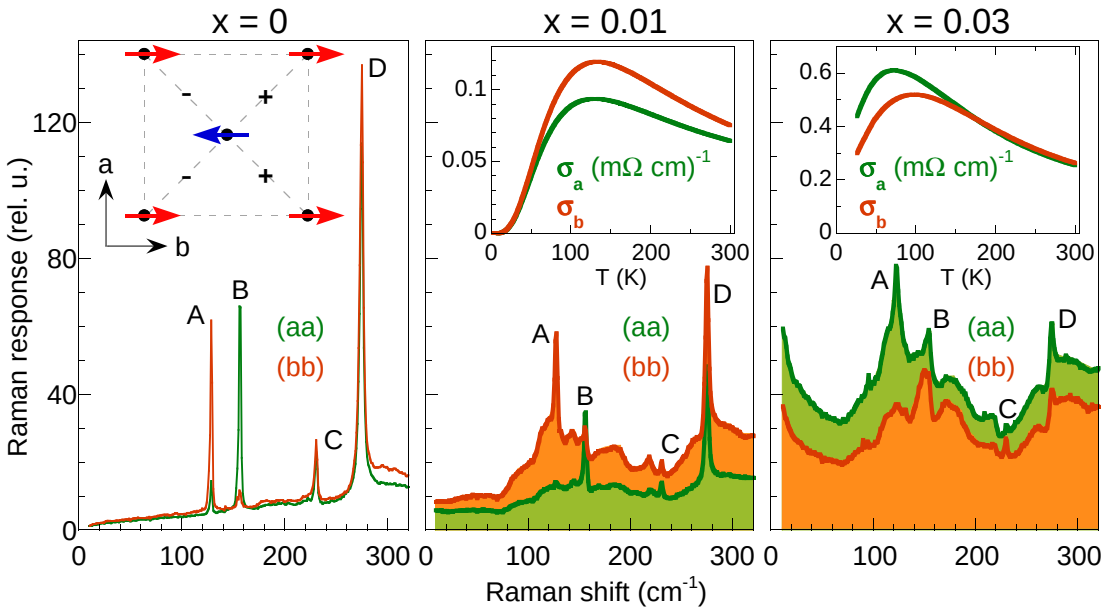

Figure 4.15: Main panels show (from left to right) T = 10 K Raman data in (*aa*) and (*bb*) polarizations in x = 0, 0.01 and 0.03 $La_{2-x}Sr_xCuO_4$. *A*, *B*, *C* and *D* denote 4 of the 5 fully symmetric Raman modes in the LTO phase. The inset in the left panel shows a unit cell of the LTO structure, the directions of spins on Cu sites and the axes notations (see also Figs. 4.2 and 4.6). The insets for the x = 0.01 and 0.03 panels show *dc* conductivities along the *a* and *b* axes. The same vertical scale was used for the Raman spectra in panels (a), (b) and (c).

on the phononic and electronic Raman continuum. A summary of our results in this perspective is shown in Fig. 4.15. The left panel shows T = 10 K Raman data in La_2CuO_4 taken in (*aa*) and (*bb*) polarizations. The axes notation is shown in the inset. Both these symmetries probe fully symmetric excitations and, in terms of phonons, there are 5 allowed in the LTO phase. Four of them, denoted by *A*, *B*, *C* and *D* are in the energy region below 300 cm^{-1}. All the five A_g modes and their atomic displacements will be discussed in more detail in the section devoted to Nd doped $La_{2-x}Sr_xCuO_4$. For now we remark that while in the insulating La_2CuO_4 the Raman continuum is, as expected, very weak at low temperatures, there is a tremendous intensity anisotropy in the *A* and *B* phonons. Mode *A* is seen clearly in (*bb*) polarization and has almost vanishing intensity in (*aa*) polarization and the situation is reversed for mode B.

In the middle panel we observe that the anisotropy in these two modes is preserved. However one can note that we observe intense Raman backgrounds (shaded areas),

quite different in intensity in (aa) versus (bb) polarizations. The relative intensities of the continua match the anisotropy in the dc conductivity along the a and b axes [105] shown in the inset. Looking at the $x = 0.03$ data (right panel) one can notice that the sign of the low temperature resistivity anisotropy changes with respect to the $x = 0.01$ case. Similarly, the Raman background in (aa) polarization becomes stronger than in (bb) polarization and this change is also accompanied by the reversal of the intensity anisotropy of the A and B phonons. This switch is a remarkable effect. Could it be that it is induced by structural changes, in particular a 90° rotation of the CuO_6 octahedra between 1 and 3% Sr doping? X-ray data showed that this is not the case, suggesting that the reversal is due to the development of a new kind of anisotropy in the spin-charge dynamics at low doping, possibly occuring as the the system crosses at low temperatures the boundary of the long range AF order. Beyond this observed switch between 1 and 3% doping, the strong phononic anisotropy seen most clearly in La_2CuO_4 data is an interesting problem by itself. Since it is determined by the CuO_6 octahedra tilt around the a-axis, one may suspect that the p_z orbitals of the apical Oxygens may be involved in the coupling process and its hybridization with in plane orbitals is not negligible. We remark one other point in regard to the phononic features shown in Fig. 4.15. While in La_2CuO_4 the observed number of modes does not exceed the number predicted by group theory (we observe also the 5^{th} mode in (cc) polarization at 430 cm^{-1}, see Fig 4.20), a much larger number of additional features sitting on top of the Raman continuum is seen for $x = 0.01$ and 0.03. It is possible that this is connected to charge and/or spin supermodulation within the 2D Cu-O planes. While not explained, the experimental observations in Fig. 4.15 pose intriguing questions, some of them, like the possibility of 2D spin and/or charge order, being tied to problems actively scrutinized in relation to the occurence of superconductivity in cuprates.

4.3 Spin and lattice dynamics at commensurate $x = 1/8$ Sr doping in $La_{2-x-y}Nd_ySr_xCuO_4$

4.3.1 Motivation: Intrinsic spin/charge modulations in the CuO_2 planes?

The origin of the interest in studying lattice and electronic dynamics in 2D cuprates at carrier concentrations commensurate with the lattice is essentially due to the increased tendency of the doped system to form real space patterns characterized by certain periodic modulations of the charge and spin density. Among correlated systems, this situation is not peculiar to high T_c's but it has been discussed for instance in different type of materials like manganites or nickelates. Ground states in which charges self organize in quasi-1D 'rivers' (called stripes) acting as AF domain walls were predicted at the mean field level as early as 1989 [129] and later it has been proposed that the charge and/or spin ordering is not necessarily static, but the carriers could form electronic liquid-crystal like phases [130].

From the experimental point of view, one of the observed '$x = 1/8$' effects, discovered initially in $La_{2-x}Ba_xCuO_4$ [131] was a suppression of superconductivity manifested through a decrease of the transition temperature T_c. This was also seen in Nd doped $La_{2-x}Sr_xCuO_4$ [132]. In fact a similar observation (but in terms of the *onset* of superconductivity as seen by magnetization measurements [133]) was made in Nd free $La_{2-x}Sr_xCuO_4$ at 1/8 Sr doping. The 'stripology' in cuprates got a lot of momentum after the discovery of a constellation of neutron Bragg peaks in $La_{1.475}Nd_{0.4}Sr_{0.12}CuO_4$. The data showed superlattice peaks associated with static spin and hole ordering, the magnetic moment modulation being characterized by a wavelength twice as big as the one observed for the charge [134]. Some of the effects discussed above are illustrated in Fig. 4.16.

The almost complete suppression of T_c in $La_{1.475}Nd_{0.4}Sr_{0.12}CuO_4$ as well as the fact that in this compound neutron scattering sees long ranged charge and spin su-

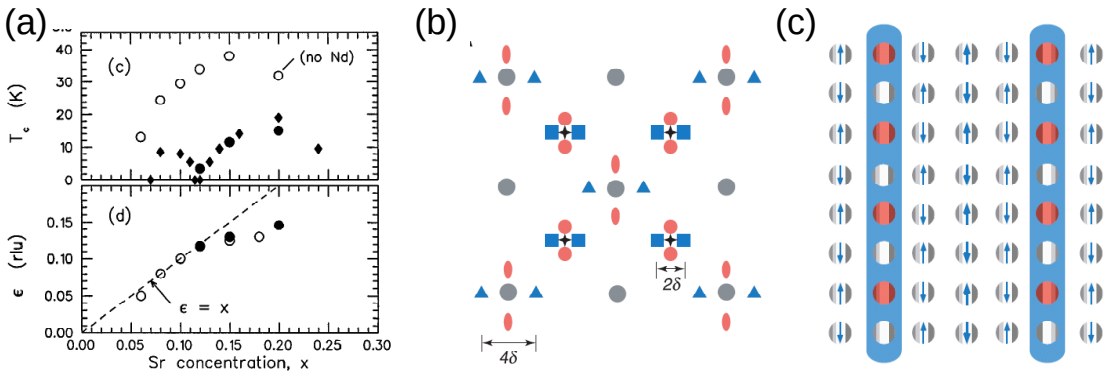

Figure 4.16: (a) The superconducting temperatures (upper panel) and the evolution of the incommensurate splitting (lower panel) in $La_{2-x}Sr_xCuO_4$ (empty symbols) and $y = 0.4$ $La_{2-x-y}Nd_ySr_xCuO_4$ (filled symbols) as a function of Sr concentration x. Data from Ref. [132]. The symbol ϵ in (a) is denoted by δ in (b) and (c). Neutron scattering: reciprocal and real space are shown in panels (b) and (c). In (b) the grey circles at $(2\pi/a)(m,n)$ with (m,n) being a pair of integers correspond to fundamental structural Bragg peaks in the HTT phase. The black stars at $(2\pi/a)(m,n)+(\pi/a,\pi/a)$ are for the commensurate AF Bragg peaks. The points separated by 2δ are incommensurate dynamic or static peaks which replace the AF Bragg peaks upon Sr doping. Their associated wavelength is $\lambda_{spin} = 1/\delta$. The points separated by 4δ correspond to the charge order with $\lambda_{charge} = 1/2\delta$ in $y = 0.4$ $La_{1.475}Nd_{0.4}Sr_{0.12}CuO_4$. In (c) the real space charge-spin strucure inferred from the results in (b). Charges are confined in the blue channels and the blue arrows on the extrnal grey circles indicate the magnitude and direction of the magnetic moments on Cu sites.

permodulations suggested that the stripes may be the 'looked for' competing state to superconductivity. The presence of the incommensurate magnetic peaks also in Nd free $La_{2-x}Sr_xCuO_4$ and their observation in *elastic* neutron scans at $x = 1/8$ doping show that $La_{2-x-y}Nd_ySr_xCuO_4$ with $x = 1/8$ are some of the most suitable 2D cuprate compounds to look for the effects of such modulations. It is important to note that while in Nd doped $La_{2-x}Sr_xCuO_4$ the charge ordring was also confirmed by X-rays [135], this is not the case (yet) in Nd free samples. Raman spectroscopy can be a powerful technique in this respect because optical phonons can be used as local probes of fast changes in the charge distribution and magnetic Raman scattering provides information about local AF correlations. However, it can also provide information regarding the side effects of Sr substitution and what we argue in the study presented in the following is that some of those effects, structural distortions as well as the disorder introduced by Sr substitution, are important at 1/8 doping in

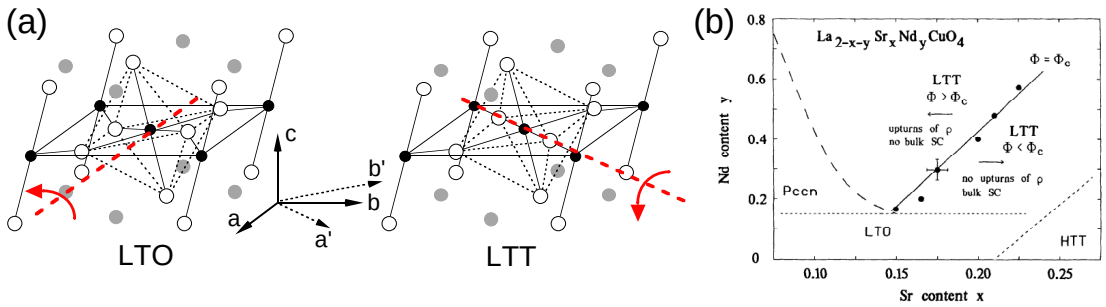

Figure 4.17: (a) Buckling of the CuO_2 planes and the tilt pattern of the CuO_6 octahedra in the LTO and LTT phases. (b) A schematic of the T = 10 K structural phase diagram of $La_{2-x-y}Nd_ySr_xCuO_4$ as a function of x(Sr) and y(Nd) (from Ref. [98]). The main point of this plot is that the LTT region characterized by a CuO_6 tilt angle $\Phi > \Phi_c \approx 3.6°$ has no bulk superconductivity (SC) and low temperature insulating behavior while SC is found in the LTT region with $\Phi < \Phi_c$. In other words it is proposed that there is a critical buckling angle compatible with long range SC and that the stabilization of the LTT phase suppresses SC correlations.

$La_{2-x}Sr_xCuO_4$ irrespective of Nd concetrantion [102].

It was mentioned in the introduction that in $La_{2-x-y}Nd_ySr_xCuO_4$ the various changes in the crystal structure are due to the lattice mismatch between the cation and Cu-O layers. Like $La_{2-x}Sr_xCuO_4$, the $La_{1.475}Nd_{0.4}Sr_{0.12}CuO_4$ compound undergoes a transition from the HTT to the LTO phase above room temperature. This transition is followed around $T_{LTT} = 70$ K by another structural change, from the LTO to the low temperature tetragonal (LTT) phase where the CuO_6 octahedra tilt around an axis parallel to the Cu-O-Cu bonds. The structural order parameter of these transitions is the libration of the CuO_6 octahedra shown in Fig. 4.17. It was noticed in $La_{1.475}Nd_{0.4}Sr_{0.12}CuO_4$ that the LTO-LTT transition takes place over a range of temperatures and that disorder in the striped phase leads to a glassy nature of the ground state. Intermediate states characterized by a tilt angles in between those of the LTO and LTT phase have also been proposed [98]. The coexistence in $La_{2-x-y}Nd_ySr_xCuO_4$ of several phases in a complex mixture was suggested by transmission electron microscopy [103].

So there are interesting topics associated to the presence of Nd, but after all why are these structural effects, especially the ones related to the tilt of CuO_6 octahedra, relevant to the spin and charge dynamics? The importance of the local structural

distortions for the superconducting properties characterized in cuprates by a short coherence length should not be ignored. The stabilization of the LTT phase was observed to trace the suppression of superconductivity in Nd doped $La_{2-x}Sr_xCuO_4$ [136] and also in the related $La_{2-x}Ba_xCuO_4$ compound [137]. A critical value of the CuO_6 tilt was associated with the stabilization of magnetic against superconducting order, see Fig. 4.17b and Ref. [98]. Rapid suppression of superconductivity, similar to that due to Cu replacement by non-magnetic impurities, was observed with increasing the cation radius variance [138].

In this context our study provides direct spectroscopic information about the LTO-LTT transition in $La_{1.475}Nd_{0.4}Sr_{0.12}CuO_4$ and local deviations from the average structure existent in Nd doped and Nd free $La_{2-x}Sr_xCuO_4$ structures. The persistent fluctuations of the structural order parameter down to T = 10 K reveal substantial disorder in the cation-oxygen layers. The distinct Raman signatures accompanying a transition to a state with deep spin/charge modulations are not observed in the temperature dependence of the two-magnon (2M) scattering around 2200 cm^{-1} and the c-axis polarized phonons below 500 cm^{-1} [102].

4.3.2 Inhomogeneous CuO_6 octahedra distribution in $x = 1/8$ $\mathbf{La_{2-x-y}Nd_ySr_xCuO_4}$

In the following we will show Raman data from $La_{2-x-y}Nd_ySr_xCuO_4$ with the following doping concentrations: $x \approx 1/8$, $y = 0$; $x \approx 1/8$, $y = 0.4$; and $x = 0.01$, $y = 0$. The spectra were taken from the $(a'c)$ and (ab) faces of the $x = 1/8$ $La_{2-x-y}Nd_ySr_xCuO_4$ samples and from the (ac) surface of a $x = 0.01$ $La_{2-x}Sr_xCuO_4$ crystal as determined by X-ray diffraction. See Fig. 4.17 for axes notations. Note that they are consitent with the ones in Fig. 4.2, the primed letters corresponding to directions parallel to the Cu-O-Cu bonds The laser excitation energy used was $\omega_{in} = 1.92$ eV.

Raman spectra taken in the (ca') geometry may provide direct information about

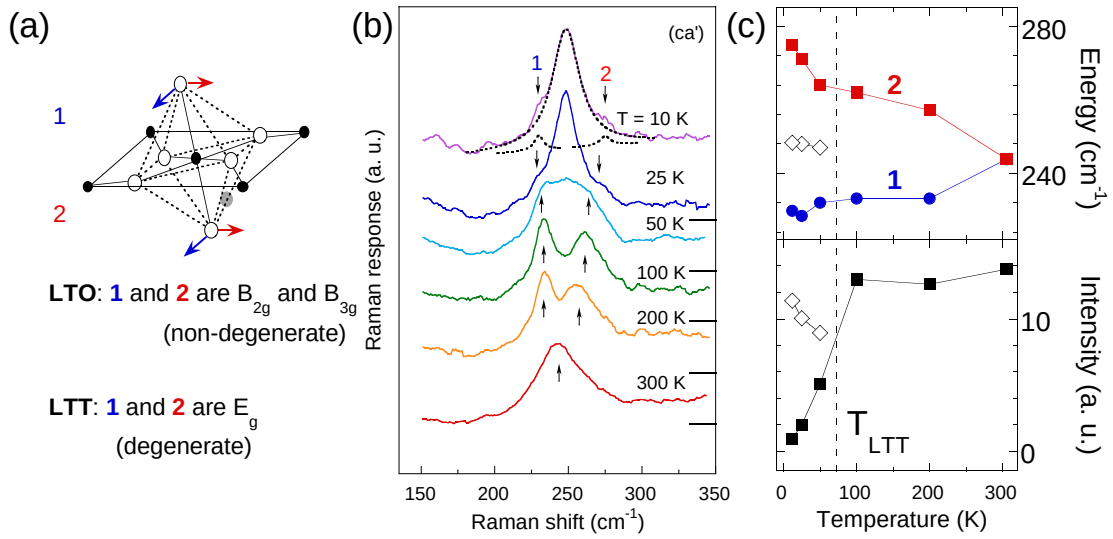

Figure 4.18: (a) Cartoon with the apical Oxygen vibrations having B_{2g} and B_{3g} symmetry in the LTO phase and degenerate with E_g symmetry in the LTT phase. (b) Temperature dependence of the O modes described in (a) in $La_{1.475}Nd_{0.4}Sr_{0.12}CuO_4$. The finite intensity of modes 1 and 2 even at T = 10 K shows that there exists a residual orthorhombicity at this temperature. (c) The temperature dependence of the energies (upper panel) and intensities (lower panel) of the phonons in (b) obtained by Lorentzian fits.

tetragonal to orthorhombic distortions. In this polarization we probe phononic modes with B_{2g} and B_{3g} symmetries in the LTO phase which become degenerate with E_g symmetry in the LTT phase. In Fig. 4.18 we show the temperature dependence of the modes around 250 cm^{-1} corresponding to the apical O vibrations parallel to the Cu-O plane in $La_{1.475}Nd_{0.4}Sr_{0.12}CuO_4$ [139]. One can think about the spectral changes in analogy to the evolution with temperature of the orthorhombically split X-ray diffraction Bragg peaks [136]. We observe a broad peak around 245 cm^{-1} at room temperature which, with cooling, becomes resolved into two components, one hardening and one softening. A new central peak can be seen at 50 K around 248 cm^{-1} which gains spectral weight as the temperature is decreased to 10 K. While the total integrated intensity of the modes remains constant, Fig.4.18c, we observe a redistribution of spectral weight among the three modes as a function of temperature. The split components become weaker but can still be seen as 'orthorhombic satellites' of the central peak down to 10 K. The coalescence of the features into the 248 cm^{-1} mode signals the recurrence of a phase with tetragonal symmetry which should be

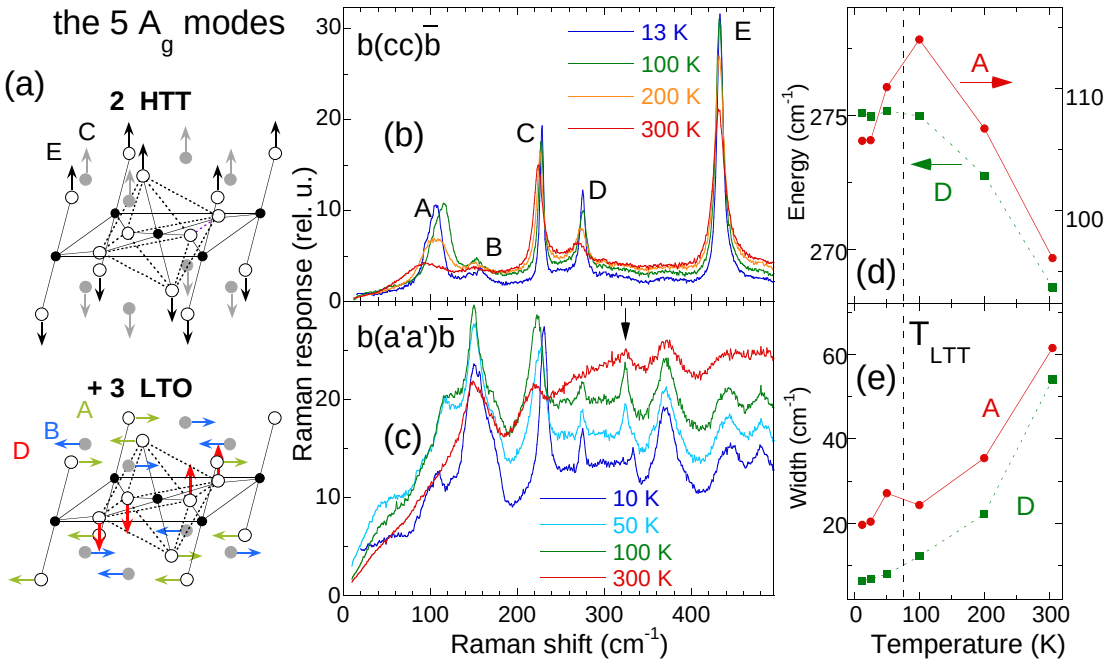

Figure 4.19: (a) Group theory predicts two A_{1g} modes in the HTT phase (denoted by C and E) and the appearance of 3 additional A_g phonons in the LTO phase (denoted by A, B and D). They are linear combinations of the atomic displacements shown in this panel. Temperature dependence of the $b(cc)\bar{b}$ (panel b) and $b(a'a')\bar{b}$ (panel c) polarized Raman spectra. In (d) and (e) we show the temperature dependent energies and intensities of modes A and D from panel (b).

the expected LTT phase of $La_{1.475}Nd_{0.4}Sr_{0.12}CuO_4$. However, the finite residual intensity of the satellites appearing on the tails of the broad central peak shows an incompletely developed LTT phase and that even at 10 K there exists about 7% LTO phase (determined from the relative ratio of phonon intensities). Note that the width of the main peak at T = 10 K is comparable to the widths of the components of the doublet seen at temperatures as high as 200 K.

Raman data in (cc) polarization is well suited for the study of lattice dynamics due to weaker coupling to underlying electronic excitations. Temperature dependent Raman spectra in this scattering geometry are shown in Fig. 4.19b. Group theory predicts five fully symmetric modes at $k = 0$ in each of the LTO and LTT phases and only two for the HTT phase. The two fully symmetric modes of the HTT along with the additional three modes in the LTO phase are shown in Fig. 4.19a. In Fig. 4.19b we observe all the five phonons corresponding to the LTO and LTT phases and they are denoted by A, B, C, D and E. Four out these five modes can also be seen in Fig. 4.15

where the same notation was used. Although every one of these excitations should be considered as linear combinations of all the A_g movements depicted in Fig. 4.19a, one could roughly say that they are mainly composed of the following vibrations. The modes C and E (which at T = 10 K are found at 228 and 433 cm^{-1}) are inherited from the HTT phase and they correspond to the *c*-axis vibrations of La/Sr/Nd and O atoms respectively, see the upper part of Fig. 4.19a. Mode A is the soft mode of the HTT-LTO transition (the CuO_6 octahedra tilt), mode B is mainly due to the vibration of La/Sr/Nd atoms in the direction imposed by the CuO_6 tilt and mode D consists of *c*-axis vibrations of the in-plane O atoms [139, 140, 141]. The energies of the last three phonons at the lowest temperature are: 106 cm^{-1} (mode A), 156 cm^{-1} (mode B) and 275 cm^{-1} (mode D).

The above qualitative description indicates that we could expect a strong coupling between the lowest energy modes (A and B). These two excitations can be distinguished in Fig. 4.19b from the other ones because they remain much broader and look like composite features even at the lowest temperature in comparison with the the modes C, D and E which harden and sharpen smoothly through the LTO-LTT transition taking place around 70 K. As seen in Fig. 4.19b, the temperature variation of the intensities of the modes C and E inherited from the HTT phase is not as pronounced which is not surprising. A comparison of the temperature dependent energy and full width at half maximum (FWHM) of modes A and D is shown in Fig. 4.19d-e. The large variation in energy and width of mode A above the transition (see also the inset of Fig. 4.20), the softening below 70 K, as well as its energy around 110 cm^{-1} in agreement with neutron scattering studies [142] show that this mode corresponding to the octahedra tilt is the soft mode of the structural changes [140]. The smooth decrease in the energy in the LTT phase is only apparent because this space group is not a subgroup of the LTO group and as a result a true LTO-LTT transition is expected to be of first order. Although unresolved due to broadening effects, the large width of mode A around 70 K shows the coexistence of the LTO and LTT tilts, the latter appearing as a result of folding of the LTO *Z*-point to the Γ-point of the LTT

phase which was observed also in La_2NiO_4 [143].

We infer from our data that the large FWHM of mode A reflects the spatial distribution of the octahedra tilt. The simultaneous broadening of the mode B shows coupling between the OP and La/Nd/Sr vibrations and as a result the influence of the dynamics in the cation-O layers on the properties of Cu-O planes. Both modes B and C involve cation displacements as discussed above, the former perpendicular and the latter parallel to the c axis. However, at 10 K the FWHM of mode C is 8 cm^{-1}, smaller compared to the FWHM of mode B which is around 20 cm^{-1}. We conclude that the large observed widths of the modes A and B are mainly caused by the locally fluctuating OP and not due to the inhomogeneous broadening introduced by the simultaneous presence of La, Nd and Sr in the inter-layer composition which should have been reflected also in a large width of mode C.

It is interesing to compare the (cc) polarized phononic spectra with those in which the polarization of the incoming photon field is parallel to the CuO_2 planes. Fig. 4.19c shows the temperature dependent Raman spectra in the $b(aa)\bar{b}$ geometry. Different coupling to the electronic degrees of freedom when the polarization of the incident field is parallel to the Cu-O planes leads to a stronger intensity in the underlying Raman continuum relative to the phononic features and also a different intensity/shape of the fully symmetric features observed in (cc) polarization. A continuous suppression with cooling of the electronic background is due to the opening of a pseudogap in $La_{1.475}Nd_{0.4}Sr_{0.12}CuO_4$ [144]. The electron-phonon coupling allows the observation of additional peaks around 370 and 480 cm^{-1} evolving smoothly from 300 to 10 K, both of which allowing an interpretation in terms of two-phonon scattering if some anharmonic interaction is taken into account. Marked by an arrow in this panel is a B_{1g} symmetric excitation in the LTO phase which shows a jump from 325 to 335 cm^{-1} as the crystal enters in the LTT phase.

In order to understand the surprising behavior of the tilt pattern as reflected in the phononic data from Fig. 4.19 a comparison with different materials from the same class is useful. In Fig. 4.20 we show the 10 K (cc) polarized Raman spectra of three

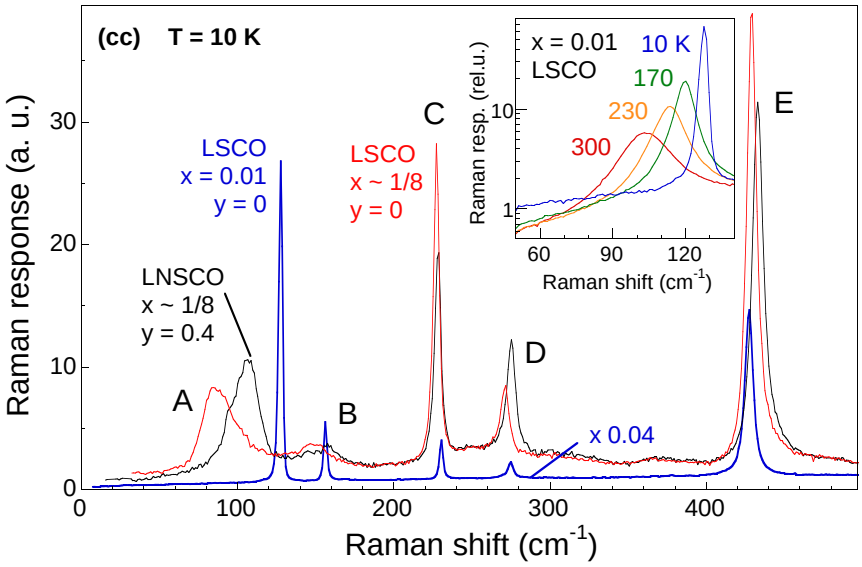

Figure 4.20: T = 10 K Raman spectra in $b(cc)\bar{b}$ configuration for $x = 1/8; y = 0$ (red), $x = 1/8; y = 0.4$ (black) and $x = 0.01; y = 0$ (blue) $La_{2-x-y}Nd_ySr_xCuO_4$. The inset shows the temperature dependence in $b(cc)\bar{b}$ polarization of the the intensity of mode A (CuO_6 octahedra tilt) in x = 0.01 $La_{2-x}Sr_xCuO_4$.

crystals: $La_{1.475}Nd_{0.4}Sr_{0.12}CuO_4$, x = 0.01 and 0.12 $La_{2-x}Sr_xCuO_4$. For $x = 0.01$ $La_{2-x}Sr_xCuO_4$ mode A has a FWHM of 2.5 cm^{-1} (Note in the inset the strongly temperature dependent intensity and width which is a characteristic of a soft mode). For $x \approx 1/8$ LSCO the same phonon is around 85 cm^{-1} and its FWHM of about 23.5 cm^{-1} is larger than the width of mode A in the Nd doped crystal where it is slightly below 20 cm^{-1}. Comparison of these relative phononic widths confirms the conclusion discussed before that Nd doping of LSCO crystals and the closer proximity to the T′ phase induced by Nd doping in the La_2CuO_4 structure [145] cannot be responsible for the large observed broadening effects. Intrinsic phonon anharmonicity would lead to a broad mode A in $x = 0.01$ LSCO which is not the case. Neither the can tilt disorder across twin domains be the cause of such dramatic effects because the volume fraction occupied by these boundaries is expected to be very small [103]. The 7% relative ratio of the orthorhombic satellites to the central peak in Fig. 4.18b would rather be consistent with such a small contribution. If the satellites are indeed due to twinning effects the data show that at 10 K the larger LTT domains are separated by regions of pure LTO tilt. The absence of the broadening effects on the vibrations

along the c-axis points towards an 'anisotropic' disorder relating primarily to bond randomness along directions parallel to the CuO planes.

Could the spin-lattice coupling or the interaction with the stripe-ordered carriers in CuO_2 planes be the main cause of broadening? Stripe correlations are enhanced in $La_{1.475}Nd_{0.4}Sr_{0.12}CuO_4$ which displays however a smaller width of mode A. Also, it is not clear why only the modes A and B would be affected by this interaction. In this sense one expects the movements of the in-plane atoms to be more sensitive to stripe ordering but we see no similar effects on mode D. Although less probable, spin-lattice induced broadening cannot be completely ruled out and the answer to this question lies in a Sr doping dependence of the (cc) polarized spectra. Our data can be reconciled however with recent studies of local structure in Nd free and Nd doped $La_{2-x}Sr_xCuO_4$ systems [146]. Model analysis of the pair distribution function from X-ray absorption fine structure suggests that in this material class the average structure determined by diffraction is different from the local pattern which is characterized by disorder in the CuO_6 tilt direction and magnitude [146]. The Raman data shown in Figs. 4.19 and 4.20 are spectroscopic evidences that the $La_{2-x-y}Nd_ySr_xCuO_4$ system is characterized by disorder in the cation layers and that the locally fluctuating octahedra tilt is responsible for the observed effects.

By comparing $La_{2-x-y}Nd_ySr_xCuO_4$ with compounds like the nickelates [147, 148] or manganites [149, 150] where charge and spin modulations are well established [151], information about the relative magnitude of charge disproportionation can be gained. New Raman active modes have been observed below the charge ordering within the Mn-O layers in $La_{0.5}Ca_{0.5}MnO_3$ [149] and also in $Bi_{1-x}Ca_xMnO_3$ [150]. Conspicuous changes in the lattice dynamics have also been observed in x = 0.33 and 0.225 $La_{2-x}Sr_xNiO_4$ by Raman scattering [147, 148]. Lowering of the crystal symmetry at the stripe ordering transition gives rise to folding of the Brillouin zone and the appearance of new $k = 0$ phononic modes. Charge localization creates non-equivalent Ni sites generating phonon 'splitting'. The c axis stretching modes corresponding to La and apical oxygens split by 14 and 30 cm^{-1} respectively [147].

Within about 3 cm^{-1} resolution imposed by the phononic widths we do not observe such splitings in our spectra. The ratio of the integrated intensities of the split oxygen modes in Ref. [147] is about the same as the ratio of doped versus undoped Ni sites. If we assume the same relation to hold for the case of cuprates, a factor of 12% in split phononic intensity should have been seen in our spectra. However, the latter argument has to take into account that different electron-phonon coupling might change this proportionality relation. Last but not least is the observation that we see, at least in (cc) polarized spectra only the phononic excitations predicted by group theory for the LTO/LTT phases. We conclude that any charge ordering taking place in our case is much weaker than in the related compounds referred to above. This is not contradicting X-ray diffraction data [135] which estimated a factor of 10^{-2} between the relative magnitude of charge modulations in cuprates and nickelates.

4.3.3 Two-magnon Raman scattering in $x = 1/8$ $\mathbf{La_{2-x-y}Nd_ySr_xCuO_4}$ and $x = 0 - 0.03$ $\mathbf{La_{2-x}Sr_xCuO_4}$

Two-magnon (2M) Raman scattering provides an additional way to look at the effects of stripe correlations on magnetic excitations. For 2D square lattices the 2M peak is predicted to be seen in the B_{1g} channel, probed by (ab) polarization [7, 9]. Fig. 4.21 shows 2M scattering around 2200 cm^{-1} at 300 and 10 K taken with the resonant $\omega_{in} = 3.05$ eV incident frequency. As in other tetragonal 2D AF's [40] we observe the spin pair excitations in the expected scattering geometry. The $c(a'b')\bar{c}$ polarization shows a featureless background which probably has a contribution from luminiscence.

In $La_{2-x}Sr_xNiO_4$ there is a clear signature of the effect of stripe ordering on the high energy spin pair excitations. In the undopd case (x = 0) the 2M Raman band is seen around 1650 cm^{-1} [40]. At 33% Sr doping this excitation is not present at that frequency but instead, two peaks at lower energies, 720 and 1110 cm^{-1} [147], are observed below the magnetic ordering temperature, see Fig. 4.21b. In Ref. [147], assuming an unrenormalized value for the superexchange $J \approx 240$ cm^{-1} with respect

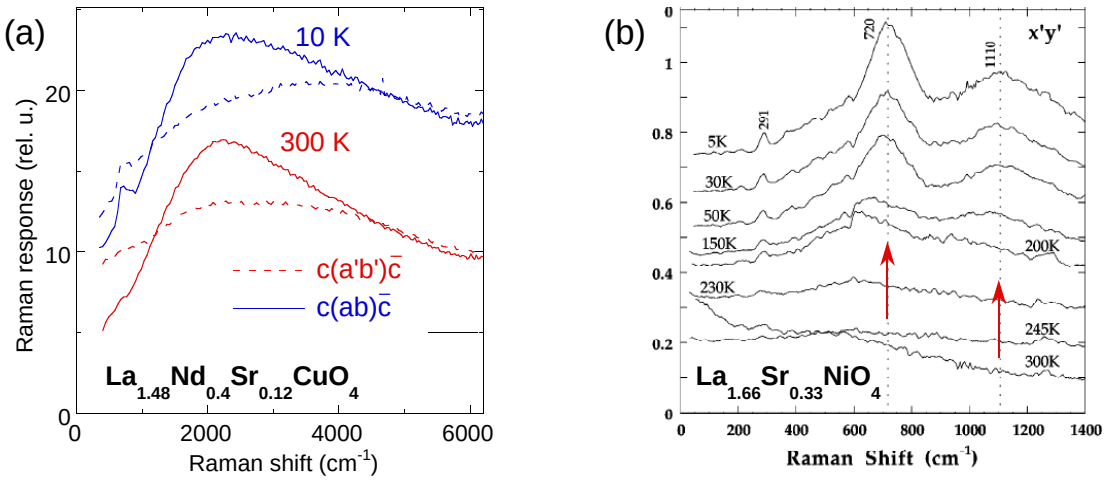

Figure 4.21: (a) Two-magnon Raman scattering in $La_{1.475}Nd_{0.4}Sr_{0.12}CuO_4$ for T = 300 (red) and 10 K (blue). The T = 10 K spectra is vertically off-set. Dashed (solid) lines are for spectra in $c(a'b')\bar{c}$ and $c(ab)\bar{c}$ polarizations respectively. (b) Two-magnon scattering in the striped phase of $La_{\frac{5}{3}}Sr_{\frac{1}{3}}NiO_4$ from Ref. [147]. The two red arrows stand for two magnetic bands corresponding to two spin exchange channels, see text.

to the unoped case, it is proposed that these peaks originate from the two spin exchange channels opened due to the stripe order, one of them within and the other one across the antiphase AF domains depicted in Fig. 4.16. A more recent neutron scattering study, whose authors are however in favor of a renormalization of the magnetic super-exchange in the stripe phase, is in support of this assignment regarding the higher frequency peak at 1110 cm^{-1} ($\approx 2 \cdot 70$ meV) by finding that the upper edge of the spin-wave dispersion branch is around 70 meV [152]. Irrespective of the microscopic origin, the 2M scattering is definitely a good probe for the study of local effects induced by the stripe order. Comparison with our high energy Raman spectra shown in Fig. 4.21a shows, as in the case of phonons, that in $La_{2-x-y}Nd_ySr_xCuO_4$ we observe only slight changes from 300 to 10 K emphasizing weak local spin modulations in this compound.

The differences we observe between cuprates and nickelates can be related to the much stronger carrier self-confinement in the latter [153]. It has also been shown [154] that anomalies in phonon dispersions occur in $La_{2-x}Sr_xCuO_4$ at points in the Brillouin zone commensurate with charge ordering wavevectors inferred from neutron scattering studies. But as discussed, the charge modulation in Nd doped $La_{2-x}Sr_xCuO_4$, where

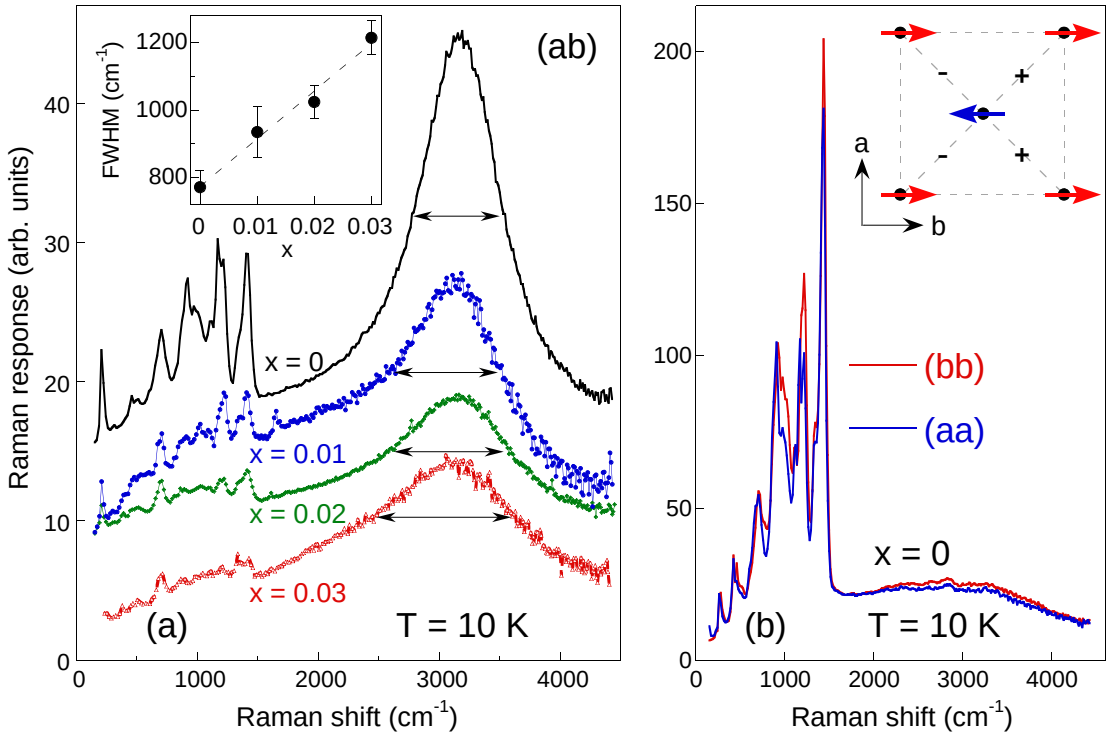

Figure 4.22: T = 10 K data in $La_{2-x}Sr_xCuO_4$. (a) The Raman two-magnon excitation around 3000 cm^{-1} in (ab) polarization for $x = 0 - 0.03$. Spectra are vertically offset. The sharp features below about 1500 cm^{-1} are higher order phonons. The inset shows the full width at half maximum for the four dopings. (b) Raman data in a detwinned La_2CuO_4 crystal (see section 1.2 in this chapter) in (aa) and (bb) polarizations. Note that the strong two-magnon feature is absent in this polarization and the anisotropy of the spectra at high frequencies.

the stripe correlations were shown to be stabilized, is too weak to produce observable changes in the lattice unit cell. The number of phononic modes we observe can be explained solely in terms of LTO/LTT distortions. Our data, however, do not contradict the possible existence of charge modulations in the Cu-O plane. In fact, the dynamics in the cation-O layers and the magnitude of octahedra tilt disorder affects the carrier distribution and our Raman results impose constraints on the magnitude of the charge modulations.

In the context of sensitive short wavelength magnetic excitations to possible spin/charge modulations in the transition metal oxygen planes, it would be interesting to take a look at the evolution with hole concentration of the 2M excitation in lightly doped $La_{2-x}Sr_xCuO_4$ crystals. The purpose is to check whether one can find at high frequencies (2000 - 4000 cm^{-1}) anisotropy effects similar to those observed in

Fig. 4.15. Our Raman results rearding these issues are shown in Fig. 4.22. In panel (a) we show the 2M feature at low temperatures in the B_{1g} channel (probed in (ab) polarization, see the axes notations in Figs. 4.2 and 4.17) for four dopings.

The length of the arrows roughly indicate the evolution of the scattering width with increasing x from 0 to 0.03. We found quite a sizeable effect in terms of the 2M FWHM. In the undoped sample the FWHM is around 770 cm^{-1} and although the in plane correlation lengths remain large in the lightly doped regime [96], we observe an approximately linear increase of about 60% with doping from $x = 0$ to 0.03 (inset of Fig. 4.22b). One may try to correlate this to the increase in the low energy electronic Raman backround seen in Fig. 4.15 in parallel polarization. We remark that although this enhancement is obvious for (aa) and (bb) scattering geometries, we checked that in (ab) configuration the intensity of the Raman background at T = 10 K is doping independent. It is easier to understand that the magnetic spin-wave gap excitations in the long wavelength limit disappear together with the disappearance of long range magnettic order, however, the drastic change in the two-magnon scattering, which in principle requires 'good' AF correlations on a much smaller scale (about 4 lattice constants), is not so straightforward to grasp. For an explanation one may resort again to the argument that in the Cu-O plane, a hle enetering the O2p bands is more delocalized and one hole breaks effectively more magnetic bonds than just one between a pair of nearest neighbor spins.

Regarding possible anisotropy effects, Fig. 4.22b shows that the (aa) and (bb) polarized spectra look very much alike at high frequencies and although there are differences, the second and third order phononinc scattering is much less sensitive to the macroscopic orthorhombicity than the one phonon excitations in the 0 to 500 cm^{-1} region. Unfortunately, as predicted by the Fleury and Loudon (see Ref. [7, 9]) and seen in Fig. 4.22, the strongest 2M scattering is supposed to be seen in B_{1g} tetragonal channel which in not probed in (aa) and (bb) polarizations ((aa) and (bb) configurations probe A_{1g} + B_{2g} tetragonal symmetries) so we cannot directly probe the effects of the macroscopic lattice spin anisotropy on the strong 2M feature from

Fig. 4.22a. What we can however say is that if the finite Raman background between 2000 and 4000 cm^{-1} has some fully symmetric (A_{1g}) magnetic contribution from higher order light scattering Hamiltonian, see Ref. [155], the influence of the lattice orthorhombicity on that contribution is neligible.

4.4 Summary

Two aspects in connection with the magnetic properties of $La_{2-x-y}Nd_ySr_xCuO_4$ single crystals were discussed in some detail. One of them was related to long wavelength magnetic excitations in $x = 0$, 0.01, and 0.03 $La_{2-x}Sr_xCuO_4$ detwinned crystals as a function of doping, temperature and magnetic field. Two magnetic modes were observed within the AF region of the phase diagram. The one at lower energies was identified with the spin-wave gap induced by the antisymmetric DM interaction and its anisotropic properties in magnetic field could be well explained using a canonical form of the spin Hamiltonian. A new finding was a magnetic field induced mode whose dynamics allowed us to discover a spin ordered state outside the AF order which was shown to persist in a 9 T field as high as 100 K above the Néel temperature T_N for x = 0.01. We proposed for the field induced magnetic order a state with a net WF moment in the CuO plane and analyzed the field induced modes in the context of in-plane magnetic anisotropy. For these single magnon excitations we mapped out the Raman selection rules in magntic fields and we also found that their temperature dependent spectral weight (in the presence of a constant external magnetic field) was peaked at the Néel temperature.

The second aspect was related to phononic and magnetic Raman scattering in $La_{2-x-y}Nd_ySr_xCuO_4$ with three doping concentrations: $x \approx 1/8$, $y = 0$; $x \approx 1/8$, $y = 0.4$; and $x = 0.01$, $y = 0$. We observed that around 1/8 Sr doping and independent of Nd concentration there exists substantial disorder in the tilt pattern of the CuO_6 octahedra in both the orthorhombic and tetragonal phases which persist down to 10 K and are coupled to bond disorder in the cation layers. The weak magnitude of existing

charge/spin modulations in the Nd doped structure did not allow us to detect specific Raman signatures on lattice dynamics or two-magnon scattering around 2200 cm^{-1}.

It is possible that the disovery of weak charge modulations in the hole doped 2D Cu-O_2 planes characteristic of high T_c materials is just a matter of time. The problem of doped Mott-Hubbard insulators seems however to be one in which numerous possible ground states are allowed and the supremacy of any one of them could require really fine tuning of microscopic parameters. In this respect, even if such a charge density modulation were observed, the question whether it helps understanding the mechanism of superconductivity or not would still need to be answered.

Chapter 5

Electronic properties of α'-NaV_2O_5

5.1 General properties of NaV_2O_5 and motivation for a spectroscopic study

Introduction – $\alpha'-NaV_2O_5$ is one of the several phases in the class of $Na_xV_2O_5$ systems [156] and until now it is by far the most studied of them. Since 1996 this compound (denoted in the following simply by NaV_2O_5) has received considerable attention because it was thought to be the second realization, after $CuGeO_3$, of a quasi-one dimensional (1D) *inorganic* material displaying a spin-Peierls (SP) transition. The interest was justified given the scarcity of inorganic materials having this property, which is quite interesting especially for the scientific community working in the field of low dimensional quantum spin systems. However, it turned out that the physics of NaV_2O_5 is more complicated and intriguing than that and the degrees of freedom involved are not only the ones describing the spins and the lattice.

What is a SP transition? We discussed in Chapter 3 the general properties of a Peierls distortion which is a transition to charge density wave state. This means that below some temperature T_P the crystal gets distorted and the electronic density acquires a periodic spatial modulation, a process during which the loss in elastic energy is compensated by the gain in the kinetic energy of the electrons. A crucial

role is played by the nesting properties of the Fermi surface (i.e., the property that enables one to connect points of the Fermi surface by wavevector characteristic of other excitations, in this case phonons) which makes low dimensional systems especially susceptible to such an instability. A pure SP transition is one in which the lattice distortion is caused by the magneto-elastic coupling, the gain in energy in this case being related to the spin degrees of freedom [157]. In other words, it is a lattice instability driven by the magnetic interactions. This phenomenon leads to the formation of a spin-singlet ($S = 0$) ground state and the opening of a spin-gap in the magnetic excitation spectrum, i.e., a finite energy is required to excite the system from its ground state to lowest triplet ($S = 1$) state. A signature of a SP state is thus an isotropic activated temperature dependence in the uniform magnetic susceptibility below the transition at T_{SP}. In addition, as opposed to an usual Peierls transition, the direct participation of the spins leads to specific predictions for the dependence of T_{SP} on external magnetic field H [158]. This has to do with the fact that in the spin case the filling factor of the electronic band and accordingly the magnitude of the nesting wavevectors can be varied continuously by a magnetic field. This statement should not be taken *ad litteram*, but in the sense that the magnetic problem can be mapped onto a fermion like system by using a transformation of the spin operators, the magnetic field playing the role of the chemical potential, see Refs. [157, 158] for more details.

So what is the difference between $CuGeO_3$ and NaV_2O_5 ? In the former, the SP nature of the transition observed around 14 K was inferred from the exponential drop in the magnetic susceptibility below this temperature and especially from the dependence of T_{SP} on an applied external field [159], see Fig. 5.1a. As predicted by theory, it was found that the field dependence was quadratic, $1 - T_{SP}(H)/T_{SP}(H = 0) = \alpha \cdot [(\mu_B H)/(k_B T_{SP}(H = 0))]^2$. Moreover, the experimental proportionality factor $\alpha = 0.46$ was also in very good agreement with the theoretical mean field value [158]. Finally, neutron scattering experiments and detailed investigations of the field-temperature phase diagram confirmed the previous SP interpretation [160].

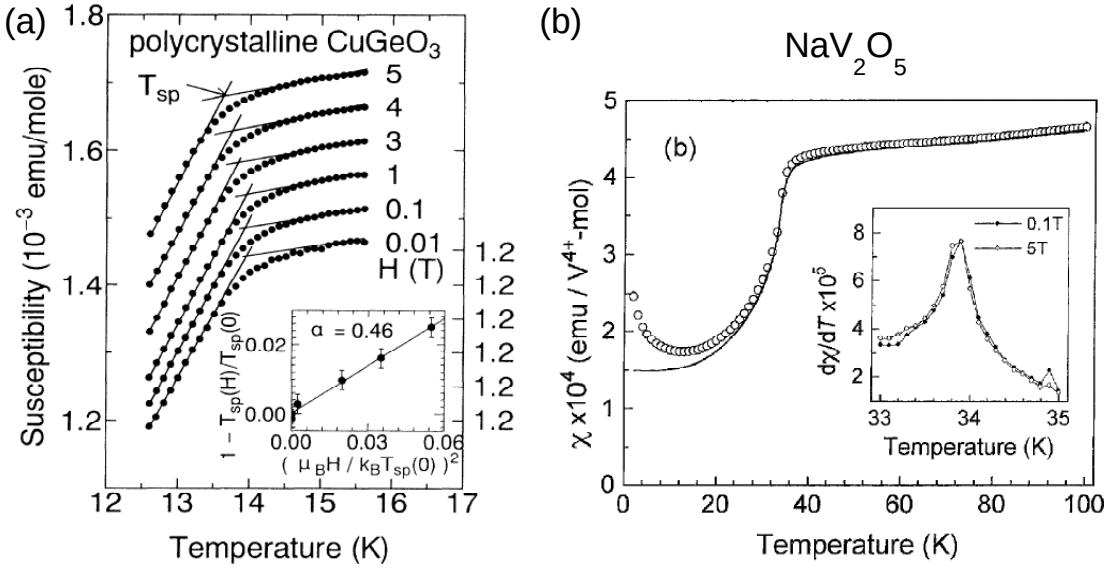

Figure 5.1: (a) Magnetic susceptibility of polycrystalline $CuGeO_3$ as a function of temperature for several values of external magnetic fields. Inset: the reduced temperature $1-T_{SP}(H)/T_{SP}(H=0)$ as a function of the dimensionless parameter $\mu_B H/k_B T_{SP}(H=0)$; the proportionality coefficient is 0.46. Data from Ref. [159]. (b) Temperature dependent susceptibility in powder samples of NaV_2O_5 . The inset shows the derivative $d\chi(T)/dT$ as function of temperature for 0.1 and 5 T. Data from Ref. [156].

As for NaV_2O_5 , many common properties with $CuGeO_3$ were observed. In 1996 an isotropic activated behavior below $T_c = 34$ K was observed by Isobe and Ueda [156], see Fig. 5.1b. Soon after that there appeared the first report of X-ray and inelastic neutron scattering (INS) data in NaV_2O_5 [161]. The authors reported the existence below $T_c \approx 35$ K of superlattice peaks due to a modulation given by $k = (2\pi/2a, 2\pi/2b, 2\pi/4c)$. This wavevector characterizes distortions corresponding to unit cell doubling along the a and b axes and quadrupling along the c direction. In the same paper, INS results showed that the transition is accompanied by the opening of a spin gap whose value was estimated to be $\Delta_S \approx 9.8$ meV. So far these results are qualitatively similar to the ones in $CuGeO_3$ but it is worth noting that a value $2\Delta_S/k_B T_c$ of approximately 6.5 already suggests a departure from the mean field value 3.52. The interpretation in terms of a simple SP transition became more questionable when experiments in magnetic fields were performed. Note the inset of Fig. 5.1 where the susceptibility derivative is shown for two values of the external field. Specific heat measurements in chemically well characterized crystalline samples of $Na_xV_2O_5$

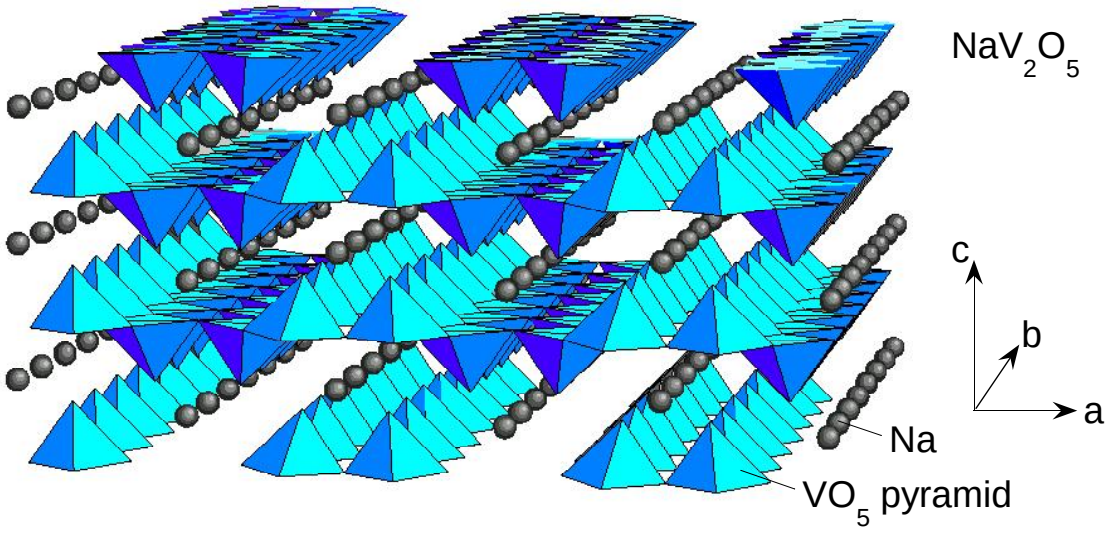

Figure 5.2: The 3D crystal structure of NaV_2O_5 (adapted from Ref. [163]). Na atoms form 1D chains along the b-axis and pairs of corner sharing VO_5 pyramids pointing in the same direction form V_2O_5 ladder rungs. The legs of these ladders run along the b-axis, see also Fig. 5.3.

with $0.95 \leq x \leq 1$ in fields up to 16 T revealed a single λ-shaped anomaly at $T_c = 33.5$ K and an isotropic decrease of the anomaly with $\Delta T_c \propto H^2$ [162]. However, the proportionality factor, the parameter α introduced in the previous paragraph, was found to be only 20% of the mean field value [158]. Similar measurements aided by magnetic susceptibility data showed a $T_{SP}(H = 0) - T_{SP}(H = 14T) \approx 0.15$ K, about a factor of 7 smaller than the expected value [163]. Heat capacity measurements also pointed out incompatibilities with a simple SP transition [164]. The authors of this paper could not reconcile the mean field predictions of the magnetic contribution to the heat capacity with the experimental data: the specific heat jump $\delta C/k_B T_c$ was found to be a factor of 20 higher than 1.43, which is the mean-field value, if the linear contribution $C = \gamma T$ at high temperatures was fixed to the theoretical expectations for a 1D $S = 1/2$ antiferromagnetic (AF) chain.

The discussion above gives us a feeling about some of the important parameters and energy scales one has in mind when discussing the properties of NaV_2O_5. The connection made with the 1D AF $S = 1/2$ chain will get support from the description of the crystal structure which is done in the following and will become more clear also in the next section where other properties of NaV_2O_5 in the high temperature phase

are discussed. However, we conclude from what has been said that in order to explain quantitatively the experimental findings one has to take into account other degrees of freedom, contrary to the initial belief that at T_c one deals solely with a magnetically driven phase transition. It has become clear that the coupling of the lattice to the charge degrees of freedom is crucial for understanding the details of what happens at T_c. The slow advance in this field was also due to the difficulty in the interpretation of X-ray diffraction data and because of a wrong identification of the crystal structure in an early study [165] which generated a plethora of subsequent papers which were at odds with each other. Diffraction anomalous fine structure spectroscopy (also called resonant X-ray diffraction, an example of which was discussed in Chapter 3 in connection to the existence of a density wave order in doped two-leg ladder structures) finally brought more understanding of the nature of the charge ordering in NaV_2O_5 , see Ref. [166] and citations therein. However, in spite of years of intensive investigation of both the high and low temperature phases of NaV_2O_5 , no microscopic model has successfully explained all the features of the transition and, as we will discuss in more detail, the nature of prominent excitations seen in spectroscopic experiments as well as the light coupling mechanisms to the collective spin and/or charge excitations is still far from being clear.

Structure and electronic properties – The crystal structure of NaV_2O_5 is shown in Fig. 5.2. It contains Vanadium-Oxygen planes stacked along the c-axis and separated by Na chains. Each V-O plane is formed from pairs of edge sharing VO_5 pyramids running along the b-axis (the vertices of the pyramids in every such pair of chains are pointing in opposite direction along the c-axis), each pair being connected in turn to a neighboring one by corner sharing pyramids. In the (ab) plane, see also Fig. 5.3, one can identify two-leg ladder (2LL) units, very similar to the ones found in $Sr_{14-x}Ca_xCu_{24}O_{41}$ compounds. One can look for instance at a pair of adjacent rows of VO_5 pyramids pointing in the same direction along the c-axis. The rungs of the ladder, oriented along the a-axis are formed by a pair two V ions bridged by an O atom which is at the common corner of two pyramids.

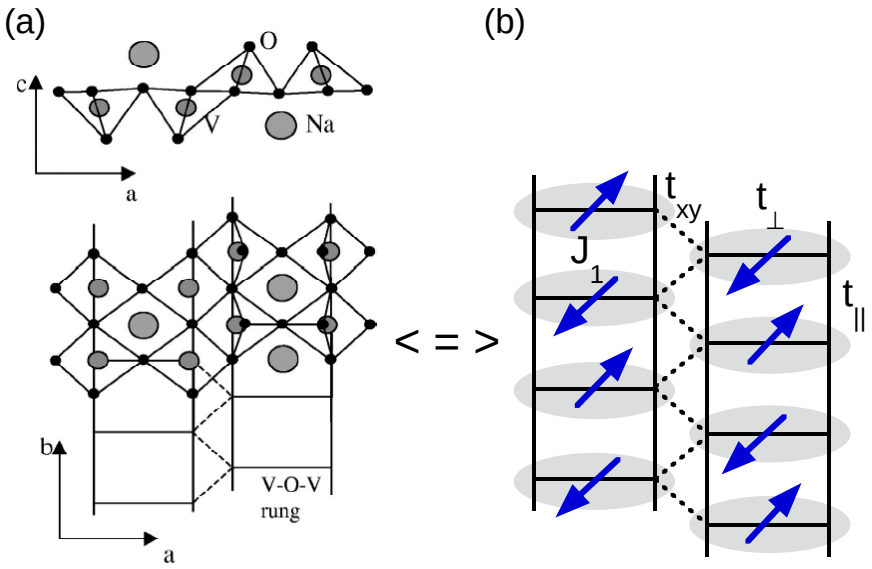

Figure 5.3: (a) Schematic representation of the NaV_2O_5 in the (010) (upper figure) and (001) (lower figure) planes (from Ref. [167]). (b) Cartoon with the spin structure in the high temperature phase. The structure can be mapped on a weakly interacting array of quasi 1D $S = 1/2$ spin chains. J_1 is the superexchange between neighboring spins along the b-axis and $t_\perp$, $t_\parallel$ and t_{xy} are the rung, leg and inter-ladder hopping parameters.

Can this structure be mapped onto an array of quasi-1D electronic units? A valence counting for $Na^+V_2O_5^{2-}$ shows that the formal V valence is 4.5+. The electronic configuration of a neutral V atom is $3d^34s^2$, so a V^{5+} ion has a closed shell configuration while the V^{4+} has one $3d$ electron on the upper shell. On the average there is one electron shared by two V ions and this makes the 2LL's to be at quarter filling factor. The initially proposed non-centrosymmetric $P2_1mn$ crystal symmetry group at 300 K [165] allowed for two inequivalent V positions, interpreted as magnetic V^{4+} and non-magnetic V^{5+} sites. The magnetic properties were thought to be determined by rows of $S = 1/2$ V^{4+} ions along a leg of a ladder (with the other one remaining magnetically inert), each row of V^{4+} ions being only weakly coupled to to the adjacent one due to large separation between them. It is now accepted based on X-ray diffraction studies that above T_c the correct space group is the centrosymmetric $Pmmn$ group [168, 169, 170]. This is important in what regards the number of distinct of V atoms existent in the high temperature phase: the inversion center and the two vertical mirror planes (i. e. perpendicular to the (ab) plane) imply that there is only one type of V atoms with an effective valence of 4.5+. The fact that NaV_2O_5 is in a

mixed-valence state is further supported by nuclear magnetic resonance (NMR) studies which confirmed the average oxidation state of all vanadium atoms to be $V^{4.5+}$ [171].

Accordingly, one can think about the ladder structure of NaV_2O_5 as having on each rung an electron equally shared by pairs of V atoms forming the rungs. Susceptibility data also indicate that the coupling between the spins of these electrons is antiferromagnetic (AF) [156]. The local symmetry splits the five-fold degeneracy of the d shell and makes the d_{xy} band (the zero's of the wave function are along the a and b axes) the lowest in energy compared to the bands generated by the other orbitals [168]. Consequently, the d_{xy} orbital is the relevant atomic state for the analysis of the low energy charge excitations. How about the quasi one dimensionality? A density functional calculation [168] of the energy bands and their mapping on tight-binding models yields for the hopping terms the following values: a rung hopping $t_\perp \approx 0.38$ eV, a leg hopping $t_\parallel \approx 0.17$ eV and a inter-ladder hopping $t_{xy} \approx 0.012$ eV. A difference of more than an order of magnitude between the intra-ladder and inter-ladder wavefunction overlap is theoretical proof for the quasi-1D nature of the system. As we will show later in relation to the low temperature phase, the dispersions of the low energy collective excitations along the a-axis, which were found to be much smaller than the ones along the leg direction, confirm experimentally this hypothesis. This is also true at 300 K, as can be inferred from the band dispersions derived from an angle resolved photoemission (ARPES) study [172].

In a regular Fermi liquid system, the V valence would make this compound metallic. However, an insulating character inferred from resistivity measurements was confirmed to exist both above and below T_c [164]. This behavior is due to correlation effects [173] and it is explained below within a simple model. Consider a rung having one electron in a bonding orbital. The next excitation would be a transition to the antibonding state situated somewhere about $2t_\perp$ above. Assuming that the on-site Coulomb energy U is infinite, i.e. no two electrons can be found on the same V d shell, an electron can hop only on an empty site of a neighboring rung. However, this will

cost an energy of the order of $2t_\perp$. The quarter filled ladder becomes thus equivalent to a half filled Hubbard chain with an "effective" on-rung repulsion $U_{eff} = 2t_\perp$ [173], explaining in principle why the vanadium ladders are insulating.

Experimental – In the following we will discuss properties of the high and low temperature phases of NaV_2O_5 , concentrating on the results of our Raman scattering experiments. The single crystal we measured had the $a \times b \times c$ dimensions around $2 \times 4 \times 0.5$ mm and was grown as described in [174]. Data were taken in a backscattering geometry using linearly and circularly (the latter only at the lowest temperatures in magnetic fields) light from a Kr^+ laser. All the data were corrected for the spectral response of the spectrometer. In addition, the resonance profile at 300 K took into account the change in the optical properties of the material as the excitation energy ω_{in} was swept from infra-red (IR) to violet, see Chapter 2 for a description. The incident photons propagated along the c-axis and by (xy) we denote a polarization configuration with the incoming photon polarization $\mathbf{e}_{in} \parallel \hat{x}$ and outgoing polarization $\mathbf{e}_{out} \parallel \hat{y}$.

5.2 Magnetic Raman continuum in the high temperature phase ($T \geq 34$ K)

5.2.1 Experimental properties: polarization, resonance and temperature dependence

Before illustrating the experimental properties of the observed broad Raman continua, we show the main features of the absorption spectrum in an energy range up to about 4 eV [175]. The absorption properties will be discussed in some detail because we will use these results in the analysis of our resonance Raman study. Optical conductivity data from Ref. [175] are shown in Fig. 5.4. The spectra show the relevant energy scales involving electron dynamics along and across the legs. The left panel the electric field

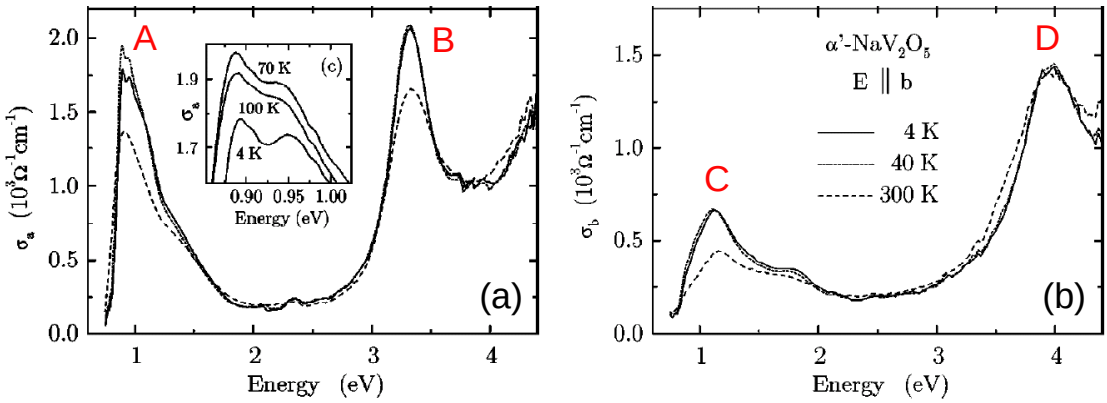

Figure 5.4: Optical conductivity at 4, 40 and 300 K for electric fields $E \parallel a$ (left) and $E \parallel b$ (right) from Ref. [175]. The letters A, B, C and D mark the main absorption features in the 0 - 4 eV energy range.

is was polarized along the rung direction while in the right panel the polarization was parallel to the legs direction. The a-axis polarized spectra show a strong peak at 0.9 eV (peak A) with a shoulder at 1.4 eV and another peak at 3.3 eV (peak B). A similar, but blueshifted sequence, is observed for light polarization along the b direction, the energies of the observed excitations being around 1.2 (peak C), 1.9 and 3.9 eV (peak D). It should be noted that the relevant electronic orbitals to be taken into account when discussing excitations in this energy range are the Vanadium $3d$ and Oxygen $2p$ states.

In Ref. [175] the authors assign peak A to an optical transition from a bonding to an anti-bonding orbital made out of symmetric (and antisymmetric) combinations of d_{xy} orbitals of the two V atoms forming a rung. This is the fundamental gap of the optical spectrum. This interpretation was supported on one hand by an ARPES study [172] which shows that the top of the bands generated by the O $2p$ orbitals are about 3 eV below the V $3d$ manifold as well as by a band structure calculation [168] and on the other hand, by a study of the evolution of this excitation with Ca doping in $Na_{1-x}Ca_xV_2O_5$ [175]. It has been observed that the spectral weight of this peak decreases linearly with Ca concentration which is consistent with a diminishing intensity due to the fact that with two electrons per rung (Ca has a 2+ valence) the many-body 2-particle state no longer allows a low energy bonding-antibonding transition [176]. The above mentioned Ca dependence was also used to rule out the

scenario that the 0.9 eV peak is a result of V $3d \leftrightarrow 3d$ transition, the argument being that such an excitation would be proportional to the number of V^{4+} ions which increases with Ca doping. If peak A is essentially an on-rung excitation, peak C at 1.1 eV was assigned to an optical excitation involving neighboring rungs [175]. The final wave function is different than the one corresponding to peak A because it involves combination of states having one rung with zero electrons and another one being doubly occupied, the red-shift of about 0.3-0.5 eV seen in a-axis polarization reflecting thus excitonic effects for the on-rung electron hole pair.

As for peaks B and D, they are thought to arise likely from transitions between O $2p$ and V $3d_{xy}$ manifolds. Remarkable is also the substantial absorption all the way up to 4 eV and even beyond which explains the black color of the NaV_2O_5 crystals. We will discuss in the following polarization, resonance of the Raman continuum we observe in the 0 - 200 meV energy range as well as its temperature dependence. A discussion of our proposed scenario for its origin will be contrasted to other present interpretations.

Polarization properties – Fig. 5.5 shows three room temperature Raman spectra taken in (aa), (bb) and (ab) polarizations and using the $\omega_{in} = 1.65$ eV excitation energy. The (ab) polarized spectrum has the lowest intensity and it is rather featureless. Next in terms of the overall background intensity comes the spectrum in (bb) polarization. Several relatively sharp features are seen at 420, 530 and 968 cm^{-1} and also some weaker ones at lower energies, 177, 230 and 300 cm^{-1}. Besides these modes, there is a broad excitation peaked at 680 cm^{-1}, but not particularly strong. The sharp modes are phonons, excitations which were studied intensively both by Raman and IR spectroscopy [177]. The strong continuum which extends all the way from the origin and having a main a peak around 680 cm^{-1} becomes the most prominent feature of the Raman spectrum in (aa) polarization. There are differences in phonons, for instance in this geometry we see two modes close to 420 cm^{-1} as opposed to only one in (bb) configuration and also the 968 cm^{-1} peak is not present. We also note the observation of a smaller shoulder at about 200 cm^{-1} and, interestingly, of

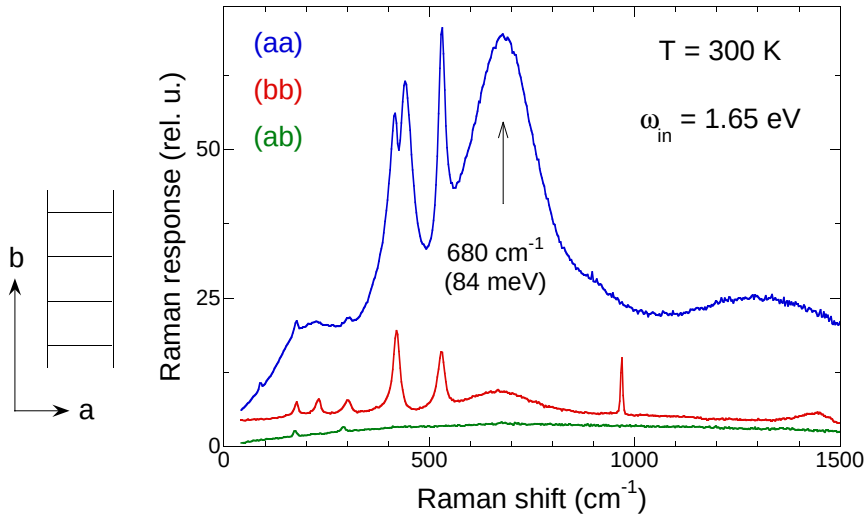

Figure 5.5: T =300 K Raman spectra of NaV_2O_5 in (aa), (bb) and (ab) polarizations taken using $\omega_{in} = 1.65$ eV laser excitation energy.

another excitation around 1320 cm^{-1}, which is approximately twice the energy of the main peak at 680 cm^{-1}.

Raman resonant profile at $T = 300$ K – In Fig. 5.6 we show the dependence of the intensity of this continuum as a function of the energy of the incoming photons ω_{in}. The resonance behavior is shown for the three polarizations shown in Fig. 5.5. Line colors for each of the spectra shown are chosen so that they roughy correspond to the actual color of the laser excitation beam in the visible spectrum. Besides the usual spectrometer/detector correction, the spectra shown in this figure were corrected for the optical properties of the crystal. The absorption coefficients the refraction indexes as well as the transmission at the sample interface were calculated using the real and the imaginary parts of the complex dielectric function provided to us by the authors of Ref. [175]. The spectral weight of the Raman continuum in the (aa) polarized spectra seems to be peaked at the extremities of the excitation range of the Kr^+ laser, 1.55 and 3.05 eV respectively. As for the $\omega_{in} = 1.65$ eV spectrum shown in Fig. 5.5, the broad Raman band is present also in (bb) polarization and the resonant enhancement in this configuration follows roughly the behavior in (aa) geometry. Obvious signatures of the (bb) polarized continuum can be seen for instance in the $\omega_{in} = 1.55$, 1.65, 1.92 or 3.05 eV spectra, while for excitation energies corresponding to the yellow, green and

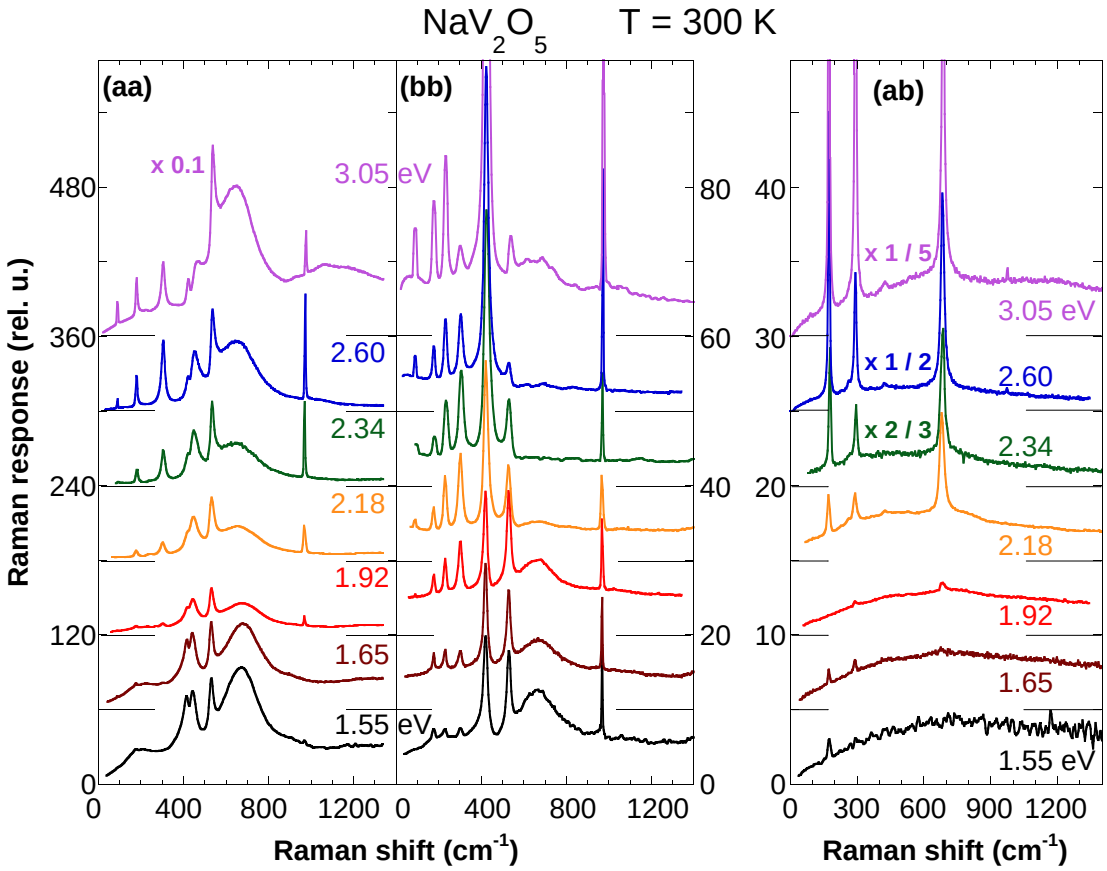

Figure 5.6: Raman response at $T = 300$ K in (aa) (left panel), (bb) (middle panel) and (ab) (right panel) polarizations for different incoming photon energies. Note the relative intensity scales for the three polarizations as well as the multiplication factors used for the 3.05 eV spectrum in (aa) polarization and 3.05, 2.60 and 2.34 eV spectra in (ab) configuration.

blue in the visible spectrum this Raman band is absent. It is important to note that although in cross polarization we do not observe a similar structure of the continuum as in (aa) and (bb) geometries, i.e. a broad Raman band peaked around 680 cm^{-1}, the overall intensity of the Raman background is excitation dependent, and a simple inspection of the right panel in Fig. 5.6 suggests that in (ab) configuration we see a slight decrease of the background as ω_{in} is decrease from 1.55 to 1.92 eV followed by an uprise at the other end of the spectrum, see the multiplication factors used for the 2.34, 2.60 and 3.05 eV.

The large width of the observed continuum makes it a distinct feature compared with the other sharp phononic lines seen in the spectra of Fig. 5.6 and points strongly to its electronic origin. Since the phonons are not the focus of the present study,

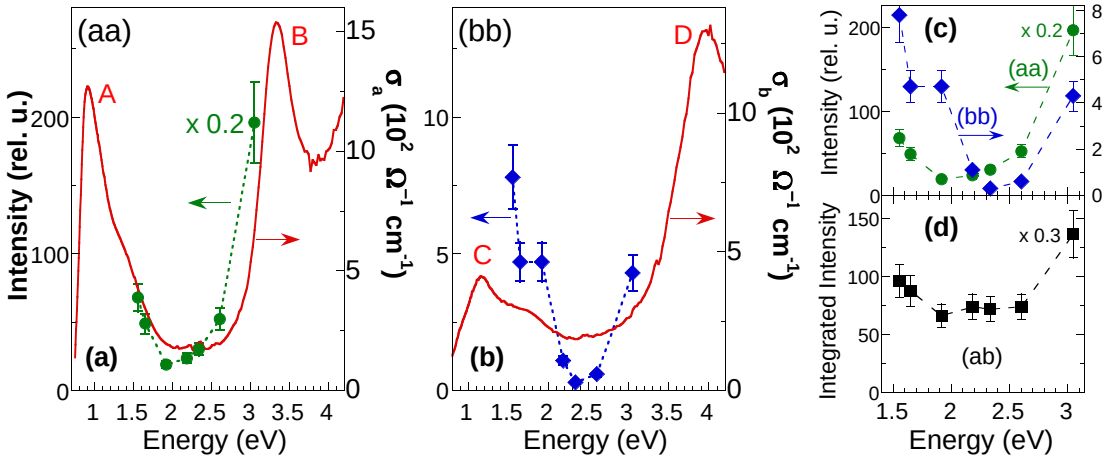

Figure 5.7: (a) Intensity of the electronic Raman band (extracted from the 680 cm^{-1} peak hight) in (aa) polarization as function of the excitation energy ω_{in} (green solid circles). Dashed lines are guides for the eye. The a-axis optical conductivity σ_a is plotted on the right scale (solid red line). (b) The b-axis optical conductivity σ_b is shown by a solid red line, and the resonant profile in (bb) polarization is shown by blue diamonds. (c) Resonance profiles in (aa) (left scale) and (bb) (right scale) polarizations from panels (a) and (b) but this time plotted together. The same symbols as in (a) and (b) are used. Note the blue shift of the profile in (bb) configuration. (d) The intensity of the continuum in (ab) polarization obtained by integrating the Raman response, $\int \chi''(\omega)\, d\omega$, between 100 and 1200 cm^{-1} with the phonons masked. The optical conductivity data is courtesy of the authors of Ref. [175].

we make only a few remarks about these features at room temperature. The interested reader can consult Raman and IR studies in Refs. [177, 178, 179] for a detailed analysis of their behavior as a function of polarization, excitation energy and temperature along with some lattice dynamical calculations. In all three polarizations we observe an enhancement in the Raman intensity of the low energy phonons in the 100 - 400 cm^{-1} energy range. Some of the phonons situated in the region where the electronic Raman band is more intense have a pronounced asymmetric (Fano) shape due to the interaction with the underlying continuum. The 531 cm^{-1} mode (assigned to V-O$_{leg}$ stretching mode [177]) is proof for the interaction between the the lattice and the electronic degrees of freedom [178], see for instance the spectra corresponding to excitation energies $\omega_{in} \geq 2.34$ eV in (aa) polarization.

Fig. 5.7a-b shows the Raman resonant excitation profile for the 680 cm^{-1} band plotted against the optical conductivity data, see Fig. 5.4 and Ref. [175]. The red line is the the optical conductivity $\sigma(\omega)$ and the same notations as in Fig. 5.4 are used for the main four absorption features seen in a and b axes polarized spectra. The dots

represent the intensity of the Raman band extracted from the 680 cm^{-1} peak height. This way of analyzing the data was chosen in the absence of a suitable fitting function for the background and also because of the presence of strong phononic features interacting with the continuum. The resonant enhancement towards both ends of the visible spectrum remarked in the discussion of Fig. 5.6, can be clearly observed here. The efficiency of the inelastic cross section follows very closely the absorption bands, showing that this excitation is always seen 'in resonance'. Importantly, if the resonance profiles for (aa) and (bb) polarizations are plotted together, see the inset of Fig. 5.7c, one can observe that the blue shift of the b-axis polarized optical peaks with respect to the peaks in the a-axis spectra is also reflected in the dependence of the Raman band intensity as a function of excitation frequency. Although the clean phononic selection rules we see in the data which can be easily checked for instance by comparison of cross and parallel polarized spectra, see Figs. 5.15 and 5.16, are strong reasons to believe that the (bb) continuum is not a result of sample misalignment in conjunction with polarization "leakage" from the (aa) spectra, the agreement between the blue shift seen in both the optical spectra and the resonance profile for the two polarizations leaves no doubt that the feature seen in (bb) data is a true Raman signal.

The 680 cm^{-1} peak is absent in (ab) polarization, but we still see in this case a signal which is excitation energy dependent. This signal is not coming from spurious effects related to crystal quality and the complete absence of scattering in the 0-2Δ energy region in the low temperature phase, where $\Delta = 66$ cm^{-1} is the T = 10 K low temperature spin gap which opens below $T_c = 34$ K, supports this statement. In Fig. 5.7d we show the integrated (ab) polarized Raman response $\chi''(\omega)$ between 100 and 1200 cm^{-1} with the sharp phononic features masked. As was the case for the data in parallel polarizations, we observe again an enhancement in the background for the lowest and highest excitation energies ω_{in}.

According to the interpretation of the optical features seen in Fig. 5.4, the intermediate electronic states responsible for the resonant behavior involve on-rung bonding-antibonding transitions, inter-rung excitations as well as transitions from

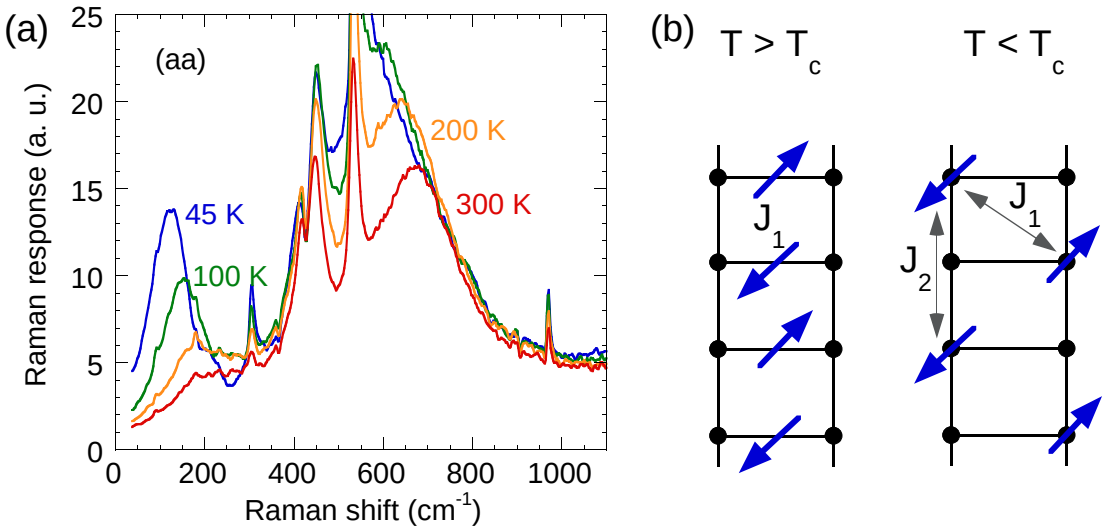

Figure 5.8: (a) Raman scattering continuum in NaV_2O_5 taken in (aa) polarization at 300, 200, 100 and 45 K using the $\omega_{in} = 1.83$ eV excitation energy. Note the softening of the band peaked at 680 cm^{-1} at room temperature as well as the development of another continuum at frequencies below 200 cm^{-1}. The sharp modes are phonons. (b) Cartoon showing the average distribution of the valence electrons provided by V atoms (represented by solid black dots) within a given ladder above (left) and below the transition (right). The picture on the right does not show the additional lattice dimerization and the alternation of the nearest neighbor superexchange J_1, see the following section for a more detailed discussion of the low temperature phase.

the lower O $2p$ states to the V $3d$ bands. Irrespective of the interpretation, we established so far that the continuum peaked at 680 cm^{-1} appears in both (aa) and (bb) polarizations, the peak is not present in cross polarization and is a strongly excitation energy dependent feature, which allows us to clearly see its next overtone for incoming photon frequencies $\omega_{in} \geq 2.6$ eV or $\omega_{in} \leq 1.65$ eV.

Temperature dependence for $34 < T < 300$ K and the role of fluctuations above the critical temperature – We show in Fig. 5.8a the dependence on temperature of the Raman continuum as we cool down from 300 K to just about the transition. The data are taken in (aa) polarization and the excitation energy used was $\omega_{in} = 1.83$ eV. We remark two effects regarding this spectra. The first is the downshift with cooling of the strong Raman band in the 680 cm^{-1} region accompanied by an increase in its spectral weight from the low energy side. Although the interaction with the 530 cm^{-1} phonon may lead to an additional shift compared to its "bare" energy, one can observe by simple inspection of the spectra a substantial softening of

about 80 cm^{-1} with cooling from 300 to 45 K. No qualitative changes in the band are seen with further decreasing temperature below the transition.

The second effect is the appearance of another band below 200 cm^{-1}. The 0-200 cm^{-1} energy region is important because this is where many new collective excitations are seen below $T_c = 34$ K as a result of lattice distortions and the opening of the spin gap. By now it is established that below T_c the in-plane ordering of the spin/charges on the outer Vanadium d shell involves, in each ladder, a zig-zag pattern like the one shown in Fig 5.8b [166]. The band at low energies can thus be understood as a precursor of the strong and sharp collective modes in the ordered phase, see Section 5.3. It is important that this continuum exist in an incipient form at 300 K and can be clearly seen already at 200 K. Similarly with the band peaked at 680 cm^{-1}, this low energy counterpart gains substantial spectral weight from the low energy side with cooling. We consider the data in Fig. 5.8a as proof that the transition at 34 K is preceded almost up to 300 K by strong fluctuations of the low temperature order and suggest that the reason the critical temperature is so low is not because of intra-ladder dynamics, but it is rather due to the phasing of the zig-zag charge order between coplanar and inter-layer ladders. This statement is supported by frequency and temperature dependent electron spin resonance (ESR) linewidth, see Ref. [180]. At 36 K the authors of this work estimate a characteristic frequency of about 700 GHz (≈ 25 cm^{-1}), for the precursor fluctuations.

We also note that the topology of the ladder at quarter filling and the charge pattern below T_c suggest that other magnetic terms are important beside the nearest neighbor exchange J_1 shown in Figs. 5.3b and 5.8b. For instance, if one compares in Fig. 5.8b the low temperature exchange path between two V atoms sitting on two adjacent rungs (which is related to J_1) to the exchange path between next nearest neighbors (which is related J_2), one can argue that the difference may not necessarily be large. On the contrary, the superexchange J_2, taking place on a straight line across one vanadium and two O_{leg} atoms, could be comparable to J_1. A quantitative estimation of possible competing interactions would be very welcome and important

for the interpretation of the magnetic excitation spectrum. The statements about the importance of other magnetic terms is supported by measurements of the temperature dependent magnetic susceptibility and its comparison with the theoretical expectations within the model of 1D AF Heisenberg chains characterized only by nearest neighbor exchange, see Ref. [174]. The authors of this work show that the measured susceptibility $\chi(T)$ above 34 K is not in good quantitative agreement with the predictions of $S = 1/2$ uniform Heisenberg chain with only nearest neighbor interaction. The data can be reconciled with theory only if additional magnetic exchanges are included and/or the superexchange itself is temperature dependent. In view of the discussion above, we believe that a significant temperature dependence of the effective magnetic interactions as well as of the relative importance of competing exchange terms could be understood if one invokes the increasing charge imbalance on each V-O-V rung with cooling.

5.2.2 Interpretation of the Raman continuum in terms of multi-spinon Raman scattering

In discussing the nature of the Raman band we have to acknowledge the existence of a substantial body of prior spectroscopic (Raman and IR) work, see for instance Refs. [176, 177, 178, 179, 181], as well as concomitant or subsequent to our study [182, 183]. Interesting properties were observed in addition to what has been discussed in the previous section. One of them is its dependence on the Na concentration in $Na_xV_2O_5$ crystals [182]. With a decrease of the Na concentration a pronounced weakening in the continuum intensity as well as a downshift in energy from 680 to about 480 cm^{-1} has been observed as x was varied from from 1.0 to 0.85 (and implicitly decreasing the number of rung electrons). Another property is related to the presence of a broad continuum of excitations in the far IR part of the optical conductivity data, extending from very low frequencies (below about 100 cm^{-1}) almost up to the electronic excitations seen around 1 eV, when the electric field was parallel to

the a-axis [176]. This continuum, whose energy scale resembles much the one seen in Raman spectra, was interpreted by the authors of Ref. [176] in terms of "charged two-magnon" excitations. In order to insure an electric dipole coupling to these double spin flip excitation the authors had to introduce a rather artificial charge asymmetry between the legs of each ladder, represented by an energy difference for the single particle on-site energy depending if it sits on the left or right of the V-O-V rung. Moreover, the model, which includes the hopping parameters $t_\perp$ and $t_\parallel$ together with Coulomb repulsion U for double site occupancy, neglects the Coulomb interaction between nearest neighbor sites which seems to be an important ingredient for the analysis of charge dynamics of the quarter filled ladder [173]. While the energy scales certainly suggest a common origin for the Raman and IR continua, the interpretation of both of these features is a matter of debate.

The common interpretation of the Raman continuum is that it is related to Raman active transitions between crystal split d levels of the V atoms [179, 182], while the interaction with the phonons resulting in the so called Fano shape is due to electron-phonon coupling. This assignment is not however based on specific calculations. On the contrary, its energy scale seems to be too low as band structure calculations [168] show that the splitting between vanadium d bands involves energies at least of the order of 2500 cm^{-1}. The temperature dependence showed in Fig. 5.8 remains also unexplained in this scenario. In fact, it was pointed out in Ref. [181] that with cooling the broad band should recover the discrete nature of an excitation between well defined atomic electronic levels. The band remains however broad to the lowest temperatures (around 5 - 10 K) measured.

Although the possibility that the Raman continuum has a magnetic origin was mentioned in literature, this idea has been ruled out, see Refs. [179, 181, 182] and the main argument was that this excitation appears only in (aa) polarization and it is not present in (bb) polarization. The latter geometry was considered the expected scattering configuration where a two-magnon type excitation should be observed if one takes into account the spin structure shown in Fig. 5.3b and also the fact that,

according to the Fleury-Loudon Hamiltonian [7, 9], the b-axis is parallel to the dominant exchange path. A second reason was that a two-magnon continuum peaked at 680 cm^{-1} would yield a value of the nearest neighbor superexchange J_1 too large in comparison to estimations from magnetic susceptibility [174] and inelastic neutron scattering [184]. We will return to this issue later in this section. For the moment we mention that it was demonstrated in Figs. 5.6 and 5.7 that the continuum, although weaker, is present also in the configuration when the incoming and outgoing photons are parallel to the ladder legs. Moreover, a strong argument in our view against d to d transitions is the presence of the second overtone of this excitation around 1320 cm^{-1}, see Fig. 5.5, whose weaker intensity suggests that it results from second order scattering. There is no intrinsic reason that the crystal field split bands are distributed in such a way that another set of Raman allowed transitions is to be found at exactly double the frequency of the main peak. Finally, there is a counterpart of this Raman continuum in the spin-Peierls compound $CuGeO_3$ whose origin is generally agreed on to be in double spin-flip processes [185]. The different energy scales of the continua in $CuGeO_3$ and NaV_2O_5 can be understood in a simple way if one takes into account the ratio of the dominant magnetic exchange interactions in these two compounds.

The above arguments allow us to propose that the origin of the Raman band peaked at 680 cm^{-1} is magnetic and that it represents a two-magnon like continuum of excitations. Moreover, we will show in the following that this assignment is compatible with its temperature dependence, resonance and polarization properties, which further strengthen the identification of the origin of this band as magnetic. We will also discuss the possibility of reconciling the obtained value for the magnetic superexchange with the ones existent in the literature. Given the fact that in the high temperature phase NaV_2O_5 can be mapped onto an array of weakly interacting $S = 1/2$ AF chains (see Fig. 5.3), we will discuss first their characteristic excitations within the Heisenberg model.

Excitations out of a quasi 1D $S = 1/2$ AF chain and the two spin-flip Raman continuum – The purpose in this part is to show that a broad band as

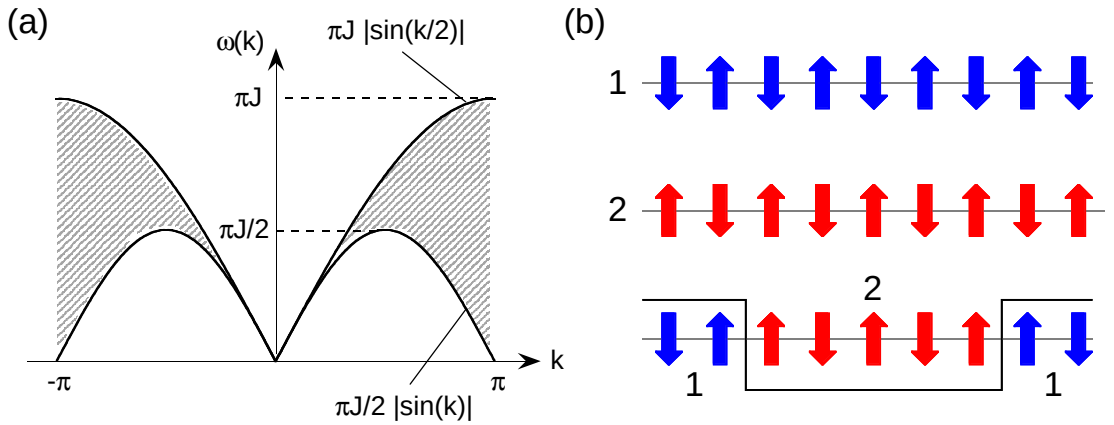

Figure 5.9: (a) Excitation spectrum of a 1D $S = 1/2$ AF linear chain with nearest neighbor Heisenberg exchange J. The lower line, $(\pi J/2)|\sin(k)|$ is the dispersion for one spinon. The $\pi J|\sin(k/2)|$ curve marks the higher energy edge of the two-spinon continuum. (b) Cartoon with a two spinon excitation. 1 and 2 are two degenerate configurations in the AF ground state. The two spinon excitation in the lower part can be thought of as a pair of domain walls between regions of type 1 and 2. The total spin of this state compared to the states 1 and 2 amounts to one spin flip.

observed experimentally is consistent with the theoretical predictions for spin-flip excitations in a 1D AF $S = 1/2$ chain. Consider a system like in Fig. 5.8b and the Hamiltonian:

$$H = J_1 \sum_{(i,j)=NN} \mathbf{S}_i \cdot \mathbf{S}_j \; + \; J_2 \sum_{(i,j)=NNN} \mathbf{S}_i \cdot \mathbf{S}_j \tag{5.1}$$

where $\mathbf{S}_i$ and $\mathbf{S}_j$ represent spins on chain sites i and j respectively while NN and NNN stand for nearest neighbor ($j = i \pm 1$) and next nearest neighbors in the same ladder ($j = i \pm 2$). J_1 and $J_2 = \alpha J_1$ are the corresponding superexchange integrals and we consider the case where both of them are positive. The NNN term leads to spin frustration, but due to the larger spatial separation in the high temperature phase it is generally expected that J_2 is only a fraction of J_1. Let us look at the $J_2 = 0$ case first. The excitations out of a $S = 1/2$ 1D AF chain in this limit are gapless domain wall solitons called spinons which have a dispersion given by $\omega(k) = \frac{\pi J}{2}|\sin(k)|$ [186]. Spinons carry a spin of 1/2 and they can be created only in pairs, each pair corresponding to one spin flip and thus having integer spin. In some sense one can think about a magnon like excitation as being composed out of two spinons. Similarly, a state with two spin flips (two-magnon Raman scattering) would correspond to the creation of four spinons. Figure 5.9a shows the excitation spectrum of the spinons

and the continuum of two-particle excitations. Panel b is an intuitive visualization of a two-spinon excitation carrying a total spin $S = 1$.

Here we come back again to a remark made in Chapter 3: which way provides a better description of the spin dynamics, one that starts from true elementary excitations (in our case the spinons which are fractional spin excitations) or a description in terms of elementary triplet ($S = 1$) excitations, which are bosonic modes (corresponding to the known textbook magnons in the case where there is long range magnetic order and a semi classical approach applies)? This question is probably most relevant for the $S = 1/2$ 1D AF chain with only NN interactions because this is the archetype of a gapless critical model whose true elementary excitations are known to be the spinons, and not triplons (elementary triplets) [186]. This question was addressed by the authors of Ref. [45], who perturbatively calculated spectral densities for various operators R connecting the ground state to states with different number of excited triplets according to: $I(\omega) = \sum_f | < f|R|0 > |^2 \delta(\omega_f - \omega_0 - \omega) = -\pi^{-1} Im[< 0|R(\omega + \omega_0 - H)^{-1} R|0 >]$ where H is given by Eq. 5.1 with $J_2 = 0$, $|f >$ and $|0 >$ denote excited and the ground state while ω_f and ω_0 represent their energies. Using a continuous unitary transformation which conserves the number of elementary triplets and appropriate interactions R, they could evaluate separate relative contributions to $I_{tot} = \int_0^\infty d\omega \; I(\omega) = \sum_{n=1}^\infty \; I_n$ from sectors with only one, two and three triplets (the total intensity being calculated using the sum rule $I_{tot} =< 0|R^2|0 > - < 0|R|0 >^2$). The main result was that the sum rule is very well fulfilled by taking into account only the contributions up to (and including) three triplets [45], implying that there is no necessity to resort to fractional excitations. It would be interesting to check if this statement remains true at all energies, an issue which could be addressed probably by evaluating relative contributions to energy and wavevector dependent spectral densities, $I(k, \omega)$.

How does the excitation spectrum evolve with increasing the NNN frustrating parameter $\alpha = J_2/J_1$? It turns out that for $0 \leq \alpha \leq \alpha_c$ the excitation spectrum remains gapless and qualitatively the same as in Fig. 5.9 [187] and the true excitations

are again spinons. However, there is a critical value $\alpha_c \approx 0.24$ above which the low energy spectrum develops a finite spin gap. The spin-spin correlations become short ranged from the power law fall-off characteristic of the uniform unfrustrated chain. For an intuitive picture, the value $\alpha = 0.5$ is very interesting because in this case the ground state is doubly degenerate and it is known exactly to be made of products of NN singlets. In the notation of Eq. 5.1, this means that for this value of α the two degenerate ground states are $|0>_1 = 2^{N/2} \prod_{i=1}^{N} (|\uparrow_{2i-1}> |\downarrow_{2i}> - |\downarrow_{2i-1}> |\uparrow_{2i}>)$ and $|0>_2 = 2^{N/2} \prod_{i=1}^{N-1} (|\uparrow_{2i}> |\downarrow_{2i+1}> - |\downarrow_{2i}> |\uparrow_{2i+1}>)$. The value of $\alpha = 1/2$ for 1D chains is known as the Majumdar-Ghosh point [188]. This is also the moment to advertise the compound discussed in Chapter 6, $SrCu_2(BO_3)_2$, which is the only experimental realization of a two-dimensional structure, well described by a NN and NNN Heisenberg terms, having an exactly known ground state. Similarly to the 1D case, this ground state can be also written in terms of independent nearest neighbor singlet states.

As was also discussed in the previous chapters, in the absence of spin-orbit coupling and because of the spin selection rules, Raman scattering usually couples to double spin flip states *via* the photon induced spin exchange process [7, 9]. The effective spin Hamiltonian corresponding to this interaction in the off-resonance regime is given by:

$$H_{int} \propto \sum_{<i,j>} (\mathbf{e}_{in} \cdot \mathbf{r}_{ij})(\mathbf{e}_{out} \cdot \mathbf{r}_{ij}) \mathbf{S}_i \cdot \mathbf{S}_j \tag{5.2}$$

where $\mathbf{r}_{ij}$ is the vector connecting these sites and $\mathbf{e}_{in}/\mathbf{e}_{out}$ are the unit vectors corresponding to the incoming/outgoing polarizations. Because the light wavevector is very small, the total momentum of the excitations probed has to be zero. From Fig. 5.9 one can infer that the energy range spanned by four spinon excitations with zero total momentum is quite large: from $\omega = 0$ up to $\omega = 2\pi J$. One also expects that the Raman form factor is peaked in the middle of this region, at $\omega = \pi J$, reflecting the divergence in the spinon density of states at this energy. The large energy range corresponding to the multi-spinon continuum along with the well established inelastic light coupling to double spin flip excitations is thus compatible with the existence of

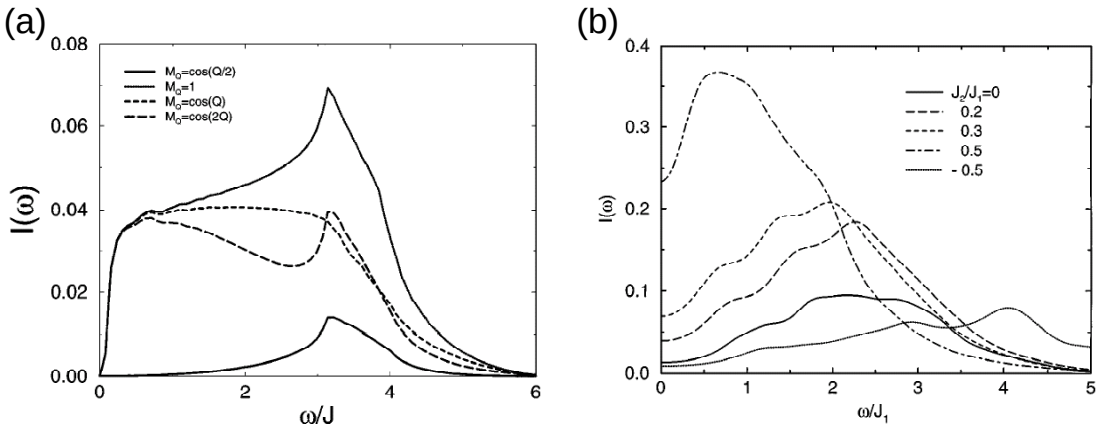

Figure 5.10: (a) Raman intensity for four spinons evaluated with different matrix elements, $M = \cos(Q/2), 1, \cos(Q), \cos(2Q)$, from Ref. [189]. A nearest neighbor (NN) Fleury-Loudon interaction (Eq. 5.2) corresponds to $M = \cos(Q)$ and a next nearest neighbor (NNN) interaction to $M = \cos(2Q)$. (b) Raman intensity for the Heisenberg model (Eq. 5.1) for various ratios of the NNN exchange J_2 with respect to the NN term J_1. Note that an increase of J_2/J_1 results in a downshift of the four spinon continuum spectral weight. The results in this panel are also from Ref. [189].

the broad Raman continuum observed in Figs. 5.5, 5.6 and 5.8.

In fact numerical calculations using the Hamiltonian Eq. 5.1 and an interaction of the form $H_{int} \propto \sum_i \mathbf{S}_i \cdot \mathbf{S}_{i+2}$ revealed that the Raman intensity corresponding to the four spinon excitations corresponds indeed to broad continuum like feature, see Fig. 5.10a and Ref. [189]. Note that this interaction is nothing else but a particular form of Eq. 5.2 for (bb) polarization (polarization along the chain direction) where a NNN term was chosen. It is also important to observe that because of the commutation relations with the system Hamiltonian, the interaction H_{int} could have been as well chosen to be $H_{int} = \sum_i \mathbf{S}_i \cdot \mathbf{S}_{i+1}$, i.e. to describe spin exchange between NN spins, but in this case it would have been necessary to include NNN terms in Eq. 5.1 so that $[H, H_{int}] \neq 0$. While the exact shape of the four-spinon continuum from Fig. 5.10a does not exactly correspond to the experimental findings in NaV_2O_5 (Figs. 5.5 and 5.6) or $CuGeO_3$ (Ref. [185]), it nevertheless proves that the four spinon Raman continuum is an excitation relevant on an energy scale ranging from zero up to energies of about $6J$ (which corresponds to the $0 - 2\pi J$ range inferred from Fig. 5.9). The overestimation of the low energy spectral weight has to do with the choice for the Raman matrix elements. One can compare Fig. 5.10a with results obtained by ex-

act diagonalization and/or mean field approximation for the frustrated spin chain [190, 191]. These calculations reproduce better the experimental findings because the divergence at πJ is replaced by a broader peak and also because they eliminate the preponderant low frequency part.

Discussion of the temperature dependence – Here we intend to show that the temperature dependence from Fig. 5.8a is also consistent with an interpretation of the continuum in terms of multi-spinon excitations. The experimental observation there was related to the softening of the Raman band with cooling from room temperature to about 40 K. An interesting connection can be made between Fig. 5.10b and the discussion about the role of fluctuations and higher order magnetic exchange terms regarding the results in Fig. 5.8a-b. In this respect, note also that, according to Eqs. 5.1 and 5.2, the inclusion of terms beyond the nearest neighbor (either in the system Hamiltonian or in the interaction Hamiltonians) are crucial for observing any inelastic magnetic signal.

Fig. 5.10b shows that there is a substantial overall downshift in the four-spinon spectral weight with increasing the NNN frustrating interaction J_2. When we analyzed the data in Fig. 5.8a-b we brought evidence that the fluctuations of the low temperature order start at high temperatures and also that magnetic susceptibility results cannot be understood if only the NN exchange J_1 is taken into account. In particular, we discussed that the tendency of the charges to arrange themselves in a zig-zag pattern can make the NNN exchange J_2 an important parameter. So the reasoning goes as follows: (1) decreasing the temperature leads to a more and more pronounced charge disproportionation along the left and right legs of the ladder; (2) this may lead on one hand to a decrease of J_1 because the exchange path gets modified (the two electrons on a rectangular plaquette formed by two rungs will like to stay along the diagonal) and on the other hand to a relative increase of J_2 because the NNN Vanadium atoms become connected by a straight, shorter superexchange path; (3) according to Fig. 5.10, both effects in (2) will lead to a softening of the four spinon Raman continuum. While still speculative (in the absence of a quantitative

estimation of the charge imbalance as a function of temperature or of quantitative microscopic calculations of the relative strengths of the magnetic interactions) our point was to provide a possible basis for the understanding of the data in Fig. 5.8.

Discussion of polarization properties – In a strictly 1D system, because any two spin sites can be connected only by vectors $\mathbf{r}_{ij} \parallel \hat{b}$-axis, the Fleury-Loudon polarization selection rules (Eq. 5.2) would not allow coupling in a polarization perpendicular to the chain direction, the (aa) configuration. However, we do observe scattering in this geometry.

Here is the place to reiterate some issues about the symmetry of the high temperature phase. The importance of symmetry resides in the fact that it is the most direct way to establish the spin/charge pattern above T_c. We discussed in the introduction that more recent X-ray scattering as well as NMR data support a centrosymmetric group in the high temperature phase and the existence of only one type of V atoms with an average valence of +4.5. This means that, because the rung hopping $t_\perp$ is the dominant term compared to the inter-ladder hopping t_{xy} or the overlap along the chain direction $t_\parallel$ [168], on each rung there is only one electron which is rapidly hopping from the left to the right side making (averaged over the timescale characteristic of each experimental probe) the two rung vanadium atoms look equivalent. At a quantum mechanical level, one can think about the electronic wavefunction as a superposition of 'instantaneous' states having electrons arranged in different configurations so that when the charge density is averaged over the left and right legs of the ladder one gets (almost) equal fractional charges $q = e/2$.

In spite of the preference of the centrosymmetric group $Pmmn$ [163, 168, 169, 170] over the $P2_1mn$ group [165], this assignment is not entirely unambiguous and the analysis of the X-ray data becomes quite involved because both the crystallographic symmetries render almost identical diffraction patterns [163]. In fact a small, finite charge imbalance between V-O-V ladder legs existent even at room temperature could not be completely excluded. This is fully consistent with the Raman data in Fig. 5.8 which shows that the effects of the fluctuations of the low temperature zig-zag order

can be tracked down at all measured temperatures above $T_c = 34$ K and that this temperature has to do mostly with the inter-ladder phase coherence. This in turn means that locally and on relatively short time scales the charge pattern on each ladder is different from the average distribution seen by X-ray diffraction and that a cartoon for the high temperature phase like the one shown in Fig. 5.3 is only an idealized approximation.

If one agrees with the notion that inside each ladder the charge/spin distribution is not strictly 1D, then the selection rules derived from Eq. 5.2 allow scattering in (aa) polarization. So four spinon continuum should be seen in both (aa) and (bb) geometries, consistent with our experimental observations. This also implies that the temperature dependence of the magnetic Raman band should track the evolution of the zig-zag order in the V-O planes, in particular we should observe an increase of its spectral weight with cooling, a process driven by closer proximity to the low temperature phase. This is one aspect we already noted when discussing the Raman results, i.e. that the softening of the 680 cm^{-1} peak is also accompanied by an increase in the spectral weight on the lower energy side. Once the selection rules allow it, the peak in (aa) can be imagined as being the result of the well known phonon induced spin exchange process: an electron-hole pair is created by an electron dipole interaction involving bonding-antiboding V $3d$ orbitals and O $2p$ bands, see Fig. 5.4; in the intermediate state two pairs of spinons are emitted before the collapse into an excited spin state. Why is the signal in (aa) stronger than in the expected geometry (bb)? This has to do with the fact that the coupling when the electric field is perpendicular to the ladder is different from that along the b-axis and this is especially the case with the Raman vertex in resonance conditions. We showed in Fig. 5.6 that the intensity of the Raman band follows very closely the features seen in absorption, so one cannot talk about off-resonant conditions. In this respect we note that quite different couplings in (aa) with respect to (bb) polarization of fully symmetric excitations are also observed for phonons, see Fig. 5.5. It is known from the case of 2D cuprates that very strong enhancements of the magnetic signal can occur

[53] and they have been observed in resonant Raman spectra [192]. A quantitative understanding of the anisotropy in the (aa) and (bb) intensities would require specific evaluations of the Raman matrix elements, but in principle it is compatible with our observations

A zig-zag pattern also implies finite magnetic scattering in (ab) polarization. In Fig. 5.7d we show that the integrated intensity in this geometry is excitation energy dependent, but the 680 cm^{-1} peak is not observed. In fact this is not surprising, because the spin flip scattering in cross polarization should have a different form factor and it belongs to a different irreducible representation in an orthorhombic group. As a result, it is a priori expected to have a different spectral shape than in parallel polarization. Due to the distinct form factor in different scattering configurations, the Raman intensity integrates from different parts off the Brillouin zone and symmetry properties may lead to the cancellation of the zone boundary divergence in the density of states at πJ. Examples in this regard are again the 2D cuprates where the inclusion of terms beyond the nearest neighbors in the effective light coupling Hamiltonian led automatically to the appearance of magnetic scattering not only in B_{1g}, but also in A_{1g} and B_{2g} symmetry channels [49]. However, the spin pair scattering in each channel comes in with its own resonance and spectral properties.

Evaluation of the magnetic superexchange – The peak position of the four spinon continuum at 680 cm^{-1} (84 meV) (see Fig. 5.5) and the expected maximum in the Raman response at πJ_1 reflecting the divergence in the density of states (see Fig. 5.10a) lead to an estimation for the NN superexchange $J_1 \approx 27$ meV (218 cm-1 or 310 K). Given the spectral weight downshift induced by the presence of the NNN term J_2 (Fig. 5.10b) we can say that this value is a lower bound for the NN superexchange. Our value is in good agreement with the initial determination of J_1 from a fit to the magnetic susceptibility data [156] by the Bonner-Fisher prediction (Ref. [193]) as well as with the estimation from charged bi-magnon continuum observed in the optical conductivity data [176]. The interpretation of the IR absorption data relies, as discussed in the beginning of section 1.2.2, on a global charge asymmetry between

the ladder rungs. Seemingly artificially introduced, this assumption may be regarded retrospectively in a more favorable light in the context of strong fluctuations of the low temperature order. It is also possible that the difficulties in a precise distinction of the symmetry in the high temperature phase can be related to the same phenomenon. As for the magnetic susceptibility data from Ref. [156], it was pointed out in a more recent paper, Ref. [174], that it could not be reproduced quantitatively in subsequent studies. Moreover, the authors of this latter work obtained from an approximate fit (because they argued that the data cannot be quantitatively fit by a simple Bonner-Fisher expression involving only NN Heisenberg interactions) a value for J_1 which is almost twice as high as ours.

A fit to the experimental dispersion of the elementary triplet excitation in the low temperature phase obtained in a INS study, see Ref. [184], allowed the extraction of a value $J_1 \approx 60$ meV, also about a factor of two higher than 27 meV. Regarding this data we note that the maximum neutron energy transfer was 40 meV while the inferred maximum for the triplet dispersion was 93 meV. Accordingly, the value of the energy at the zone boundary, which is of crucial interest to us (see Fig. 5.9), was not determined directly but only by using an approximate fitting function [184]. Neither the authors of the INS work, nor those of Ref. [174] consider the possible influence of NNN exchange terms which we believe play an important role in determining the structure of the magnetic excitation spectrum.

We conclude by saying that our estimation for the lower bound of the superexchange, while not contradicting other analyses, is still too far apart to be explained by error bars. In our view, a quantitative determination of the relevant $J's$ is still an open issue and the underlying reason is in the strongly fluctuating low temperature order and the induced frustration effects. We also believe that the overall consistency between the interpretation of the strong Raman band in the high temperature phase in terms of multi-spinon excitations and our experimental findings strongly argues for its magnetic origin.

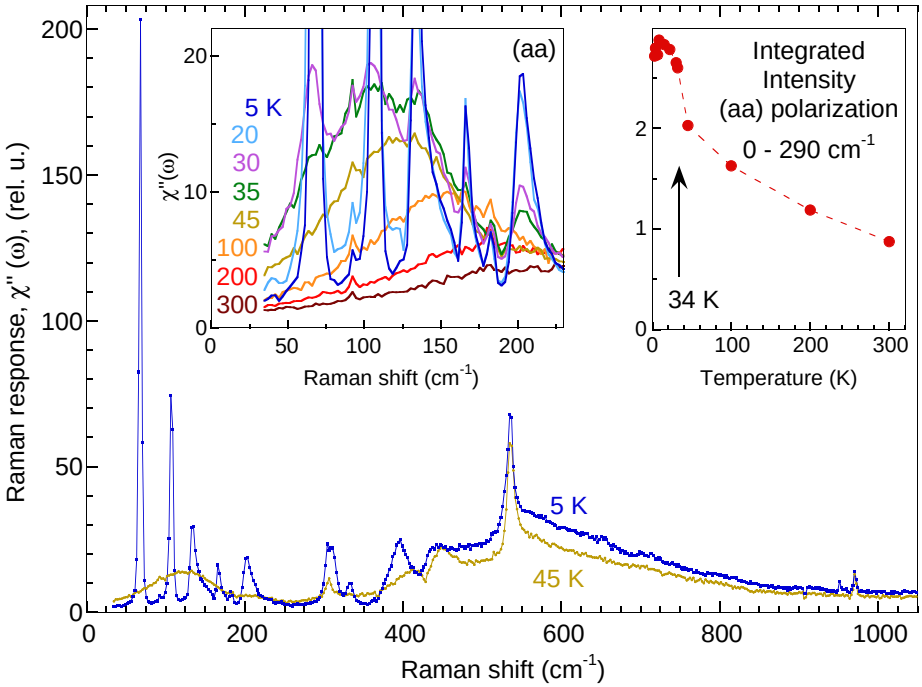

Figure 5.11: The main panel shows the Raman response $\chi''(\omega)$ in (aa) polarization for T = 45 and 5 K. The data is taken using the $\omega_{in} = 1.92$ eV excitation energy. Left inset: Temperature dependence of the (aa) polarized spectra in the 0-250 cm^{-1} region. The data for 45 and 5 K are zoomed in spectra from the main panel. Right inset: Integrated intensity, $\int \chi''(\omega)\, d\omega$, between 0 and 290 cm^{-1} as a function of temperature.

5.3 Collective excitations in the low temperature phase of NaV_2O_5 ($T \leq 34$ K)

5.3.1 General features of the transition

In the main panel of Fig. 5.11 we show two Raman spectra taken at 45 and 5 K in (aa) polarization. One can notice that drastic changes occur across the transition at 34 K especially at low frequencies where many new modes appear. The most prominent three features below 150 cm^{-1} are a very strong mode at 66 cm^{-1}, another one around 105 cm^{-1} and the sharp edge at 134 cm^{-1} ($\approx 2 \cdot 66$ cm^{-1}) marking the onset of a continuum. Other new excitations which are clearly seen in the T =5 K spectrum are found around 166, 202, 308, 332, 393 and 949 cm^{-1}. Besides these modes, other weaker excitations are seen around 122 and 182 cm^{-1}. In Fig. 5.8 we argued that the strong temperature dependence in the low frequency part of the spectra and the

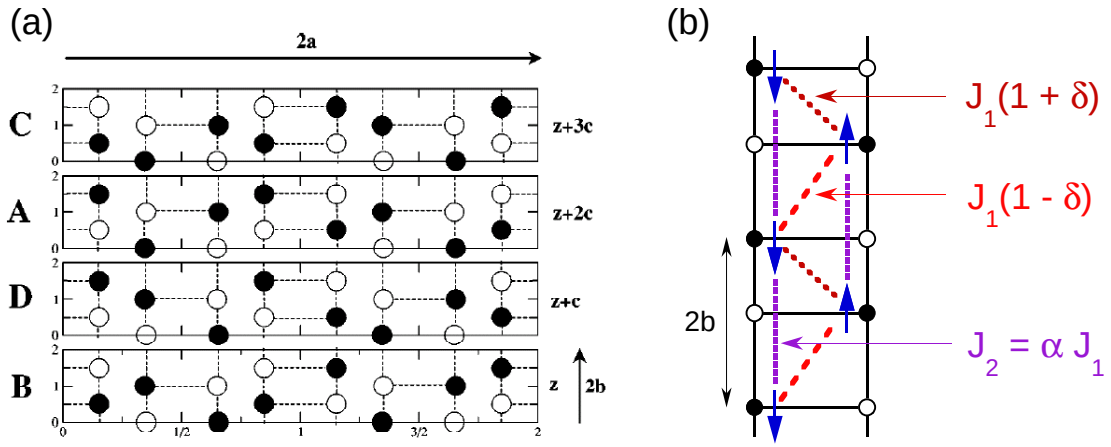

Figure 5.12: (a) Schematic representation of the 3D charge/spin order (from Ref. [166]). Black (open) circles are V^{4+} (V^{5+}) atoms. Each of the four rectangles shown represents a unit cell in the low temperature phase. The sequence *B D A C* represents one of the stacking sequences along the *c*-axis which are consistent with X-ray diffraction data, i.e. it has to the inter-layer phasing of the zig-zag order in each layer. Note the doubling (along *a* and *b* directions) and the quadrupling of the unit cell along the *c*-axis. (b) Cartoon with the zig-zag order and relevant intra-ladder magnetic interactions. The parameter δ characterizes the dimerization of the superexchange due to the unit cell doubling along the ladder legs. Inter-ladder interactions are not shown.

development of the low frequency continuum between 0 and 250 cm^{-1} is a precursor feature signaling fluctuations of the low temperature order at temperatures above T_c. That this is true can be seen in the left inset of Fig. 5.11 which shows that below about 34 K, this broad excitation 'splits' into very sharp resonances. While above T_c the individual ladders do not know about each other at large distances, below 34 K a global phase coherence of the charge and lattice dynamics is established. Also, the drop in the 0-200 cm^{-1} continuum marks the opening of a gap in this energy region. The integrated Raman response in the 0-290 cm^{-1} region, $\int \chi''(\omega)\, d\omega$ shown in the right inset of Fig. 5.11, increases with decreasing T almost all the way down to the lowest measured temperature, their weight relating most probably to the variation of the charge/spin order and lattice distortion in the low temperature phase.

How are these changes to be understood and what are the energy scales below T_c? As for the crystal structure it is known that in the V-O layers there is a doubling of the unit cell along both the *a* and *b* directions [161, 166, 194]. Moreover, in every ladder there is a zig-zag type ordering of the Vanadium valence electrons rendering, crudely speaking, V^{4+} and V^{5+} atoms on each rung of the ladder, see one rectangle

in Fig. 5.12a. Given the $2a \times 2b$ supercell, there are exactly four realizations of this superstructure in each plane, and they are denoted by A, B, C and D. The existence of four such possibilities to accommodate the zig-zag order provided a clue for the understanding of the quadrupling of the lattice constant along the c-direction. Initially an average face centered orthorhombic structure was proposed to explain the X-ray data at low temperatures [194]. The authors proposed a stacking disorder pattern along the c-axis rendering an effective global orthorhombic structure characterized by the face centered space group $Fmm2$. However, this group has two mirror planes parallel to the c-axis which is at odds with the zig-zag order in each plane. The resolution of this problem suggested in Ref [194] was that because X-rays are sensitive only to the average structure, a model lacking mirror symmetry in each plane but having the appropriate stacking disorder along the c axis can be in accordance with the measured diffraction pattern. A later resonant X-ray study argued for a lower (monoclinic) symmetry of the low temperature structure and proposed only two almost degenerate stacking patterns perpendicular to the ladder planes [166]. One of them, the B D A C model is shown in Fig 5.12a. It was proposed that the true crystal structure below T_c involves the existence of stacking faults of different possible patterns. The data was suggested to reflect the presence of competing arrangements along the c direction of nearly degenerate units. This may lead to a rich phase diagram as a function of a parameter which could directly affect the inter-layer interactions. Indeed, X-ray diffraction data under pressure, see Ref. [195], show the development of a series of modulation wavevectors corresponding to an array of commensurate phases in the $P - T$ diagram. The complicated observed sequences were qualitatively understood within the devil's-staircase-type phase transitions driven by two (presently unknown) competing interactions along c.

The above details and the discussion in the previous section give an idea about the difficulty in understanding quantitatively what exactly happens with the structure both above and below the transition. However, what can be surely said about the changes in the in-plane magnetic interactions as a result of the transition? A quali-

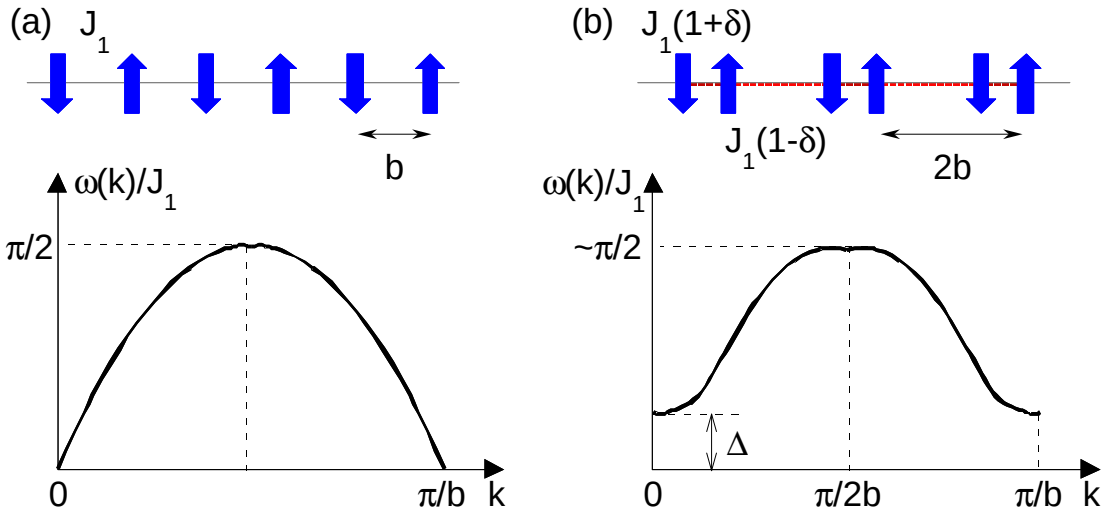

Figure 5.13: (a) Cartoon showing the dispersion of the elementary excitations (spinons) in a uniform $S = 1/2$ AF chain (the same as in Fig. 5.9a). (b) Qualitative changes in the (slightly) dimerized Heisenberg chain. The unit cell along the chain becomes $2b$ and the alternation of superexchange is given the parameter δ (the same as in Fig. 5.12). The elementary excitations are $S = 1$ triplets and a spin gap Δ opens up at the Brillouin zone center. Apart from logarithmic corrections, Δ scales as $\delta^{2/3}$ [196].

tative picture of what happens inside a given ladder can be obtained from Fig. 5.12b. The unit cell doubling along the b direction leads to an alternation in the NN superexchange J_1 which is quantified by the parameter δ. Due to the particular arrangement of charges in the zig-zag pattern, it seems that the NNN term may also play an important role in the spin dynamics. The single ladder hamiltonian can be thus written as:

$$H = J_1 \sum_i [(1 + (-1)^i \delta)\mathbf{S}_i \cdot \mathbf{S}_{i+1} \; + \; \alpha \mathbf{S}_i \cdot \mathbf{S}_{i+2}] \tag{5.3}$$

The charge/spin order coupled to the lattice dimerization in the direction perpendicular to the ladders may lead to a complicated 2D pattern of magnetic exchanges (see for instance the discussion in the caption of Fig. 5.14). However, assuming a relatively weak inter-ladder coupling, which is confirmed experimentally by the small dispersion of the magnetic modes along a-axis, one can assume that the backbone Hamiltonian for the magnetic interactions is given by Eq. 5.3, i.e. a dimerized and frustrated 1D AF $S = 1/2$ chain.

We will discuss later the excitations from dimerized and frustrated chains in more detail. This topic has been the focus of many theoretical studies [196, 197, 198].

Here we are preoccupied only with the main result of the dimerization of the NN exchange, which is shown in Fig. 5.13a-b. If in the uniform case, panel a, the excitation spectrum is gapless (see also Fig. 5.9), any finite dimerization δ will open up a spin gap at the Brillouin zone center. This gap, denoted by Δ, scales as $\Delta \propto \delta^{3/2}$ apart from logarithmic corrections [196, 197]. Given the fact that in the absence of any dimerization a gap can be opened only due to frustration for $\alpha \geq \alpha_c \approx 0.24$, one can see that in the (δ, α) parameter space the spin gap and the magnetic excitation spectrum in general can be quite complicated. Results of calculations for concrete sets of parameters are shown for instance in Fig. 5.17. This figure will be discussed later in connection with the possible observation of Raman active magnetic collective modes in the low temperature phase. As for the short wavelength excitations, we mention that in general, for quite a wide range of parameters δ and α, the energies of the elementary triplet excitations at the zone boundary are not strongly renormalized from $\pi J_1/2$, which is the value corresponding to the uniform NN AF spin chain.

The low temperature phase has been quantitatively explored by various techniques. INS data show that below T_c there are two close-by gapped magnon excitations which have a large dispersion along the b-axis (inferred to be of about 80 meV - 645 cm^{-1}) and the corresponding $k = 0$ values between 8 and 11 meV (see the caption of Fig. 5.14 for a discussion) [184]. The magnitude of the a-axis modulation is much smaller, of the order of only 1 meV, confirming weak inter-ladder interaction. We note that one of the spin gaps found by INS is situated at 8.3 meV (66.9 cm^{-1}), an energy which, within error bars, is equal to the one corresponding to the very strong Raman active mode seen at 65.9 cm^{-1} in Fig. 5.11 below T_c. Note that the double folding of the branch corresponding to the 8.3 meV spin gap (shown in Fig. 5.14b) leads to the appearance of another Brillouin zone center feature with an energy of 10.9 meV (87.9 cm^{-1}). The presence of spin-orbit coupling allows the observation of some of these elementary triplet excitations also in far IR [199] and ESR spectra [200]. A low temperature gap of 8.13 meV (65.5 cm^{-1}) is determined with high resolution by these two techniques.

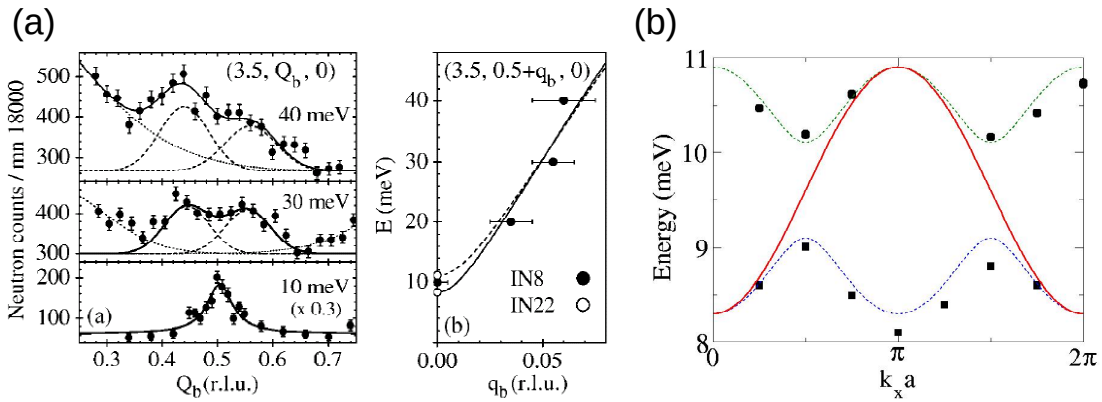

Figure 5.14: Inelastic neutron scattering data from Ref. [184] (a) Left panel: Constant energy scans along the chain direction. The wavevector Q_b is defined in units of $1/b$. Right panel: Energy dispersion of the elementary triplet excitation along the chain direction (b-axis); $q_b = Q_b - 0.5$. The empty and filled circles at $q_b = 0$ in this figure correspond to data taken on two thermal neutron spectrometers, IN8 and IN22. (b) Dispersion along the a-axis for $Q_b = 1$ of the elementary triplet branch showing the folding of this excitation due to the unit cell doubling in the direction perpendicular to the ladders. Consequently, its periodicity is π/a. The red line corresponds to the unfolded branch; note that its periodicity is $2\pi/a$. According to the interpretation in Ref. [184], in the Brillouin zone of the high temperature phase there is a second branch analogous to the one shown by the red line and very close in energy, whose dispersion is phase shifted by $\pi/2$. The reason this branch appears is because the superexchange J_1 are slightly different in adjacent ladders as a result of charge/spin ordering. In the low temperature phase this second branch gets folded too (see Fig. 4 in Ref. [184]), and the data in (a) refers to this particular excitation. In the end, there are four Brillouin zone center modes corresponding to 8.3 (66.9) and 10.9 (87.9) meV (cm^{-1}), from the first branch shown in panel (b) and to 9.1 (73.4) and 10.1 (81.5) eV (cm^{-1}) from the second branch.

We observed so far that the transition at 34 K involves several aspects: (1) crystallographic distortions leading to doubling of the in-plane lattice constants along and across the ladder legs as well as a quadrupling of the unit cell in a direction parallel to the c-axis; (2) in-plane zig-zag charge ordering which has a very complicated pattern in a direction perpendicular to the plane; (3) development of gapped magnetic branches (with spin gaps in the 9 meV energy range) which are much more dispersive along the ladder legs than in the transverse direction. The question is what is the driving force of this transition? Is it a spin-Peierls transition as it was initially thought, is it driven only by Coulomb forces which stabilize the zig-zag ordering, leading also to lattice distortions *via* electron-phonon coupling or does it occur mainly as a result of a structural instability? Note that in the latter two scenarios the opening of a spin gap in the magnetic excitation spectrum is a by-product of the

lattice/charge ordering rather than the main cause of the transition.

The arguments against an ordinary spin-Peierls scenario were mentioned in the introduction and they rely mainly on the absence of magnetic field effects on T_c, the absence of other incommensurate states at high fields and the observation of a large entropy release at the transition which could not be accounted by the spin degrees of freedom alone. Seo and Fukuyama proposed in Ref. [201] a model Hamiltonian containing single d_{xy} V orbitals and taking into account on-rung, ladder leg and inter-ladder hopping parameters $t_\perp$, $t_\parallel$ and t_{xy} (see Fig. 5.3), as well as on site (U) and nearest neighbor Coulomb interactions $V_\perp$, $V_\parallel$ and V_{xy} (these latter notations are in correspondence with the notations used for the hopping parameters). Three stable AF solutions were found within the Hartree approximation and they correspond to: (1) the uniform phase (all V atoms are equivalent, i.e. what is thought to be realized in the high temperature phase); (2) the chain type having V^{4+} atoms on a given ladder leg and V^{5+} ions on the other (which would correspond to the initial room temperature crystal structure determination [165]); (3) the zig-zag type, which is the one shown in Fig. 5.12. It was found that for a large (and relevant) range of parameters, including the ones proposed in Ref. [168], the lowest energy state (above a small critical value of the intersite Coulomb interaction defined as $V = V_\perp = V_\parallel = V_{xy}/\sqrt{2}$) is one having zig-zag order with alternate charge disproportionation on each rung. Depending on the relative magnitude of the hopping parameters it was proposed that the drop in susceptibility below T_c is related to a singlet state formation of essentially localized pairs of spins. The zig-zag order was also found consistent with the observed in-plane unit cell doubling. As a result, the authors suggested that the charge ordering due to Coulomb interaction is the driving force of the transition at 34 K in NaV_2O_5 [201].

Using a similar Hamiltonian except for excluding double occupancy of V d_{xy} orbitals, equivalent to making $U \to \infty$, a subsequent study confirmed the stabilization of the zig-zag pattern [173]. The authors of Ref. [173] also pointed out that this kind of charge ordering along with inter-ladder correlations will automatically lead to an alternation of the exchange integrals along the ladder direction, $J_{i,i+1} = J_1(1 + (-1)^i\delta)$,

where i is a rung index. This alternation will open up a spin gap and lead to an exponential drop of the susceptibility below T_c. Another important point was related to the interaction between charges *via* lattice distortions: the zig-zag structure is also favored by the displacements of the rung O atoms which are pushed by the large V^{4+} ions.

More recent exact diagonalization results, see Ref. [202], also support the prominent role of the Coulomb interactions for the 34 K transition in NaV_2O_5 . The authors highlight the importance of phonons in the stabilization of the zig-zag structure, especially of the alternate c-axis displacements of the V atoms in the low temperature phase, which were seen in X-ray data [170]. It was found that the coupling of the electrons to the lattice can substantially reduce the critical value of the intersite Coulomb repulsion (see the previous paragraph) at which the formation of the charge ordered state occurs.

Interestingly, besides the low energy spin excitations arising as a result of dimerization, the characteristic low energy charge excitations are proposed to be soliton-like modes, similar to some degree to the spinons which are domain walls between degenerate ground state configurations, see Fig. 5.9. In this case, for an individual ladder there are two equivalent zig-zag patterns forming the ground state, the difference between them being a lattice translation with a high temperature lattice constant b. A low energy kink-like excitation will involve local on-rung electron hopping and will smoothly interpolate between the two degenerate configurations, see for instance Fig. 6 in Ref. [202]. One can conclude this section dedicated to the nature of the low temperature phase by saying that both experimental and theoretical works are strongly in favor of a transition driven by Coulomb interactions, with the spin gap formation playing only a secondary role.

5.3.2 Observation of a folded triplet excitation. Selection rules and interpretation

Polarization properties and selection rules in magnetic fields – We discussed in the previous section that INS data reported the existence of Brillouin zone center spin flip excitations around 11 meV. At low temperatures and in (ab) polarization we observe a relatively weak feature around 86 cm^{-1}, see Fig. 5.15. What relatively weak means compared to other features seen in cross and parallel polarizations can be inferred from in Fig. 5.18 where this feature is denoted by T in the lower left panel. In finite external fields this feature has the following properties: it shows no shift for $\mathbf{B}$ parallel to the a-axis but we observe a splitting for the other two orthogonal directions of the external magnetic field. Both the upward and downward dispersing branches change their energies in an approximately linear fashion, with a proportionality factor given by one Bohr magneton μ_B. This shows that we are looking at a $S = 1$ excitation and we identify it with the elementary zone center triplet seen by neutron scattering. Note that in finite fields there is an extra mode around 90 cm^{-1}. This is a fully symmetric phononic feature which appears because in finite magnetic fields, the orthorhombic (or even smaller) crystal symmetry leads to a Farady rotation of the polarization inside the sample preventing the observation of clean selection rules. In fact the finite field spectra were taken after the polarization optics were rotated in order to minimize the intensity of strong features seen in parallel polarization (for instance the 66 cm^{-1} mode from Figs. 5.11 and 5.18).

Fig. 5.15 reveals an interesting behavior of the 86 cm^{-1} mode. Because of the spin selection rules, Raman scattering usually couples to singlet ($S = 0$) excitations. The observed magnetic field dependencies clearly indicate the triplet nature of this mode. This is possible in the presence of spin-orbit coupling which mixes the spin and orbital degrees of freedom, see the Introduction for a more detailed discussion. In what follows we try to identify the coupling mechanism responsible for the experimental observations from Fig. 5.15 as well as the corresponding selection rules.

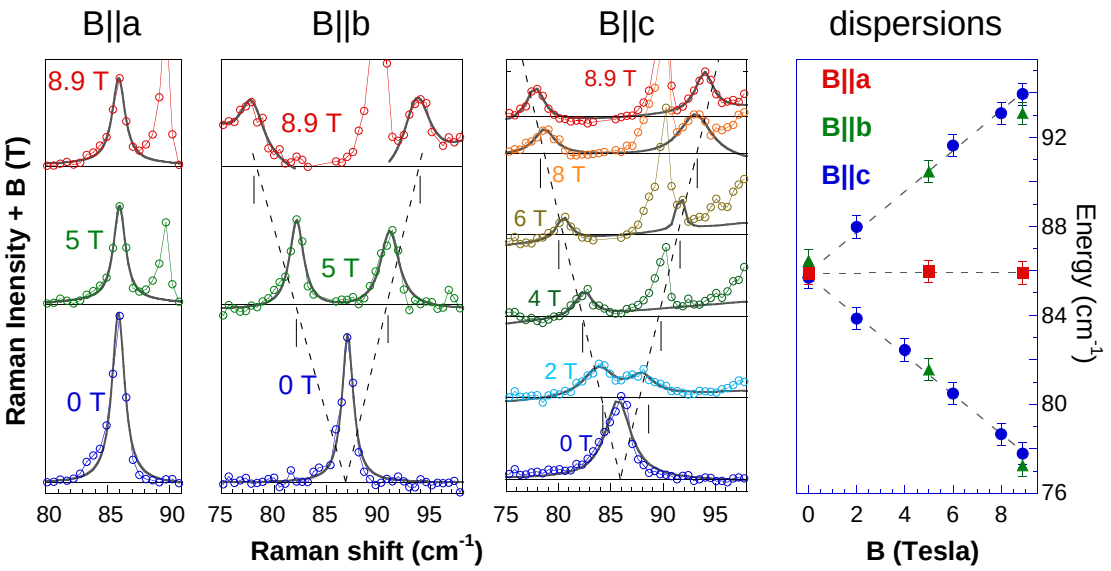

Figure 5.15: From left to right, the first three panels show Raman response at 5 K as a function of magnetic field. Each spectrum is off-set by an amount equal to the value of the field at which is was taken. The colored symbols are data and the thick dark grey lines through the data points are results of Lorentzian fits to the triplet component(s). The feature appearing around 90 cm^{-1} in finite fields is a phonon which exists also in the high temperature phase. Note that the 86 cm^{-1} mode splits for magnetic fields $\mathbf{B} \parallel \hat{b}$ and $\mathbf{B} \parallel \hat{c}$ but it does not shift for $\mathbf{B} \parallel \hat{a}$-axis. Panel (d) shows the dispersion with field of the 86 cm^{-1} mode for the three field configurations (squares for $\mathbf{B} \parallel \hat{a}$; triangles for $\mathbf{B} \parallel \hat{b}$ and circles for $\mathbf{B} \parallel \hat{c}$).

The role of the antisymmetric Dzyaloshinskii-Moriya interaction – It is often possible to capture the effects of certain spin-orbit interactions by writing effective spin Hamiltonians. Such a Hamiltonian was inferred from macroscopic considerations in 1958 by Dzyaloshinskii [118] and two years later by Moriya [119], who derived a similar expression from a microscopic approach which needed superexchange (wavefunction overlap) and spin-orbit coupling as the only ingredients. If one writes down the most general bilinear interaction between two spins at lattice sites i and j in the form $\sum_{\alpha,\beta} S_i^{\alpha} J_{ij}^{\alpha\beta} S_i^{\beta}$ and considers only the antisymmetric part of the $J_{ij}^{\alpha\beta}$ tensor, one obtains the general form of the Dzyaloshinskii-Moriya (DM) interaction:

$$H_{DM} = \sum_{(ij)} \mathbf{D}_{ij} \cdot (\mathbf{S}_i \times \mathbf{S}_j) \tag{5.4}$$

This type of interaction appears usually in crystals with lower symmetry and it is often responsible for the phenomenon of weak ferromagnetism. An example in this sense is the $La_{2-x}Sr_xCuO_4$ system discussed in more detail in Chapter 4.

The importance of the DM interaction was already suggested by ESR experiments which detected a considerable anisotropy of the absorption lines with respect to the magnetic field orientation [200, 180]. The direct observation of singlet-triplet transitions at low temperatures in ESR [200] and low frequency IR absorption spectra [199] also proposed that the DM interaction is the mechanism which allows the coupling of the photon field to single magnon excitations. We note that below $T_c = 34$ K, the local crystal symmetry is low enough to allow the presence of DM type terms between neighboring spins. In a theoretical study, Valenti *et al.* studied Raman scattering in quasi-1D AF spin chains. The authors took into account the spin Hamiltonian of Eq. 5.1 along with the DM term from Eq. 5.4 and a Fleury-Loudon coupling Hamiltonian (see Eq. 5.2) with NN and NNN spin exchange terms [203]. The main conclusion of this paper is that a single magnon excitation probed by Raman scattering has a very clear experimental signature: it should show no splitting in an external magnetic field parallel to $\mathbf{D}$ and it should split in two branches for a field perpendicular to the DM vector.

The authors of Ref. [203] also noted that there is no experimental confirmation of their prediction and so it is up to now to the best of our knowledge. Inspection of Fig. 5.15 shows that what we observe experimentally resembles closely the theoretical predictions if $\mathbf{D} \parallel \hat{a}$. Although the Raman selection rules for accessing the elementary triplet states may look complicated and were derived in Ref. [203] based on a non-trivial cluster-model approach, we believe that some understanding can be gained if we look at the problem from the weakly coupled dimer limit. That is, let us assume that the ladders are magnetically decoupled and in each individual ladder the alternation parameter δ from Eq. 5.3 is very close to unity. In this limit one deals in the zero order approximation with independent antiferromagnetically coupled spin dimers. Let us include an intra-dimer DM interaction of the form given by Eq. 5.4 and diagonalize this two spin problem in the presence of an external magnetic field. The results, exemplified for $J = 20$ and $D = 0.6J$ (which are values not extracted from any experimental data), are shown in Fig. 5.16. This simple exercise is also useful

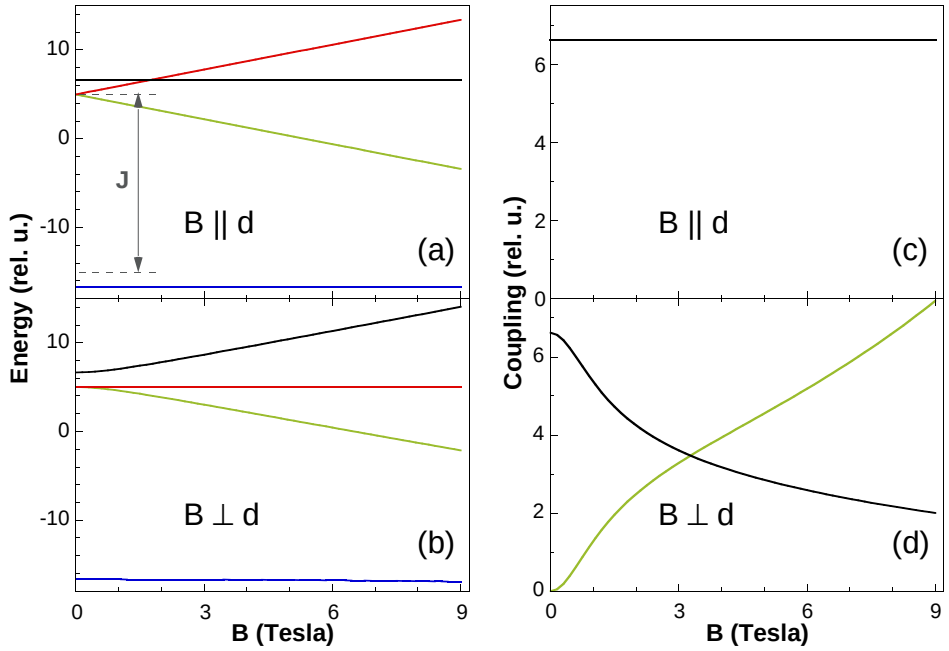

Figure 5.16: Energy levels and light couplings as a function of magnetic field for a system of two spins with Dzyaloshinskii-Moriya interaction. The Hamiltonian reads $J\mathbf{S}_1 \cdot \mathbf{S}_2 + \mathbf{D} \cdot (\mathbf{S}_1 \times \mathbf{S}_2) + g\mu_B \mathbf{B} \cdot (\mathbf{S}_1 + \mathbf{S}_2)$ with $\mathbf{D}$ chosen parallel to the $\hat{z}$ axis. The way the energy levels split for $\mathbf{B} \parallel \mathbf{D}$, panel (a), and for $\mathbf{B} \perp \mathbf{D}$, panel (b), are illustrated for $J = 20$ and $D = 12$. Panels (c) and (d) show the moduli square of the nonvanishing matrix elements of the $\mathbf{S}_1 \cdot \mathbf{S}_2$ operator between the ground state and the three excited states (the same color coding is used as on the left side of the figure).

for the understanding of some of the results in the next chapter, where a slightly more complicated system (four spins instead of two) is used in order to understand the low energy magnetism in the quantum spin system the $SrCu_2(BO_3)_2$ orthoborate. However, in spite of the additional complication, many of the features discussed here are more visible and apply to the orthoborate case.

Panels (a) and (b) show the energy levels as a function of magnetic field for two directions: perpendicular and parallel to the DM vector. In the absence of field and for $\mathbf{D} \equiv 0$ we have a singlet at energy $-3J/4$ and a triple degenerate $S = 1$ excitation at $J/4$. A DM interaction (chosen parallel to the z-axis) in zero field will mix the singlet and the triplet states, in particular the vectors corresponding to zero component of the z projection of the total spin operator $S^z = S_1^z + S_2^z$. As a result the states with $S^z = \pm 1$ will remain at J and the $1/\sqrt{2}(|\uparrow>_1 |\downarrow>_2 \mp |\downarrow>_1 |\uparrow>_2)$ states (corresponding to the singlet ground state and excited $|S = 1, S^z = 0> \equiv |1, 0>$

state respectively) will repel each other. The $|0,0>$ ground state will have an energy $\frac{-3J}{4} + \frac{J}{2}\left(1 - \sqrt{1+\frac{D^2}{J^2}}\right) \approx \frac{-3J}{4} - \frac{D^2}{4J}$ for $D \ll J$ while the $|1,0>$ state will be at $\frac{J}{4} + \frac{J}{2}\left(1 + \sqrt{1+\frac{D^2}{J^2}}\right) \approx \frac{J}{4} + \frac{D^2}{4J}$ for $D \ll J$. If the field is parallel to the DM vector, the $S^z = \pm 1$ states will split with one Bohr magneton per Tesla while the other two states will not change their energies. If the field is perpendicular to the DM vector the mixing of the states will be different and this will lead to a different splitting of the triplet multiplet, see Fig. 5.16b. Although at high fields the dispersion with field is again linear, the derivative of the energy with respect to the field as $B \to 0$ is vanishing in this second case. The curvature of the dispersion at small fields is a measure of the strength of D.

Having in mind that the Fleury-Loudon coupling contains sums of scalar products of spins, see Eq. 5.2, in Fig. 5.16c-d we evaluated the moduli square of the matrix elements of the $\mathbf{S}_1 \cdot \mathbf{S}_2$ operator and in these two panels we show all the non-vanishing terms for both field configurations. In zero field the coupling is finite only for the $|1,0>$ state. If $\mathbf{B} \parallel \hat{z}$ no additional coupling appears and the intensity of the $|0,0> \leftrightarrow |1,0>$ transition is field independent. If $\mathbf{B} \perp \hat{z}$ there will be a finite coupling to the up and down dispersing branches. The crossing points of intensities in panel (d) is also a measure of D. Overall, what these two panels say is that if the magnetic field is parallel to the DM vector one should see only one mode which does not change its energy with field, while if it is perpendicular to it two modes should be seen in finite fields, and both of them should shift with increasing field. The conclusions of this simple model are essentially the same as those of Ref. [203] which says that a local picture in terms of independent dimers is qualitatively appropriate.

According to the experimental results from Fig. 5.15a-d and the theoretical predictions from Ref. [203] our data can be understood as a result of the Raman coupling to one magnon excitations through the DM interaction with $\mathbf{D} \parallel \hat{a}$-axis in the low temperature phase. A quantitative analysis of the intensity dependence is not possible because of the induced changes in the polarization directions inside the sample when magnetic fields are applied (changes that could not be controlled rigorously) as

well as because of the appearance of the 90 cm^{-1} feature which obscured the upward dispersing branch. From the observed linear (within our resolution) magnetic field dependence of the modes energies as well as from the similar spectral weights of the split triplet components at all measured fields in the $\mathbf{B} \parallel \hat{b}$ and/or $\mathbf{B} \parallel \hat{c}$ configurations ($2 \leq B \leq 8.9$) we infer that possible non-linearities in the energy dispersions or strong variations in intensities take place below the value $B = 2$ T. Clearly, the intensity variations predicted in Fig. 5.16d are not seen in the experimental data which shows that the two peaks in panels (b) and (c) have similar intensities. We think that this discrepancy occurs because the actual spin structure is much more complicated than a simple ensemble of uncoupled spin dimers and higher order spin interactions and possibly inter-ladder interactions have to be taken into account.

We clarified the existence of a single magnon excitation at 86 cm^{-1} in Raman scattering spectra. The feature is weak compared to other observed excitations in the Raman data. The question we want to address in the following is whether we observe other magnetic modes, in the singlet channel, besides phononic excitations. This is the topic of the following section.

5.3.3 Do we observe magnetic bound states below the two-particle continuum ?

Excitations out of 1D $S = 1/2$ AF chains with dimerization and frustration – We argued in Section 1.3.1 that the relevant spin Hamiltonian for an individual ladder is given by Eq. 5.3 so a closer look at the magnetic excitation spectrum of a dimerized and frustrated spin chain is useful. We discussed there that any finite dimerization parameter δ and/or values of the frustration parameter α above a critical value will open up a spin gap $\Delta = \Delta(\delta, \alpha)$. Qualitatively, the dispersion of the elementary triplet (one magnon) excitation given by $\epsilon(k)$ looks like in Fig. 5.13b. The two triplet continuum (defined as the range of energies $\omega(k) = \epsilon(k_1) + \epsilon(k_1)$ with the wavevectors satisfying $k = k_1 + k_2$) will have a minimum at $k = 0$ and starts from

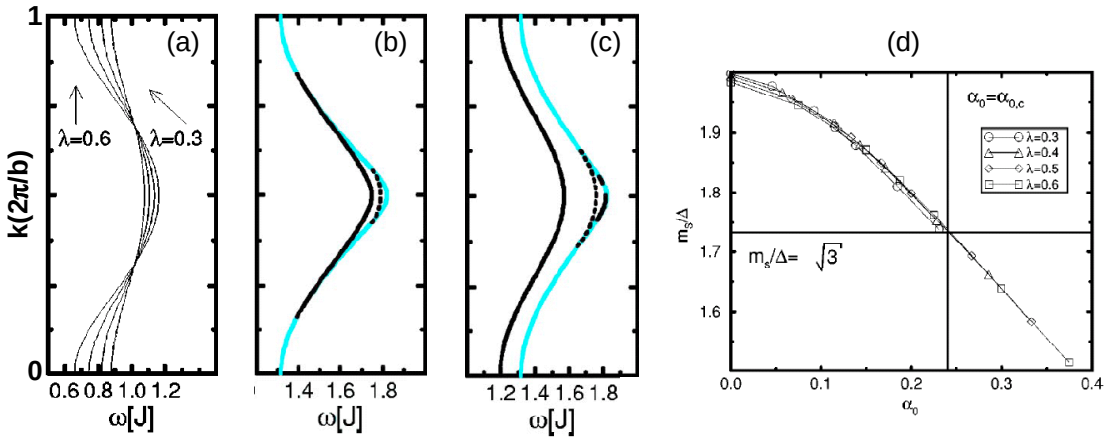

Figure 5.17: Results of perturbative calculations using continuous unitary transformations for the excitations of a 1D AF chain with dimerization and frustration (from Ref. [198]). The results shown here are for the NNN exchange $J_2 = \alpha J_1$ with $\alpha = 0.25(1-\delta)$ and the energies are given in units of $J_1(1+\delta)$. The parameter λ is defined in terms of the dimerization δ as $\lambda = (1-\delta)/(1+\delta)$. (a) Elementary triplet dispersion $\omega(k)$ for $\lambda = \{0.3, 0.4, 0.5, 0.6\}$ which translates into $(\delta, \alpha) = \{(0.54, 0.115); (0.43, 0.143); (0.33, 0.167); (0.25, 0.187)\}$. Panels (b) and (c) show two-triplet bound states (black lines) with total spin $S = 1$ and $S = 0$ respectively calculated for $\lambda = 0.6$ ($\delta = 0.25$). The lower bound of the two particle continuum is shown by the light blue line. (d) The ratio of the singlet ($S = 0$) bound states (at $k = 0$) to the value of the spin gap as a function of α (denoted by the authors of Ref. [198] by α_0) for several dimerization parameters. The vertical line corresponds to the critical frustration where a gap opens in the spin excitation spectrum in the absence of any dimerization (see the discussion related to Fig. 5.9) and the horizontal line denotes $\sqrt{3}$.

an energy $\epsilon = 2\Delta$. It turns out that the Hamiltonian of Eq. 5.3 also allows for the existence of two triplet bound states, which means that at certain wavevectors there are two triplet excitations with energies below the continuum [196, 197, 198].

An example of a perturbational calculation [198] of single and two triplet dispersions for certain points in the (δ, α) parameter space is shown in Fig. 5.17. Note that in these figures the wavevectors are on the vertical scales and the energies are on the horizontal axes. Panel (a) shows elementary triplet excitations for several points in the (δ, α) parameter space. The dispersion is similar to Fig. 5.13b, there is a rapid variation of the zone center values but not much happens at the Brillouin zone center where the energies are not far from $\pi J_1/2$ (note that the unit of energy in this figure is not J_1 but $J_1(1+\delta)$). Results for the two-particle sectors are shown in panels (b) and (c) and one can see the continuum marked by the light blue color. One important thing to note in these two figures is the occurrence of two-triplet bound states whose

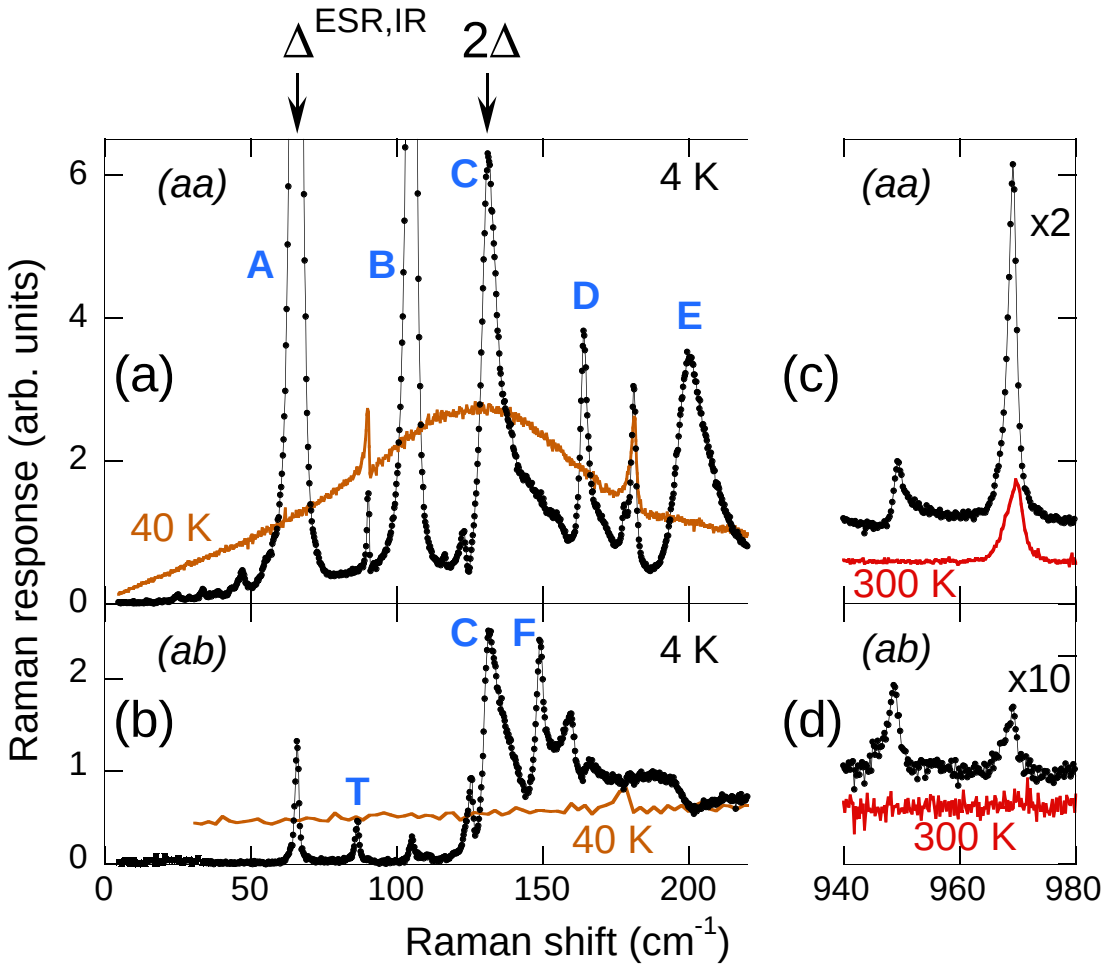

Figure 5.18: Low energy Raman scattering spectra in (aa) (upper panels) and (ab) (lower panels) polarizations at 4, 40 and 300 K measured using the $\omega_{in} = 1.92$ eV excitation. Below about 34 K many new resonances appear in the 0-200 cm^{-1} region. The arrows at the top correspond to the energies of the elementary triplet excitation determined by high resolution IR [199] and ESR [200] studies and twice that value. The 968 cm^{-1} phonon in parallel and cross polarization is shown on the right. Panel (d) shows that below T$_c$ a folded counterpart appears which is seen in both (aa) and (ab) polarizations indicating a lower crystal symmetry.

dispersions are shown by black (solid, dashed or dash-dotted lines) lines. Panel (b) shows the results for states in which two triplets are bound into a $S = 1$ state while panel (c) shows the same thing but for triplets bound in a state having a total spin $S = 0$. For each case there are more than one bound states, the difference for the numerical parameters shown being that the binding energies of the triplet bound states are finite only at finite values of k while for the singlet channel there is a branch split from the continuum in the whole Brillouin zone.

Fig. 5.17d shows the ratio of the energy of lowest singlet bound state at the

Brillouin zone center $m_{S=0}$, with respect to the value of the elementary triplet gap Δ. The vertical line corresponds to the critical value of α at which a frustration induced gap opens up in the absence of any dimerization δ. At α_c, the above ratio is $m_{S=0}/\Delta = \sqrt{3}$ (the horizontal line refers to this value) and its value decreases with increasing frustration. Note that at $\alpha = 0$, $m_{S=0}/\Delta \approx 2$, and this is true irrespective of the chosen values for δ which means that it is the frustration which leads to finite binding energies of the singlet bound states. One interesting point which is not shown in panel (d): there exists a singular point, the Majumdar-Ghosh point given by $(\delta, \alpha) \equiv (0, 0.5)$ (see the discussion of Fig. 5.9), where $m_{S=0}/\Delta$ equals unity. At this point the single magnon and the two-magnon bound state are degenerate, which is a remarkable property of the Hamiltonian of Eq. 5.3 [196].

Experimental observations and discussion – How is this discussion related to our experimental findings in NaV_2O_5 ? In Fig. 5.18 we show several Raman spectra with the purpose of emphasizing the new excitations which appear below the phase transition. We discuss first an aspect related to the crystal symmetry in the low temperature phase and illustrated in panels (c) and (d) of this figure. We show there four Raman spectra, two in (aa) polarization at 300 and 4 K, Fig. 5.18c, and two in (ab) polarization at the same two temperatures, Fig. 5.18d. In the high temperature phase the V-O_{rung} stretching mode [177, 179] is present at 969 cm^{-1} in parallel polarizations, but not in (ab) geometry and, therefore it is a fully symmetric excitation of the $Pmmn$ space group. Below T_c this mode acquires a second component, seen at 948 cm^{-1}, due to the in-plane unit cell doubling, i.e. we assign it to a folded phononic branch. More importantly, both the 968 and 949 cm^{-1} excitations are seen not only in (aa) but also in (ab) polarization. The simultaneous presence of these modes in both the diagonal and off-diagonal components of the Raman tensor indicates that in the low temperature phase the double reflection symmetry of the $Fmm2$ group is broken. Our data confirm the resonant X-ray data [166] which argues for a lower (monoclinic) symmetry below T_c.

We comment now on the spectra shown in Fig. 5.18a-b. In panel (a) we show the

emergence of new (aa) polarized collective modes in the low temperature phase and several of them are indexed by letters: A (56.9cm^{-1}), B (105.0 cm^{-1}), C (131.2 cm^{-1}), D (164.0 cm^{-1}) and E (200.4 cm^{-1}). In panel (b) we similarly marked the modes T (86.5cm^{-1}) and F (149.0cm^{-1}) seen in the (ab) polarized spectra. This list of modes does not exhaust all of the new excitations appearing in the low temperature phase but highlights a few of them which are of importance for the following discussion. What is the origin of these new modes? Are they phonons, are they magnetic or are they some collective topological charge excitations of the type described in Ref. [202]. While not excluding the latter option, it seems that the observation of purely charge modes is less probable because it involves higher energies of the order intersite Coulomb interactions which are of the order of eV's [173, 202]. Moreover, the characteristic energy scales of these excitations (0-25 meV) can be better related either to magnetic excitations seen in ESR, far IR or INS experiments (see Fig. 5.14) or (in the context of existing lattice instabilities which drive the 34 K transition) to the folding of low energy zone boundary phonons in the high temperature phase. Accordingly, we will focus here on the possibility of observing phonons or single/multi-triplet magnetic excitations [196, 204].

We discuss here the spin excitations scenario. This picture draws its appeal primarily from the fact that the Hamiltonian of Eq. 5.3, which seems to be a good description for the staggered spin configuration in the low temperature phase, allows for a multitude of magnetic bound states, both in the singlet and triplet channels, see Fig. 5.17. First, we note that some of the new resonances observed below the transition are definitely magnetic. In Fig. 5.15 we showed that the 86.5 cm^{-1} excitation, denoted by T in Fig. 5.18, is a $S = 1$ magnon. The singularity seen at 131.2 cm^{-1} (16.27 meV) in Fig. 5.18a-b situated at twice the energy of the spin gap value of 65.5 cm^{-1} (8.13 meV) and the continuum present from above this frequency as opposed to the clean gap seen for $\omega \leq 130$ cm^{-1} (except for a few resonances) leaves little doubt that the mode C marks the onset of the two-triplet continuum of excitations. How about the most prominent excitations denoted by A and B in

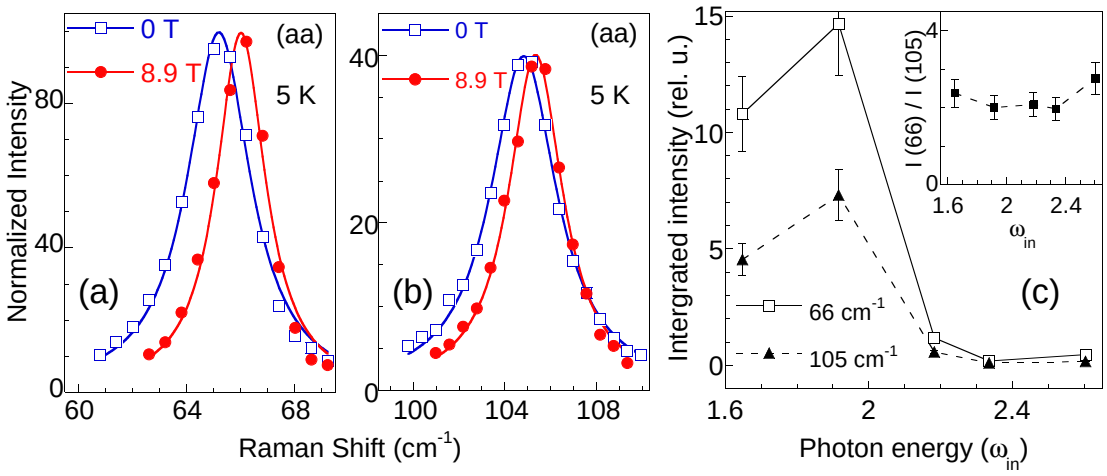

Figure 5.19: Panels (a) and (b) display the T = 5 K Raman spectra showing the magnetic field (in)dependence of the 66 and 105 cm^{-1} resonances which appear below the transition. In both cases a shift of about 0.9-1 cm^{-1} was observed as the magnetic field was varied from 0 to 8.9 T. (c) Integrated intensity of the 66 (empty squares) and 105 cm^{-1} (filled triangles) modes at 5 K as a function of the incoming photon energies ω_{in}. The inset of this panel shows that the ratio of the integrated intensities of these two modes depend only slightly on ω_{in} (as opposed to the data shown in Fig. 5.6, the data in the main panel were not corrected for the optical properties of the material; however these effects cancel out in the ratio because these modes are very close in energy).

Fig. 5.18a? The similar resonance profile of these two excitations shown in Fig. 5.19 indicates that they have a common origin. It is interesting to remark that the energy of mode A coincides with the energy of the spin gap determined with high resolution in ESR and IR absorption data [199, 200]. Can this excitation be the $k = 0$ elementary triplet? Panels (a) and (b) in Fig. 5.19 show that neither mode A nor mode B splits or shifts by more than 1 cm^{-1} in applied magnetic fields up to 8.9 T (and we checked that this is true for any direction of the applied magnetic field). Moreover, if these excitations were $S = 1$ triplets and the same spin-orbit interaction would insure the coupling to them as for mode T, one could not explain that the spectral weight of mode A is more than two orders of magnitude higher than that of mode T.

The arguments above seem to exclude the possibility that modes A and B are triplet excitations but the possibility that they are bound states in the singlet sector still needs to be explored. The ratio $\omega_B/\Delta = 1.59$ appears to qualify mode B for a singlet bound state according to Fig. 5.17d. How about mode A, can it be also a singlet bound state? As discussed previously, a singlet bound state degenerate

with the spin gap is only realized for a singular combination of parameters, $(\delta, \alpha) \equiv (0, 0.5)$. It deserves further argumentation why this set of values is realized in the low temperature phase of NaV_2O_5. However, assuming that this is the case, one could assign mode B to the folded counterpart of mode A. In this scenario one could also argue that the magnetic frustration may be the driving force of the transition at 34 K in the following way [204]. The tendency for zig-zag ordering increases the value of the NNN frustrating interaction J_2. At 34 K, $\alpha = J_2/J_1$ reaches the critical value α_c (see the caption of Fig. 5.17) and a gap opens in the magnetic excitation spectrum. Further cooling will push α close to 0.5 and the singlet bound state gets very close (practically degenerate) to the spin gap. Going into more details of this pictures some of the other excitations can be understood as combination modes or continuum edges. For instance, based on energy considerations, one can say that F = A + B, H = B + B or that mode F in Fig. 5.18b is the A + T continuum edge.

However, the fact that the physics of the Majumdar-Ghosh point is realized for a singular combination of parameters makes this appealing scenario less probable. The variety of selections rules which have been experimentally observed in Raman, ESR and IR data still needs to be explained. The second possibility is to assign the main new features appearing below T_c in the 0-200 cm^{-1} energy range to folded phonons. In fact, this scenario is supported by the small but finite shift observed in Fig. 5.19a-b. This is what one expects in a simple two level system: one phonon, one close by magnon along with some off-diagonal matrix elements because of a non-vanishing spin-phonon interaction. As expected, the shift of the 65.9 cm^{-1} mode (of about 0.8 cm^{-1}) is slightly higher than the shift of the 105 cm^{-1} mode (of abut 0.5 cm^{-1}) which is further apart in energy from the spin gap value. Based on lattice dynamical calculations and the relative temperature dependence of the spin gap seen in ESR data [200] and that of the energies of measured IR active modes, a more recent study also argues for the phononic nature of modes A and B [183].

We conclude this section by saying that many features of the transition at 34 K in NaV_2O_5 are still under debate and more than just a clarification is needed re-

garding the nature of the observed excitations or the effects of the electron-phonon interactions.

5.4 Summary

In this chapter we studied electronic excitations in NaV_2O_5 by Raman scattering and the transition taking place at $T_c = 34$ K. From the description of the crystal structure and the discussion of the electronic properties as seen by various techniques we showed that NaV_2O_5 can be thought of as an array of quasi one-dimensional (1D) two-leg ladders at quarter filling factor. Two models were proposed to capture the essential physics of the magnetic degrees of freedom: one for the high temperature phase (Heisenberg chains with nearest and next nearest antiferromagnetic interactions, see Eq. 5.1), and another model for the low temperature phase (Heisenberg chains with dimerization and frustration, see Eq. 5.3).

Three main topics were discussed. The first was related to a broad continuum of excitations found in the 200-1500 cm^{-1} range and peaked around 680 cm^{-1} in parallel polarizations. In literature a magnetic origin of this feature was ruled out and a scenario involving crystal field excitations was proposed instead. The resonant Raman profile of this excitation, the polarization selection rules and the presence of its overtone in resonance conditions allowed us to conclude that the origin of this feature is magnetic. More precisely, we proposed that it arises as a result of light coupling to multi-spinon Raman excitations. Within this scenario we also argued for a scenario explaining the puzzling temperature dependence of the magnetic continuum in terms of an increasing role of next nearest neighbor frustration and in the context of a strongly fluctuating low temperature phase.

The second topic was related to the observation of a folded $S = 1$ magnetic mode which displayed very clear selection rules as a function of the magnetic field orientation, see Fig. 5.15. We proposed that the coupling of the photon field to this excitation takes place *via* the antisymmetric, Dzyaloshinskii-Moriya (DM), interac-

tion which, in a simple dimer model, can also explain the observed selection rules: no splitting or shifts for magnetic fields parallel to the DM vector and the observation of two (upward and downward) dispersing branches for fields perpendicular to the DM vector.

Finally, we discussed the nature of several new resonances seen below T_c and focussed on the possibilities that they are either folded phonons or singlet bound states of two triplet excitations. In particular we emphasized the existence of two modes at 66 and 105 cm^{-1}, the first one being degenerate with one of the spin gap modes. In the spin excitations scenario we proposed a model in which frustration has a determinant role. However, in order to accommodate theoretical results with the observed energies, a very particular set of parameters characterizing the dimerized and frustrated spin chains (the Majumdar-Ghosh point) had to be invoked. The above argument and the small energy shifts in magnetic fields up to 9 T suggested that the strong mode degenerate with the elementary triplet as well as the 105 cm^{-1} mode are phonons. The conclusion of our study is that many features of the spin/charge and lattice dynamics in NaV_2O_5 are still to be understood.

Chapter 6

Collective magnetic excitations in $SrCu_2(BO_3)_2$

6.1 Introduction: Why $SrCu_2(BO_3)_2$?

Several properties make $SrCu_2(BO_3)_2$ a unique and one of the most interesting quantum magnets [205]. This compound is a 2D spin system with a disordered ground state even at very low temperatures and a spin gap of about 24 cm^{-1} (3 meV) in the magnetic excitation spectrum [205, 206]. It has been established that the elementary excitations in this system, which consist of a transition from the singlet (S = 0) ground state to the lowest energy triplet (S = 1) state, are local, weakly dispersive in the reciprocal space while many-'particle' magnetic states are more mobile, i.e. show more dispersion. The strengths of the relevant magnetic interactions place this compound close to a quantum critical point (QCP) separating the gapped phase from a gapless state having long range magnetic AF order. Moreover data in high magnetic fields show plateaus at commensurate (1/8, 1/4 and 1/3) values of the saturation magnetization [206, 207, 208]. The plateau states can be thought of as crystalline arrangements of magnetic moments separating regions of continuous rise in magnetization, these latter regions allowing for an interpretation in terms of Bose-Einstein condensation of triplet excitations [209]. It has also been suggested [210] that doping

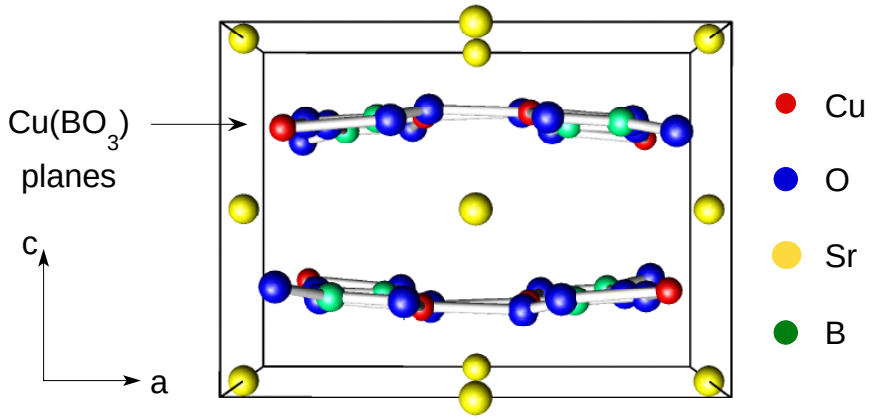

Figure 6.1: 3D view of the $SrCu_2(BO_3)_2$ crystal showing the layered structure along the c-axis. Above 395 K the $Cu(BO_3)$ planes are flat, mirror symmetry elements.

in this system (regarded as a Mott-Hubbard insulator) may lead to a superconducting phase mediated by antiferromagnetic (AF) fluctuations, a mechanism similar in spirit to one of the scenarios proposed for the high T_c cuprates [211].

The first synthetization of $SrCu_2(BO_3)_2$ was achieved in 1991 by Smith and collaborators [212] but the authors did not ellaborate on the magnetic properties. This compound was rediscovered in 1999 by Kageyama *et al.* [206], who also pointed out the outstanding magnetic properties and the importance of $SrCu_2(BO_3)_2$ in the physics of low dimensional quantum magnets. The crystal belongs to the tetragonal symmetry and it has a layered structure in which $Cu(BO_3)$ units are separated by closed shell Sr^{2+} atoms, see Fig. 1. At T = 395 K the system undergoes a 2^{nd} order phase transition from the space group $I4/mcm$ to $I\bar{4}2m$ on cooling from high temperature. In the $I4/mcm$ phase the planes containing the Cu atoms are flat and they form mirror symmetry elements. Below 395 K the transition can be intuitively understood as the buckling of the Cu planes which lose their mirror symmetry.

The magnetic properties of $SrCu_2(BO_3)_2$ are determined by the $S = 1/2$ spins sitting on the Cu^{2+} sites. The crystal structure imposes a distribution of the magnetic moments in weakly coupled 2D layers which define the (ab) planes. In each of these sheets the spins form orthogonal dimer lattices and the c-axis is perpendicular to them. The in-plane magnetic interactions can be described in an effective spin model by taking into account the magnetic exchange between nearest neighbor Cu spins

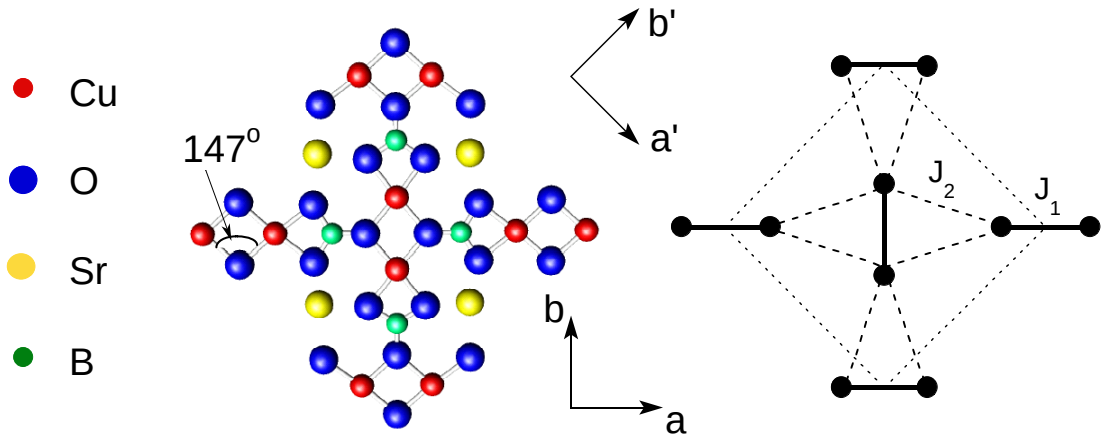

Figure 6.2: Left: The (ab) planes and crystal axes notation. Right: The effective magnetic lattice with the unit cell of the dimer structure being shown by the short dashed square. The circles are the $S = 1/2$ Cu spins, the solid and long dashed lines represent the intra-dimer (J_1) and inter-dimer (J_2) AF superexchange interactions. Below 395 K [213] the vertical and horizontal dimers become slightly non-coplanar, see Fig. 6.1

bridged O atoms forming a 147° Cu-O-Cu bond which points toward an AF coupling denoted by J_1, see Fig 6.2. Besides this interaction one can consider the next nearest neighbor super-exchange taking place *via* the BO_3 complexes. Curie-Weiss type fits of the high temperature magnetization data suggets that this coupling, denoted by J_2, is also AF. Indeed, as we will discuss later, these two terms seem to capture many aspects regarding the magnetic properties of $SrCu_2(BO_3)_2$. The addition of a weak inter layer exchange J' to the above two terms constitute the starting point for treating the 3D spin dynamics in this compound.

The schematic of the magnetic lattice is shown in Fig. 6.2 where the nearest neighbor AF bonds are represented by a solid line while the next nearest neighbor interaction is shown by dashed lines. Note an important property of this lattice: ignoring the solid bonds (the J_1 interactions), the topology of the spin structure, determined by the J_2 bonds, is equivalent to that of a 2D square lattice. The corresponding Hamiltomian for one $Cu(BO_3)$ plane reads:

$$\hat{H} = J_1 \sum_{(i,j)\ NN} \mathbf{S}_i \cdot \mathbf{S}_j + J_2 \sum_{[i,j]\ NNN} \mathbf{S}_i \cdot \mathbf{S}_j \qquad (6.1)$$

Here i and j are nearest neighbor (NN) or next nearest neighbor (NNN) Cu sites.

Why is a Raman study of this compound interesting? Several magnetic properties, features of the exitation spectrum or the occurences of the magnetization plateaus, can be explained by taking into account the J_1 and J_2 interactions. As will be discussed in the review of the main theoretical results, this compound is believed to be characterized by a ratio $x = J_2/J_1$ close to 0.7, which is the value around which the system ground state changes. One reason to study this compound is that an accurate determination of this ratio is still missing and this is important due to the proximity to the QCP. In this regard the recent observation of a mode below the spin gap brings into question the quantitative determination of the AF exchange parameters of the system since the existence of such excitation has not been predicted by theory. Another reason is brought about by a different set of questions related to the way the external radiation field couples to magnetic excitations. Magnetic modes in the triplet sector have been probed spectroscopically, besides inelastic neutron scattering (INS) [206, 220], also by electron spin resonance (ESR) [221, 222] and infrared (IR) [223, 225] absorption experiments. The nature of the mixing interactions originating in spin-orbit coupling which usually allows transitions from the singlet ($S = 0$) to excited ($S = 1$) states is still to be understood. Our approach, which is a study of collective magnetic excitations in terms of symmetry, resonance and coupling mechanisms in external magnetic fields, is illuminating in this respect.

This chapter will be focussed on the low temperature properties of $SrCu_2(BO_3)_2$. The discussion of the low temperature phononic excitations as seen in Raman spectra in the next part will be followed by a review of experimentally found magnetic properties with an emphasis on spectroscopic techniques. Then we will present a description of the basic properties emerging from the Hamiltonian 6.1 which describes a Shastry-Sutherland lattice and the structure of the magnetic excitation spectrum. The effects of other interactions, in particular of the antisymmetric Dzyaloshinskii-Moriya (DM) terms, will be described. Then we will present our low temperature Raman data and discuss our results in reference to the open questions mentioned above.

6.2 Low temperature phononic spectra in $SrCu_2(BO_3)_2$

The analysis of the low temperature lattice dynamics is important for several reasons. In general this is because there are many examples of low dimensional crystaline compounds which undergo transitions to phases in which the appearance of a spin gap in the magnetic excitation spectrum is accompanied by real space lattice symmetry breaking due to spin-phonon coupling. The lowering of the crystal symmetry may involve newly allowed phononic modes which could be checked directly in the Raman spectra. In the particular case of $SrCu_2(BO_3)_2$ spin-lattice interaction has been suggested to be relevant to the magnetic dynamics at low temperatures and/or high magnetic fields. In order to explain the selection rules of the transitions seen in IR absorption, spin-phonon induced antisymmetric DM spin interactions have been invoked [225]. It has been argued that this coupling will induce virtual phonon transitions which will instantaneously lower the crystal symmetry, allowing for non fully-symmetric effective singlet triplet mixing terms. On the other hand the spin-lattice coupling was taken into account in order to be able to describe the spin density profile at high fields in the magnetization plateaus states. NMR data brought evidence for the broken translational symmetry at the 1/8 plateau by the existence of at least 11 inequivalent Cu sites [208]. The role of the phonons coupled adiabatically to the spin degrees of freedom in this case is to lift the degeneracy of the ground state, picking a state with a certain magnetization texture and allowing the ground state magnetization to be a defined quantity.

So far the study of phononic excitations has been especially focussed in relation to the structural phase transition at T = 395 K [213, 214]. The lattice soft mode of the 2^{nd} order transition from the $I4/mcm$ to the $I\bar{4}2m$ group can be seen in Fig 6.3. The phonon which condenses belongs to the B_{1u} representation of the higher symmetry group and, in terms of Cu atoms, it involves mainly an alternate displacement along the c-axis of the nearest neighbor dimers, see Fig 6.1.

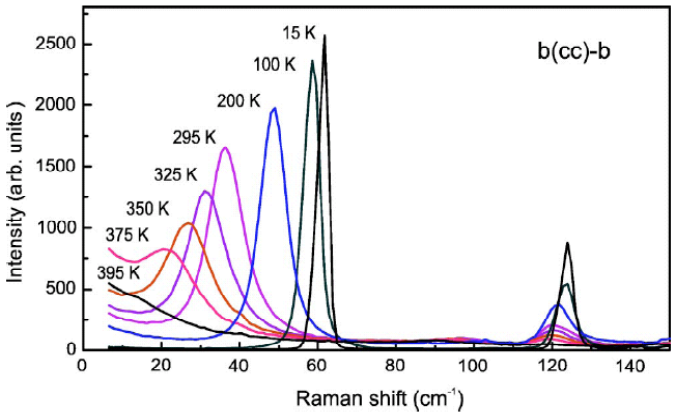

Figure 6.3: The fully symmetric soft mode below the $I4/mcm$ - $I\bar{4}2m$ transition from Ref. [214] seen in *cc* polarization. Note the strong two-phonon excitation around 120 cm^{-1}.

A symmetry analysis of the phononic excitations in $SrCu_2(BO_3)_2$ is done in the following. The unit cell contains 4 formula units and a total of 44 atoms. The number of $k = 0$ modes is given by $3 \times 44/2 = 66$, the factor of 2 coming from the fact that the unit cell is body centered. In this case, the symmetry lowering at 395 K does not change the numer of atoms in the unit cell. The associated point group of the $I4/mcm$ space group is D_{4h} while D_{2d} corresponds to $I\bar{4}2m$. The analysis is based on the tables in Ref. [226] and uses the site symmetry approach. Oxygen atoms mediating the intra-dimer superexchange (O1) and the Oxygens allowing for

Table 6.1: Symmetry of the phononic excitations of $SrCu_2(BO_3)_2$ in the high ($I4/mcm$, point group D_{4h}) and low ($I\bar{4}2m$, point group D_{2d}) temperature phases. The first column contains the atom types and the rest of the columns correspond to irreducible representations of the point groups.

	$I4/mcm$										$I\bar{4}2m$				
At.	A_{1g}	A_{2g}	B_{1g}	B_{2g}	E_g	A_{1u}	A_{2u}	B_{1u}	B_{2u}	E_u	A_1	A_2	B_1	B_2	E
Cu	1	1	1	1	1	-	1	1	-	2	2	1	1	2	3
O1	1	1	1	1	1	-	1	1	-	2	2	1	1	2	3
O2	2	2	2	2	2	1	1	1	1	4	3	3	2	2	6
B	1	1	1	1	1	-	1	1	-	2	2	1	1	2	3
Sr	-	1	-	-	1	-	1	-	-	1	-	1	-	2	2

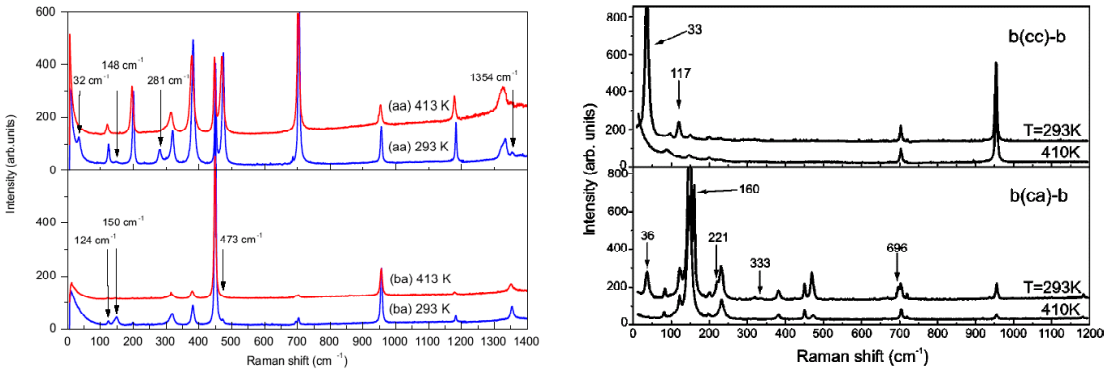

Figure 6.4: Phononic data from Ref. [213] (left) and Ref. [214] (right) showing in plane and out of plane polarized spectra above and below the structural transition. Newly allowed Raman phonons are marked by arrows.

the inter-dimer superexchange (O2) occupy a different symmetry positions. In the high temperature phase the Cu, O1 and B atoms have C'_{2v}, O2 atoms have C_s and Sr atoms occupy D_4 site symmetries respectively. Table 6.1 summarizes the number of modes corresponding to each atom both above and below the transition. The part of the table related to the $I\bar{4}2m$ group can be easily inferred from the analysis of the high temperature phase. One has to drop the 'u' and 'g' indices (corresponding to odd and even modes) because the inversion symmetry is lost and by using compatiblity tables which show that the representations $A_{1u}, A_{2u}, B_{1u}, B_{2u}$ of the D_{4h} point group become B_1, B_2, A_1, A_2 representations (in this order) in D_{2d}. Both the E_u and E_g representations remain double degenerate.

Inversion symmetry breaking results in the fact that certain phonons, which were dipole active, become Raman allowed. The appearance of several new modes below 395 K is shown in Fig. 6.4 where data from Refs. [213, 214] is reproduced. Notable are the shoulders appearing around 160 and 220 cm^{-1} below 395 K in *ca* polarization (which probes double degenerate modes with E symmetries) suggesting either an almost degeneracy of E_u and E_g modes in the high temperature phase or, even more interestingly, the possibility that the symmetry of the low temperature phase is lower than what has been inferred so far and accordingly, the modes corresponding to higher dimensional representations become non-degenerate. [213, 214] is reproduced.

We show in Fig. 6.5 our low temperature Raman data taken with in plane polar-

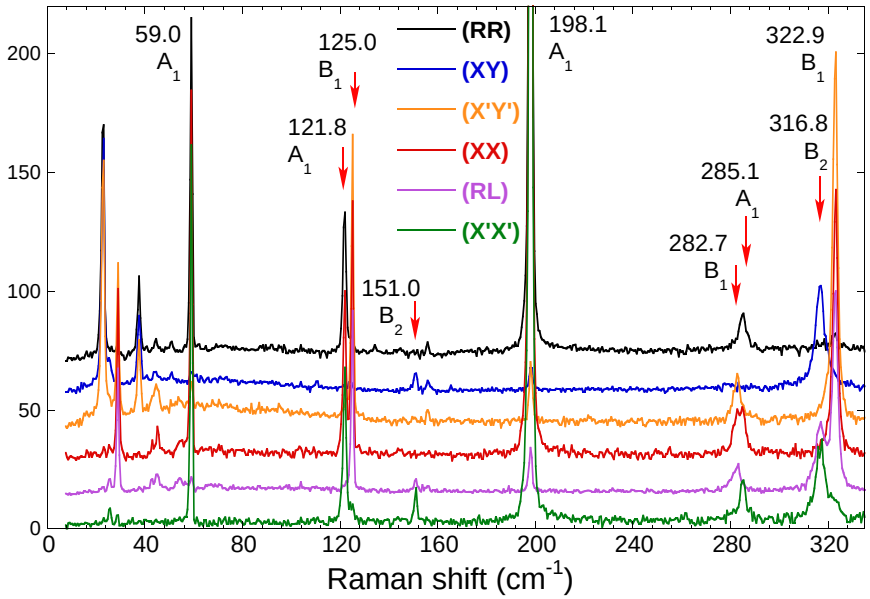

Figure 6.5: Raman data at T $\approx$ 3 K in six polarizations taken with the 1.92 eV laser excitation energy. The energy and symmetry of the modes above 60 cm^{-1} are shown in the figure.

izations and using $\omega_L = 1.92$ eV laser excitation energy. In the D_{2d} group the (RR), (RL), (aa), (ab), $(a'a')$ and $(a'b')$ probe $A_1 + A_2$, $B_1 + B_2$, $A_1 + B_1$, $A_2 + B_2$, $A_1 + B_2$ and $A_2 + B_1$ symmetries respectively. The modes below 60 cm^{-1} are not indexed since they are magnetic and will be discussed in the next section. The modes are sharp and they are sitting at this low temperature on a flat background with almost vanishing intensity. The 60 cm^{-1} mode corresponds to the soft mode of the structural transition. At 121.8 cm^{-1} we observe in the A_1 channel the two phonon excitation seen also in (cc) polarization, Fig. 6.3, and very close to it another sharp mode with B_1 symmetry. We observe, similarly to the spectra shown in Fig. 6.4b, several pairs of modes having very similar energies. For example doublet structures are observed around 284 cm^{-1} where we see a pair of A_1 and B_1 excitations and also two modes having B_1 and B_2 symmetries are found around 320 cm^{-1}.

One way to explain this behavior is to follow up the suggestion in Ref. [214] and assume that in the high temperature phase there are phonons which are odd and even with respect to inversion but very close in energy and to try to identify them by looking at similar atomic vibrations corresponding to 'u' and 'g' representations

respectively. The (A_1,B_1) group around 284 cm^{-1} in Fig. 6.5 would correspond in this scenario either to a group of (A_{1g},A_{1u}) or (B_{1g},B_{1u}) in the high temperature phase since A_{1u} representation becomes B_1 and B_{1u} representation becomes A_1 at low temperatures. Similar reasoning would suggest for the (B_1,B_2) group around 320 cm^{-1} that it originates either from a pair of (B_{1g},A_{2u}) or (B_{2g},A_{1u}) modes above 395 K. We perfomed a symmetry analysis of the $k = 0$ atomic vibrations. The conclusion is that this approach does not provide an a priori reason for the quasi-degeneracy and one has to perform a quntitative normal mode energy calculation by using appropriate inter-atomic elastic constants. There is a simple way to see why this is true. Looking at the character table of the D_{4h} group it can be noticed that the gerade modes are symmetric with respect to the mirror simmetry in the Cu(BO_3) planes while the ungerade modes are antisymmetric with respect to this symmetry operation.

This means that the 'u' phonons in the high temperature phase correspond to vibrations of the atoms along the c-axis while the 'g' modes consist of in-plane movements. Due to the different oscillation pattern it is hard to explain the closeness of phononic energies at this qualitative level. We note that one can easily find vibrations corresponding to different group representations which involve similar oscillations at the 'molecular' level (for instance groups of atoms forming the Cu-O spin dimer structure or pairs O2 atoms between nearest neighbor dimers) and having a certain inter-molecular phase pattern, but they do not correspond to the experimentally observed symmetries. We suggest that, remaining within the conclusions of X-ray studies which have not found evidence for additional crystallographic changes at low temperatures, good candidates for understanding this intriguing behavior are provided by the inter-dimer BO_3 molecular complexes whose rotations as a whole around the a' and c-axes or whose in and out of the plane translations may turn out to be similar in energy.

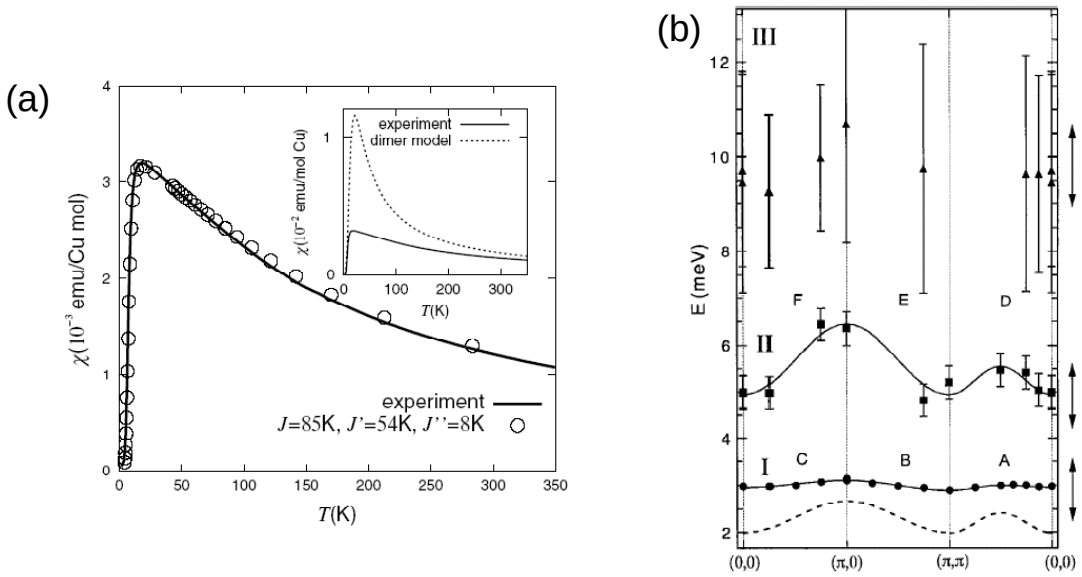

Figure 6.6: Temperature dependence of the magnetization (a) and inelastic neutron scattering results as a function of in plane wavevectors at low temperatures in $SrCu_2(BO_3)_2$ (b) from Ref. [206]. The solid line in (a) shows the result of a fit from numerical calculation using $x = J_2/J_1 = 0.635$, $J_1 = 59$ cm^{-1} (7.32 meV) and also an interlayer coupling $J_3 = 5.5$ cm^{-1}. The interactions J_1 and J_2 alone provide a good description of the low temperature data, including specific heat, but a finite J_3 was necessary to explain the high temperature behavior of the magnetization where a Weiss temperature θ = -92.5 K was obtained from the fit between 160 and 400 K [206].

6.3 Magnetic properties of $SrCu_2(BO_3)_2$

6.3.1 Experimental and theoretical reviews

Experimental review – In this part we discuss data which relate to the most interesting properties and set the relevant energy scales of $SrCu_2(BO_3)_2$. Magnetization and INS data provided for the first time evidence for the existence of a gapped phase in this compound [206]. Fig. 6.6a shows that there is a drop in χ below about 15 K suggesting a gapped phase. Another important thing pointed in the inset of this figure is the strong suppression of the magnetization peak around 20 K compared to the prediction of a simple dimer model which points towards the importance of other magnetic interactions. Neutron scattering, Fig. 6.6, probed the excitations out of this phase and confirmed the existence of a gap of about 3 meV (24 cm^{-1}) and found additional excitations around 5 and 9 meV. Notable is the flat dispersion (less than 6%)

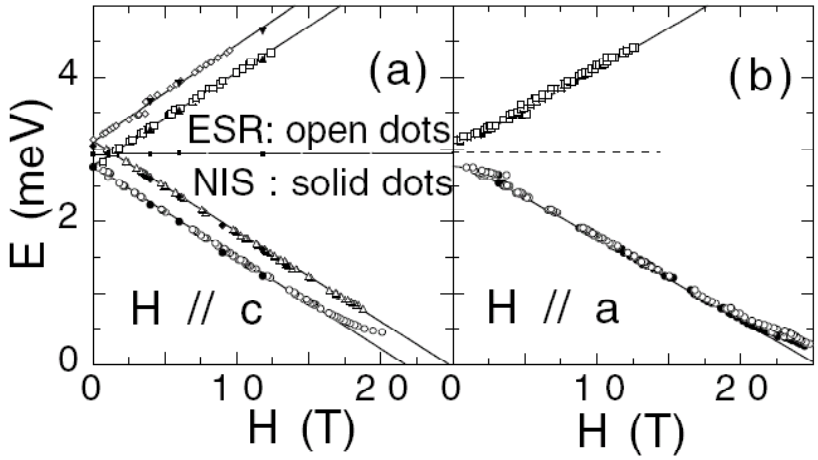

Figure 6.7: Netron (Ref. [220]) and ESR (Ref. [221]) data at low temperatures as a function of magnetic fields parallel (a) and perpendicular (b) to the c-axis.

of the gap branch seen at 3 meV as a function of in-plane wavevectors meaning that the lowest excitations are very local. The dispersion of the higher energy branches is more pronounced suggesting more mobile excitations in the multi-triplet channels. The inability of the dimer model to describe the experimental data suggests that inter-dimer interactions are important and points towards a very interesting physics of frustration in this system.

Besides INS and magnetization, ESR and IR data in magnetic fields confirmed the magnetic nature of these excitations. These experiments, along with high resolution INS data display a rich internal structure of the magnetic excitations and various selection rules for in and out of the plane applied magnetic fields, see Fig. 6.7. In particular, the gap multiplet is shown to be made of 6 branches, which is expected since the unit cell contains 4 spins and therefore exciting a triplet on each of them while the other one is in a singlet state will give a total of 6 excitations. Out of these 6 modes, 4 are seen to be symmetrically disposed around the gap value $\Delta = 24.2$ cm^{-1}. The observed splitting suggests that besides the superexchange interactions there are other low energy scale interactions which have to be taken in to account.

Theoretical review – This section discusses the salient properties of the magnetic structure of $SrCu_2(BO_3)_2$ and the excitations of the Hamitonian 6.1. Among them, the ground state properties, the localization of the elemetary triplets leading to

the dispersionless magnon branches from Fig. 6.6b, the existence of strongly bound two-triplet states as well as the presence of additional spin orbit couplings generating the fine structure seen in Fig. 6.7.

In the approximation given by Eq. 6.1 the wavefunction given by the direct product of singlet dimers is always an eigenstate of the system and it can also be shown that it is the ground state for a continuous set of parameters $x = J_2/J_1$. For the proof of the eigenstate one has to take into account only the second term in 6.1 since the dimer product is obviously an eigenstate of the AF coupled independent dimers. The application of the $J_2(\mathbf{S}_1 \cdot \mathbf{S}_3 + \mathbf{S}_2 \cdot \mathbf{S}_3)$ on the $|s_{12} > \otimes |s_{34} >$ vanishes because the operator $(\mathbf{S}_1 + \mathbf{S}_2)$ applied to the singlet state $|s_{12} >$ vanishes. This is essentially due to the different parity of the singlet and triplet states with respect to the $1 \leftrightarrow 2$ exchange and the fact that on the orthogonal dimer lattice the Hamiltonian conserves the parity. This remains true even if the interalyer coupling is considered [205].

For $x \leq 0.5$ one can show that the singlet dimer product, $|\psi >$, is indeed the ground state. The Hamiltonian 6.1 can be written as $\hat{H} = \sum_i^{N_t} \hat{h}_i$ where N_t is the number of triangles of the type formed by the spins 1, 2 and 3 in Fig. 6.8 and $\hat{h}_i = (J_1/2)(\mathbf{S}_1 \cdot \mathbf{S}_2) + J_2(\mathbf{S}_1 \cdot \mathbf{S}_3 + \mathbf{S}_2 \cdot \mathbf{S}_3)$. The ground state of each $\hat{h}_i$ is $e_g^i = -3/8 J_1$ if $x \leq 0.5$. Accordingly, denoting the true ground state of $\hat{H}$ by $|\phi >$, one has $E_g = < \phi|\hat{H}|\phi > = \sum_i^{N_t} < \phi|\hat{h}_i|\phi > \geq -3/8 J_1 N_t$ because $|\phi >$ is a variational function for $\hat{h}_i$. Considered as a variational wavefunction for $\hat{H}$ and taking into account that the action of the second term in Eq. 6.1 on $|\psi >$ is identically zero, one obtains immediately that $< \psi|\hat{H}|\psi >= -3/4\ J_1 N_d = -3/8\ J_1 N_t$ because the number of dimers, N_d, is half of that of the triangles. On account of the variational principle, the true ground state energy satisfies $E_g \leq -3/8 J_1 N_t$. From the two inequalities one obtains that $E_g = -3/8 J_1 N_t$ and so the product of singlet dimers is indeed the ground state. The underlying reason for these beautiful properties is the fact that the magnetic lattice of $SrCu_2(BO_3)_2$ is a realization of a 2D Shastry-Sutherland model which up to now has been dicussed only at a theoretical level.

Turning to the question of the flat dispersion of the excitations in the one-triplet

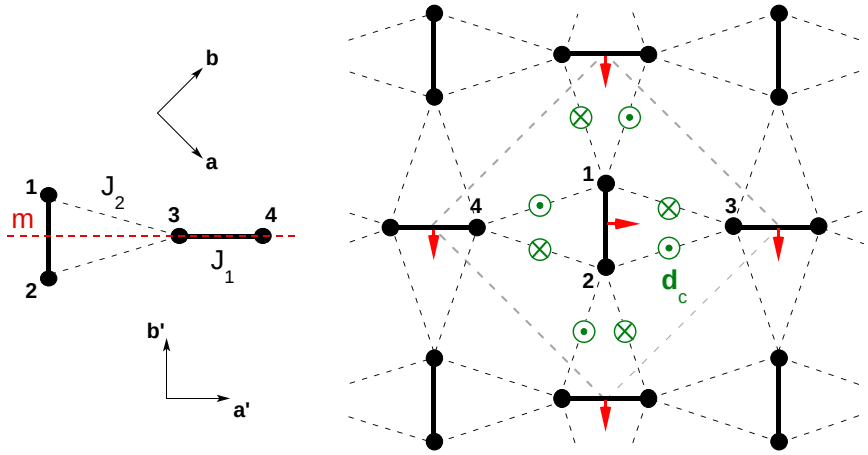

Figure 6.8: Left: Cartoon with two nearest neighbor dimers discussed in the text related to the exact ground state and hopping of triplet excitations. m denotes a mirror plane; the singlet and triplet states on the $1-2$ dimer will have different symmetries with respect to this reflection operator. Right: The unit cell of the magnetic lattice from Fig. 6.2 with the inter-dimer Dzyaloshinskii-Moriya term suggested in Ref [220] which is parallel to the c-axis. The arrows perpendicular to each dimer correspond to our proposed antisymmetric intra-dimer interaction leading to singlet-triplet mixing.

sector one can consider in Fig. 6.8 the case of two nearest neighbor orthogonal dimers having an excited triplet state on the vertical bond and a singlet on the horizontal one. The propagation of the triplet on the horizontal bond by the NNN term in Eq. 6.1 is only possible if a triplet is left behind on the vertical dimer. This is due to the reflection symmetry of singlet and triplet excitations with respect to a mirror plane parallel to the horizontal bond, Fig. 6.8a and the fact that the Hamiltonian of the system must be a fully symmetric operator. If a triplet is left behind, then the hopping of one triplet to a neighboring dimer is very restricted and is possible only by virtually forming closed paths of triplets, the smallest of these paths involving three adjacent dimers. As a result, one triplet hopping appears only in the 6^{th} order of perturabation theory showing that these excitations are very localized in real space and explaining the flat k dispersion seen in Fig. 6.6. The motion of two triplets is different however. It has been shown [215] that in this case correlated hopping processes can occur and it was found that two-particle hopping appears in 2^{nd} order perturbation theory. This explains the larger dispersion seen by INS for the excitations around 5 meV.

We saw that the products of dimer singlets is the ground state of $\hat{H}$ at least

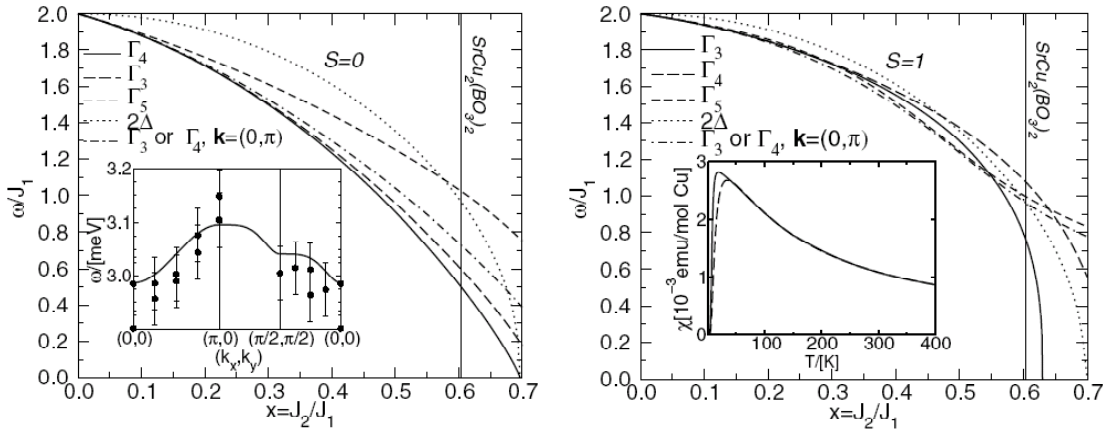

Figure 6.9: Predictions for the two-triplet bound states in the singlet (left) and triplet (right) of a perturbative analysis of the Shastry-Sutherland Hamiltonian of Eq. 6.1 from Ref. [215]. Γ_1, Γ_2, Γ_3, Γ_4 and Γ_5 correspond to A_1, B_1, B_2, A_2 and E in the notation of Table 6.1.

for $x \leq 0.5$. What is the value of x above which this is no longer true? That there should be a finite value is obvious from the fact that in the limit $x \to \infty$ the lattice is topologically equivalent to a 2D square lattice which has long range order at T = 0 K and a spin-wave approximation is more appropriate. Theoretical work [205, 215, 216, 218] shows that below a ratio $x = J_2/J_1 \approx 0.7$ the ground state remains the same and the system has a finite spin gap, Δ to the lowest excited $S = 1$ state. The spin gap is equal to J_1 for $x = 0$ but with increasing this ratio Δ gets renormalized down due to many body effects, see Fig. 6.9. At high values of x the system has long range order, other possible intervening states separated by QCP's have been proposed to exist around $x = 0.7$. The gap renormalization as a function of x is shown in Fig. 6.9. As shown here and also in the parameters used to fit magnetization data in Fig. 6.6, $SrCu_2(BO_3)_2$ is closed to a QCP having a gap renormalized significantly, to a bit more than 50% of the 'bare' value given by $J_1 \approx 85$ K (59 cm^{-1} or 7.3 meV), see Ref. [205].

Another characteristic of this magnetic lattice seen in Fig. 6.9 is the exsistence of bound states in the two-triple sectors, see Fig. 6.9. These are states which have an energy below the inset of the two-magnon continuum starting at 2Δ. Many of these have been predicted along with their symmetries. The vertical line in Fig. 6.9 showing the position of $SrCu_2(BO_3)_2$ in the phase diagram was inferred from the

experimentally found values of the spin gap $\Delta = 24$ cm^{-1} (3 meV) and the observation by Raman scattering of a strong and sharp resonance (attributed to collective $S = 0$ two-triplet bound state) around 30 cm^{-1} [224]. We will discuss such excitations in the next section devoted to the analysis of low temperature Raman data in $SrCu_2(BO_3)_2$.

Before that, another observation in connection to the experimental results shown in Fig. 6.7: there it is seen that the 6 branches of the gap multiplet around 24 cm^{-1} are split in three pairs of doublets. Cépas and collaborators proposed that this is due to the existence of inter-dimer DM interactions which have a direction parallel to the c-axis, see Fig. 6.8. The proposed Hamiltonian (for the spins in the unit cell) reads:

$$\hat{h}_c = \vec{d}_c^{\,13}(\mathbf{S}_1 \times \mathbf{S}_3) + \vec{d}_c^{\,14}(\mathbf{S}_1 \times \mathbf{S}_4) + \vec{d}_c^{\,23}(\mathbf{S}_2 \times \mathbf{S}_3) + \vec{d}_c^{\,24}(\mathbf{S}_2 \times \mathbf{S}_4) \tag{6.2}$$

The DM vectors satisfy $\vec{d}_c^{\,13} = \vec{d}_c^{\,24} = -\vec{d}_c^{\,14} = -\vec{d}_c^{\,23}$ due to the crystal symmetry, in particular due to the existence of mirror planes orthogonal to the dimers as shown in Fig. 6.8 and the existence of C_2 rotation axes parallel to the c-axis and passing through the middle of the dimers. It was found that this interaction reproduces the behavior in magnetic fields perpendicular and parallel to the (ab) plane, which is shown by solid lines in Fig. 6.7. The energy of the upper and lower pairs is given by $\Delta \pm d_c$ and they remain degenerate, see also Fig 6.11c where we show symmetry analysis results. Importantly, the inter-dimer DM interactions parallel to the c-axis are allowed both above and below the structural phase transition at 395 K. Other DM terms, for instance the red arrows in Fig. 6.8, the are not allowed above T_c because the $Cu(BO_3)$ plane is a mirror symmetry element.

6.3.2 Magnetic Raman scattering results in $SrCu_2(BO_3)_2$

Here are some experimental details related to our data discussed in the following. The spectra were taken from the (ab) single crystal surface in a backscattering geometry. We used an incident power of about 0.6 mW focussed on a 100 μ diamter spot. The crystallographic axes orientation was determined by X-ray diffraction. The data in magnetic fields, taken at a sample temperature of about 3 K, were acquired having the

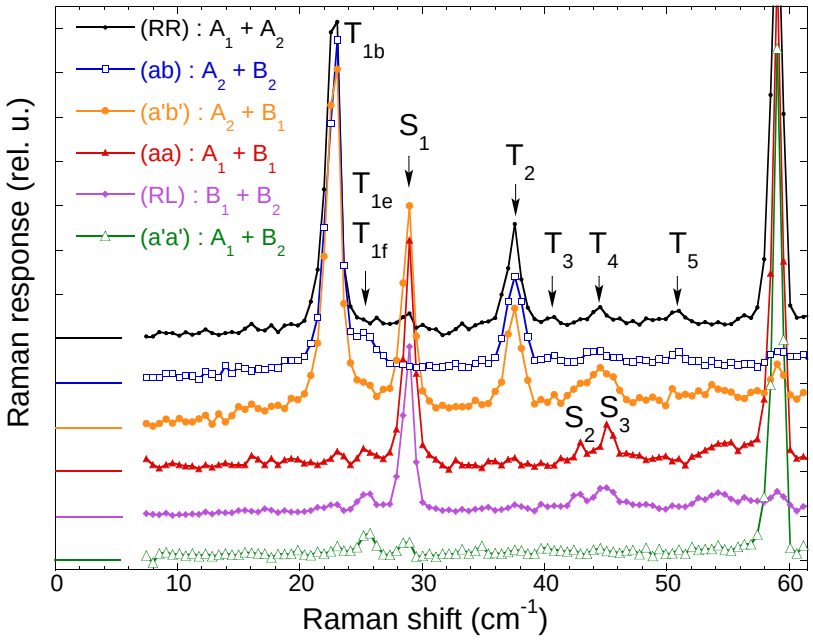

Figure 6.10: Zero field Raman data in $SrCu_2(BO_3)_2$ tken with $\omega_L = 1.92$ eV excitation energy at T = 3 K in six polarizations. The legend shows the tetragonal symmetries probed in each scattering geometry.

continuous flow cryostat inserted in the horizontal bore of a superconducting magnet. We used the $\omega_L = 1.92$ and 2.6 eV excitation energies of a Kr^+ laser and a triple-grating spectrometer for the analysis of the scattered light. The data were corrected for the spectral response of the spectrometer and detector. Polarization configurations are denoted by $(\mathbf{e}_{in}\mathbf{e}_{out})$ where these two vectors are along the polarization direction of the incoming and outgoing photons. Circular polarizations are deonoted by (RR) and (RL) where $\mathbf{e}_{in,out} = (\hat{a} \pm i\hat{b})/\sqrt{2}$.

In Fig. 6.10 we show six low temperature Raman spectra in zero applied field and using a laser frequency $\omega_L = 1.92$ eV. The symmetries probed by each polarization in the tetragonal group are shown in the legend. The mode seen at 60 cm^{-1} is the soft mode of the structural transition, also seen in Fig. 6.3, which belongs as expected to the fully symmtric representation. Three strong features are seen in the spectra at 23, 29 and 38 cm^{-1} and they are denoted by T_{1b}, S_1 and T_2. These excitations belong to the A_2, B_1 and A_2 representations respectively. Besides these three modes, we observe several other weaker excitations. Among them we see a set of three A_2 symmetric modes denoted by T_3, T_4 and T_5. One can also observe the presence of

other very weak feature at 25.5 cm^{-1} in all polarization configurations except (RR). This suggest that at this frequency there are two quasi-degenerate excitations and that they belog to the B_1 and B_2 representations which would justify their observations in five out of six scattering geometries. The symmetry analysis discussed later confirms indeed the above assumption. The modes are denoted by T_{1e} and T_{1f}. A summary of the zero field energies and their experimentaly observed symmetries can be found in Table 6.2. The energy at which we observe these modes, the comparison with the INS, ESR and IR data, part of which are shown in Figs. 6.6 and 6.7 as well as our data in magnetic fields confirm the magnetic origin of these modes and the predominant $S = 1$ character of the 'T' modes. The T_{1b}, T_{1e} and T_{1f} excitations modes seem thus to belong to the spin gap multiplet while T_2, T_3, T_4 and T_5 would correspond to multi-particle $S = 1$ channels.

The zone center elementary excitations are generated by the spins within the magnetic unit cell. If the picture of real space localized elementary triplets is true, then one expects that the analysis of the 4-spin cluster forming the unit cell is able to predict correctly the experimentally observed symmetries of these excitations. Accordingly we calculated the energies and symmetries of the excitations generated by the magnetic cluster shown in Fig. 6.11a and the Hamiltonian of Eq. 6.1. The total number of states, 16, consist of two singlet, $S = 0$, states, three triplet, $S = 1$, states and one quintuplet, $S = 2$ state. The energies are shown in Fig. 6.11a as a function of $x = J_2/J_1$ and one can observe their linear variation with the this ratio. The points at $x = 0$ and $x = 1$ can be easily undestood. The first one corresponds to two independent AF coupled by J_1 on the bonds $1 \leftrightarrow 2$ and $3 \leftrightarrow 4$ so the energies will be just the sum of those corresponding to singlet and/or triplet states sitting on each dimer separately. For the second point one can see that $[\hat{H}, \mathbf{S}_{tot}] = 0$ so the energies will be, up to a constant factor, equal to the total spin eigenvalues $S(S+1)$ (in units of $\hbar^2$). Starting with four $S = 1/2$ spins one can have for the total spin the values $S = 0, 1$ and 2.

The cluster in Fig. 6.11a belongs to the D_{2d} group which is, as it should be,

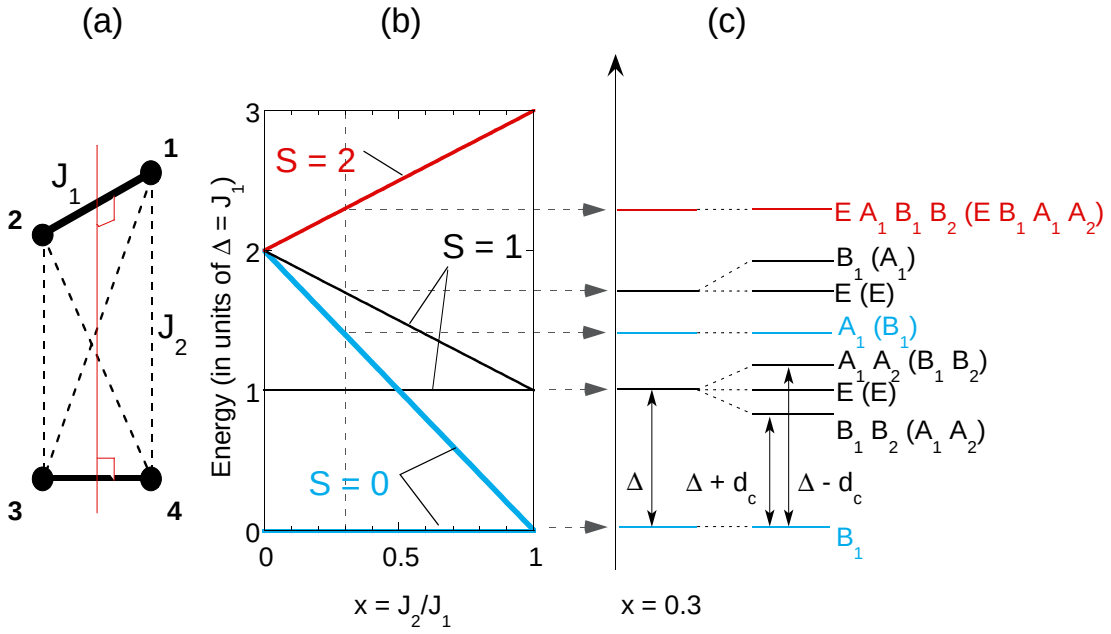

Figure 6.11: (a) The cluster used for the symmetry analysis of the $k = 0$ modes generated by the four spins in the unit cell of Fig. 6.8. (b) The eigenvalues of the Hamiltonian corresponding to the 4-spin cluster in (a) taking into account the J_1 and J_2 terms as a function of the ratio $x = J_2/J_1$. (c) Results of the symmetry analysis for this cluster in the D_{2d} group. The energy levels correspond to a value $x = 0.3$. On the right we show the energy splittings and the absolute and relative to the ground state (in parenthesis) symmetries of the 16 magnetic modes when a finite inter-dimer DM interaction d_c is present. A finite intra-dimer DM term d_{ab} will further split the modes which belong to the one-dimensional representations, see Fig.6.8.

the point group associated with the space symmetry of the crystal. We performed the group symmetry analysis of the eigenstates by decomposing the representation obtained starting with the canonical spin basis (the direct product of $|\uparrow>$ and $|\downarrow>$ spinors representing each Cu atom) into the irreducible representations of the D_{2d} point group. Each symmetry element of the D_{2d} group involved the action on spinor state in the orgin of the coordinate system as well as the corresponding permutation of spin indices. Using projection operators we block diagonalized the Hamiltonian and numerical analysis (including the DM terms shown in Fig. 6.8 and discussed in more detail later) allowed us to identify the energy and the predominant spin character of each eigenstate.

Indeed, as it is shown in the right-most column of the Table 6.2 and Fig. 6.11c, the symmetries of the observed one-triplet excitations correspond to the results of group

Table 6.2: Collective spin excitations in zero field: notation, the predominant spin character, S_{tot} and z projection S_z, energy and transition symmetries as observed experimentally and predicted from the 4-spin cluster in Fig. 1 corresponding to $k = 0$ excitations.

Mode	S_{tot} (S_z)	Energy	Symmetry	
			Experiment	Group Theory
T_{1a}	1 ($\pm$1)	22.8	-	A_{1g}
T_{1b}	1 ($\pm$1)	22.8	A_{2g}	A_{2g}
T_{1c}	1 (0)	24.2	-	E
T_{1d}	1 (0)	24.2	-	E
T_{1e}	1 ($\pm$1)	25.6	B_{1g}	B_{1g}
T_{1f}	1 ($\pm$1)	25.6	B_{2g}	B_{2g}
S_1	0 (0)	28.9	B_{1g}	-
T_2	1	37.5	A_{2g}	-
T_3	1	40.8	A_{2g}	-
S_2	0	43.0	B_{1g}	-
T_4	1	44.5	A_{2g}	-
S_3	0	45.2	B_{1g}	-
T_5	1	50.9	A_{2g}	-

theory analysis. The latter predicts for the six elementary triplets the A_1, A_2, B_1, B_2 and E symmetries, see Fig. 6.11. The E modes, T_{1c} and T_{1d}, cannot be observed in zero field when the light propagates parallel to the c-axis because they are accessible only in (ca) or (cb) polarizations. The fully symmetric T_{1a} mode which, within the spin model including J_1, J_2 and the out-of-plane inter-dimer DM interaction proposed in Ref. [220], should be degenerate with the strong T_{1b} (A_2 symmetric) excitation at 22.8 cm^{-1} is also not observed. This is most probably due to a much weaker coupling to light in this symmetry channel. The analysis shown in Fig. 6.11 shows that the pair of T_{1e} and T_{1f} modes at 25.6 cm^{-1} are to be seen in the B_1 and B_2 symmetry

channels which explains the weak feature seen in Fig. 6.10 in all polarizations except the (RR) scattering geometry. The observation of the T_{1e} (T_{1f}) modes with B_1 (B_2) symmetries 2.8 cm^{-1} above the A_2 symmetric mode T_{1e} allows the determination of the magnitude of the inter-dimer interaction d_c (see Fig. 6.11) and also of its absolute sign because a sign change will interchange the position of these modes around the gap Δ. Finite intra-dimer Dzyaloshinskii-Moriya interactions (red arrows in Fig. 6.8) will split slighlty the energies of the states in Fig. 6.11 which belong to the one dimensional representations. These effects will be discussed in more detail later where we analyse quantitatively the behavior of the spin excitations in magnetic fields applied parallel and perpendicular to the c-axis.

We turn now to the discussion of two-triplet states. Besides the singlet ground state and six one-triplet states, the symmetry analysis of the 4-spin cluster shown in Fig. 6.11 predicts the following: one $S = 0$ two-triplet bound state to be observed in the B_{1g} channel, three branches with A_1 and double degenerate E symmetries which belong to another bound $S = 1$ excitation and five branches of a quintuplet ($S = 2$) state to be accessed in the A_1, A_2, B_1 and E channels. Their symmetries, along with the energies for the particular value $x = 0.3$ chosen as an example, are shown in Fig. 6.11c. We observe that due to symmetry reasons none of the A_2 symmetric modes from T_2 to T_5 having energies higher than 30 cm^{-1} qualify for an interpretation as triplet bound states generated within the 4-spin cluster. This is consistent with the fact that larger cluster sizes are necessary in order to capture the more delocalized nature of these excitations which implies that they have contributions from the differents parts of the Brillouin zone. The fact that the existence of the strong A_2 symmetric bound triplet state at an energy $1.55 \cdot \Delta = 37.5$ cm^{-1} has not been predicted by high order perturbative analysis [215] suggest that other spin interactions have to be taken into account in order to explain the excitation spectrum. Apparently, symmetry considerations would allow the 28.9 cm^{-1} feature denoted by S_1 in Fig. 6.10 to be interpreted as the singlet bound state of two triplets within a unit cell. As we show in the following section, this 28.9 cm^{-1} mode does not shift in external

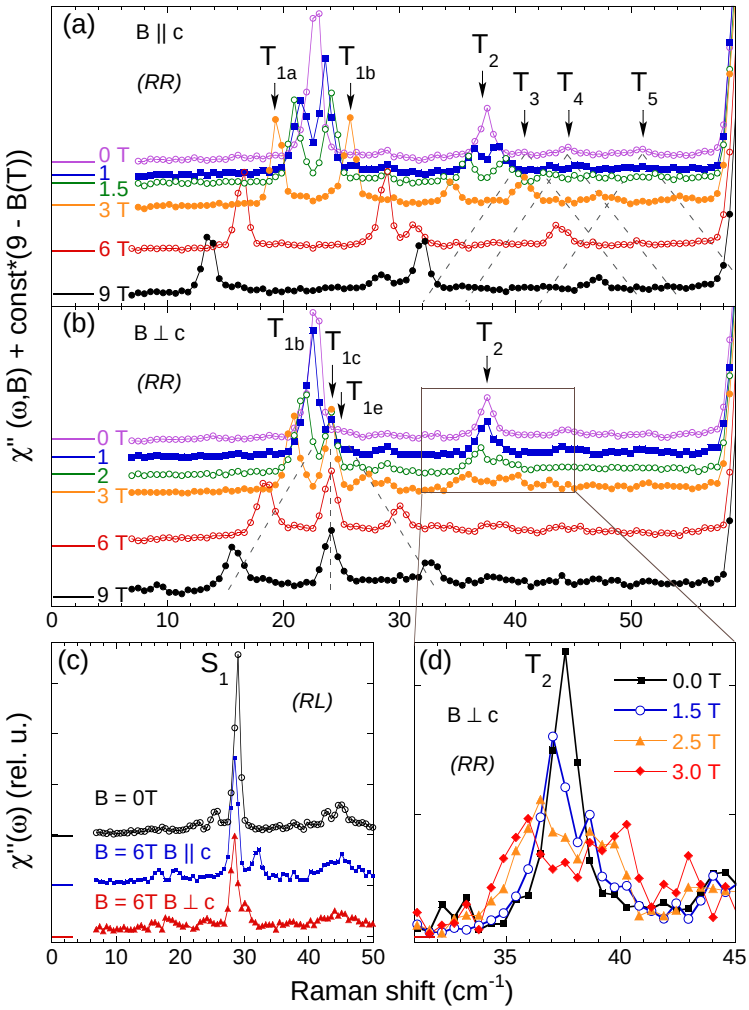

Figure 6.12: Magnetic field dependences of the magnetic excitations at T = 3 K using the $\omega_L = 1.92$ eV excitation energy in the following geometries: (a) (RR) $\vec{B} \parallel \hat{c}$. (b) (RR) $\vec{B} \perp \hat{c}$. In (c) the (RL) polarized data is shown for 0 and 6 T magnetic fields for both $\vec{B} \parallel \hat{c}$ and $\vec{B} \perp \hat{c}$. In (a) and (b) the vertical shift is proportional to the magnetic field difference with respect to the 9 T spectrum and the dashed lines are guides for the eye.

fields, which is compatible with a collective singlet excitation as discussed in [224], but suggests that its internal structure is not the one derived from the 4-spin cluster.

In Fig. 6.12, using the same mode notations, we show the influence of an external magnetic field applied parallel and perpendicular to the c-axis on the low temperature Raman spectra from Fig. 6.10. The relevant aspects are the following. In panel (a) we observe the splitting of the T_{1a} and T_{1b} modes in magnetic fields B $\parallel c$, the B = 1 T showing that the A_2 mode (T_{1b}) present in zero field disperses upwards with increasing the magnitude of the field. Dashed lines in this figure mark the dispersion of the much

weaker modes T_3, T_4 and T_5. In Fig. 6.12b one of the E modes becomes Raman active due to symmetry lowering for $\vec{B} \perp \hat{c}$ configuration and we observe three dispersing branches of the gap multiplet. Fig. 6.12c shows that the B_1 symmetric excitation at 28.9 cm^{-1} does not change its energy with field, only a very small negative shift of the order of 0.5 cm^{-1} from 0 to 6 T is seen because of the crossing with the upward dispersing gap branches seen in (RR) polarization. Panel (d), which is a zoomed in region of Fig. 6.12b, shows that several modes become Raman active in finite fields $\vec{B} \perp \hat{c}$ around 38 cm^{-1} where the T_2 excitation lies. The internal structure of this higher energy multiplet is composed of modes dispersing up, down or independent of magnetic field. Remarkable is their similar selection rules and dynamics in magnetic fields of the collective modes around 38 cm^{-1} and 24 cm^{-1}. The emergence in finite fields of several strong modes in the spin gap region precludes the observation of the weak T_{1e} and T_{1f} modes from Fig. 6.10.

Fig. 6.13 summarizes the magnetic field dependencies of the energies and spectral weights of the most intense Raman excitations. The symbols in Fig. 6.13a-d correspond to experimental data, dashed lines are guides for the eye while the solid lines are results of a numerical diagonalization of a 4-spin cluster using the same set of parameters. Taking into account that the 4-spin cluster neglects many-body gap renormalization effects (see Fig. 6.9) leading to a singlet-triplet energy independent of $x = J_2/J_1$ as well as the fact that when using periodic boundary conditions there is an effective doubling of the J_2 and inter-dimer DM interactions from Eq. 6.2, we chose the following values: $J_1 = \Delta = 24.2$ cm^{-1} which is the value of the spin gap, see the Table 6.2; $x = 0.556$ from the ratio of the energies of the sub-gap mode at 21.5 cm^{-1} [222, 225] with respect to the gap Δ (see Fig. 6.11); an inter-dimer DM term parallel to the c-axis, $d_c = 1.4$ cm^{-1}, which produces the splitting of the $T_{1a,b}$ and $T_{1e,f}$ branches from 24.2 cm^{-1} (our value is consistent to the one proposed in the literature [220]); finally, from the magnetic field value around which the intensities crossing in Fig. 6.13 takes place, the value chosen for the intra-dimer interaction was $d_{ab} = 2.66$ cm^{-1}.

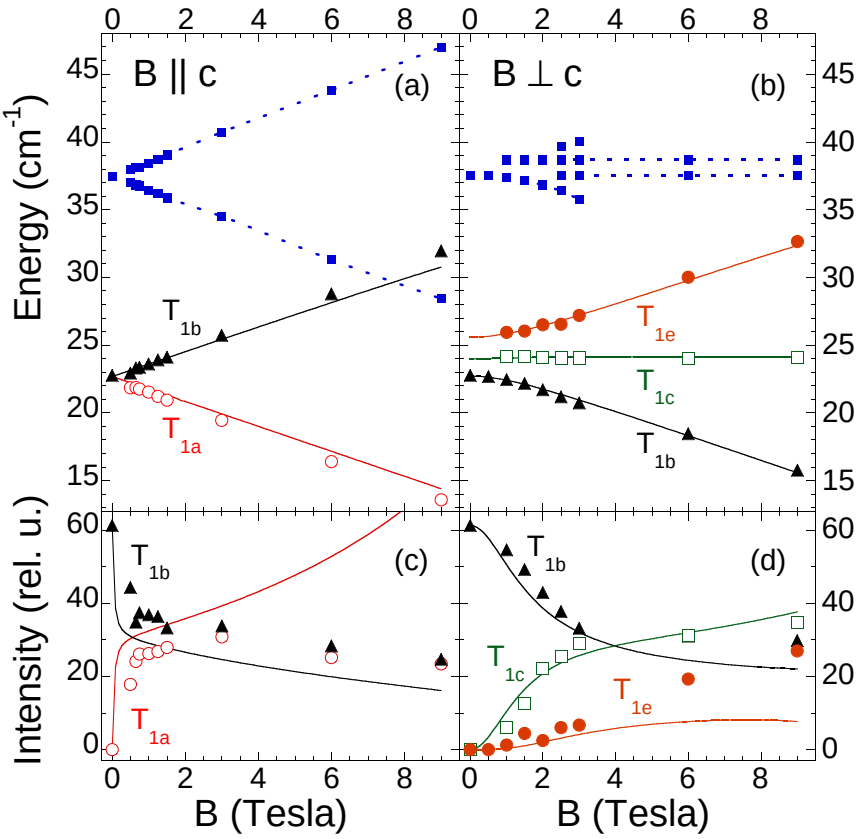

Figure 6.13: Energies (panels a and b) and intensities (panels c and d) of the spin excitations for $\vec{B} \parallel \hat{c}$ (right) and $\vec{B} \perp \hat{c}$ (left) from Fig. 3a-b. Symbols represent experimental points, solid lines are the results of 4-spin cluster diagonalization as described in the text, dashed lines are guides for the eye.

The term containing the intra-dimer DM interaction is proposed by us in order to explain the coupling and selection rules with magnetic fields. Symmetry considerations impose in the $I\bar{4}2m$ group for the directions of the in plane DM vectors the ones depicted in Fig. 6.8 with the Hamiltonian reading:

$$\hat{h}_{ab} = \vec{d}_{ab}^{12}(\vec{S}_1 \times \vec{S}_2) + \vec{d}_{ab}^{34}(\vec{S}_3 \times \vec{S}_4) \tag{6.3}$$

The interaction terms responsible for the coupling to the external photon field and which were used for the calculation of intensities in Fig. 6.13c-d are discussed in the next part. We also plotted (filled squares and dashed lines) the field dependence of other higher energy modes observed in Fig. 6.12.

We remark an overall qualitative agreement for this choice of parameters which suggests that the intra-dimer interaction has to be taken into account in the spin Hamiltonian. The agreement is quantitative as regards the energies and the intensity

variations for the $\vec{B} \perp \hat{c}$ case. The term described in Eq. 6.3 plays a crucial role in obtaining a finite coupling to the excited $S = 1$ triplets which is not realized by the d_c terms in Eq. 6.2. Regarding the apparent degeneracy of the T_{1a} and T_{1b} as well as that of the T_{1e} and T_{1f} modes although they belong to different representations, we note that these two groups of excitations are split by $\hat{h}_{ab}$ but the splitting is very small, of the order of $d_{ab}^2/\Delta \approx 0.25$ cm^{-1}. The largest discrepancy between the experimental data and the calculation is seen in Fig. 6.13. One aspect in this regard is that the value d_{ab} had to be chosen greater than that of d_c. This is intriguing because the d_c term is allowed by symmetry both above and below the structural phase transition at 395 K [213] whereas the existence of a finite intra-dimer DM interaction is allowed only below 395 K when the mirror symmetry of the (ab) plane is just slightly broken. Additional terms may be responsible for this disagreement, possible candidates being in-plane components of the inter-dimer DM interaction, which should also be allowed below the structural phase transition.

We discuss now the issue related to the existence of a magnetic mode *below* the spin gap value [222, 225]. In order to reproduce the upward dispersion with fields $\vec{B} \parallel \hat{c}$ of the T_{1b} mode we had to choose a value of x which is greater than 0.5, otherwise this excitation would have displayed a downward dispersion. From Fig. 6.11 we observe that a ratio of $x = J_2/J_1 \geq 0.5$ implies that the position of the bound singlet state is below Δ. We suggest that this state is responsible for the observations of the 21.5 cm^{-1} mode in Refs. [222, 225]. The presence of this excitation will also influence the specific heat measurements and, in conjunction with the finite intra-dimer interaction d_{ab}, also the low temperature magnetization data whose quantitative understanding has not been achieved yet [205]. The existence of this magnetic mode is at odds with theoretical predictions [215, 216, 218]. However, the experimental finding of the set of A_2 symmetric modes (T_2 to T_5 in Fig. 2, all of them below the two-magnon continuum starting at $2\Delta \approx 48$ cm^{-1} and also not predicted by theory) already shows that the understanding of the spin dynamics in higher particle sectors is not complete.

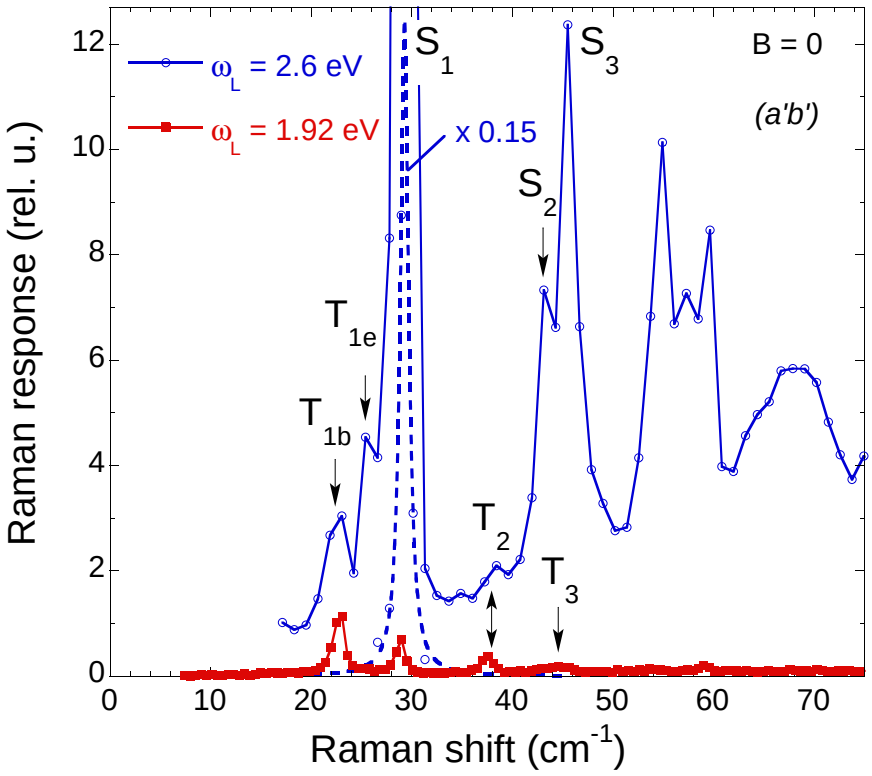

Figure 6.14: T = 3 K Raman data in $(a'b')$ polarization for $\omega_L = 1.92$ (filled squares) and 2.6 eV (empty circles) excitation energies. The data points corresponding to the resonantly enhanced singlet bound state at 29 cm^{-1} are multiplied by 0.15 and the corresponding line represents a Lorentzian fit.

Fig. 6.14 shows two low temperature Raman spectra taken in $(a'b')$ polarization with two incoming laser frequencies, $\omega_L = 1.92$ and 2.6 eV. The point we make is that we observe two types of behaviors. Firstly we notice that the intensities of the group of A_2 symmetric modes, T_{1b} and T_2 is about the same for the two photon energies used. On the other hand, the modes corresponding to the group formed by the T_e, S_1, S_2 and S_3 resonances are more than two orders of magnitude stronger for $\omega_L = 2.6$ eV than for $\omega_L = 1.92$ eV. Other modes in the 50 to 70 cm^{-1} energy range also become visible in the $\omega_L = 2.6$ eV spectrum.

Our data prove that the coupling to these two groups of excitations takes place by two distinct light scattering mechanisms. The resonance of the B_1 symmetric T_e magnetic mode, enhanced for $\omega_L = 2.6$ eV, is similar to the one corresponding to S_1, S_2 and S_3 excitations as well as to the behavior of the new modes seen around 55, 59 and 68 cm^{-1}. On the account of this similarity alone, one cannot identify

the latter as magnetic bound states as well. However, the lack of energy shift in magnetic fields and the results of perturbational analysis regarding energy scales and symmetries [215] are not contradicting their interpretation as Raman active collective $S = 0$ magnetic bound states [224].

We discuss below the nature of the two light coupling mechanisms to magnetic excitations. As for the set of A_2 symmetric modes we propose that the coupling takes place *via* the spin-orbit coupling which can be written in an effective form as $(\mathbf{e}_{in} \times \mathbf{e}_{out})\vec{S}^z_{tot}$ [7]. This interaction Hamiltonian probes excitations with A_2 symmetry and the calculated magnetic field dependence in Fig. 6.13 is also in agreement with the experimental results. The coupling to the T_{1e} and T_{1f} modes from Fig. 6.10 can be understood if we invoke the usual effective spin interaction corresponding to the photon induced spin exchange process $\sum_{<i,j>}(\mathbf{e}_{in} \cdot \mathbf{r}_{ij})(\mathbf{e}_{out} \cdot \mathbf{r}_{ij})\vec{S}_i \cdot \vec{S}_j$. Here the sum runs over pairs of lattice sites, $\vec{S}_i$ and $\vec{S}_j$ are the exchanged spins on sites i and j respectively, while $\mathbf{r}_{ij}$ is the vector connecting these sites [7]. Writing down the explicit expression of this interaction for several polarizations in the 4-spin cluster approximation (Figs. 6.8 and 6.11) one indeed gets finite coupling in B_1 and B_2 channels for the triplet T_{1e} and T_{1f} states. This explains the presence of the 25.6 cm^{-1} modes in all polarizations except (RR).

The difference in the coupling strengths seen in Fig. 6.14 is thus understandable because these two coupling mechanisms need not be simultaneously in resonance with the same high energy excited electronic states. The photon induced spin exchange Hamiltonian has been usually invoked in order to explain Raman active $S = 0$ two-magnon type excitations in various magnetic systems [7]. $SrCu_2(BO_3)_2$ is an example where this Hamiltonian, in the presence of singlet-triplet mixing DM interactions, can be used to account for coupling to $S = 1$ states. A remaining question is why do we not see the bound singlet mode with an energy below Δ for any of the two excitations used? In principle the photon induced spin exchange, resonant in this case at higher photon energies, could provide coupling to this excitation also, as to the 28.9 cm^{-1} mode denoted by S_1. One possible explanation to be explored in more detail from a

theoretical point of view is that the Raman form factors for exciting a pair of magnons both at $k = 0$ is vanishing as opposed to the case of a pair of zone boundary modes. For instance this is the case when the Raman vertex is calculated for the 2D square lattice within the spin-wave approximation and using the Fleury-Loudon interaction Hamiltionian. Consequently, the 21.5 and the 28.9 cm^{-1} excitations could be both attributed to $S = 0$ bound states originating from different parts of the reciprocal space and having substantially different binding energies.

6.4 Summary

We showed in this chapter low temperature Raman data on phononic and magnetic excitations in $SrCu_2(BO_3)_2$. Regarding the former, in the 0 to 350 cm^{-1} range we find several pairs of quasi-degenerate modes which have different symmetries. Group theoretical analysis suggests that the existence of these modes is related to quite different atomic vibrational pattern, i.e. in-plane and c-axis motions and as a result a quantitative investigation would be very interesting. Collective magnetic excitations were studied in terms of symmetry, resonance and coupling mechanisms in zero and applied magnetic fields. The analysis of the 4-spin cluster shown in Figs. 6.8 and 6.11 allows us to understand the group symmetries of the zero field Brillouin zone center spin gap branches around 24 cm^{-1} confirming the picture of local elementary one-triplet modes. By considering an additional intra-dimer DM interaction we are also able to understand the observed selection rules and intensity variations of the spin gap branches in external magnetic fields applied parallel or perpendicular to the dimer planes. These selection rules also require that the energy of the $S = 0$ two-triplet bound state made out of magnons confined within a unit cell is *below* Δ (in the 4-spin cluster this is equivalent to $x \geq 0.5$ in Fig. 6.10) suggesting a very high binding energy for this two particle excitation. The 4-spin cluster analysis fails to account for the two-triplet excitations which shows that they have contributions from the differet parts of the reciprocal space. The existence of a set of four modes

below the onset of two-triplet continuum, at 37.5, 40.8, 44.5 and 50.9 cm^{-1}, in the A_2 symmetry channel, shows that further theoretical analysis is required in order to understand the nature of these composite excitations. Finally, we identified two effective magnetic light scattering Hamiltonians responsible for the coupling to the magnetic modes which allowed us to explain their resonance behavior.

Chapter 7

Conclusions

This work illustrates results obtained on several solid crystalline materials by using inelastic (Raman) scattering. The technique consists of shining focussed laser light onto the sample and then analyze the inelastically scattered light due to the interaction of the incoming photons with the internal excitations of the measured crystal. The control over the polarization state of the photons, the variation of the frequency of the incident light as well as changes in the temperature and external magnetic field allow in principle some conclusions about the characteristics of the excitation spectra in these materials to be drawn. The materials studied belong to the family of correlated electronic systems, they have magnetic $S = 1/2$ ions and the predominat exchange interactions J are antiferromagnetic (AF). To some degree, any of the above mentioned materials can constitute a paradigm for a certain class of low dimensional quantum magnets. For each particular case studied here it was argued why one can identify within the crystal structures quasi one or two dimensional (1D or 2D) subunits which are weakly interacting with each other from the magnetic point of view. Examples are the quasi-1D AF spin chains in NaV_2O_5 , the quasi-1D coupled double-chain structures (forming two-leg ladders) in $(Sr,La)_{14-x}Ca_xCu_{24}O_{41}$, the 2D dimer structure of $SrCu_2(BO_3)_2$ and the 2D square lattice of $La_{2-x}Sr_xCuO_4$. Although topics related to the lattice, charge dynamics and their interplay with the magnetic degrees of freedom are discussed, the emphasis is on the magnetic scattering

from elementary and multi-triplet (magnon) excitations from these compounds.

Raman scattering couples to single magnons (which carry a spin $S = 1$) due to the spin-orbit coupling. This kind of Brillouin zone center excitations is usually seen at lower frequencies and their energy scale is set by small parameters. This is the case in $La_{2-x}Sr_xCuO_4$ or NaV_2O_5 but in two-leg ladders or the dimer structure of $SrCu_2(BO_3)_2$ the situation can be different and the spin gap (defined as the lowest enegy transition from the singlet ground state to an excited $S = 1$ state) turns out to be a good fraction of the main magnetic exchange J. On the other hand, the most often encountered light coupling mechanism to magnetic excitations in AF materials is to a pair of Brillouin zone boundary magnons bound together in a $S = 0$ state. Such two-magnon like excitations set the scale of the high magnetic energy scales because they are typically seen at energies of several $J's$.

In spite of the fact that the variety in the nature of the ground states and spin correlations in each compound is reflected in the magnetic excitation spectra, we are able to find besides differences, also similarities in the spectral shape as well as in the selection rules and microscopic coupling mechanisms in zero or finite external magnetic fields. For example we find that two-magnon scattering from 2D square antiferromagnets is similar regarding the scattering width with the multi-spinon excitations from quasi 1D AF $S = 1/2$ chains. This is however very different from the two-magnon scattering from two-leg ladder materials which shows that the crossover from one to two dimensions is not a smooth process. As for the single magnon excitations in $La_{2-x}Sr_xCuO_4$, NaV_2O_5 or $SrCu_2(BO_3)_2$, it turns out that their salient properties in external magnetic fields could be explained by invoking the presence of the antisymmetric, Dzyaloshinskii-Moriya (DM), interaction. We present below the main results of this study in an order which roughly tries to follow what happens as the dimensionality of the spin systems is increased.

We argued that, at 300 K in NaV_2O_5 , the magnetic properties due to the V atoms which are in a mixed valence state can be mapped onto an array of weakly coupled two-leg ladders at quarter filling factor, which is equivalent (to a certain degree)

to a 1D AF spin chain. We identified the Raman continuum present in parallel polarizations and peaked around 80 meV to four spinon excitations. As opposed with other interpretations in the literature, this assignment was found consistent with the resonance and polarization properties as well as the presence of the second overtone around 160 meV. In particular, the resonance study and the comparison with the optical conductivity data in the 1 - 3 eV frequency region allowed us to show that the multi-spinon continuum is present in parallel polarization not only when the electric field was perpendicular to the chain directions (a-axis) but also when the incoming and outgoing polarizations were along the chains (b-axis). These findings are consistent with the Fleury-Loudon selection rules in the presence of frustrating second neighbor exchange interactions. Particularly important in this respect was the observation of signatures of the fluctuating low temperature zig-zag charge order in the quarter filled ladders (that becomes long ranged at 34 K) up to room temperature. A lower bound for the nearest neighbor magnetic exchange $J \approx 27$ meV was extracted from the peak of the four spinon continuum which, in the absence of any frustrating next nearest neighbor interaction, is situated at πJ.

Below $T_c = 34$ K NaV_2O_5 undergoes a charge ordering transition accompanied by lattice distortions. As opposed to the uniform chain in the high temperature phase when the magnetic excitation spectrum is gapless, below T_c the chains become dimerized and the elementary spin excitations acquire a gap. Low temperature data in magnetic fields reveal the existence of a Raman active magnetic mode at 10.5 meV which appears because of the backfolding of the magnetic branch due to the unit cell doubling along the a-axis. In agreement with theoretcal predictions we show that a simple dimer model which takes into account an antisymmetric DM interaction is able to explain the main selection rules: no splitting or shifts for magnetic fields parallel to the DM vector and the observation of two dispersing modes for fields perpendicular to the DM vector.

$Sr_{14-x}Ca_xCu_{24}O_{41}$ crystals contain Cu-O planes made out of coupled AF chains forming again two-leg ladder structures, but this time they are close to the half filling

factor. The two-magnon excitation, which is a feature analogous to the four spinon continuum in the uniform 1D AF chain, was found at energies $3J \approx 370$ meV. In contrast to the multi-spinon excitation continuum or its counterpart in the 2D square antiferromagnets, this excitation displays a very narrow spectral width. This (unexplained so far) property could be related to the existence of a modulated component superimposed on the characteristic exponential decay of the spin-spin correlations in the two-leg ladder ground state. It is possible that the narrow width could be also related to the existence of magnetic bound states below the continuum which steal a lot of spectral weight from the two-particle continuum which should provide relaxation for the two magnon feature. The resonance study we performed in $Sr_{14}Cu_{24}O_{41}$ shows that, similarly to the insulating 2D layered cuprate materials, the two magnon is in resonance when the incoming laser energy is close to the O2p - Cu3d optical transitions. As opposed to the latter materials, only one broad peak in the resonance profile was observed for the 1.5 - 3.05 eV excitation energy range.

$Sr_{14}Cu_{24}O_{41}$ crystals are not exactly at half filling but they contain a small amount of doped holes (the hole concentration was estimated to be about around 0.07 per Cu atom). The low energy dielectric response and the quasi-elastic Raman response suggested the existence of a charge density wave ground state with short range correlations persistent well above 300 K. A subsequent soft X-ray scattering study confirmed our observations. Moreover, it established that the density wave state is not accompanied by any detectable lattice distortions which means that it is driven by long range many-body interactions. We found that the quasi-elastic Raman scattering is an electronic excitation characterizing $Sr_{14-x}Ca_xCu_{24}O_{41}$ crystals from x = 0 to x = 12 suggesting that density wave correlations are also present up to high temperatures in these crystals. It is possible that the peculiar *dc* transport properties, very similar to the high temperature superconductors in the underdoped limit, could be related to the presence of short ranged collective electronic excitations.

One can reach the two dimensional limit by increasing inter-ladder interactions. A 2D square lattice antiferromagnet has long ranged magnetic order at 0 K and this is

pulled at finite temperatures by inter-layer interactions. An example is $La_{2-x}Sr_xCuO_4$, which is one of the high temperature superconductors. The excitations out of the ordered state can be viewed as spin-waves. Within the Heisenberg model the spin-waves are gapless excitations but in the long wavelength limit gaps may be induced by the presence of small anisotropy terms. Two magnetic modes were observed within the AF region of the phase diagram ($x \leq 0.01$). The one at lower energies ($\approx$ 2 meV) could be identified with the DM induced spin-wave gap. Its anisotropic dispersion obtained for different orientations of the magnetic fields could be explained using a canonical form of the spin Hamiltonian. At slightly higher energies ($\approx$ 5 meV) we found another type of magnetic excitations which appear in the Raman spectra only in finite magnetic fields parallel to the CuO planes and perpendicular to the easy magnetization axis. At 300 K, magnetic fields above 7 T induce a spin-flop like transition to another magnetically ordered state whose staggered component of the magnetization is perpendicular to the direction of the applied field. The selection rules for this spin gap mode, proposed to arise as a result of the in plane XY anisotropy, as well as its temperature dependent spectral weight in finite magnetic fields remain as interesting problems to be pursued.

Anoher aspect we studied was related to possible signatures in the phononic and high energy two-magnon spectra of spin/charge supermodulations at commensurate hole doping concentrations in $x \approx 1/8$ $La_{2-x}Sr_xCuO_4$ and $x \approx 1/8$ and $y \approx 0.4$ $La_{2-x-y}Nd_ySr_xCuO_4$. The weak magnitude of possibly existing charge/spin modulations in the Nd doped structure did not allow us to detect specific Raman signatures on lattice dynamics or two-magnon scattering around 2200 cm^{-1}. We found instead that at these dopings there exists substantial disorder in the CuO_6 octahedra tilts showing that the local structure is different than the average distribution seen by X-ray scattering.

A 2D compound with a disorderd ground state is $SrCu_2(BO_3)_2$. The particular topology of the magnetic exchange interactions makes it very different from $La_{2-x}Sr_xCuO_4$. The excitation spectrum is gapped and a good description of its

magnetic excitations can be achieved starting from the uncoupled dimer limit, similarly to the NaV_2O_5 case, rather than from spin-waves which are characteristic of magnetically ordered states. Our study was focussed on symmetry, resonance and coupling mechanisms to these excitations in zero and applied magnetic fields. The orthogonal arrangement of the spin dimers and the magnetic frustration lead to very localized (in real space) elementary triplet modes which have a charateristic energy of about 3 meV. Indeed, our experimental findings regarding the symmetry of the one triplet modes could be explained by considering a simple two-dimer model forming the unit cell. The inclusion of an additional intra-dimer DM interaction allowed also us to understand the observed selection rules and intensity variations of the spin gap branches in external magnetic fields applied parallel or perpendicular to the dimer planes. A resonance study shows that there are two distinct light coupling mechanisms to these excitations. One is proposed to be the Fleury-Loudon interaction which usually couples to two-magnon excitations and another one is proportional to the z projection of the total spin operator. The finding of several other bound collective magnetic modes at higher energies in the multi-particle channel along with their experimentally determined symmetries is at odds with theoretical predictions and show that further work is required in order to understand the nature of these composite excitations.

References

[1] W. Hayes and R. Loudon, *Scattering of Light by Crystals*, Wiley, New York 1978.

[2] M. G. Cottam and D. J. Lockwood, *Light Scattering in Magnetic Solids*, Wiley, New York 1986.

[3] M. V. Klein, in *Dynamical Properties of Solids*, edited by G. K. Horton and A. A. Maradudin, North-Holland, Amsterdam, 1990, Vol. 6.

[4] M. V. Klein, Chap. 4 in *Light Scattering in Solids I*, edited by M. Cardona, Springer-Verlag, 1983.

[5] P. M. Platzman and N. Tzoar, Phys. Rev. **136**, A11 (1964).

[6] T. Moriya, J. Phys. Soc. Japan **23**, 490 (1967).

[7] P. A. Fleury and R. Loudon, Phys. Rev. **166**, 514 (1968).

[8] G. F. Koster, *Properties of the thirty-two point groups*, M.I.T. Press. 1963.

[9] B. S. Shastry and B. I. Shraiman, Phys. Rev. Lett. **65**, 1068 (1990); B. S. Shastry and B. I. Shraiman, Int. J. of Mod. Phys. B, **5**, 365 (1991).

[10] E. M. McCarron *et al.*, Mater. Res. Bull. **23**, 1355 (1988).

[11] T. Siegrist *et al.*, Mater. Res. Bull. **23**, 1429 (1988).

[12] E. Dagotto and T. M. Rice, Science **271**, 618 (1996).

[13] E. Dagotto, Rep. Prog. Phys. **62**, 1525 (1999).

[14] E. Dagotto , J. Riera, and D. Scalapino, Phys. Rev. B **45**, 5744 (1992); T. M. Rice, S. Gopalan, and M. Sigrist, Europhys. Lett. **23**, 445 (1993).

[15] T. Osafune *et al.*, Phys. Rev. Lett. **82**, 1313 (1999).

[16] M. Uehara *et al.*, J. Phys. Soc. Jpn. **65**, 2764 (1996).

[17] S. Maekawa, Nature **273**, 1515 (1996).

[18] S. Sachdev, Science **288**, 475 (2000).

[19] T. Osafune *et al.*, Phys. Rev. Lett. **78**, 1980 (1997).

[20] N. Nücker *et al.*, Phys. Rev. B **62**, 14384 (2000).

[21] M. Kato *et al.*, Physica C **258**, 284 (1996).

[22] Y. Mizuno *et al.*, Physica C **282**, 991 (1997).

[23] P. W. Anderson, Exchange in insulators, Ch. 2 in Magnetism, Vol. 1, ed. Rado and Suhl, Academic Press (1963).

[24] M. Takigawa *et al.*, Phys. Rev. B **57**, 1124 (1998).

[25] T. Fukuda *et al.*, Phys. Rev. B **66**, 012104 (2002).

[26] R. S. Eccleston *et al.*, Phys. Rev. Lett. **81**, 1702 (1998).

[27] L. P. Regnault *et al.*, Phys. Rev. B **59**, 1055 (1999).

[28] H. Kitano *et al.*, Europhys. Lett. **56**, 434 (2001).

[29] K. Magishi *et al.*, Phys. Rev. B **57**, 11533 (1998).

[30] M. Azuma *et al.*, Phys. Rev. Lett. **73**, 3463 (1994).

[31] T. Barnes *et al.*, Phys. Rev. B **47**, 3196 (1993).

[32] L. D. Fadeev and L. A. Takhtajan, Phys. Lett. **85A**, 375 (1981).

[33] S. R. White *et al.*, Phys. Rev. Lett. **73**, 886 (1994).

[34] J. Oitmaa *et al.*, Phys. Rev. B **54**, 1009 (1996).

[35] M. Matsuda *et al.*, J. of Applied Phys. **87**, 6271 (2000).

[36] M. Kenzelmann *et al.*, Phys. Rev. B **66**, 024407 (2002); see also W. J. Buyers *et al.*, Phys. Rev. Lett. **56**, 371 (1986).

[37] C. Knetter *et al.*, Phys. Rev. Lett. **87**, 167204 (2001).

[38] S. Trebst *et al.*, Phys. Rev. Lett. **85**, 4373 (2000); S. Trebst, PhD Thesis, Bonn University, 2002.

[39] G. Blumberg *et al.*, Phys. Rev. B **53**, R11930 (1990).

[40] S. Sugai *et al.*, Phys. Rev. B **42**, 1045 (1990).

[41] S. Sugai and M. Suzuki, Phys. Status Solidi (b) **215**, 653 (1999).

[42] A. Gozar *et al.*, Phys. Rev. Lett. **87**, 197202 (2001).

[43] M. Windt *et al.*, Phys. Rev. Lett. **87**, 127002 (2001).

[44] T. Nunner *et al.*, Phys. Rev. B **66**, 180404 (2002).

[45] K. P. Schmidt *et al.*, Phys. Rev. Lett. **90**, 167201 (2003).

[46] S. Brehmer *et al.*, Phys. Rev. B **60**, 329 (1999).

[47] A. A. Katanin and A. P. Kampf, Phys. Rev. B **60**, R100403 (2002) and references therein.

[48] C. M. Canali and S. M. Girvin, Phys. Rev. B **45**, 7127 (1992); A. W. Sandvik *et al.*, Phys. Rev. B **57**, 8478 (1998).

[49] R. R. P. Singh *et al.*, Phys. Rev. Lett. **62**, 2736 (1989).

[50] K. P. Schmidt, C. Knetter and G. S. Uhrig, Europhys. Lett. **56**, 877 (2001).

[51] A. Gößling *et al.*, Phys. Rev. B **67**, 052403 (2003).

[52] J. M. Tranquada *et al.*, Nature **429**, 534 (2004).

[53] A. V. Chubukov and D. M. Frenkel, Phys. Rev. Lett. **74**, 3057 (1995); A. V. Chubukov and D. M. Frenkel, Phys. Rev. B **52**, 9760 (1995).

[54] T. Tohyama *et al.*, Phys. Rev. Lett. **89**, 257405 (2002); H. Onodera, T. Tohyama and S. Maekawa, Physica C **392-396**, 203 (2003).

[55] P. J. Freitas and R. R. P. Singh, Phys. Rev. B **62**, 14113 (2000).

[56] A. Gozar, Phys. Rev. B **65**, 176403 (2002).

[57] H. Eisaki *et al.*, Physica C **341-348**, 363 (2000).

[58] M. W. McElfresh *et al.*, Phys. Rev. B **40**, 825 (1989).

[59] P. Knoll *et al.*, Phys. Rev. B **42**, 4842 (1990).

[60] C. Homes, private communications.

[61] A. Gozar *et al.*, Phys. Rev. Lett. **91**, 087401 (2003).

[62] G. Blumberg *et al.*, Science **297**, 584 (2002).

[63] A. A. Abrikosov and I. A. Ryzhkin, Adv. Phys. **27**, 147 (1978).

[64] T. Ohta *et al.*, J. Phys. Soc. Jpn. **66**, 3107 (1997); C. Bougerol-Chaillout *et al.*, Physica C **341-348**, 479 (2000).

[65] N. Ogita *et al.*, Physica B **281&282**, 955 (2000).

[66] E. Orignac *et al.*, Phys. Rev. B **57**, 5812 (1998); R. A. Hyman *et al.*, Phys. Rev. Lett. **76**, 839 (1996).

[67] Z. V. Popović *et al.*, Phys. Rev. B **62**, 4963 (2000).

[68] M. Yoshida *et al.*, Phys. Rev. B **44**, 11997 (1991).

[69] F. Nori *et al.*, Phys. Rev. Lett. **75**, 553 (1995).

[70] S. L. Cooper *et al.*, Phys. Rev. B **42**, R10785 (1990).

[71] M. Troyer, H. Tsunetsugu and T. M. Rice, Phys. Rev. B **53**, 251 (1996).

[72] D. Poilblanc, D. J. Scalapino and S. Capponi, Phys. Rev. Lett. **91**, 137203 (2003) and references therein.

[73] D. Poilblanc *et al.*, Phys. Rev. B **62**, R14633 (2000).

[74] D. Poilblanc *et al.*, Phys. Rev. Lett. **75**, 926 (1995).

[75] S. R. White, I. Affleck and D. J. Scalapino, Phys. Rev. B **65**, 165122 (2002).

[76] L. Balents and M. P. A. Fisher, Phys. Rev. B **53**, 12133 (1996).

[77] S. Katano *et al.*, Phys. Rev. Lett. **82**, 636 (1999).

[78] H. Mayaffre *et al.*, Science **279**, 345 (1998).

[79] G. Grüner, Density waves in solids (Perseus, Cambridge, MA, 1994).

[80] H. Fröhlich, Proc. Roy. Soc. London **A223**, 296 (1954).

[81] L. Degiorgi *et al.*, Phys. Rev. B **44**, 7808 (1991).

[82] P. A. Lee, T. M. Rice and P. W. Anderson, Solid State Commun. **14**, 703 (1974).

[83] G. Grüner, Rev. Mod. Phys. **60**, 1129 (1988).

[84] R. J. Cava *et al.*, Phys. Rev. B **30**, 3228 (1984).

[85] P. B. Littlewood, Phys. Rev. B **36**, 3108 (1987).

[86] M. Born and K. Huang, Dynamical theory of crystal lattices (Oxford, 1954).

[87] M. V. Klein, Chap. 4 in Light Scattering in Solids I, (Ed. M. Cardona, Springer-Verlag, 1983)

[88] P. Abbamonte *et al.*, Hole crystallization in the spin ladder of $Sr_{14}Cu_{24}O_{41}$, accepted for publication in Nature.

[89] P. Abbamonte *et al.*, Science **297**, 581 (2002) and references therein.

[90] F. F. Balakirev *et al.*, cond-mat/9808284 preprint.

[91] T. Vuletić *et al.*, Phys. Rev. Lett. **90**, 257002 (2003).

[92] T. Vuletić *et al.*, cond-mat/0403611 preprint.

[93] T. Takahashi, Phys. Rev. B **56**, 7870 (1997).

[94] M. A. Kastner *et al.*, Rev. Mod. Phys. **70**, 897 (1998) and references therein.

[95] J. G. Bednorz and K. A. Müller, Z. Phys. B - Condensed Matter **64**, 189 (1986).

[96] B. Keimer *et al.*, Phys. Rev. B **46**, 14304 (1992).

[97] I. Bozovic *et al.*, Phys. Rev. Lett. **89**, 107001 (2002).

[98] B. Büchner *et al.*, Phys. Rev. Lett. **73**, 1841 (1994).

[99] J. M. Tranquada *et al.*, Nature **375**, 561 (1996).

[100] B. Keimer and M. Reehuis, private communications.

[101] A. Gozar *et al.*, Phys. Rev. Lett. **93**, 027001 (2004).

[102] A. Gozar *et al.*, Phys. Rev. B **68**, 052511 (2003).

[103] Y. Horibe, Y. Inoue and Y. Koyama, Phys. Rev. B **61**, 11922 (2000); Y. Inoue, Y. Horibe, and Y. Koyama, Phys. Rev. B **56**, 14176 (1997).

[104] A. N. Lavrov *et al.*, Phys. Rev. Lett. **87**, 017007 (2001).

[105] Y. Ando *et al.*, Phys. Rev. Lett. **88**, 137005 (2002).

[106] Y. Ando, A.N. Lavrov, and S. Komiya, Phys. Rev. Lett. **90**, 247003 (2003).

[107] S. Wakimoto *et al.*, Phys. Rev. B **60**, R769 (1999).

[108] M. Matsuda *et al.*, Phys. Rev. B **65**, 134515 (2002).

[109] A.N. Lavrov, S. Komiya, and Y. Ando, Nature **418**, 385 (2003).

[110] R. Coldea *et al.*, Phys. Rev. Lett. **86**, 5377 (2001).

[111] S. Chakravarty, B. I. Halperin and D. R. Nelson, Phys. Rev. B **39**, 2344 (1989).

[112] N. D. Mermin and H. Wagner, Phys. Rev. Lett. **17**, 1133 (1966).

[113] T. Thio *et al.*, Phys. Rev. B **38**, 905 (1988).

[114] M. Matsuda *et al.*, Phys. Rev. B **42**, 10098 (1990); H.-Q. Ding, Phys. Rev. Lett. **68**, 1927 (1992).

[115] A. W. Sandvik *et al.*, Phys. Rev. B **57**, 8478 (1998).

[116] Rajiv R. P. Singh, Phys. Rev. B **39**, R9760 (1989).

[117] J. Lorenzana, J. Eroles and S. Sorella, Phys. Rev. Lett. **83**, 5122 (1999).

[118] I. Dzyaloshinskii, J. Phys. Chem. Solids **4**, 241 (1958).

[119] T. Moriya, Phys. Rev. **120**, 91 (1960).

[120] T. Moriya, Weak Ferromagnetism, Ch. 3 in Magnetism, Vol. 1, ed Rado and Suhl, Academic Press (1963).

[121] L. Shekhtman, A. Aharony and O. Entin-Wohlman, Phys. Rev. Lett. **69**, 836 (1992); L. Shekhtman, O. Entin-Wohlman and A. Aharony Phys. Rev. Lett. **47**, 174 (1993).

[122] C. J. Peters *et al.*, Phys. Rev. B **37**, 9761 (1988).

[123] M A. Kastner *et al.*, Phys. Rev. B **38**, 6636 (1988).

[124] P. W. Anderson, Phys. Rev. **86**, 694 (1952).

[125] A. Aharony *et al.*, Phys. Rev. Lett. **60**, 1330 (1990); R.J. Gooding *et al.*, Phys. Rev. B **55**, 6360 (1997).

[126] B. Keimer *et al.*, Z. Phys. **91**, 373 (1993).

[127] T. Thio *et al.*, Phys. Rev. B **41**, 231 (1990).

[128] F. Keffer, Handbuch der Physik, ed. S Flügge, Springer-Verlag, Berlin, 1966.

[129] J. Zaanen and O. Gunnarsson, Phys. Rev. B **40**, R7391 (1989).

[130] S. A. Kivelson, E. Fradkin and V. J. Emery, Nature **393**, 550 (1998).

[131] A. R. Moodenbaugh *et al.*, Phys. Rev. B **38**, 4596 (1988).

[132] J. M. Tranquada *et al.*, Phys. Rev. Lett. **78**, 338 (1997).

[133] K. Yamada *et al.*, Phys. Rev. B **57**, 6165 (1998).

[134] J. M. Tranquada *et al.*, Nature **375**, 561 (1995); J. M. Tranquada *et al.*, Phys. Rev. B **54**, 7489 (1996).

[135] M.V. Zimmermann *et al.*, Europhys. Lett. **41**, 629 (1998).

[136] M.K. Crawford *et al.*, Phys. Rev. B. **44**, R7749 (1991).

[137] J.D. Axe *et al.*, Phys. Rev. Lett. **62**, 2751 (1989).

[138] Judith A. McAllister, and J. Paul Attfield, Phys. Rev. Lett. **83**, 3289 (1999).

[139] I. Ohana *et al.*, Phys. Rev. B **39**, 2293 (1989).

[140] S. Sugai *et al.*, Phys. Rev. B **39**, 4306 (1989).

[141] W.H. Weber *et al.*, Phys. Rev. B **38**, 917 (1988).

[142] T.R. Thusrton *et al.*, Phys. Rev. B **39**, 4327 (1989).

[143] G. Burns *et al.*, Phys. Rev. B **42**, R10777 (1990).

[144] M. Dumm *et al.*, Phys. Rev. Lett. **88**, 147003 (2002).

[145] A. Manthiram, and J.B. Goodenough, J. Solid State Chem. **92**, 231 (1991).

[146] D. Haskel *et al.*, Phys. Rev. Lett. **76**, 439 (1996); S.-W. Han *et al.*, Phys. Rev. B **66**, 094101 (2002).

[147] G. Blumberg, M.V. Klein, and S-W. Cheong, Phys. Rev. Lett. **80**, 564 (1998); K. Yamamoto *et al.*, Phys. Rev. Lett. **80**, 1493 (1998).

[148] Yu.G. Pashkevich *et al.*, Phys. Rev. Lett. **84**, 3919 (2000).

[149] M.V. Abrashev *et al.*, Phys. Rev. B **64**, 144429 (2001).

[150] S. Yoon *et al.*, Phys. Rev. Lett. **85**, 3297 (2000).

[151] C.H. Chen, S-W. Cheong, and A.S. Cooper, Phys. Rev. Lett. **71**, 2461 (1993); C.H. Chen, and S-W. Cheong, Phys. Rev. Lett. **76**, 4042 (1996).

[152] A. T. Boothroyd *et al.*, Phys. Rev. B **67** 100407 (2003).

[153] V. I. Anisimov *et al.*, Phys. Rev. Lett. **68**, 345 (1992).

[154] R. J. McQueeney *et al.*, Phys. Rev. Lett. **87**, 077001 (2001).

[155] P. E. Sulewsky *et al.*, Phys. Rev. Lett. **67**, 3864 (1991).

[156] M. Isobe and Y. Ueda, J. Phys. Soc. Jpn. **65**, 1178 (1996).

[157] E. Pytte, Phys. Rev. B **10**, 4637 (1974); M. C. Cross and D. S. Fisher, Phys. Rev. B **19**, 402 (1979).

[158] L. N. Bulaevskii, A. I. Buzdin and D. I. Khomskii, Solid State Commun. **27**, 5 (1978); M. C. Cross, Phys. Rev. B **20**, 4606 (1979).

[159] M. Hase, I. Terasaki and K. Uchinokura, Phys. Rev. Lett. **70**, 3651 (1993).

[160] For a review of $CuGeO_3$ properties see J. P. Boucher and L. P. Regnault, J. de Physique I **6**, 1939 (1996).

[161] Y. Fujii *et al.*, J. Phys. Soc. Jpn. **66**, 326 (1997).

[162] W. Schnelle, Yu. grin and R. K. Kremer, Phys. Rev. B **59**, 73 (1999).

[163] A. Damascelli, Ph. D. Thesis, 1999.

[164] J. Hemberger *et al.*, Europhys. Lett. **42**, 661 (1998).

[165] P. A. Carpy and J. Galy, Acta Cryst. B **31**, 1481 (1975).

[166] S. Grenier *et al.*, Phys. Rev. B **65**, R180101 (2002); Y. Joly, S. Grenier and J. E. Lorenzo, Phys. Rev. B **68**, 104412 (2003).

[167] M. J. Konstantinović *et al.*, Phys. Rev. B **65**, 012404 (2002).

[168] H. Smolinski *et al.*, Phys. Rev. Lett. **80**, 5164 (1998).

[169] A. Meetsma *et al.*, Acta Cryst. C **54**, 1558 (1998).

[170] J. Lüdecke *et al.*, Phys. Rev. Lett. **82**, 3633 (1999).

[171] T. Ohama *et al.*, Phys. Rev. B **59**, 3299 (1999); T. Ohama *et al.*, J. Phys. Soc. Jpn. **69**, 2751 (2000).

[172] K. Kobayashi *et al.*, Phys. Rev. Lett. **80**, 3121 (1998).

[173] M. V. Mostovoy and D. I. Khomskii, Solid State Commun. **113**, 159 (2000); M. V. Mostovoy, D. I. Khomskii and J. Knoester, Phys. Rev. B **65**, 064412 (2002).

[174] D. C. Johnston *et al.*, Phys. Rev. B **61**, 9558 (2000).

[175] C. Presura *et al.*, Phys. Rev. B **61**, 15762 (2000); C. Presura *et al.*, Phys. Rev. B **62**, 16522 (2000).

[176] A. Damascelli *et al.*, Phys. Rev. Lett. **81**, 918 (1998); A. Damascelli *et al.*, Phys. Rev. B **61**, 2535 (2000).

[177] S. A. Golubchik *et al.*, J. Phys. Soc. Jpn. **66**, 4042 (1997); Z. V. Popović *et al.*, Solid State Commun. **110**, 381 (1999); M. N. Popova *et al.*, J. Exp. Theor. Phys. **88**, 1186 (1999).

[178] M. J. Konstantinović *et al.*, Phys. Stat. Sol. **215**, 661 (1999).

[179] M. J. Konstantinović *et al.*, J. Phys.: Condens. Matter **11**, 2103 (1999); M. J. Konstantinović *et al.*, Solid State Commun. **112**, 397 (1999).

[180] H. Nojiri *et al.*, J. Phys. Soc. Jpn. **69**, 2291 (2000).

[181] M. Fischer *et al.*, Phys. Rev. B **60**, 7284 (1999).

[182] M. J. Konstantinović *et al.*, Phys. Rev. B **65**, 012404 (2001); M. J. Konstantinović *et al.*, Phys. Rev. B **65**, 245103 (2001).

[183] M. N. Popova *et al.*, Phys. Rev. B **65**, 144303 (2002).

[184] B. Grenier *et al.*, Phys. Rev. Lett. **86**, 5966 (2001).

[185] P. H. M. van Loosdrecht *et al.*, Phys. Rev. Lett. **76**, 311 (1996).

[186] L.D. Faddeev and L.A. Takhtajan, Phys. Lett. A **85**, 375 (1981); J. des Cloizeaux and J. J. Pearson, Phys. Rev. **128**, 2131 (1962).

[187] G. Castilla, S. Chakravarty and V. J. Emery, Phys. Rev. Lett. **75**, 1823 (1995).

[188] C. K. Majumdar and D. K. Ghosh, J. Phys. C **3**, 911 (1970); J. Math. Phys. (N.Y.) **10**, 1388, (1969).

[189] R. R. P. Singh, P. Prelovšek and B. S. Shastry, Phys. Rev. Lett. **77**, 4086 (1996).

[190] V. N. Muthukumar *et al.*, Phys. Rev. B **54**, R9635 (1996).

[191] W. Brenig, Phys. Rev. B **56**, 2551 (1997).

[192] G. Blumberg *et al.*, Phys. Rev. B **53**, R11930 (1996).

[193] J. C. Bonner and M. E. Fisher, Phys. Rev. **135**, A640 (1964).

[194] S. van Smaalen *et al.*, Phys. Rev. B **65**, R060101 (2002).

[195] K. Ohwada *et al.*, Phys. Rev. Lett. **87**, 086402 (2001).

[196] S. Trebst, Ph. D. Thesis, Bonn University, 2002.

[197] G. S. Uhrig and H. J. Schulz, Phys. Rev. B **54**, R9624 (1996); G. Bouzerar, A. P. Kampf and G. I. Japaridze, Phys. Rev. B **58**, 3117 (1998); S. Trebst *et al.*, Phys. Rev. Lett. **85**, 4373 (2000); C. J. Hammer, W. Zheng and r. R. P. Singh, Phys. Rev. B **68**, 214408 (2003).

[198] K. P. Schmidt, C. Knetter and G. S. Uhrig, Phys. Rev. B **69**, 104417 (2004).

[199] T. Rõõm *et al.*, Phys. Rev. B **69**, 144410 (2004).

[200] S. Luther *et al.*, J. Phys. Soc. Jpn. **67**, 3715 (1998).

[201] H. Seo and H. Fukuyama, J. Phys. Soc. Jpn. **67**, 2602 (1998).

[202] M. Aichhorn *et al.*, Phys. Rev. B **69**, 245108 (2004); E. Ya. Sherman *et al.*, Phys. Rev. B **48**, 648 (1999).

[203] R. Valenti, C. Gros and W. Brenig, Phys. Rev. B **62**, 14164 (2000).

[204] G. Blumberg *et al.*, unpublished.

[205] For a recent theoretical review see S. Miyahara and K. Ueda, J. Phys.: Condens Matter **15**, R327 (2003).

[206] H. Kageyama *et al.*, Phys. Rev. Lett. **82**, 3168 (1999).

[207] K. Onizuka *et al.*, J. Phys. Soc. Japan, **69**, 1016 (2000).

[208] K. Kodama *et al.*, Science **298**, 395 (2002).

[209] T. M. Rice *et al.*, Science **298**, 760 (2002).

[210] B. S. Shastry and B. Kumar, Prog. Theor. Phys. Supp. **145**, 1 (2002).

[211] P. W. Anderson, Science **235**, 1196 (1987).

[212] R. W. Smith and D. A. Keszler, J. Solid State Chem. **93**, 430 (1991).

[213] K. Sparta *et al.*, Europhys. J. B **19**, 507 (2001).

[214] K.-Y. Choi *et al.*, Phys. Rev. B **68**, 104418 (2003).

[215] C. Knetter *et al.*, Phys. Rev. Lett. **85**, 3958 (2000).

[216] S. Miyahara and K. Ueda, J. Phys. Soc. Japan (Suppl.), **69**, 72 (2000).

[217] C. Knetter and G. S. Uhrig, Phys. Rev. Lett. **92**, 027204 (2004).

[218] S. Miyahara and K. Ueda, Phys. Rev. Lett. **82**, 3701 (1999).

[219] H. Kageyama *et al.*, Phys. Rev. Lett. **84**, 5876 (2000).

[220] O. Cépas *et al.*, Phys. Rev. Lett. **87**, 157205 (2001).

[221] H. Nojiri *et al.*, J. Phys. Soc. Japan, **68**, 2906 (1999).

[222] H. Nojiri *et al.*, J. Phys. Soc. Japan, **72**, 3243 (2003).

[223] T. Rõõm *et al.*, Phys. Rev. B **61**, 143342 (2000).

[224] P. Lemmens *et al.*, Phys. Rev. Lett. **85**, 2605 (2000).

[225] T. Rõõm *et al.*, cond-mat/0405434.

[226] D. L. Rousseau, R. P. Bauman and S. P. S. Porto, J. Raman Spectroscopy **10**, 253 (1981).

Vita

Adrian Mihai Gozar was born on July 23, 1974 in Targu-Mures, Romania. He lived there until he finished high school at the age of 18. After deciding to go into physics and a long internal debate about what college he should go to, the University of Bucharest was chosen against the Physics Department of the University of Cluj Napoca, a beautiful and old Transylvanian city, very close to his birthplace and located in a nice hilly region. If that had to do with a premonition that he has to get used to a topographically flat area surrounded by cornfields is still an unanswered question. In 1997 he graduated with a degree of Bachelor of Science in physics and in 1998 also got a Master of Science degree from the University of Bucharest. He enrolled in the Ph.D. program at the University of Illinois in 1998 and held a teaching assistantship until 1999. While still a student at the University of Illinois, he has been doing research at Bell Laboratories, Lucent Technologies in New Jersey since the Fall of 1999. In 2004 he was awarded the Goldhaber Fellowship from Brookhaven National Laboratory, which is the place where, in the near future, he intends to continue trying to understand what physics is about.